A Computational Study of Icing Effects on the Performance of an S-Duct Inlet

By

Wonjin Jin

Submitted to the graduate degree program in Aerospace Engineering and the Graduate Faculty of the University of Kansas School of Engineering in partial fulfillment of the requirements for the degree of Doctor of Philosophy

---

Dr. Ray R. Taghavi, Committee Chairperson
John E. & Winifred E. Sharp Professor of Aerospace Engineering

---

Dr. Chuan-Tau Lan
Professor Emeritus of Aerospace Engineering

Dr. Saeed Farokhi
Professor of Aerospace Engineering

Dr. Ronald M. Barrett
Associate Professor of Aerospace Engineering

Dr. Mario A. Medina
Associate Professor of Civil, Environmental and Architectural Engineering

Date defended:_____

The Dissertation Committee for Wonjin Jin certifies that this is the approved version of the following dissertation:

A Computational Study of Icing Effects on the Performance of an S-Duct Inlet

Dr. Ray R. Taghavi, Committee Chairperson
John E. & Winifred E. Sharp Professor of Aerospace Engineering

Dr. Chuan-Tau Lan
Professor Emeritus of Aerospace Engineering

Dr. Saeed Farokhi
Professor of Aerospace Engineering

Dr. Ronald M. Barrett
Associate Professor of Aerospace Engineering

Dr. Mario A. Medina
Associate Professor of Civil, Environmental and Architectural Engineering

Date approved:_____

Abstract

The performance of a diffusing S-duct inlet (M2129) is computationally studied for the effects of inlet icing. Different ice accretion shapes, predicted by numerical analysis in the literature reviewed, are simulated on the inlet lip. Two commercial codes, FLUENT and STAR-CCM+ are used for the steady- and unsteady-state computations. The shear-stress transport (SST) κ-ω turbulence model and large eddy simulation (LES) turbulence model are applied in the computations. The glaze ice shape, which is characterized by intrusive horns, degrades inlet performance, while the effect of the streamlined rime ice shape is negligible. At the free-stream Mach number of M_∞=0.23, the glaze ice causes a 3.2 percent decrease in the total pressure recovery and a 26 percent reduction in the inlet mass flow rate. This result comes from the massive flow separation and flow blockage from the glaze ice horns. The total pressure recovery is further decreased by 22.8 percent, as the free-stream Mach number increases to M_∞=0.85, due to the increased internal blockage and formation of internal shocks in the S-duct inlet. Also, the glaze iced inlet induces 6.6 percent increase in the engine thrust loss and the specific fuel consumption at M_∞=0.25. The level of the ice-induced flow blockage by the ice accretion is also important for the inlet performance. The symmetrical glaze ice that covers the entire inlet lip portion causes a nearly 11.8 percent decrease in the total pressure recovery at M_∞=0.475, whereas the top- or bottom-asymmetrical glaze ice that accretes on a ¼ portion of the inlet lip leads to just a 2.5 percent decrease. Also,

the dynamic inlet distortion level, which is represented by the total pressure fluctuation at the engine face, is almost doubled with the symmetrical glaze ice when compared to the asymmetrical glaze ice. Therefore, the dynamic inlet distortion is proportional to the total pressure recovery that corresponds to the steady-state inlet distortion. Furthermore, the application of local angles of attack and local sideslip angles for the iced S-duct inlet contributes to the further degradation of the inlet performance, regardless of the ice shapes. However, the angles that provide the most distortion for each ice shape all differ due to the combined effects of the angle of attack or sideslip angle, icing location, and downward duct curvature. In addition, both the steady-state inlet distortion and dynamic inlet distortion become most severe at the highest angles tested: symmetrical (α=+20º), top-asymmetrical (α=-20º), bottom-asymmetrical (α=+20º), and side-asymmetrical glaze (β=-20º). Finally, a strongly coupled temperature-total pressure distortion is created at the engine face under the icing condition. This coupling, as measured by the total pressure distortion parameter, increases the engine face distortion by 6.97 percent in the glaze iced inlet at M_∞=0.85 when the inlet wall is heated to 350 K.

\

Acknowledgments

The author wishes to express sincere appreciation to his advisor, Professor Ray R. Taghavi for patient guidance and continuous encouragement through the duration of his studies at the University of Kansas.

The author also would like to acknowledge the contributions of Dr. Chuan-Tau Lan in providing the inspiration of this research and considerable advise. The author wishes to thank Dr. Saeed Farokhi for valuable advice on this research and constructive discussions. The author's gratitude is also extended to other committee numbers, Dr. Ronald M. Barrett and Dr. Mario A. Medina for helpful comments and suggestions.

The author was fortunate to have had the assistance of Mr. Adam Hock and Mr. Charles Henry in using the computing cluster at the Information and Telecommunication Technology Center (ITTC) at the University of Kansas.

The author's most appreciation goes to his parents, Mr. Choong-Man Jin and Mrs. Choon-Ja Hur, for unlimited love and support throughout his entire life. This dissertation is dedicated to the author's parents.

Finally, the author is deeply and forever indebted to his wife, Min-Jung and his daughter, Se-Joeng, for understanding and sacrifice during the time of his study.

Table of Contents

Table of Contents (cont.)

Nomenclature

Symbol	Definition	Unit
A	Area	m^2
$\vec{A}$	Surface area vector	m^2
D_{th}	Throat diameter	m
F_n	Engine net thrust	kN
k	Thermal conductivity	W/m-K
L	Length	m
M	Mach number	-
M_{th}	Throat Mach number	-
M_∞	Free-stream Mach number	-
$\overline{M}$	Area-averaged Mach number	-
P	Pressure	kPa
Ps	Static pressure	kPa
Ps_{ef}	Static pressure at engine face	kPa
Pt	Total pressure	kPa
$Pt_{,max}$	Maximum total pressure	kPa
$Pt_{,min}$	Minimum total pressure	kPa
Pt_{PD}	Total pressure at peak distortion	kPa
Pt_∞	Freestream total pressure	kPa
Pt_{ef}	Total pressure at engine face	kPa
Pt_{th}	Total pressure at engine face	kPa
$\overline{Pt}$	Area-averaged total pressure	kPa
$\overline{Pt}_{ef}$	Area-averaged total pressure at engine face	kPa
$\overline{Pt}_{ef\text{-}clean}$	Area-averaged total pressure at engine face of clean inlet	kPa
$\overline{Pt}_{ef\text{-}INS}$	Instantaneous area-averaged total pressure at engine face	kPa
$\overline{Pt}'$	Area-averaged total pressure fluctuation at the engine face	kPa

Nomenclature (cont.)

Symbol	Definition	Unit
$\overline{Pt}'_{rms}$	rms of total pressure fluctuation at engine face	kPa
$Pt(\theta)$	Lowest area-average total pressure in a sector of θ extent	kPa
$\overline{Q}_{ef}$	Area-averaged dynamic pressure at engine face	kPa
R	Radius	m
R_{ef}	Engine face radius	m
R_{th}	Throat radius	m
S_ϕ	Source of ϕ per unit volume	-
$T_{ef,max}$	Maximum static temperature at the engine face	°C or K
$T_{ef,min}$	Minimum static temperature at the engine face	°C or K
$\overline{T}_{ef}$	Area-averaged static temperature at the engine face	°C or K
Ts	Static temperature	°C or K
Ts_∞	Freestream static temperature	°C or K
Tt_∞	Freestream total temperature	°C or K
T_w	Wall temperature	°C or K
Δt	Time step size	sec.
ΔT	Static temperature increment	°C or K
$\Delta T_{ef,\,max}$	Maximum static temperature distortion at the engine face	°C or K
u_τ	Friction velocity	m/sec.
V	Velocity	m/sec.
$\vec{\upsilon}, \vec{V}$	Velocity vector	m/sec.
V_∞	Free-stream velocity	m/sec.
x, X	Geometrical axial direction	m
Δx	Spatial derivative in X-direction	m
y, Y	Geometric radial direction	m

Nomenclature (cont.)

Symbol	Definition	Unit
y_p	Distance from point P to the wall	m
y^+	Wall function	-
z, Z	Geometric radial direction	m
Z_{cl}	Z-direction Cartesian coordinates along the duct centerline	m
ΔZ_{cl}	Centerline offset distance in Z-direction	m

Greek Symbols

α	Angle of attack	deg.
β	Sideslip angle	deg.
δ_v	Viscous length scale	-
ε	Dissipation rate	-
ϕ	Scalar quantity	-
$\nabla\phi$	Gradient of ϕ	-
κ	Turbulence kinetic energy	m^2/sec^2
λ_{max}	Local maximum Eigen value	-
μ	Micro-	-
μ	Viscosity	kPa-sec.
ν	Kinematic viscosity	$m^2/sec.$
θ	Circumferential angle	deg.
ρ	Density	Kg/m^3
τ_w	Wall shear stress	k Pa
ω	Specific dissipation rate	-
Γ_ϕ	Diffusion coefficient for ϕ	-

Nomenclature (cont.)

Symbol	Definition	Unit
$\vec{\Omega}$	Vorticity vector	rad/sec.

Acronyms

AGARD	Advisory Group for Aerospace Research and Development	-
BWB	Blended-wing body	-
CFD	Computational fluid dynamics	-
CFL	Courant-Friedrichs-Levy or Courant number	-
CPU	Central processing unit	-
DC(θ)	Total pressure distortion coefficient	-
DES	Detached eddy simulation	-
DNS	Direct numerical simulation	-
DP	Total pressure distortion parameter	-
FAA	Federal Aviation Administration	-
IRA	Icing Research Tunnel at NASA Glenn Research Center	-
ITTC	Information and Telecommunication Technology Center	-
LES	Large eddy simulation	-
LEWICE	Lewis Ice Accretion Code	-
LWC	Liquid water contents	g/m^3
MB	Mega byte	-
MVD	Mean volume diameter	mm
NACA	National Advisory Committee for Aeronautics	-
NASA	National Aeronautics and Space Administration	-
PD	Peak distortion parameter	-
RAM	Random access memory	-
RANS	Reynolds averaged Navier Stokes	-

Nomenclature (cont.)

Symbol	Definition	Unit
RCS	Radar cross section	-
RNG	Re-normalized group	-
rms	Root mean square	-
rpm	Revolution per minute	r/min.
RSM	Reynolds stress model	-
S-A	Spalart-Allmaras	-
SFC	Specific fuel consumption	g/kN·sec
SST	Shear stress transport	-
TD	Temperature distortion parameter	-
UAV	Unmanned aerial vehicles	-
UCAV	Unmanned combat air vehicle	-
VG	Vortex generators	

List of Tables

List of Figures

List of Figures (cont.)

List of Figures (cont.)

List of Figures (cont.)

List of Figures (cont.)

List of Figures (cont.)

List of Figures (cont.)

List of Figures (cont.)

1. Introduction

Aircraft flying through clouds made of super-cooled water droplet are always subject to ice accretions on their surfaces, such as a leading edge of wings, engine inlet lips, and tail-planes. It is known that 803 aviation accidents and incidents from 1975 to 1988 were related to in-flight icing problems.[1] Therefore, the ice accretion phenomenon has been one of the most serious meteorological problems to the aircraft. Icing accretion is also hazardous to unmanned aerial vehicles (UAV). 25 percent of the U. S. Army's UAV flights still encountered icing problems in Kosovo, although they were not initially flown during the winter, and flights were not launched when icing was forecast.[2]

The ice accretion types are determined by meteorological parameters, such as liquid water contents (LWC), water droplet size (mean volume diameter, MVD), and flight conditions, such as temperature, flight speed, and icing time. The ice accretion types are generally classified as *rime* and *glaze*, according to the meteorological parameters and flight conditions. Rime ice type has a relatively smooth shape, and it accretes on the aircraft's surface at lower temperature [3] and lower value of LWC.[4] On the other hand, glaze ice type is characterized by thick horns, and it occurs at higher temperature conditions with higher LWC.[3]

In the past decades, numerous numerical and experimental studies have been conducted to predict the characteristics of ice accretion on the wings and airfoils, and the icing effects on the aerodynamic performance. Therefore, relatively less attention has been paid to the icing effects on the performance of the aircraft inlets for gas

turbine engines. This state of affairs is due to the fact that the large portion of in-flight icing accidents and incidents have been caused by the ice accretion on the wing section of low-speed aircraft, not equipped with proper ice protection systems.[5]

However, ice accretion on an engine inlet is still hazardous for the entire engine system and aircraft under some real-world operating conditions. In particular, ice accretion on an engine inlet lip can alter the gross shape of the inlet lip, resulting in the deterioration of a *steady-state inlet distortion* at the inlet engine face, which is represented by total pressure recovery, due to strongly separated-boundary layers. Furthermore, ice particle ingested from the inlet lip have a potential to damage the engine compressors, and can cause a power loss and engine flame out in severe cases.[6],[7] If the engine inlet has a double-curvature geometry with a diffuser shape (diffusing S-duct inlet) for installation purpose, the secondary flow and adverse pressure gradient in the inlet can contribute to a worse distortion, when coupled with icing effects.

Unsteadiness that accompanies vortex shedding phenomena from a duct curvature and from the horns of ice accretion would give rise to a time-dependent distortion at the engine face, i.e., *dynamic inlet distortion*. The sharp peaks of dynamic distortion behavior, which last in a time scale of the order of compressor through-flow time, can lead to a compressor stall and engine surge. Inlet wall-heating, a common method for ice protection, causes a temperature distortion, which is accompanied by density distortion as well, in an inlet. The density distortion creates a non-uniform velocity field that can affect total pressure distortion: inlet wall-heating can bring about the coupled temperature-total pressure distortion.

In actual icing conditions, the ice accretion shape on an engine inlet lip is not necessarily always symmetrical in a circumferential direction of an inlet. If ice accretes on a specific portion of an inlet lip, i.e., asymmetrical ice accretion, the flow starts with an asymmetry that will only be amplified in a diffusing S-duct inlet. Angle of attack or sideslip angle is also a source of flow-asymmetry in the engine inlet, which may cause windward lip separation in addition to asymmetrical inlet flow.

An application of the computational fluid dynamics (CFD) techniques to the icing problem has an advantage over the experimental method in that it can economically reconstruct the low-temperature (below Ts_{∞}=-30 ^{o}C) environment in which ice accretion occurs. Also, CFD simulations are much safer because the experimental tests, including in-flight tests, are always accompanied by numerous risk factors that may be caused by ice.

Therefore, based on the above arguments and assumptions, the primary purposes of the present study are to investigate:

- The effects of two different inlet ice accretion types: rime and glaze on the performance of an S-duct inlet.
- The combined effects of inlet icing and the free-stream Mach numbers (M_{∞}=0.13 to 0.85).
- The effects of symmetrical and asymmetrical ice accretion shapes.
- The effects of inlet icing on the dynamic inlet distortion.
- The effects of ice horn thickness.

- The combined effects of inlet icing and angles of attack or sideslip angles.
- The combined effects of inlet icing and angle of attack or sideslip angle on the dynamic inlet distortion.
- The combined effects of inlet icing and wall heat transfer on the coupled total pressure- temperature distortion.

The diffusing S-duct inlet in this study is the M2129 type-inlet, which has been extensively investigated in other experimental and computational studies. Also, the ice shapes, considered in this study, are based on numerically-predicted geometrical data for ice shapes in the literature.[8] The geometric modeling of the M2129 S-duct inlet with the ice accretion is performed using GAMBIT software.[9] In addition, the computations are executed by running two commercial CFD codes, FLUENT[10] and STAR-CCM+[11], installed in the high-performance computing cluster at the Information and Telecommunication Technology Center (ITTC) at the University of Kansas.

2. Literature reviews

2.1. Ice accretion

2.1.1. Experimental study for ice accretion

Exclusive tests of ice accretion shape in different icing conditions were conducted by Addy.[12] The various airfoils in current use for commercial transports, business jets, and general aviation aircraft were tested for ice accretion in the Icing Research Tunnel (IRT) at the NASA Glenn Research Center. In his study, numerous ice accretion shapes: rime, glaze, and mixed ice, were observed in the different icing conditions with various free-stream velocities, total and static temperatures, liquid water contents (LWC), mean volume diameters (MVD), and testing times. The icing conditions were primarily selected from the Federal Aviation Administration's (FAA) certification envelopes.

Papadakis, *et al*.[13] provided a comprehensive water droplet impingement database for a range of test geometries, including airfoils, finite wings, and an S-duct engine inlet. In particular, experimental impingement tests for an actual S-duct turboprop engine inlet with a scavenge duct showed a considerable impingement along the engine external lip and at the splitter nose dividing the engine flow from the scavenge flow. Some impingements were also observed along the interior sidewall of the main inlet duct for the cases of MVD=21 and 94 μm. In general, the

impingement intensity at all inlet locations tested increased as the droplet size increased from 11 to 94 μm.

In the earlier tests, only the stagnation region had been examined. However, Hansman, *et al*.[14],[15] examined the entire area from the stagnation line to the horn region of glaze ice shapes. A faired 3.5-inch diameter metal-clad and a 2-inch aluminum cylinder were used to simulate the aircraft surfaces. The study indicated that the *feather growth*, into the direction of flow, was prevalent in the horn regions for mixed and glaze accretions in the stagnation region. In very wet conditions with high LWC at warmer temperatures, surface water-runback dominated the off-stagnation region and different types of glaze horn growth, which tended to grow radially, were observed.

Most research studies of ice accretion on airfoils aimed at quantifying the lift, drag, and aerodynamic stability of iced aircraft wings. However, Venkataramani, *et al*.[16] were primarily concerned with the mass rate of ice accretion on aircraft engine stator and rotor blade. They conducted experimental and analytical study of ice accretion on airfoils, typically used in the booster stages of an aircraft engine (General Electric GE90-115B). They found that, over the ranges of variables, the mass ice accretion was a function of the product of LWC, velocity, time, and the Reynolds number of the droplet.

2.1.2. Computational study for ice accretion

Due to recent advances in computational fluid dynamics (CFD), the approach of numerical simulation for the physics of ice accretion has been widely used. Most computational simulations of ice accretion have been carried out by using Lewis Ice Accretion Code: LEWICE.[17] This software was first developed in 1983, as a result of university grants and in- house research at the NASA Lewis Research Center. The LEWICE code embodies an analytical ice accretion model that evaluated the thermodynamics of the freezing process that occurs when super-cooled droplets impinge on a body. The atmospheric parameters; free-stream temperature, pressure, and velocity, and meteorological parameters; LWC, MVD, and relative humidity, can be specified to determine the shape of the ice accretion.[18]

The computational results are typically compared to the experimental data, both qualitatively and quantitatively. While the qualitative comparisons had been favorable, the previous studies did not demonstrate a validation process that quantitatively determined the accuracy of an ice prediction code. Therefore, Wright [18] conducted the quantitative measurements on experimental ice shape and compared the predicted ice shape using LEWICE 2.0, in the following parameters:

- Icing limits
- Maximum and minimum ice thickness (horn length)
- Maximum ice thickness angle (horn angle)
- Ice area

The results of the shape comparison were analyzed to determine the range of meteorological conditions under which LEWICE 2.0 was within the experimental repeatability. The comparison showed that the average variation of the computational results from the experimental data was 7.2 percent, while the overall variability of the experimental data was 2.5 percent.

The simulation of an exact shape of ice accretion is difficult and may be unnecessary, since an actual ice shape is typically extremely complicated and irregular, and only the aerodynamic degradation and design of deicing system are of main interest. Therefore, the actual ice shapes accreted in an airfoil were simplified by Chung, *et al*.[19] with various levels of smoothing factor. The ice shape smoothing is a systematic and useful way of constructing simplified ice geometry for the complicated and irregular actual ice shapes accreted on an airfoil. The numerical results in their study showed that a moderately simplified ice shape on an airfoil produced a similar airfoil performance, in terms of lift and drag, compared to the performance induced by an accurately simulated ice shape. Therefore, it was found that a *reasonable* simplification of a complicated ice accretion shape was acceptable, producing little difference in numerical simulations for the performance of airfoils.

Bidwell, *et al*.[8] made the collection efficiency results and ice accretion calculations for a sphere, a swept wing, swept wing tip, axisymmetric inlet, and Boeing 737-300 inlet (asymmetric inlet) by using LEWICE3D code.[20] In particular, they numerically defined the typical rime and glaze ice shape on the axisymmetrical inlet in the icing conditions; V_∞=25 m/s: Ts_∞=-29.9°C: LWC=0.2g/m^3: MVD=20.36 μm: icing time=30min. and V_∞=25 m/s: Ts_∞=-9.3°C: LWC=0.695g/m^3:

MVD=20.36 μm: icing time=30min. for rime and glaze, respectively. Note that these rime and glaze ice shapes are applied in the present study to investigate the effects on the performance of the M2129 S-duct inlet. Their numerical simulations of ice accretion shapes were compared with the experimentally-measured ice geometrical data of Papadakis, *et al*.[21] All of the ice shape predictions looked reasonable and appeared representative of the conditions from which they were derived. In addition, the basic shapes of rime and glaze ice accretion on the lip of the axisymmetrical inlet and BOEING 737-300 inlet did not differ far from those of ice accretions on a sphere and wings.

2.2. Icing effects

2.2.1. Experimental study for icing effects

The first actual flight test for investigating inlet icing effects on the performance of a turbojet engine was conducted by Acker, *et al*.[22] The types of engine used in the investigation were two turbojet engines with 10 and 11 stage axial flow compressors, respectively. Although the engines were provided with electrical anti-icing boots on the inlet lips, tests were conducted without these anti-icing devices. The operating conditions were natural icing conditions during the actual flight test: LWC was 0.1 to 0.9 g/m^3, and MVD was 10 to 27 μm. They found that ice accretion on the engine inlet resulted in reduction of engine thrust ranging from 9 to 26 percent and an increase in engine tail-pipe temperature of 0 to 160 ^{O}F. The effects

of icing on engine air flow, and on the combined efficiency of the compressor and inlet diffuser were of approximately the same order of magnitude as the thrust losses. The greatest effect of icing on engine performance occurred at LWC=0.9 g/m^3. Also, the test data indicated that ice accretion on the inlet guide vanes accounted for approximately one-half of the total reduction in engine performance caused by ice formations on the air-inlet surfaces. Furthermore, during several flights, the large ice formations on the several components of the engine inlet broke away almost instantaneously and were swept through the compressor, resulting in a momentary decrease in engine speed by approximately 1000 rpm.[22]

Gelder, *et al*.[23] first studied total pressure distortion and total pressure recovery of a supersonic nose inlet in the subsonic icing conditions. Ice was formed on a full scale unheated-supersonic nose inlet in the NASA Lewis icing tunnel. Also, LWC was varied from 0.65 to 1.8 g/m^3 at Ts_∞=15^{o}F and 0^{o}F. The addition of ice to inlet components caused increased total pressure distortion levels and reduced total pressure recovery compared with clear-air values, and the losses increasing with time in icing. In particular, in the icing condition of LWC=1.3 g/m^3 with MVD=16 μm, and in the test condition of a free-stream Mach number of 0.27, total pressure distortion increased from about 6 percent in clear air to 12.5 percent after 2 minutes of icing time. Concurrently, the total pressure recovery decreased from about 98 to 94.5 percent. For the comparable operating conditions, but with the inlet at a 12° angle of attack, a change in distortion level occurred from about 9 to 14 percent with a decrease in total pressure recovery from 97 to 94 percent. The combination of glaze ice, high-corrected weight flow, and high angle of attack yielded the highest levels of

distortion and lowest values of total pressure recovery. The general character of the engine face distortion with an iced inlet was the same as that for the clean air inlet except for steeper pressure gradients (distortion patterns). The total pressure gradients with the inlet studied were predominantly radial, with circumferential gradients occurring at angle of attack.

The test of the performance of an airfoil with actual ice accretion is difficult in a normal wind tunnel, since the ability to control the test temperature under the icing condition is limited. Therefore, installing a simulated ice shape, made from wood or plastic, is an alternative method for the testing of icing effects. Bragg, *et al*.[24] provided a description of the flowfield, resulting from the simulated ice accretion on the leading edge of an airfoil, creating a growth centered at the stagnation point with a backward-facing step like geometries on both the pressure and suction surfaces. They described the flowfield that the laminar or transitional boundary layer separated off the suction surface horn, due to a sufficiently strong adverse pressure gradient and a shear layer formed between this separated region and the inviscid flow. Pressure recovery was delayed in this region, resulting in a constant pressure plateau until the shear layer transitioned to turbulent flow. At this point, the vortex motion within the shear layer entrained an inviscid flow with higher velocity and mixed it with lower velocity flow in the separated region.

The effect of simulated ice shape geometry on airfoil aerodynamics was also experimentally investigated by Kim, *et al*.[25] The ice shapes tested were designed to simulate a single glaze ice horn with the leading edge radius, size, and airfoil surface location varied. They found that the ice horn leading edge radius had only a small

effect on airfoil aerodynamics. However, the aerodynamics performance was very sensitive to the ice shape, size, and location. An almost linear relationship between the loss in maximum lift and ice horn location back on the upper surface was found. Reynolds number was found to have little effect on the aerodynamic results on the airfoil with simulated ice shapes.[25]

Broeren, *et al*.[26] carried out the measurements of the flowfield over a GLC-305 airfoil, configured with the simulated glaze or rime ice shape. From their measurements, it was found that the separation bubbles for the glaze ice configuration were much larger than those for the rime ice case, resulting from the differences in the ice horn geometry. Other than the differences in size, the integral boundary layer characteristics were very similar, and changes in Reynolds number did not significantly affect the separation bubble characteristics.

2.2.2. Computational study for icing effects

After Potapczuk's [27] first employment of a CFD analysis to the iced-NACA 0012 airfoil, numerous computational studies were carried out to investigate the effects of ice accretion on airfoils and wings. In particular, a computational approach in aircraft icing research has been getting more attention, because of the remarkable advance of CFD techniques in recent years, and the difficulties of icing research in the actual flight tests and wind tunnel tests. The computational studies have mainly focused on the icing effects on the different airfoils and wings; however, the very

limited number of CFD studies has been conducted for the icing effects on performance of aircraft engine inlets.

Shim, *et a*l.[28] computationally analyzed the flowfields around iced airfoils using four different turbulence models: one-equation Baldwin-Barth model, Spalart-Allmaras (S-A) model, two-equation κ-ε model, and two-equation shear-stress transport (SST) κ-ω model. These models were typical Reynolds averaged Navier Stokes (RANS) based turbulence models. Analyses were performed with WIND-US code[29] for rime and glaze, and the results were compared with the experimental data. The results showed that the characteristics of the airfoils were affected by the choice of turbulence model. In general, the κ-ω SST model predicted better for the rime ice shape and the S-A model was good for the glaze ice shape. Also, it was found that the choice of turbulence model was more influential when the larger flowfield around the airfoils exhibited large scale flow separation.

The comparison of the effects of several different ice shapes on the aerodynamic performance of two-dimensional airfoils was conducted by Shim, *et al*.[30] Through the computational investigations by using WIND-US code, they found that all the ice shapes had common characteristics, according to its geometric category. Also they conjectured that an aerodynamic performance of an iced airfoil was more strongly dependent on the critical ice shape features, such as ice horns or ridges, than on the local variation of a surface roughness distribution. In addition, the geometry of the suction side of an airfoil was more influential in determining the overall aerodynamic characteristics.

Most of the computational analyses for the effects of ice accretions on the airfoils had been restricted to two-dimensional analyses, since the two-dimensional shapes of ice accretion were already complicated, and the effects of many geometrical parameters in two-dimension still remained unknown. However, Thompson, *et al*.[31] studied the icing effects for a three-dimensional wing by using Cobalt Navier-Stokes equation solver [32] with the application of the S-A turbulence model. The geometric modeling of the three-dimensional ice shapes was accomplished by extending a two-dimensional glaze (944 glaze[12]) along a spanwise direction. In addition, they obtained different three-dimensional ice shapes via various blending functions. The results showed that a moderate spanwise variation lessened the degradation of the wing performance somewhat, effectively providing less volume of ice accretion and producing smaller blockage effects. Additionally, the moderate spanwise variation induced an insignificant change in the location of the primary flow reattachment over the wing. Therefore, they concluded that the influence of a moderate spanwise variation in the ice accretion produced a minor effect on the gross performance of a wing.

The accuracy of the CFD prediction can depend on the numerical algorithm, grid quality or resolution, and ability of the turbulence model to reproduce the key flow physics. Therefore, Chi, *et al*.[33] conducted a comparative study using different CFD solvers: FLUENT, WIND-US, and PowerFLOW. Also, the performances of the following turbulence models were examined by comparing their predictions with available experimental data for the 212 rime and 944 glaze ice [12] on the GLC 305 airfoil. The examined turbulence models were: the S-A model, re-normalized group

(RNG) κ-ε model, SST κ-ω model, V^2-f model, and a differential Reynolds stress model (RSM). The results showed that for the RANS based turbulence models, both FLUENT and WIND-US were found to give nearly identical results, if the same grid size and the same turbulence model were applied to both codes. In general, the S-A model, SST model, and RNG κ-ε model performed well for the prediction of lift, while the V^2-f model and RSM model produced better results for drag coefficient prediction.

The icing effects on turbo-machineries have been of recent interests, since there have been more demands for the development of better ice protection systems for the aircraft engines. Therefore, Lee, *et al*.[34] analytically examined the icing effects on the STAGE 67A stator blade in a turbo-machinery compressor stage. The simulations of ice accretion and of its effect on the flowfield over the stator blade were carried out using LEWICE and WIND-US codes, respectively. The study revealed that changes in the flowfield due to ice accretion led to boundary layer separation, which caused a reduction in the flow turning angle, and an increase in the total pressure loss.

2.3. Summary of literature reviews

From the literature review of experimental and computational studies for ice accretion and the icing effect on the performance of the aircraft's components, the following summaries can be made:

- It was found through an experimental study that ice accretion on an engine inlet induced a decrease in total pressure recovery from 98 to 94.5 percent. Moreover, with the inlet at a 12° angle of attack, a decrease in total pressure recovery from 97 to 94 percent occurred.[23]

- Both experimental and computational studies showed that aerodynamic performance of an iced airfoil was very sensitive to ice shape, ice size, and icing location.[12], [25], [26], [30]

- Computational approach in aircraft icing research has been getting more attention because of the remarkable advance of CFD techniques in recent years and the difficulties of icing research in the flight tests and wind tunnel tests. [27], [28], [30], [31], [33], [34]

- In computational analyses, a reasonable simplification of the complicated ice accretion shape was acceptable, producing little difference in numerical simulations for the performance of airfoils.[19]

- The choice of turbulence model was influential when ice accretion induced larger flow separation.[28], [33]

Based on the literature review, the icing effects on the performance of aircraft inlets were real and substantial. However, relatively less attention has been paid to

the icing effects on the aircraft engine inlets, compared to the present and past focus on iced airfoils and wings. In addition, the computational investigations for the ice accretion characteristics on engine inlets and their effects on the inlet performance has been limited, whereas the numerous CFD studies of the icing problems for airfoils and wings have been carried out. Therefore, the icing effects on the performance of an aircraft inlet, in particular, the M2129 S-duct inlet, are investigated in the present study.

3. Theoretical consideration

In this chapter, the physics of ice accretion on the aircraft's surfaces are explained. The ice accretion is generally categorized by *rime* and *glaze* ice according to the meteorological and aviational conditions. Therefore, the characteristics of rime and glaze ice accretion are also described. In addition, the inlet shape considered in the present study is a diffusing S-duct inlet (M 2129); thus, the geometrical advantages and disadvantages of this inlet type are discussed. One of the geometrical disadvantages of the diffusing S-duct inlet is that a duct curvature always causes *total pressure distortion* at the engine face due to the secondary flow pattern and the flow separation. Therefore, the types of total pressure distortion and their impact on the engine performance are illustrated. Also, the features of *temperature distortion*, which can be induced by thermal ice protection systems, are presented in this chapter.

3.1. Physics of ice accretion

The term*, Ice accretion* or *icing,* describes the process of ice growth on a surface that is exposed to the atmosphere. The rate of the growth of ice depends on the rate of the impaction of icing particles, together with the airflow and thermal conditions, i.e., the meteorological conditions, which is local to the surface. The icing particles may exist as super-cooled water droplets, such as in freezing fog, as in

freezing rain, or as ice crystals agglomerated in the forms of snowflakes.[35] These droplets, which have a diameter of about 10 mm, can exist in the unfrozen state, down to temperatures near Ts_{∞}=-40°C.[35] Under some atmospheric conditions, forming and descending snow crystals may encounter and pass through the atmospheric super-cooled cloud droplets. A contact between the snow crystal and the super-cooled droplets results in freezing of the liquid droplets onto the surface of the crystals, and the crystal grows in the process known as *ice accretion*.

Ice accretion occurs on the surfaces of aircraft, such as a leading edge of wings and engine inlet lip, etc., in flight conditions through a cloud, which is made of super-cooled water liquid droplets. The shape and location of the accreted ice mainly depends on both meteorological and aviational factors, including free-stream temperature, liquid water content, droplet size, the speed of an aircraft, the shape of the accreting surface, and ice protection devices, such as heated surfaces or pneumatic boots. Essentially in Meteorological view point, there are four types of frozen deposits which may accumulate on a surface. These are *rime*, *glaze*, *frost*, and *wet snow*.[36], [37] However, rime, glaze, and mixed ice accretion of rime and glaze have been mainly investigated for aviational research. Rime and glaze ice accretion are classified according to the ice growth processes: dry and wet growth process, respectively.

3.2. Types of ice accretion

3.2.1. Rime ice accretion

Rime ice accretion is an ice deposit caused by the impaction of super-cooled droplets on the aircraft's surface where the temperature is below $Ts_{\infty}=0^{o}C$. In rime icing, convective and evaporative heat losses to the ambient air are sufficient to keep the surface temperature below the freezing point. The super-cooled droplets are usually associated with freezing fog and a droplet size (MVD) which is typically of around 10 μm.[35] On impaction**,** the droplets rapidly lose their latent heat of fusion and freeze in place, maintaining their nearly spherical shape.[38] This accretion process is called a *dry growth process*. The accretion is thus filled with air spaces (or air pockets) between the frozen drops, and the appearance of the brittle ice with the lower LWC, typically LWC < 0.1 g/m^3 [4], is white and opaque. This shape of ice is called *rime ice* and the accretion of rime ice tends to form forward into the free-stream, as shown in Figure 3.2.1.1(a).[39] The rapid release of the latent heat from impacting droplets generally associated with colder air temperature (less than $Ts_{\infty}=-5\ ^{o}C$ [3]) and lower LWCs on the droplets. The roughness of the surface of rime ice accretion is high because numerous small air pockets are contained inside the structure during the instant-freezing on impact.

3.2.2. Glaze ice accretion

Contrary to the dry growth condition for rime ice accretion, the time for impacting droplets to release their latent heat of fusion is relatively slow in a *wet growth condition*. In this condition, the rate of the convective and evaporative heat loss is less than the rate at which heat of fusion would be released. Therefore, the unfrozen droplets, driven by aerodynamic force, deform and move along the surfaces, or flow between frozen drops in a previously collected wet growth accretion, since only a certain fraction (the freezing fraction) of impinging water freezes upon impact. Therefore, the ice accretion structure in a wet growth condition is denser than that in a dry growth condition, and the appearance is more glossy and translucent. Consequently, the ice accretion in this condition is named as *glaze ice*, and the surface is compact and smooth.[38]

Glaze ice accretion usually occurs in warmer temperature conditions (around $Ts_{\infty}=0^{o}C$ [3]) with higher LWC on the droplets with MVD of 500 μ m,[3] because the release of the latent heat is slow in this condition as mentioned before. Actually, it is known that the higher LWC results in an adverse effect on the aircraft engine performance. During the actual flight test using turbojet engine in the natural icing conditions, LWC was 0.1 to 0.9g/m^3, and the greatest effect of icing on the engine performance occurred at LWC=0.9g/m^3.[22] The roughness of a surface of glaze icing is much lower, due to the fact that its structure approaches that of bubble-free ice. The structure of glaze ice accretion is much denser (ρ=917kg/m^3[3]), and tenaciously clings to the surfaces where it forms; accordingly, the accretion layer is much harder compared to rime ice accretion. Therefore, it is more difficult to be removed from the

surfaces of an aircraft, and is consequently more hazardous. In addition, glaze ice accretion generally forms a thicker layer, which is characterized by the horns as shown in Figure 3.2.1.1 (b).[39]

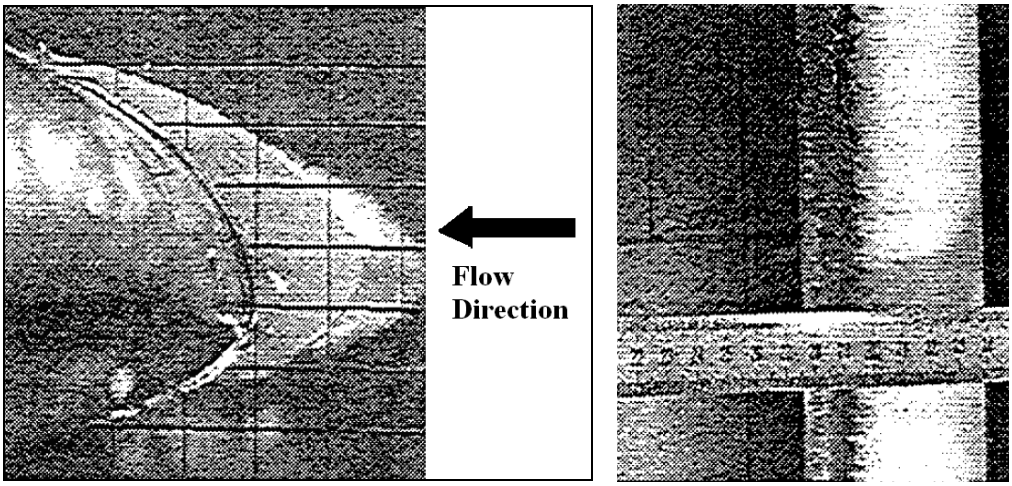

i. Side-view ii. Top-view

(a) Rime

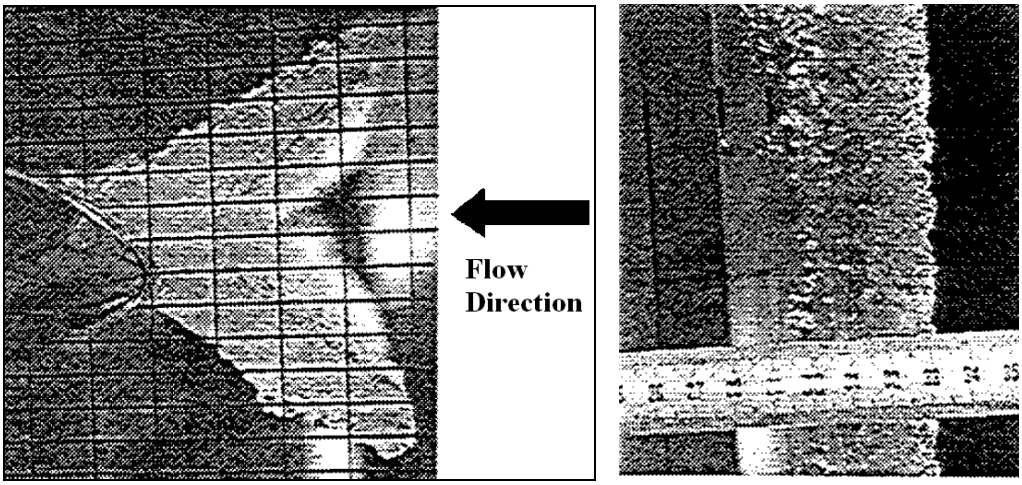

i. Side-view ii. Top-view

(b) Glaze

Figure 3. 2. 1. 1: Photographs of ice accretion shapes on airfoils[39]

3.3. S-duct inlet

S-duct inlets possess the advantages of reduced size and weight by reducing the length of entire inlet ducts. In the past, the commercial airliners such as the Boeing 727, as shown in Figure 3.3.1 (a), [40] and the Lockheed L-1011 successfully utilized S-duct inlet designs. Also, an example of this type of inlet is integrated to the design concept of NASA/Boeing's the Blended-Wing-Body (BWB) commercial transport.[41], [42] As a flush-mounted inlet is integrated on the far-aft portion of the BWB fuselage, the installation of the S-duct between the flush-mounted inlet and the engine face is the only solution for this propulsion system integration.

For military aircraft, the benefits of the S-duct inlet are more apparent. Inheritably, the combat aircraft should be compact to achieve their full agility. Therefore, S-duct inlets are integrated inside their fuselage. General Dynamics F-111, Panavia Tornado, and Lockheed Martin F-16 are well known examples of this configuration. The advent of stealth technology has driven more demands for the utilization of the S-duct inlet. A reduction of the radar cross section (RCS) is a major design factor for stealth aircraft. This trend has led to the engines buried within the fuselage fed by the S-duct inlets that do not provide a direct line of sight to the engine blade. Therefore, the stealth aircraft, such as Northrop B-2, Lockheed Martin F-22 (as shown in Figure 3.3.1 (b)[43]), and F-35, are equipped with this type of the engine inlet. The concepts of the future unmanned combat air vehicle (UCAV) also take advantage of the S-duct inlet due to the required reduction of RCS and minimization of the size and weight of inlets for the fuselage compactness.[44], [45]

The design of the M 2129 S-duct inlet was first proposed by Willmer, *et al*.[46] It has a two curvatures with a diffusing shape, and its cross-section is circular, i.e., axisymmetrical. This diffuser inlet design has been extensively used in various researches to verify the numerical codes and turbulence models [47]-[52] and to investigate inlet flow control array designs for decreasing total pressure distortion at the engine face.[53]-[55]

The geometry of a diffusing S-bend section of the M2129 S–duct inlet can be defined as follows:

The centerline of a diffusing S-bend section:[49]

$$Z_{cl} = -\Delta Z_{cl}\left[1-\cos\left(\pi X_{cl}/L\right)\right] \qquad \text{Equation (1)}$$

The radius distribution of the diffusing S-bend section, measured perpendicular to the duct centerline, is given by:[49]

$$\left(\frac{R-R_{th}}{R_{ef}-R_{th}}\right)=3\left(1-\frac{X_{cl}}{L}\right)^4-4\left(1-\frac{X_{cl}}{L}\right)^3+1 \qquad \text{Equation (2)}$$

Where, $R_{th} = 1.0$, $R_{ef} = 1.183$, $L = 7.6$, and $\Delta Z_{cl} = 2.13$.

Therefore, the area ratio of the engine face to throat is 1.4.

The overall configuration of the M2129 S-duct inlet used in this study is shown in Figure 3.3.2. The geometry of the M2129 S-duct inlet without the inlet lip, as shown in Figure 3.3.2(a), is used for the validation of computational codes in the

present study. For the cases of icing effects, the inlet lip is included in the geometry of the S-duct inlet, as seen in Figure 3.3.2(b), since ice accretion is simulated on the inlet lip.

The shape of an external and internal inlet lip are defined using the geometrical information from Reference 21, and it is shown in Figure 3.3.3.

The shape of the external inlet lip is defined using the equation of ellipse:[21]

$$\left(\frac{x}{a}\right)^n + \left(\frac{y}{b}\right)^m = 1 \qquad \text{Equation (3)}$$

Where, n=2.0, m=1.96, a=0.2234 m, and b=0.0545 m.

The shape of the internal inlet lip is also defined using Equation (3) with the different values:[21]

$$\left(\frac{x}{c}\right)^n + \left(\frac{y}{d}\right)^m = 1 \qquad \text{Equation (4)}$$

Where, n=2.0, m=2.0, c=0.056 m, and d=0.0225 m.

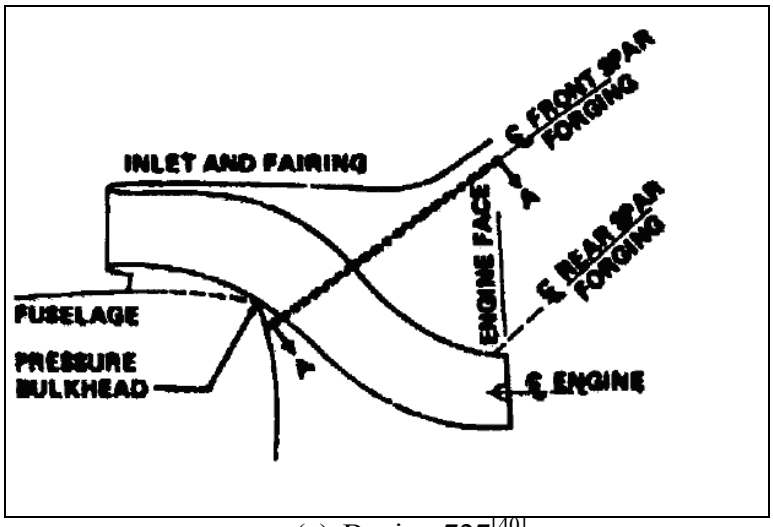

(a) Boeing 727[40]

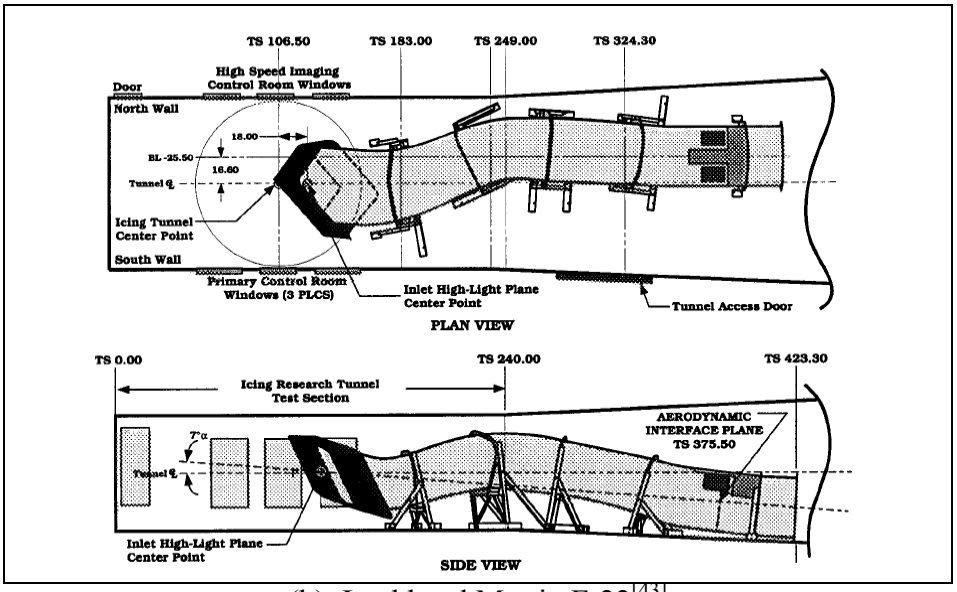

(b) Lockheed Martin F-22[43]

Figure 3. 3. 1: Examples of application of S-duct inlet

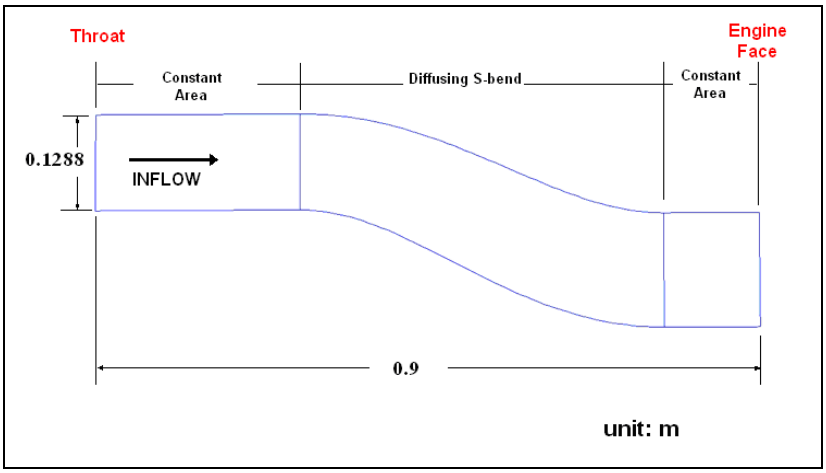

(a) Without inlet lip (for CFD code validation)

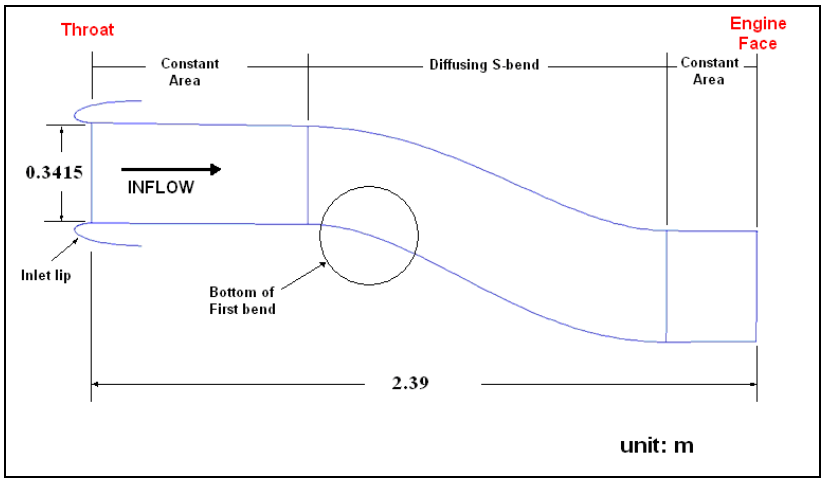

(b) With inlet lip

Figure 3. 3. 2: Geometry of the circular M2129 S-duct inlet

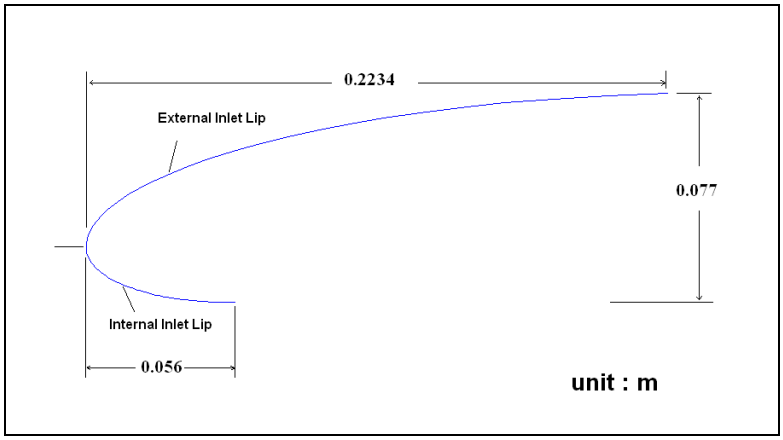

Figure 3. 3. 3: Geometry of inlet lip

3.4. Total pressure distortion in S-duct inlet

The M2129 S-duct inlet is characterized by two curvatures with a diffusing shape. It is known that a simple curved duct induces a secondary flow pattern, which is further amplified in the second bend of an S-duct. In addition, a diffusing duct has an additional burden of potential flow separation due to the streamwise-adverse pressure gradient in the diffuser. Therefore, for the M2129 S-duct inlet, the combined flow separation and secondary flow pattern contribute to the problem of engine face distortion. *Distortion* represents non-uniformity in the flow. The level of distortion that an inlet creates at the compressor face affects the stability of the compressor and engine performance. It is known that typically 1 percent inlet total pressure degradation caused by total pressure distortion leads to about 1.5 percent drop in the net installed thrust in an aircraft gas turbine engine or equivalently approximately 1.5 percent increase in its specific fuel consumption (SFC).[56]

Some of the different types of distortion are caused by non-uniformity in total pressure as in boundary layers, wakes and free shear layers, the non-uniformity in temperature as in gun gas ingestion or thrust reverser flow ingestion, or wall heating with inlet icing, and the non-uniformity in density, as created by hot gas ingestion and wall heat transfer. The penalty associated with all different types of distortion is their destabilization effect on the compressor performance and the cyclic loads they impose on compressor blades. This means that all types of distortions reduce the stability margin of a compressor or fan, potentially to the level of a compressor stall or an engine surge.

The most frequently encountered inlet distortion in flight is *total pressure distortion*, which is caused by separated boundary layers in the inlet. Under normal operating conditions, the boundary layers in the inlet are designed to be well-behaved and remain attached. However in a supersonic inlet, for example, if the boundary layer management system as in the bleed system fails to react abruptly to a change in flight condition, large patches of low-energy, low momentum flow in the inlet could push the compressor into stall or cause an engine surge.

Povodny, *et al*.[57] simulated four steady-state distortion patterns at the compressor face via screens in a ground propulsion test facility using a J-85 turbojet engine. The four types of simulated inlet distortion are shown in Figure. 3.4.1.[58] The result of compressor stall margin deterioration is shown in Figure 3.4.2.[57] The least impact on the stall margin deterioration was caused by *radial hub distortion* followed by *radial tip* and *circumferential hub*, and the highest deterioration of stall margin was caused by the *full-span circumferential distortion*. In the worst case, i.e., the full-span distortion at the 100 percent corrected speed, the engine operated at the stall boundary, i.e., with zero-stall margin.

Further research identified a critical circumferential extent of the spoiled sector that caused the maximum loss in the stall pressure ratio of a compressor at nearly $\theta=60^{o}$, as evidenced in Figure. 3.4.3.[57] This result, the critical extent, is of importance since the angular extent of distortion patches impacts the stability of the compression system.

To quantify the distortion at the engine face, two distortion parameters for total pressure are defined as:[59]

$$DP=\frac{Pt_{,max}-Pt_{,min}}{\overline{Pt}_{ef}} \qquad \text{Equation (5)}$$

$$DC(\theta)=\frac{\overline{Pt}_{ef}-Pt(\theta)}{\overline{Q}_{ef}} \qquad \text{Equation (6)}$$

Where DP denotes the total pressure distortion parameter, and DC(θ) is distortion coefficient, $Pt_{,max}$ and $Pt_{,min}$ are the maximum and minimum total pressures at the engine face, respectively, $\overline{Pt}_{ef}$ is the area-averaged total pressure at the engine face, and Pt(θ) is the lowest area-average total pressure in a sector of θ extent. The first parameter highlights the maximum distortion, whereas the second parameter accounts for a critical sector impact on distortion and compressor stability. The angular extent of the spoiled sector is taken to be $\theta=60^{o}$. Subsequently, the distortion coefficient, so calculated, is denoted by DC(60). Distortion coefficient is most useful when the distortion is of limited angular extent, e.g., $\theta=60^{o}$. However, an axisymmetric inlet is subject to axisymmetric icing, and the entire engine face can be covered by distortion. As a result, if the area-averaged total pressure at the engine face is low, DC(θ) can not be a reasonable parameter. Consequently, a better descriptor of engine face distortion in cases such as inlet icing is the total pressure recovery of the inlet and the total pressure distortion parameter defined in Equation (5). In particular, the total pressure recovery ($\overline{Pt}_{ef}/Pt_{\infty}$) is the most frequently used parameter in this study for evaluating the total pressure distortion level.

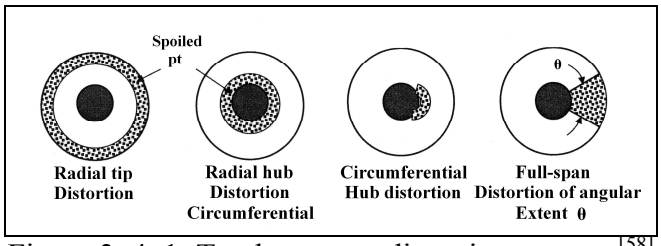

Figure 3. 4. 1: Total pressure distortion patterns[58]

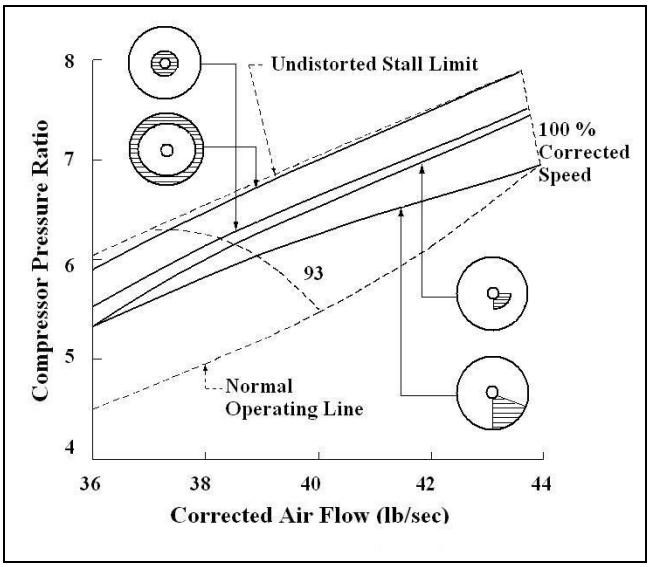

Figure 3. 4. 2: Compressor map with inlet total pressure distortion[57]
(Compressor pressure ratio; $\overline{Pt}_{ef} / Pt_{\infty}$)

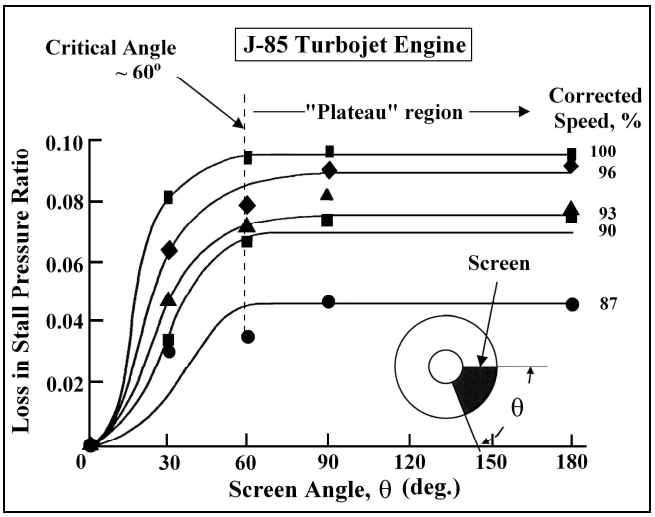

Figure 3. 4. 3: Critical circumferential extent of the spoiled sector with maximum loss in stall pressure ratio (data from Povodny, *et al*.[57])

3.5. Temperature distortion in S-duct inlet

The level of distortion that an inlet creates at the engine face affects the performance and the stability of the compressor. The distortion at the engine face includes not only total pressure distortion, but also *temperature distortion* and *density distortion*. The non-uniformity in temperature, i.e., temperature distortion, can be caused by the gun gas-ingestion, thrust reverser flow ingestion, or wall heating with inlet icing. Also, the non-uniformity in density is created by hot gas ingestion and wall heat transfer. Total pressure distortion at the engine face contributes to the degradation of an S-duct inlet duct performance. Furthermore, it reduces the stability margin of a compressor or fan, potentially to the level of a compressor stall or an engine surge. The temperature distortion also leads to a reduction in stall margin. In practice, the static temperature distortion in a flow brings about a density distortion, which in turn creates a non-uniform velocity field. In particular, heating a wall causes a density gradient to be generated normal to the wall, which is perpendicular to the static pressure gradient in a curved duct inlet. The cross product of these two gradients is proportional to the streamwise vorticity according to the vorticity dynamics equation for a compressible inviscid flow:[60]

$$\frac{D}{Dt}\left(\frac{\vec{\Omega}}{\rho}\right)=\left(\frac{\vec{\Omega}}{\rho}.\nabla\right)\vec{V}-\frac{1}{\rho}\nabla x\left(\frac{1}{\rho}\nabla P\right) \qquad \text{Equation (7)}$$

Consequently, it is impossible to create a static temperature distortion without creating other forms of non-uniformity, e.g., entropy, density, velocity, total pressure, and angularity in the flow. To quantify the impact of a spatial temperature distortion on an engine stall behavior, researchers have conducted experiments with representative data shown in Figure 3.5.1.[57] The un-distorted operating line, stall limit, and different shaft speeds are shown in dashed lines. Data points corresponding to the effect of temperature distortions of ΔT=45-120^{o}F (i.e., 25–66.7^{o}C) on the stall behavior of a variable-geometry turbofan engine high-pressure compressor are plotted in solid lines. The circumferential extents of the temperature distortions were between θ=90° and 100° in different tests. A ΔT=100^{o}F (i.e., 55.6^{o}C) distortion of about θ=90^{o}-100^{o} is seen to stall the high-pressure compressor operating at its 90 percent corrected flow. Therefore, it can be seen from the figure that a static temperature distortion affect the engine stall margin, as total pressure distortion does.

A maximum temperature distortion parameter is defined as signified by the difference between the highest and the lowest temperatures, $\Delta T_{ef,max}$ and a non-dimensional temperature distortion parameter, TD, at the engine face as:

$$\Delta T_{ef,\,max} = T_{ef,max} - T_{ef,min} \qquad \text{Equation (8)}$$

$$TD \equiv \frac{T_{ef,max} - T_{ef,min}}{\overline{T}_{ef}} \qquad \text{Equation (9)}$$

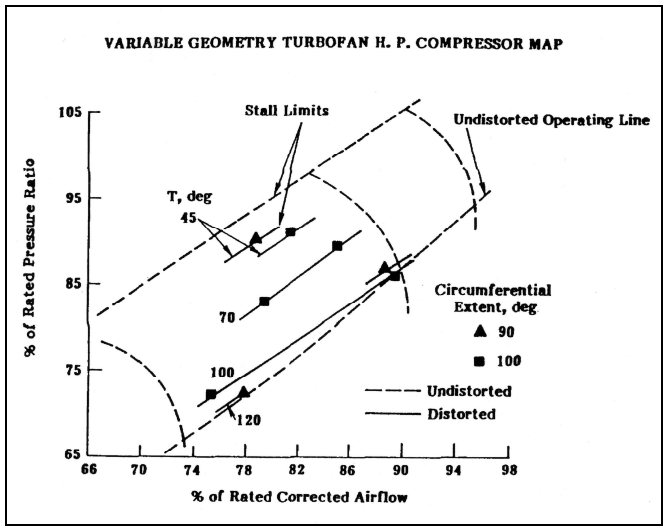

Figure 3. 5. 1: Impact of spatial temperature distortion on compressor stall[57]

4. Computational method

In this chapter, all computational methods for the present study are explained. In the aircraft icing research, the advantages of computational fluid dynamics (CFD) over the experimental methods are reviewed. Also, features of two CFD codes, FLUENT and STAR-CCM+, used in this study are covered. In addition, the strategies and descriptions of the mesh generations for the iced S-duct inlet are given in this chapter. Choosing a proper turbulence model is important in CFD computations; therefore, different turbulence models for the steady- and unsteady-state computations are tested. Finally, the results of the steady- and unsteady-state computations are validated with experimental data to show the accuracy and reliability of the two CFD codes.

4.1. CFD codes

CFD computations are now widely used to investigate the physical characteristics of a flowfield under various conditions, and to determine the performance of the engineering systems or processes that utilizes fluid dynamics. Furthermore, the importance of CFD simulations increases when an experimental investigation causes difficulties under the certain condition, or when the processes or systems do not exist or cannot be used for experimentation. Similarly, the

computational investigation of the icing effects possesses the advantages over experimental methods in two main ways. First, a CFD technique has an advantageous feature that it can economically reconstruct the low-temperature environment in which ice accretion occurs. Second, CFD simulations are much safer since the experimental tests, including in-flight tests, are always accompanied by many dangerous factors that can be caused by ice. Therefore, in the present study, the investigation of icing effects on the flowfield in the M2129 S-duct is conducted by using CFD simulations.

However, there are also limitations to the application of general CFD techniques. The first limitation is in the area of turbulent flow. Turbulent flow should be solved by the equation of motion which can be computed directly, i.e., direct numerical simulation (DNS). This method requires the fine mesh size and smaller time step size to capture the turbulent fluid motion. However, in the practical CFD simulations, the mesh size and time step size are relatively large due to the limitations of computational resources. Therefore, turbulent flow tends to be simplified and solved by using turbulence models, such as the Reynolds-averaged Navier-Stokes (RANS) based models or the large eddy simulation (LES) model. The second limitation arises when a simulation of multiphase flow is required. Like turbulent flow, practical simulations of multiphase flow need a modeling approach, ignoring many of the important details of the flow, such as droplet or particle shape and their impact on inter-phase mass, energy, and momentum transport phenomena.[61]

All CFD simulations in the present study are carried out using two commercial codes: FLUENT 6.2.12[10] and STAR-CCM+2.10.013.[11] In addition, the geometric modeling and mesh generation are conducted using GAMBIT 2.2.30 software.[9] FLUENT flow modeling software is one of the most widely used commercial CFD codes now, and it offers various physical models that can be applied to a wide array of academic and industrial problems. FLUENT code utilizes a control volume (cell) based technique and allows for choosing either segregated or coupled solver. Using either method, FLUENT solves the governing integral equations for the conservation of mass and momentum, and for energy and turbulence. In both cases, a control volume (cell)-based technique is used that consists of:[62]

- Division of the domain into discrete control volumes using a computational grid, which is generated using GAMBIT software.
- Integration of the governing equations on the individual control volumes to construct algebraic equations for the unknown discrete variables, such as velocity, pressure, temperature, and scalar quantities for turbulence. For example, the steady-state transport equation in integral form for arbitrary control volume is: [62]

$$\int \rho\phi\vec{\upsilon}\cdot d\vec{A} = \int \Gamma_{\phi}\nabla\phi\cdot d\vec{A} + \int_{V} S_{\phi} dV \qquad \text{Equation (10)}$$

- Equation (10) is applied to each control volume (cell) and discretized in the computational domain.

- Linearization of the discretized equations and solution of the resulting linear equation system yield updated values of the dependent variables.

Various discretization schemes are available, and either an explicit or implicit scheme for the linearization of the discretized equations is available for the physical models with different flow characteristics. Wall function, y^+, which indicates the resolution and quality of mesh size for a particular flow pattern, can be checked in the post-processing. In addition, various turbulence models, such as the RANS based models, large eddy simulation (LES) model, and detached eddy simulation (DES) turbulence model are available in this software.

Another commercial CFD code, Star-CCM+ was developed with the emphasis on user-friendliness in terms of the appearance and user-interaction similar to the standard software products. This code also has a comprehensive range of turbulence models, which are listed above. There is a built-in meshing tool in the code; however, the mesh generations for the present study were carried out using GAMBIT software, because GAMBIT is known to be a relatively more robust mesh-generation tool. Moreover, STAR-CCM+ also covers both segregated- and coupled-solution methods with implicit and explicit solvers. The parallel-computation performance is enhanced in STAR-CCM+. Therefore, it is known that STAR-CCM+ is the only code that is able to run a calculation that involves over one billion mesh cells.

For the present study, a high-performance computing cluster with more than 200 processors is dedicated for STAR-CCM+, while the computations using FLUENT are performed in a parallel-processing system with 8 processors. Consequently, the simulation cases that require a greater computational capability

(the cases for Chapter 5.2 to 5.9 in the present study), including all unsteady-state simulations, are carried out using STAR-CCM+. On the other hand, FLUENT is used for the cases with a relatively low computational load (the cases for Chapter 5.1).

The computing cluster is located in the Information and Telecommunication Technology Center (ITTC) at the University of Kansas, and it is shown in Figure 4.1.1. 128 computing nodes total are installed in the cluster, and each node equips with two 3.2 GHz Intel® Xeon® EM64T processors and one 4,096 MB memory. Therefore, up to 256 processors are available for the computations. However, in this study, 12 to 20 processors are dedicated to each case, because a computation with more than 20 processors induces a computation-time delay due to a relatively slow communication time between the processors.

In the present study, all computation cases include relatively high-speed flowfields, and the flowfields must be solved through fine meshes near the complicated ice-accreted regions. Therefore, a steady coupled-implicit solver is utilized for all steady-state computations, even though the usage of the solver requires a greater computational load. For the unsteady-state computations, an unsteady segregated-implicit solver is used, since the solver is the only option in using the LES turbulence model of STAR-CCM+ code.

In addition, the second-order scheme is applied for the flow- and turbulence-equations of both the steady- and unsteady-state computations in this study. Using a higher-order discretization scheme guarantees more accurate computation results; however, it lowers the speed of convergence and also requires more calculation time.

About 90 steady-state cases and 40 unsteady-state cases are set up and computed for the present study. The computation time for each steady-state case is approximately 100 to 170 wall clock hours, depending on mesh sizes. However, the computations for unsteady-state cases are continued for about 700 wall clock hour to obtain an enough time-history of flowfield variation.

Also, the calculations for steady-state cases are continued and monitored until the residuals for continuity, X, Y, Z-velocity, and turbulence factors dropped below 10^{-5} where the values of the area-averaged total pressure at the engine face change by less than 0.5 percent between runs. On the other hand, the convergence criteria for unsteady-state simulations are set to order of $10^{-3.}$ A substantially longer computation time for the unsteady-state simulations leads to a larger error value in convergence criteria. Actually, the convergence criteria of 10^{-3} for unsteady-state simulations are generally accepted a low enough level in the industrial CFD applications.

Figure 4. 1. 1: Computing cluster in the Information and Telecommunication Technology Center (ITTC) at the University of Kansas

4.2. Geometric modeling and mesh generation

A three-dimensional geometric modeling and mesh generations for the M2129 S-duct inlet with ice accretion on the inlet lip is a challenging work due to its geometrical complexity. In particular, glaze ice accretion with the horns, which protrude into the inlet inflow, offers exceptional difficulties in constructing meshes for the computational analyses in this study. To generate the meshes with structured grids, the difficulties are doubled due to the increased geometrical complexity. However, it is clear that structured-meshes guarantee a faster calculation time and

stable convergence, compared with unstructured-meshes. Geometric modeling and mesh generation for all computation cases in the present study are performed using GAMBIT 2.2.30 software, as indicated earlier.

To construct the structured-meshes, the cross-sectional planes of the S-duct inlet are divided into four sections, similar to the strategy of mesh generation, suggested in Reference 63, as shown in Figure 4.2.1(a). Note that the number of mesh cells in the near-wall region is increased, as shown in Figure 4.2.1(b), to obtain better results for the flowfield in the boundary-layer.

In the present study, two mesh sets with different mesh-sizes are considered. For the cases of Chapter 5.1, the total number of mesh cells is about 900,000, including the far-field region with the node numbers being 180, 40, 80 in the axial, circumferential, and radial direction, respectively, for the S-duct inlet. To reduce a computational load, only half of the meshes, for a symmetrical duct, are generated for this mesh-set, as shown in Figure 4.2.2. However, the finer mesh size and geometric modeling of the whole (both) S-duct, including the whole (both) far-field region, are required to investigate the asymmetrical inlet flow, caused by the application of angle of attack (or sideslip angle) or of the unsteady effects. In particular, an unsteady-state flowfield that involves a vortex shedding phenomena must be computed through the relatively fine meshes. Therefore, another set of mesh is generated for the whole S-duct inlet and entire far-field region, as shown in Figure 4.2.3. Now, total number of mesh cells is approximately 5,200,000 with the 66 mesh volumes for the S-duct inlet, ice shape, internal regions, and far-field region. The cell number decreases to 3,700,000 when the ice accretion is not considered. The numbers of nodes in the

axial, circumferential, and radial direction are 230, 160, 100, respectively, for the S-duct inlet. This mesh-set is applied for the cases of Chapter 5.2 to 5.8, and the increased computational load due to the increased mesh cell numbers is solved by using the high-performance computing cluster. Also, note that the far-field boundary is radially extended with the length of $20D_{th}$ into X-, Y-, and Z-direction upstream, as shown in Figure 4.2.4.

The ice accretion shapes, which are investigated in the present study, are defined based on the geometrical information, provided by Bidwell, *et al*.[8] In their study, typical rime and glaze ice shapes on an axisymmetric inlet lip were numerically predicted using LEWICE3D code. The icing conditions are, V_∞=25 m/sec.: Ts_∞=-29.9°C: LWC=0.2g/m^3: MVD=20.36 μm: icing time=30min. and V_∞=25 m/sec.: Ts_∞=-9.3°C: LWC=0.695g/m^3: MVD=20.36 μm: icing time=30min., for rime and glaze, respectively. Figure 4.2.5 shows the numerically-predicted ice shapes.[8] Based on the information in Figure 4.2.5, geometric modeling and structured-mesh generations are carried out for the rime and glaze ice in preparation for the computations of the present study, as shown in Figure 4.2.6. The two types of ice accretion on the inlet lip produce totally different inlet lip shapes. With rime ice accretion, the inlet lip shape is relatively still streamlined. On the other hand, the inlet lip shape is seriously distorted with glaze ice accretion, which is characterized by the intrusive ice horn to the duct inflow. Figure 4.2.7 shows the changed inlet lip shape when symmetrical glaze ice is simulated on the inlet lip. Note that, according to the study of Bidwell, *et al*., two-dimensional ice accretion shape and size are a function of the flight conditions, such as the free-stream Mach number, free-stream

temperature, and angle of attack or sideslip angle. However, a *constant* two-dimensional shape and size of ice accretion, as shown in Figure 4.2.6, are assumed for all flight conditions. Therefore, a *single-phase flow* is considered for the simulations and computations in the present study.

Based on a constant two-dimensional ice shape, in particular, glaze ice shape, *symmetrical* and *asymmetrical* ice shapes are examined in the present study. The symmetrical shape indicates the glaze ice accretion that occurs symmetrically on the inlet lip in all circumferential directions. However, for the asymmetrical shape, glaze ice only accretes on a certain portion of the inlet lip with an exactly 90° extension in a circumferential direction. In addition, the asymmetrical shapes are categorized into *top-*, *bottom-*, and *side-glaze*, according to the locations of ice accretion: θ=315°-45°, 135°-225°, and 45°-135°, respectively, based on the definition of the circumferential angle, shown in Figure 4.2.8. Both the symmetrical and asymmetrical ice shapes are assumed to simulate the ice accretion phenomena. Therefore, the design of both ice shapes in this study will help to accurately investigate the effect of the critical ice shapes on the performance of the M2129 S-duct inlet. Figure 4.2.9 shows the symmetrical and asymmetrical glaze ice shapes.

Also, the effect of the glaze ice horn thickness is investigated in the present study. Therefore, the thickness of the glaze ice horn which intrudes into the inlet inflow, as shown in Figure 4.2.6(b), is reduced to design a *sharp-glaze ice* shape. Figure 4.2.10 shows the geometry of the sharp-glaze ice and radiuses of the *sharp-* and *original-glaze ice*. The radius of the sharp-glaze ice horn is 0.0104 m, while that

of the original-glaze ice horn is 0.0142 m. Therefore, the radius of the ice horn decreases approximately 27 percent for the sharp-glaze ice.

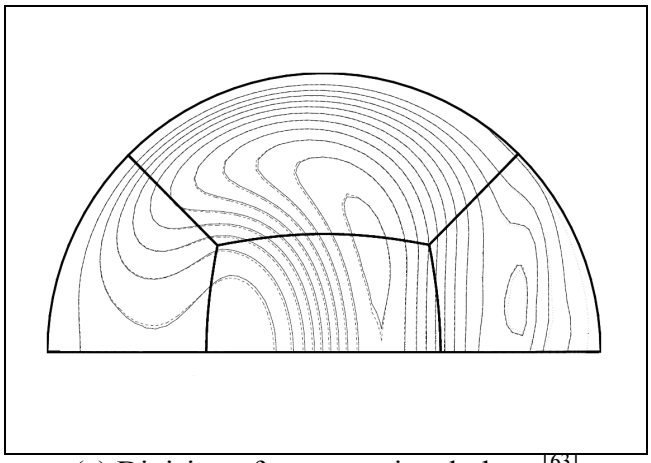

(a) Division of cross sectional plane [63]

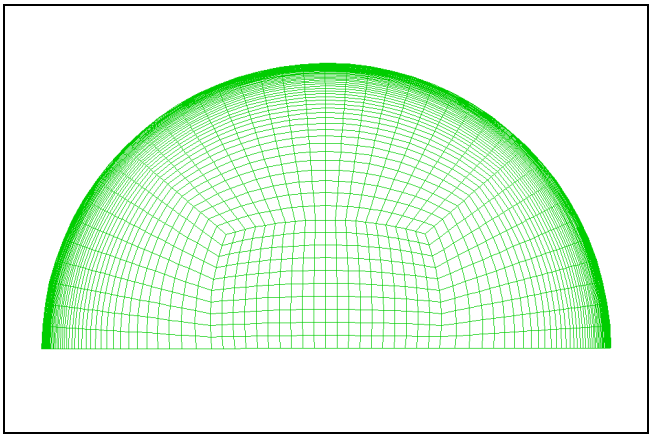

(b) Structured-mesh generation with enhanced-wall treatment

Figure 4. 2. 1: Mesh generation for cross-sectional planes

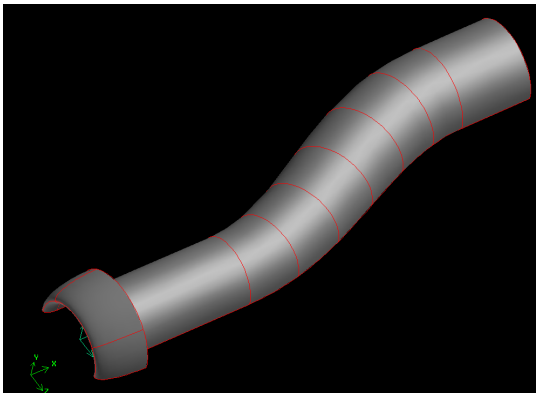

(a) M2129 S-duct inlet

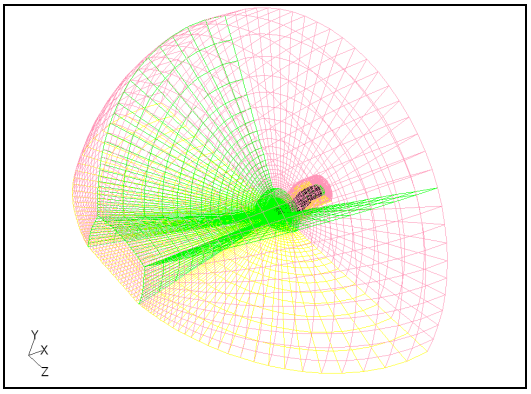

(b) Far-field region

Figure 4. 2. 2: Geometry modeling and mesh generation for half-side regions

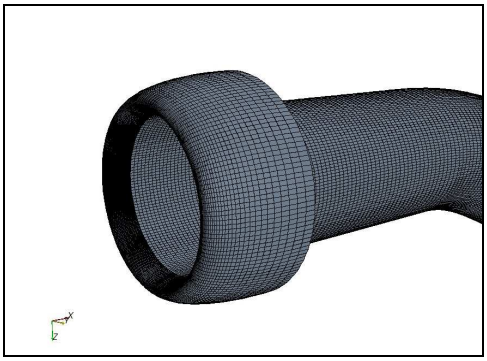

(a) Inlet lip of M2129 S-duct inlet

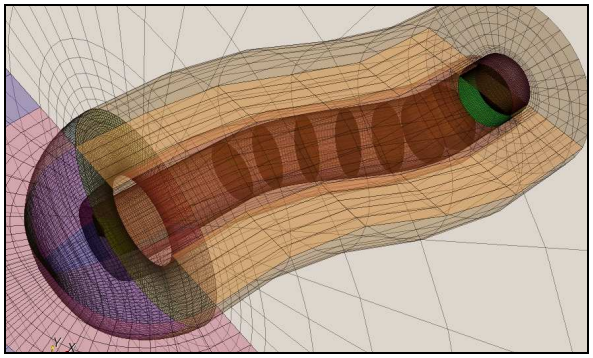

(b) Far-field and internal region

Figure 4. 2. 3: Geometry modeling and mesh generation for whole regions

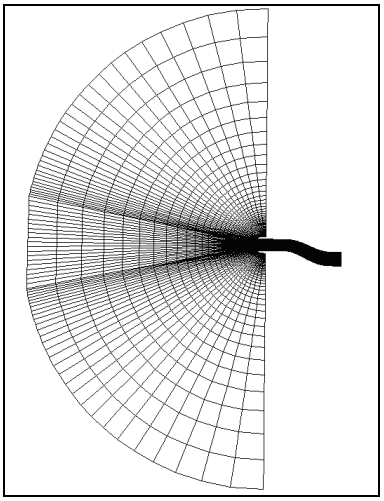

Figure 4. 2. 4: Extension of a far-filed boundary
($20D_{th}$ for X-, Y-, Z-direction)

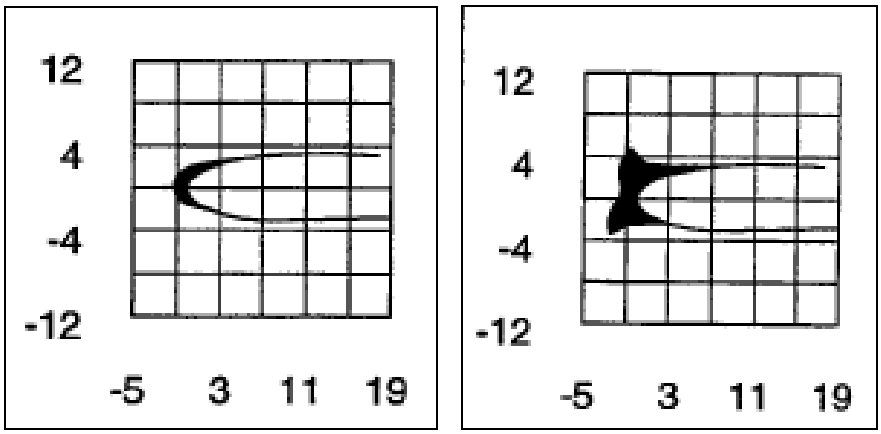

(a) Rime (b) Glaze

Figure 4. 2. 5: Numerically predicted ice shapes[8]

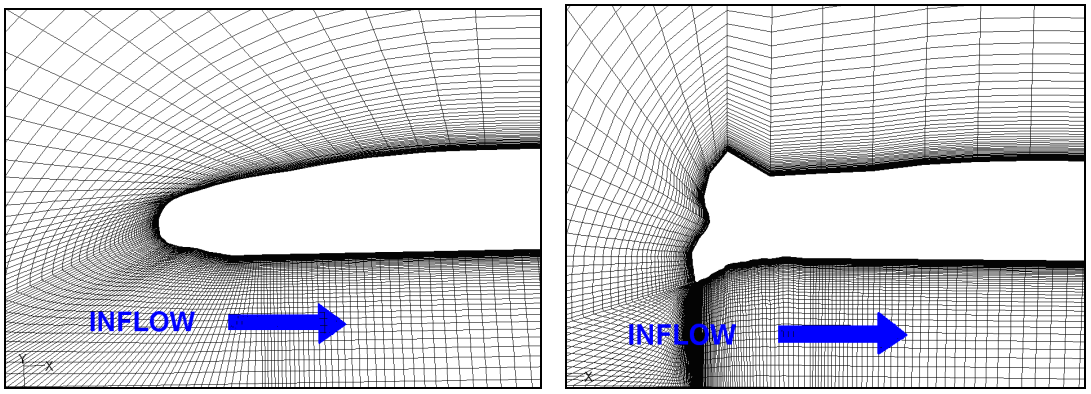

(a) Rime (b) Glaze

Figure 4. 2. 6: Geometry modeling and mesh generation for ice accretion shapes

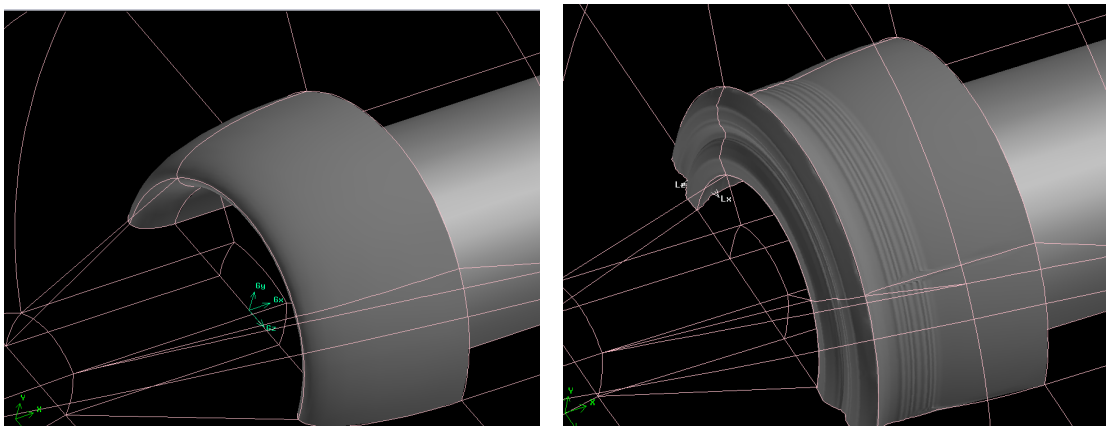

(a) Clean inlet (b) Glaze iced inlet

Figure 4. 2. 7: Change of inlet lip shape with glaze ice accretion

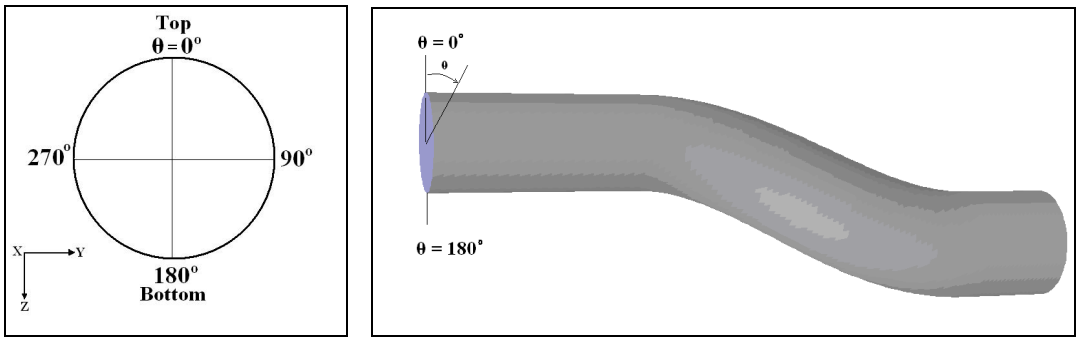

Figure 4. 2. 8: Definition of circumferential angle (θ)

(a) Symmetrical glaze

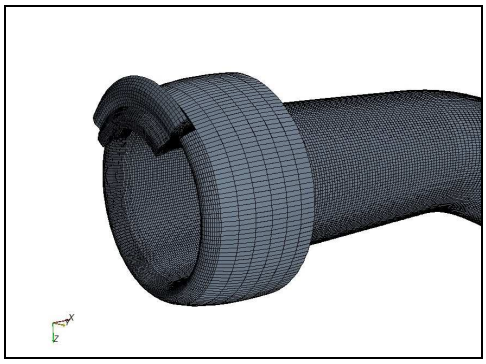

(b) Asymmetrical glaze-top (θ=315°-45°)

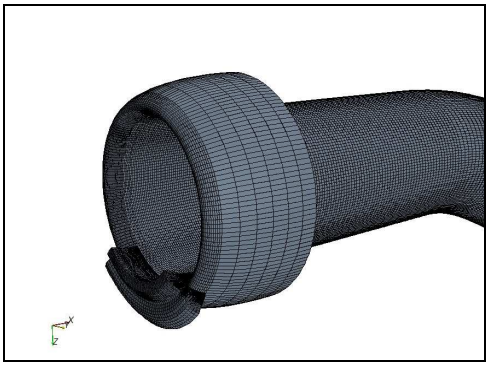

(c) Asymmetrical glaze-bottom (θ=135°-225°)

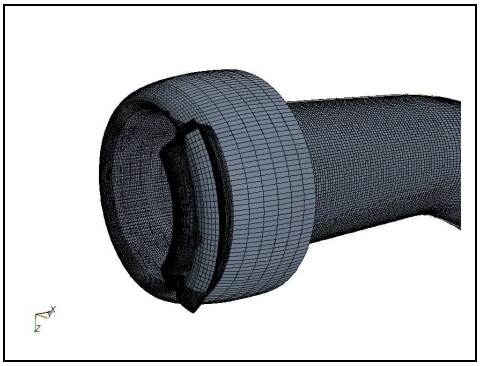

(d) Asymmetrical glaze-side (θ=45°-135°)

Figure 4. 2. 9: Different glaze ice shapes

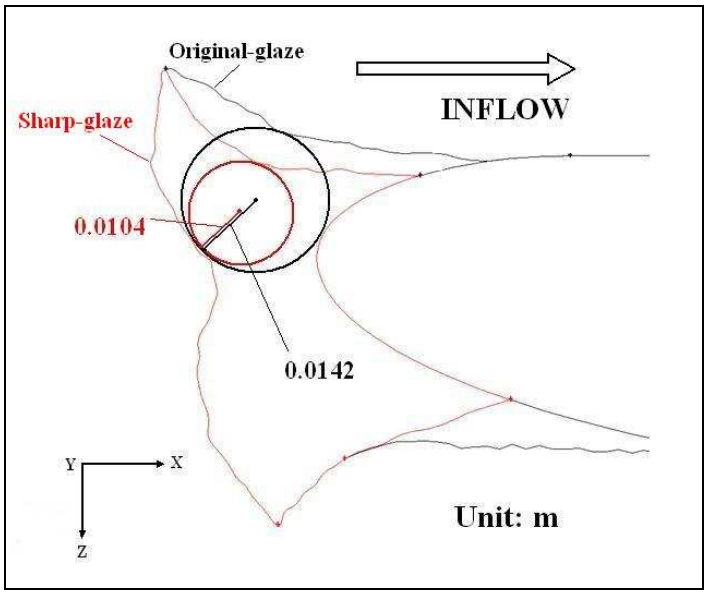

Figure 4. 2. 10: Decrease in glaze ice radius

4.3. Turbulence models

It is well known that there is no single turbulence model for all cases of flowfield, and there is the one turbulence model that performs better than the others for a specific flowfield case. Hunt, *et al*.[64] emphasized that the topological information and convergence properties are two important numerical and implementation issues for the choice of turbulence model. The topological information is important because the models that require a wall-normal vector should be avoided, since this can be ambiguous for complex three-dimensional configurations. Also, a good convergence property is an important issue because unnecessary complex source terms in turbulence model generally cause an increased numerical stiffness and slower convergence. Therefore, in CFD techniques, choosing the best turbulence model is also important for better simulation results. According to

Reference 65, the choice of a turbulence model and the trustworthiness of the turbulence model can be made easier by examining the sensitivity of the models. This requires conducting simulations with different turbulence models and comparing the results, since the strengths and weakness of each turbulence model depend on the specific applications.

Both FLUENT and STAR-CCM+ codes provide various turbulence models, such as the Reynolds-averaged Navier-Stokes (RANS) based models, detached eddy simulation (DES) model, and large eddy simulation (LES) turbulence model, for the analyses of different flowfields. In particular, the RANS based models that include the Spalart-Allmaras (S-A) model, κ-ε model, and κ-ω model, are popular for the steady-state computations, because they greatly reduce the required computational efforts and resources.

4.3.1. Turbulence models for steady-state computations

To test the performance of different turbulence models for the steady-state flowfield in the baseline M2129 S-duct inlet of the present study, the S-A model, realizable κ-ε model, and SST κ-ω turbulence model are considered. The one-equation S-A turbulence model[66] has been widely used due to its ease of implementation, relatively low cost, and good performance in aerospace applications, such as the flow simulation over an airfoil. The realizable κ-ε model[67] is also one of the most widely used turbulence models for practical engineering applications. However, the best simulation for the flow separation phenomena, known as vortex

lift-off, was predicted by applying the SST κ-ω turbulence model.[68],[69] In addition, many investigations for the simulation of compressible flows inside diffuser S-ducts and over vortex generators (VG) have been performed with the SST κ-ω model.

Hunt, *et al*.[64] proved the superiority of this turbulence model for the M 2129 S-duct inlet. In their study, with the SAUNA CFD system,[70] the best simulation for the flow separation phenomena was predicted by applying the SST κ-ω turbulence model. In addition, many computational investigations for the compressible flows inside the diffuser ducts and over the vortex generators (VG) have been carried out choosing the SST κ-ω model for different CFD-codes.[55], [71]-[74]

In particular, Menzies, *et al*.[51] simulated the flowfield in the M 2129 S-duct inlet using three different turbulence models: the S-A model, standard κ-ω model, and SST κ-ω model. The secondary flow in a region of separation was predicted with all models; however, the SST κ-ω model performed the best and compared well with the previous computational and experimental results.

Two extra transport equations are included into the SST κ-ω turbulence model equations, to represent the properties of turbulence: *turbulence kinetic energy* (κ), and *specific dissipation rate* (ω). Turbulence kinetic energy means kinetic energy per unit mass associated with eddies in turbulent flow, and the specific rate can be thought of as the variable that determines the scale of the turbulence (length-scale or time-scale). Also, the SST turbulence model is known to have an advantage in terms of performance over both the standard κ-ω model and standard κ-ε model, because it ensures the better performance in a near-wall and far-field zone.

Figure 4.3.1.1 shows the total pressure recoveries of the baseline M2129 S-duct inlet, which are calculated with FLUENT code using three different turbulence models. The total cell number is approximately 190,000 cells, and the meshes for only half of the regions are constructed to reduce the computational load. The boundary condition is the pressure inlet - pressure outlet condition, and the free-stream total pressure is Pt_∞=101.1 kPa. Note that the value of the free-stream total pressure, Pt_∞, is equal to that of the total pressure at the inlet throat, Pt_{th}. Also, the static pressure at the engine face is changed to obtain the throat Mach number range, from M_{th}=0.2 to 0.8. From the figure, it can be easily seen that all turbulence models produce relatively good agreements, as compared with the experimental data.[75]

However, the computations using the SST κ-ω turbulence model converge in a relatively steady manner, while the computations with the S-A model often show instability in convergence. The examples are presented in Figure 4.3.1.2. These two convergence-history plots are obtained during the same calculation time. The convergence-history of the S-A model is characterized by 120 percent faster iteration time because of its genetic reason, i.e., one-equation turbulence model. However, this model produces the oscillations for all equations around the residual level of 10^{-4} to 10^{-5}, except the equations for turbulence factors. On the other hand, all equations in the SST κ-ω model case converge steadily and gradually until the residual limit for convergence, 10^{-5}, although the iteration time is not as fast as that for the S-A model. Therefore, it can be concluded that the SST κ-ω model is the best option for the turbulence model in calculating the steady-state performance of the M2129 S-duct inlet in the present study.

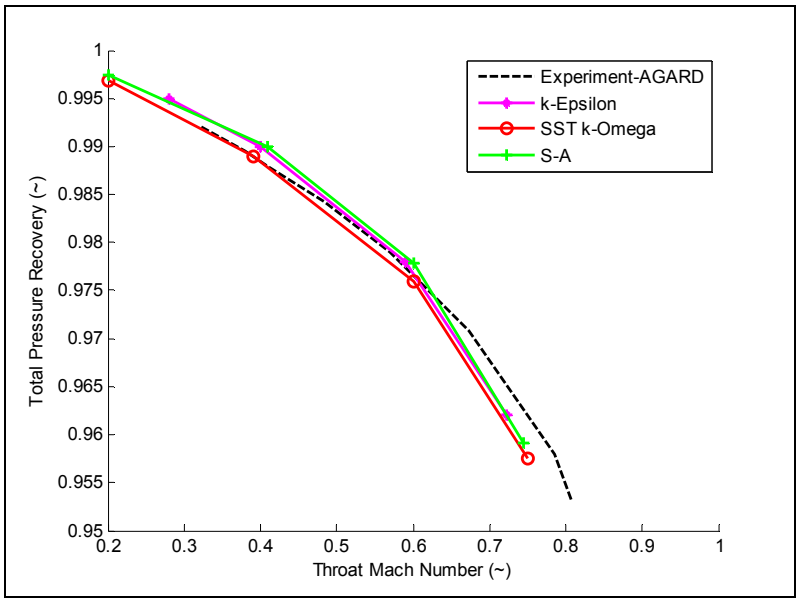

Figure 4. 3. 1. 1: Total pressure recoveries ($\overline{Pt}_{ef} / Pt_{\infty}$) of different turbulence models and experimental data[75]

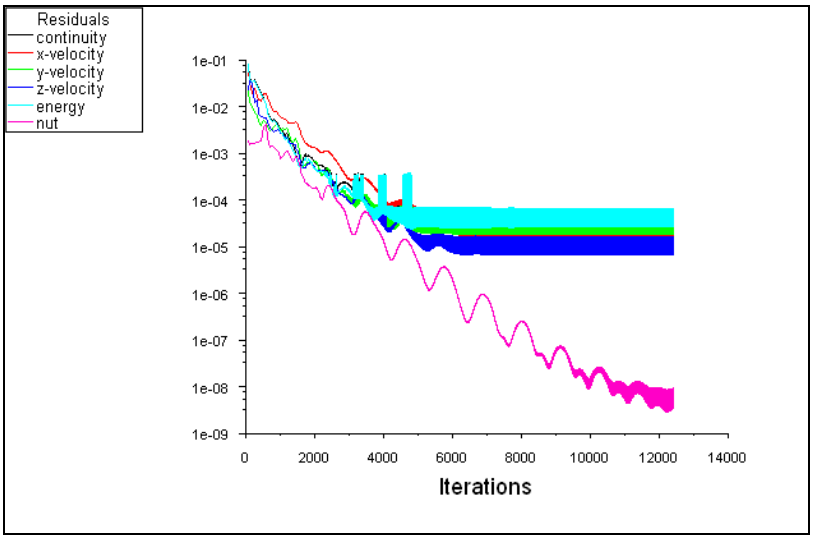

(a) S-A turbulence model

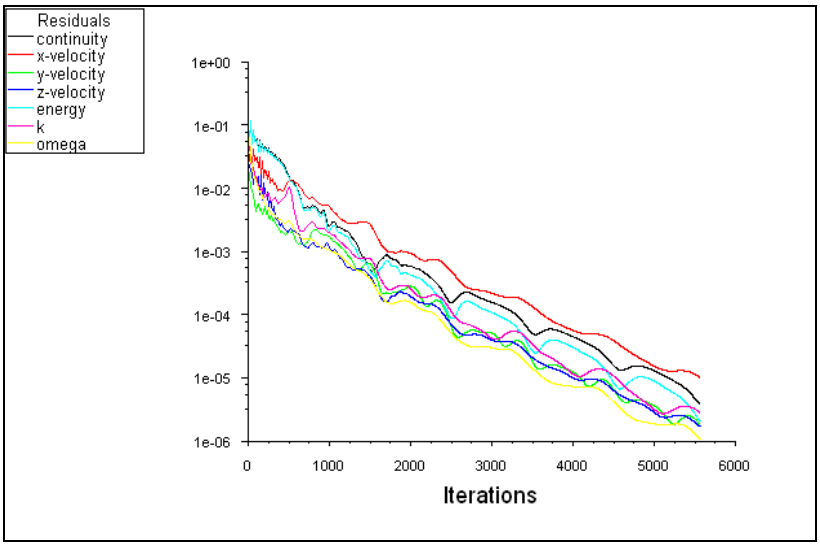

(b) SST κ-ω turbulence model

Figure 4. 3. 1. 2: Comparison of convergence-history plots of two different turbulence models

4.3.2. Turbulence models for unsteady-state computations

The nature of most turbulent flows is basically time-dependent. Consequently, a turbulence model affects the result of an unsteady-state simulation

more than it does a steady-state solution. Therefore, three different turbulence models; the RANS based SST κ-ω model with unsteady-implicit solver, DES model, and LES model, are also tested to improve the choice of the most suitable turbulence model for simulating the flow unsteadiness in the present study.

The features of the SST κ-ω turbulence model were given in the previous chapter of the present study. The DES turbulence model[76] is one that combines the features of the RANS model and LES turbulence model.[77] The DES turbulence model solves the near-wall region or shear layers using the base RANS closure model, while it treats other flow regions, including unsteady separated regions, using the LES model. The DES turbulence model is based on the one-equation S-A turbulence model.

The LES model is one of the most popular turbulence models for simulating unsteady turbulent flows. The application of this turbulence model was pioneered by Smagorinsky[78] and Deardorff.[79] Turbulent flows are known to be characterized by both large and small eddies in terms of length and time scales. In the LES model, therefore, large eddies are explicitly calculated in the same manner as in the direct numerical simulation (DNS) turbulence model. On the other hand, the small eddies in the LES models are implicitly solved by using a sub-grid scale model, which is also employed in the RANS models. Therefore, the LES turbulence model falls between the DNS and RANS model in terms of the fraction of the resolved eddy scales.[62]

It is known that the LES model is significantly affected by the mesh-size, due to the fact that the mesh-size defines the separation between the large and small

eddies. The accuracy of the LES model increases with the increase of mesh cell numbers. Therefore, the LES model needs a finer mesh than that is typically used for the steady-state RANS models.

In addition, with the LES model, the computation requires more random access memory (RAM) by two- or more-orders of magnitude and longer CPU time when compared to those for the RANS based models, since large eddies are resolved by the DNS method. Therefore, a high-performance computing capability, e.g., a parallel computing system, is required for the simulation using the LES model. In the present study, each unsteady-state computation case using the LES turbulence model needs to be run for more than 700 wall-clock hours with 12 CPUs to obtain the stable statistics of the unsteady-state flow properties.

Figure 4.3.2.1 shows the time-histories of area-averaged total pressures at the engine face of the baseline M2129 S-duct inlet with three different unsteady turbulent models. The converged steady-state solution of the SST κ-ω turbulence model is used as an initial condition for the unsteady-state flow calculations. Also, the total number of the mesh cells is about 3,700,000 for the mesh generation of the both side regions. In addition, STAR-CCM+ code is used for the unsteady-state computations with the farfield boundary condition. In case of the SST κ-ω turbulence model, as shown in Figure 4.3.2.1(a), the total pressure-history at the engine face is characterized by an almost flat line with the iterations. This fact indicates that the SST κ-ω model does not capture the total pressure fluctuation. The latter is expected in the S-duct inlet due to the flow separation at the duct curvature. The DES turbulence model also presents a constant total pressure-history pattern with time, as

shown in Figure 4.3.2.1(b). Therefore, the SST κ-ω and DES models are found to be inadequate for simulating the unsteadiness that occurs in an S-duct. However, as shown in Figure 4.3.2.1(c), the flow unsteadiness is properly predicted by the LES model, showing a fluctuating total pressure pattern with time. Based on the turbulence model tests, the LES turbulence model is chosen for the investigation of the icing effects on the dynamic distortion of the M2129 S-duct inlet in the present study. It is known that the LES turbulence model is expected to be more accurate and more reliable than the RANS models for the flows in which large-unsteadiness is significant, in particular for the flow that involves unsteady separation and vortex shedding.[80] Therefore, the LES turbulence model is considered suitable for the present study, since the flowfield in the S-duct inlet with the icing effects is characterized by unsteady flow separation which is accompanied by vortex shedding phenomena.

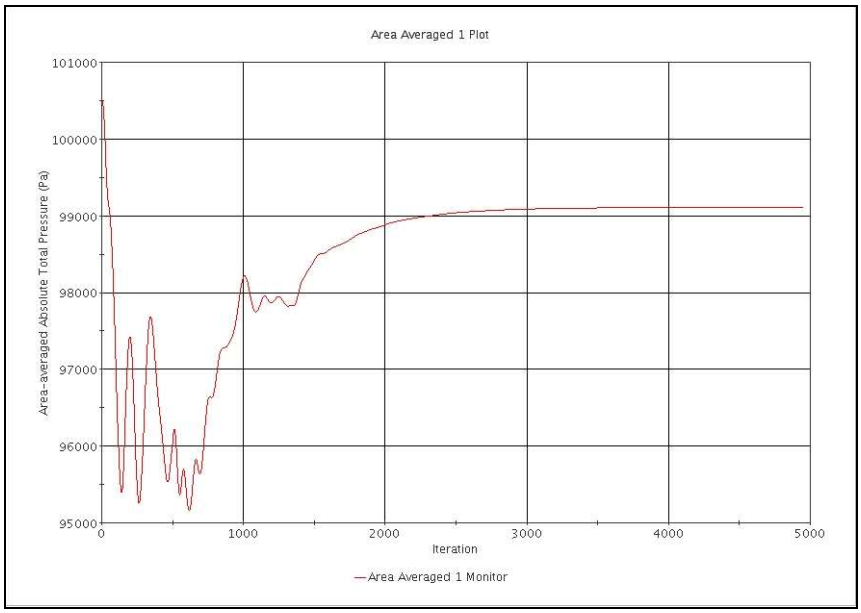

(a) SST κ- ω turbulence model- implicit unsteady solver

Figure 4. 3. 2. 1: Comparison of total pressure fluctuation at the engine face with different turbulence models (M_∞=0.34)

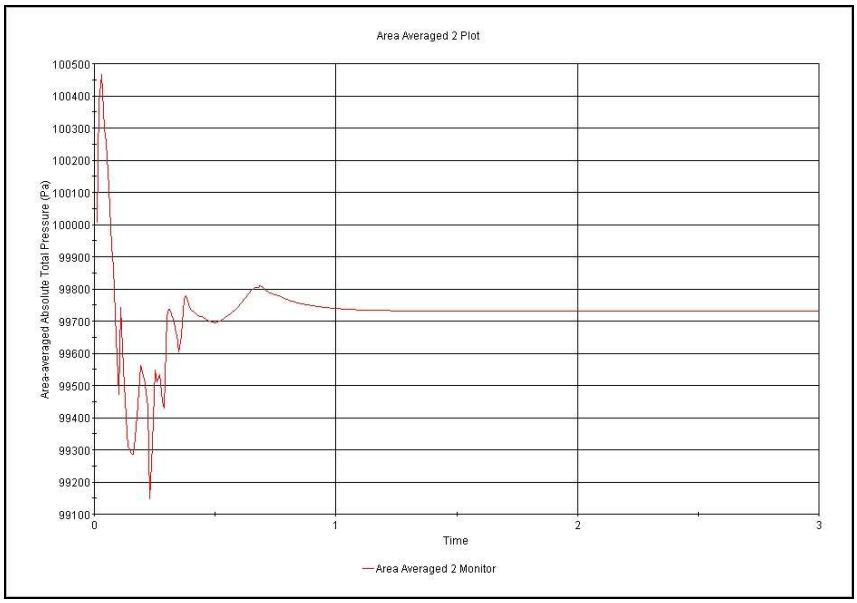

(b) DES turbulence model

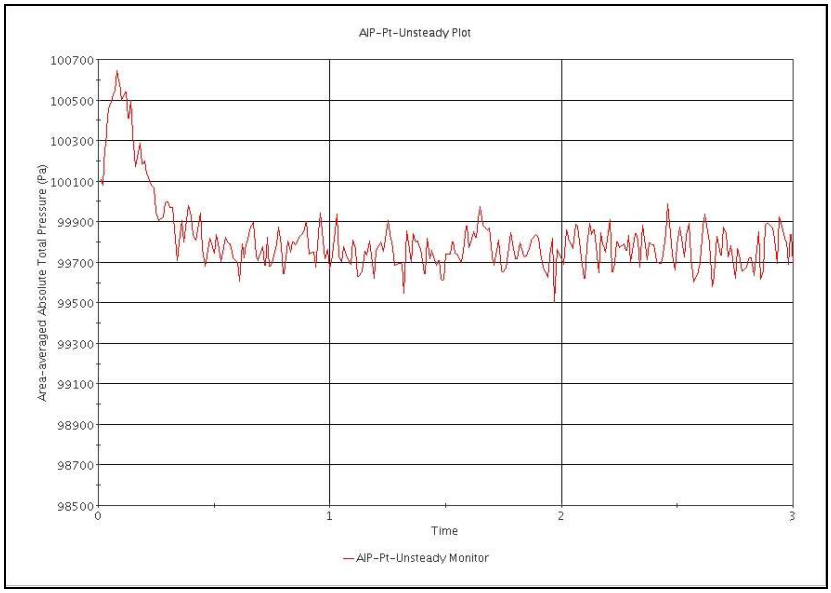

(c) LES turbulence model

Figure 4. 3. 2. 1: Comparison of total pressure fluctuation at the engine face with different turbulence models (M_∞=0.34)

4.4. Boundary conditions and physical properties of air

Boundary conditions determine the flow variables on the boundaries of the physical domain. Therefore, the setting of appropriate boundary conditions is also a critical procedure in CFD techniques. In this study, the *pressure inlet-pressure outlet* boundary condition is used for the validation cases in Chapter 4.7, and the *pressure far-field* boundary condition is applied to all cases for the investigation of the icing effects in Chapters 5.1 to 5.9. The pressure far-field boundary condition is necessary to simulate the inflow and outflow around the inlet and external lips. In addition, the pressure far-field condition in FLUENT is equivalent to the *free-stream* boundary condition in STAR-CCM+.

The pressure far-field boundary condition (or free-stream boundary condition) is to model a free-stream condition at infinity, with free-stream Mach number and static conditions being specified.[62] Also, this boundary condition is applicable if the density is calculated by using the ideal-gas law. To effectively approximate true infinite-extent conditions, the boundary of the grid must be extended far enough from the simulation region of interest. In this study, therefore, the meshes for the far-field outer boundary are extended as a circle with a radius of $20\,D_{th}$ to prevent the boundary effects on the region of interest.

Another important step in the computational setup is specifying the physical properties of air. In this study, compressible flow effects are expected, therefore, the ideal gas law is utilized as the density change relation. It is found during the calculation that the density change option also requires more memory for simulations. Additionally, other physical properties, such as thermal conductivity (k) and viscosity

(μ), are defined, and they are set for the CFD codes according to free-stream temperatures. In particular, the values of these temperature-dependant properties are significantly changed by the low-temperature environment for ice accretion. For example, the temperature conditions of the rime and glaze ice shape, which are considered in the present study, are Ts_{∞}=-29.9°C and -9.3°C,[8] respectively. These free-steam temperatures result in k=0.0217W/m-K and μ=1.56×10^{-5} kg/m-sec.[81] for the rime case, and k=0.0234W/m-K and μ=1.66×10^{-5} kg/m-sec.[81] for the glaze case. The changed properties are included into the computational setup. However, the effect of LWC on these properties is not considered in this study.

4.5. Area-averaging techniques

One of the most important quantities in analyzing the performance of an S-duct inlet is an averaged total pressure. The extension of a non-uniform and three-dimensional flow, caused by the flow separation at the curved section, must be interpreted by an averaging process to obtain a single value for the total pressure recovery of the S-duct inlet. Total pressure recovery is considered as a key parameter in assessing the performance of inlet components. Therefore, averaging non-uniform flow is an important process and the advent of CFD has led to more needs for averaging outputs. However, the exact representation of a non-uniform flow with an *equivalent* average uniform flow has been questioned.[60] In particular, Pianko, *et al*.[82] emphasized that there is no uniform flow exists which simultaneously matches

all the significant stream fluxes, aerothermodynamics, and geometric parameters of a non-uniform flow.

Although there are many difficulties in choosing a proper technique, the area averaging is widely used for practical reasons. In addition, area averaging is often the best and the only procedure available for experiments that are accompanied by a limited number of pressure probes buried in the engine.[83] Furthermore, the experimental data of total pressure recovery, which is used as a reference data for the validation in this study, is also calculated based on the area-weighted averaging process.[75] Therefore, area-weighted averaging is applied in the present study to obtain single values for the total pressure recovery.

In FLUENT the area-averaged total pressure and Mach number are defined as follows:[62]

$$\overline{Pt}=\frac{\int_A PtdA}{A}=\frac{1}{A}\sum_{i=1}^{n} Pt_i\left|A_i\right| \qquad \text{Equation (11)}$$

$$\overline{M}=\frac{\int_A MdA}{A}=\frac{1}{A}\sum_{i=1}^{n} M_i\left|A_i\right| \qquad \text{Equation (12)}$$

The area-weighted average of a quantity is computed by dividing the summation of the product of the selected field variables and computation cell-area by the total area of the surface.

4.6. Other computational setup parameters

The presence of a wall significantly affects the characteristics of turbulent flow. Since walls are the main source of mean vorticity and turbulence, the solution variables have large gradients, and the momentum and other scalar transport occurs most vigorously in the near-wall region.[84] Therefore, an accurate near-wall treatment is crucial in modeling for wall-bounded turbulent flows. The viscous shear stress (τ_w) dominates at the wall, while it is not influential in the free shear flows. Also, near the wall region, where viscous affected inner region or viscous sub-layer, the velocity profile depends upon the Reynolds number since the viscosity (ν) is an influential parameter in the region. From these quantities, the *friction velocity* can be defined:[80]

$$u_\tau = \sqrt{\frac{\tau_w}{\rho}} \qquad \text{Equation (13)}$$

The *viscous length scale* is defined:[80]

$$\delta_\nu = \nu \sqrt{\frac{\rho}{\tau_w}} = \frac{\nu}{u_\tau} \qquad \text{Equation (14)}$$

The distance from the wall measured in *viscous length* is denoted as:[80]

$$y^+ = \frac{y_p}{\delta_v} = \frac{u_\tau y_p}{\nu} = \frac{\rho u_\tau y_p}{\mu} = \frac{y_p}{\mu}\sqrt{\rho \cdot \tau_w} \qquad \text{Equation (15)}$$

The wall function, y^+ is a non-dimensional parameter which determines the relative importance of viscous and turbulent processes, and it indicates the resolution and quality of mesh size for a particular flow pattern. In particular, it is crucial in turbulence modeling to determine the proper size of the cells near domain walls. In FLUENT, it is recommended that meshes be made either coarse enough or fine enough to prevent the wall-adjacent cells from being placed outside the viscous sub-layer, and the value of y^+ fall in $y^+<5$ or $y^+>30$.[62]

For the κ-ω model, which is the main turbulence model for the steady-state simulations in the present study, the value of y^+ must be very small and the wall adjacent wall cell should be in the order of $y^+=1$ by the enhanced wall treatment.[62] Furthermore, a study on the effects of near-wall resolution on the separation characteristics of vortex lift-off was performed by Anderson and Farokhi.[47] In their study, it is found that the CFD prediction with the value of $y^+=0.5$ produces relatively better results compared to the case of $y^+=8.5$ in the region of separation and the engine face of the M2129 S-duct inlet. In particular, a lack of near-wall resolution of mesh diminished the size of the separation region. The very strong effect of the near-wall mesh resolution on the structure and strength of the flow at the engine face result from a nature of vorticity-dominated internal flow. Since the largest value of vorticity occurs in the near-wall region and the secondary flow is generated by the turning of transverse shear, the very strong effect of a near-wall mesh resolution is realized as a stronger secondary flow, which has consequently an appreciable influence on the primary flow.

In this study, the value of y^+ is found to be approximately 0.6 for the clean inlet at the higher Mach number region (M=0.38) inside the duct. On the other hand, y^+ is about 0.2 for the iced inlet case at the highest Mach number region (M=0.5). These y^+ values are small enough to produce better predictions for the vorticity-dominated internal flows in the S-duct inlet with the iced inlet lips. Figure 4.6.1 shows the increased mesh cell numbers at the near-wall region of the clean and glaze iced inlet to obtain the smaller values of y^+.

In both FLUENT and STAR-CCM+ code, a main control parameter over the time-stepping scheme is a *Courant number* (CFL) for the coupled solver.[62] The Courant number and time-step are defined as:[62]

$$\mathrm{CFL} = \lambda_{\max} \frac{\Delta t}{\Delta x} \qquad \text{Equation (16)}$$

$$\Delta t = \frac{\mathrm{CFL} \cdot \Delta x}{\lambda_{\max}} \qquad \text{Equation (17)}$$

Due to its unconditionally stable characteristics, the stability limit of a coupled-implicit scheme is different from that of a coupled-explicit scheme, since an implicit scheme offers less limitation. The value of the Courant number for a coupled-implicit scheme can be increased, depending on the complexity of the cases, unless a diverged solution occurs. The increase of the Courant number for a coupled-implicit scheme contributes to produce a faster convergence for a steady-state calculation by increasing the time-step size. Therefore, for most of the steady-state computation cases in this study, the initial value of the Courant number is set to 5,

and it is gradually increased up to 20 during the computations to accelerate calculation convergences and to reduce processor-time requirements.

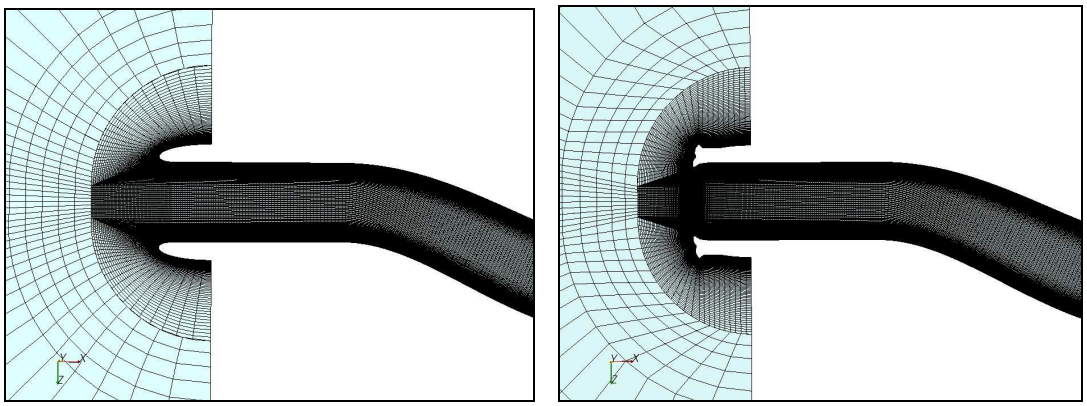

(a) Clean (b) Glaze ice

Figure 4. 6. 1: Enhanced mesh size at near-wall regions

4.7. Validation of computational methods

4.7.1. Validation of steady-state computations

Validations of the CFD analyses by using FLUENT and STAR-CCM+ are conducted for the flowfield properties in a baseline M2129 S-duct inlet. This validation process is important because a validation data for the M2129 S-duct inlet are available for the baseline case only, and no validation data can be found for the icing cases. For the validation of the steady-state computations, the size of the S-duct inlet is set according to the geometrical data from Reference 55and 75, as shown in Figure 3.3.2(a). Note that an inlet lip section is not included in the geometry. The total number of mesh cells is approximately 190,000: 100, 40, and 50 in axial,

circumferential, and radial directions. Also, only half of the meshes, according to the duct symmetry plane, are constructed to reduce a computational load. In addition, the SST κ-ω turbulence model is applied for the validations of both FLUENT and STAR-CCM+ codes.

The pressure inlet-pressure outlet are set for the boundary conditions, with the free-stream total pressure of Pt_∞=101.1 kPa and the free-stream temperature of Tt_∞=287.2 K. Note that the value of the free-stream total pressure, Pt_∞, is equal to that of the total pressure at the inlet throat, Pt_{th}. The static pressure at the engine face is changed from Ps_{ef} =82.7 kPa to 100.7 kPa to obtain the throat Mach number range, M_{th}=0.26 to 0.77.

The steady-state computational results by both FLUENT and STAR-CCM+ codes are compared to an experimental data[75] and another CFD data,[55], which was produced by WIND-US code. Figure 4.7.1.1 presents the comparison of the steady-state total pressure recovery data at the engine face station ($\overline{Pt}_{ef}$ / Pt_∞) over the range of throat Mach numbers, M_{th}=0.1 to 0.8. The comparison shows that the total pressure recoveries by FLUENT are close to the experimental data until M_{th}=0.6, and slightly under-predicts over M_{th}=0.6, while the WIND-US results over-predict the experimental data over the entire range of the throat Mach numbers. In addition, the results of STAR-CCM+ are well matched to the experimental data in all throat Mach numbers. The total pressure recovery of STAR-CCM+ is 0.9582 at Mth=0.77, while that of the experimental results is 0.958 at M_{th}= 0.785.

The flowfield properties in the duct symmetry plane, computed by using the WIND-US (M_{th}=0.8),[55] FLUENT (M_{th}=0.72), and SATR-CCM+ codes (M_{th}=0.77)

are qualitatively compared in Figures 4.7.1.2 to 4.7.1.4. All the CFD codes simulate the region of a massive flow separation at the first bend section, which is a typical flow pattern in a diffusing S-duct inlet. In addition, good similarities can be observed in the flowfield contours simulated by the three different CFD codes, although the property values are not exactly matched among the codes due to the different throat Mach number inputs.

Also, another computational setup using STAR-CCM+ code is validated with an experimental data. The computational setup is applied for most of the cases, Chapter 5.2 to 5.9, in the present study. The geometry and size of the S-duct inlet in this setup is presented in Figure 3.3.2 (b), and the geometry includes the inlet lip section without ice accretion, i.e., the baseline inlet or clean inlet. The fine meshes are generated for both sides of all regions. Therefore, total number of the mesh cells increases up to about 3,700,000. The SST κ-ω turbulence model is used, and far-field boundary condition is applied. The comparison of the total pressure recovery results with another experimental data set[53] are presented in Figure 4.7.1.5. The results by STAR-CCM+ with the fine meshes are well matched to the experimental data at all throat Mach numbers. Note that both mesh sets with two different mesh sizes (190,000cells and 3,700,000cells) produce relatively satisfactory validation results in the steady-state total pressure recovery of the inlet. Therefore, the effect of the mesh size on the steady-state computations of the present study is relatively insignificant.

From these validation processes, it can be confirmed that the steady-state flowfield simulations using both FLUENT and STAR-CCM+ are reliable, and these

CFD codes can be served as robust methods for the computational investigation of the steady-state performance of the M2129 S-duct with the effects of the inlet icing.

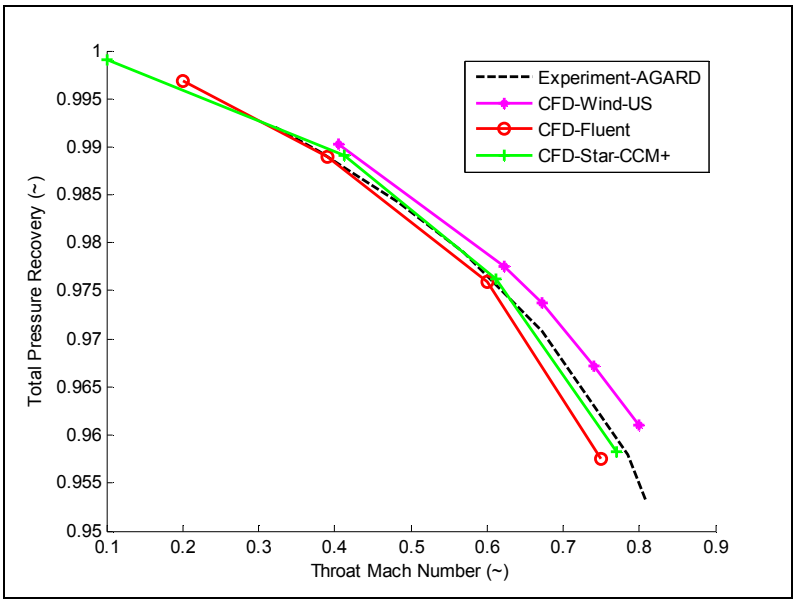

Figure 4. 7. 1. 1: Validation of total pressure recoveries ($\overline{Pt}_{ef} / Pt_{\infty}$) of FLUENT and STAR-CCM+ with experimental[75] and WIND-US data[55]

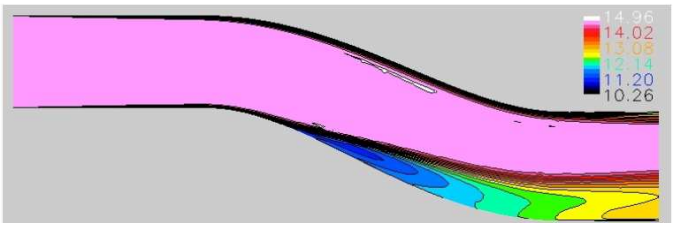

(a) WIND-US (M_{th}=0.8, unit: psi)[55]

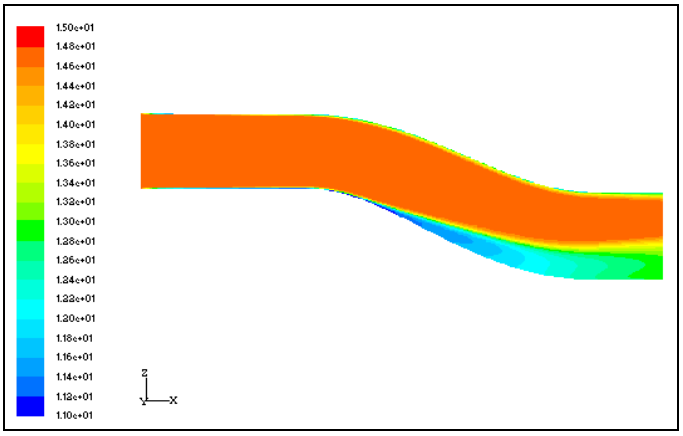

(b) FLUENT (M_{th}=0.72, unit: Pa)

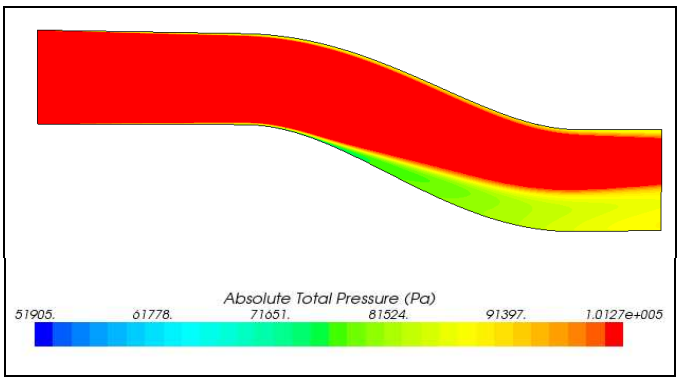

(c) STAR-CCM+ (M_{th}=0.77, unit: Pa)

Figure 4. 7. 1. 2: Validation of total pressure distribution in the duct symmetry plane

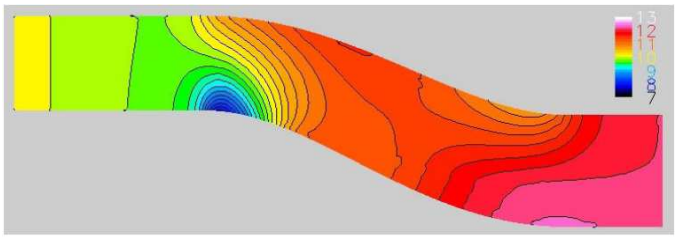

(a) WIND-US (M_{th}=0.8, unit: psi)[55]

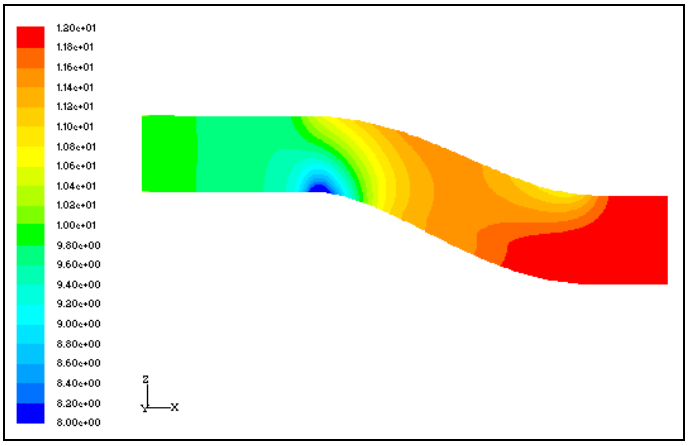

(b) FLUENT (M_{th}=0.72, unit: Pa)

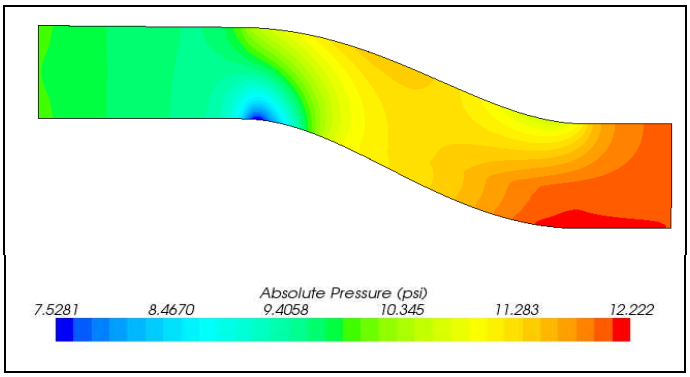

(c) STAR-CCM+ (M_{th}=0.77, unit: psi)

Figure 4. 7. 1. 3: Validation of static pressure distribution in the duct symmetry plane

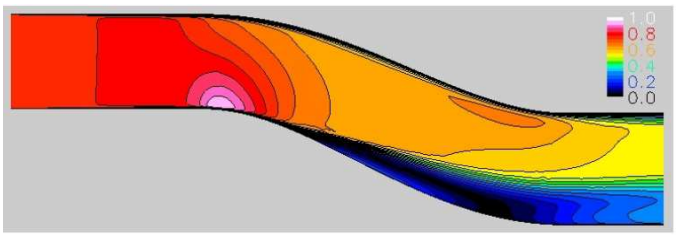

(a) WIND-US (M_{th}=0.8)[55]

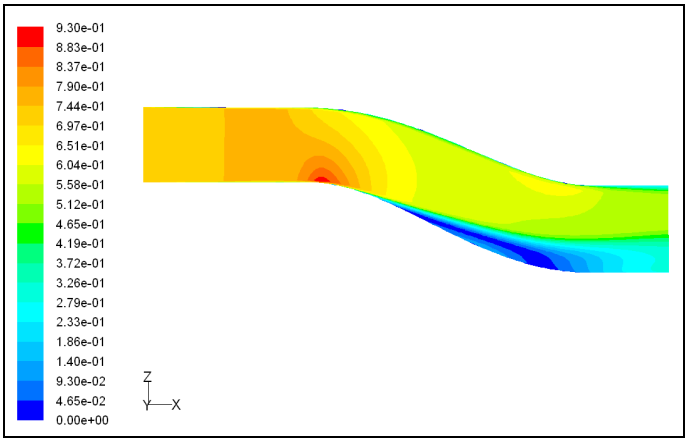

(b) FLUENT (M_{th}=0.72)

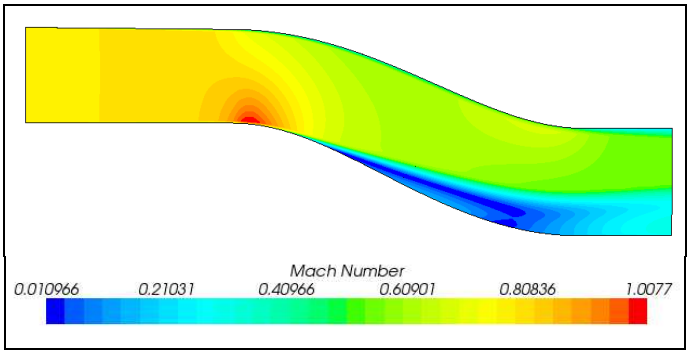

(c) STAR-CCM+ (M_{th}=0.77)

Figure 4. 7. 1. 4: Validation of Mach number distribution in the duct symmetry plane

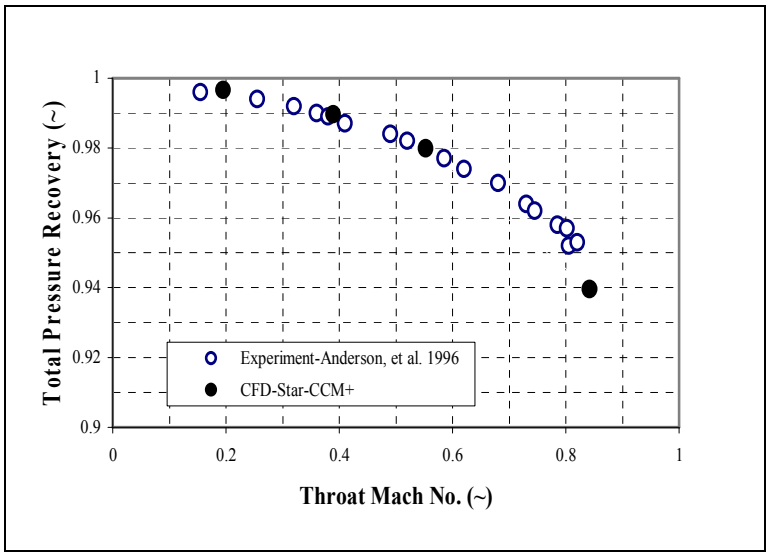

Figure 4. 7. 1. 5: Validation of total pressure recovery ($\overline{Pt}_{ef}$ / Pt_{∞}) of STAR-CCM+ code to experimental data[53]

4.7.2. Validation of unsteady-state computations

The validation of the unsteady-state results by CFD codes is crucial because the present study also investigates the icing effects on the dynamic distortion of the M2129 S-duct inlet. Therefore, the performance of STAR-CCM+ code on the unsteady-state computation is compared to an experimental data.[53] Only STAR-CCM+ code is used for the unsteady-state computations of the present study.

An unsteady-state simulation is influenced not only by a mesh size, but also by time-step size. Figure 4.7.2.1 shows the comparison of total pressure fluctuations at the engine face with the different mesh sizes: coarse mesh (about 2,600,000cells) and fine mesh (about 3,700,000cells), and different time-step size: Δt=0.0005sec., 0.001sec., and 0.01 sec. Therefore, the mesh cell numbers are increased by about 46 percent with the fine mesh case compared to the coarse mesh case, and both mesh

cases do not include an icing portion, i.e., the baseline inlet or clean inlet. Also, the LES turbulence model, which showed the best unsteady-state results in the previous chapter, is applied for this validation process. In addition, the free-stream Mach number is M_∞=0.34, and the total pressure at each time-step is an area-averaged value at the instantaneous time. The figure shows that different mesh sizes and time-step sizes result in the change of the fluctuation pattern. In particular, different time-step sizes induce major changes in the total pressure fluctuation plots. The smaller the time-step size is the more-fluctuating pattern with a lower mean value of total pressure would be produced. In addition, the case of the coarse mesh with Δt=0.001 sec. demonstrates a similar fluctuation pattern to that of the case of the fine mesh with Δt=0.0005 sec. The similarity in the fluctuation patterns is due to the fact that the deviated fluctuation pattern with the different mesh size becomes similar again with a different time-step size**.**

The calculated levels of total pressure fluctuation with two different time-step sizes (Δt=0.0005sec. and 0.01sec.), but with the same mesh sizes (3,700,000cells), are compared to the unsteady-state experimental data,[53] as shown in Figure 4.7.2.2. For the comparison, the dynamic distortion parameter, $\overline{Pt}'_{rms}/\overline{Q}_{ef}$, is defined. $\overline{Pt}'_{rms}$ represents the total pressure fluctuation at the engine face, and $\overline{Q}_{ef}$ denotes the area-averaged dynamic pressure at the engine face. In particular, $\overline{Pt}'_{rms}$ is obtained from:

$\overline{Pt}'_{rms}$ = rms (root mean square) of time-variant $\overline{Pt}'$

Where, $\overline{Pt}' = \overline{Pt}_{ef\text{-}INS} - \overline{Pt}_{ef}$ Equation (18)

$\overline{Pt}'$ represents a total pressure fluctuation, $\overline{Pt}_{ef\text{-}INS}$ denotes the total pressure at an instantaneous time, and $\overline{Pt}_{ef}$ stands for time-averaged total pressure, i.e., the total pressure value in steady-state. All quantities are the area-averaged values, which are measured at the engine face. Figure 4.7.2.2 shows that the larger time-step size case produces the relatively closer fluctuation levels around M_{th}=0.4 to 0.6, whereas the smaller time-step size induces the substantially higher fluctuation levels at most of the throat Mach-numbers, compared to the experimental fluctuation data. The excellent validation of the computed dynamic distortion levels over all Mach numbers is impossible in the present study, since the unsteady-state computational setup, such as a mesh size and time-step size, can not be optimized for all Mach numbers. In addition, the fluctuation-measurement setups in this study and in the experiment are different. In the experiment, only 8 total pressure transducers were used,[53] while about 16,000cells are employed in this study to capture the complex dynamic distortion map. However, the larger time-step size case shows relatively better unsteady-state results, as mentioned before. Therefore, the time-step size of Δt=0.01sec. is used for all unsteady-state cases in the present study, except as noted.

Note that the highest free-stream Mach number, M_∞=0.475, is excluded from the Mach number range for the unsteady-state cases of the present study, because the computational result shows the relatively large deviation from the experimental data at M_∞=0.475, which is approximately equivalent to M_{th}=0.8, as shown in Figure 4.7.2.2. However, the case of M_∞=0.13 (M_{th}=0.2) is included in the Mach number range, in spite of the deviation from the experimental data. The reason is that the

approximated values of $\overline{Pt}'_{rms}$ at M_{th}=0.2 are 0.01kPa and 0.02kPa in the experiment and computation, respectively. However, the values increase by 10 times at M_{th}=0.8 in the both experiment and computation. Therefore, the deviation at M_{th}=0.2 is much smaller, compared to that at M_{th}=0.8, and it is considered as an acceptable level. Also, the fine mesh set that includes total 3,700,000cells and 5,200,000cells for the clean and iced inlet, respectively, is applied for all unsteady-state cases, since the application of the LES turbulent model requires fine meshes.

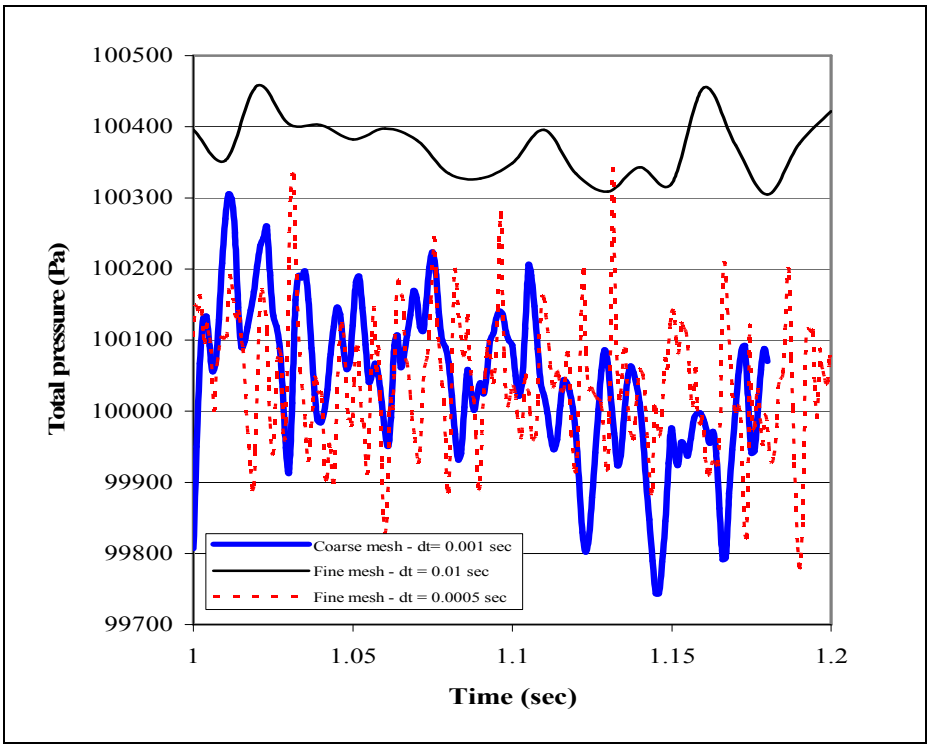

Figure 4. 7. 2. 1: Effects of mesh size and time step size
on total pressure fluctuations at the engine face
(M_∞=0.34, coarse mesh = 2,600,000 cells, dense mesh = 3,700,000 cells)

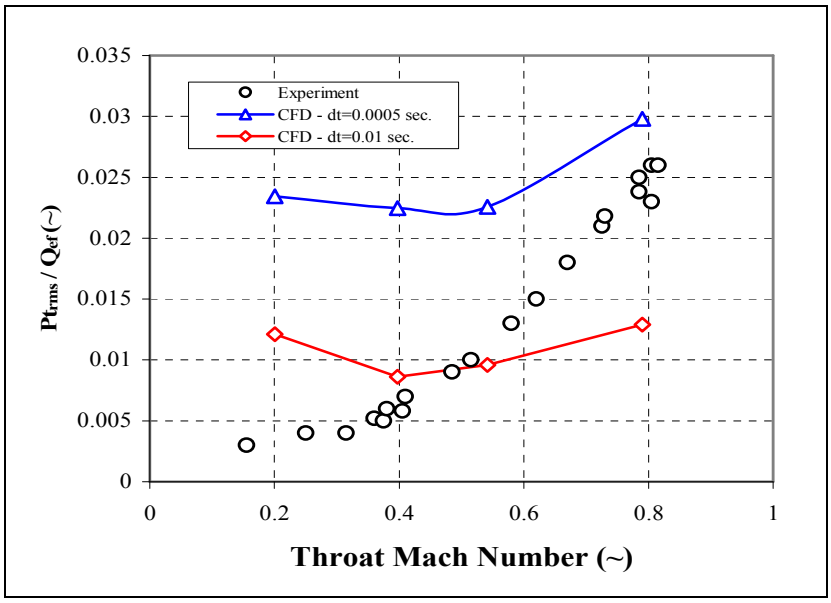

Figure 4. 7. 2. 2: Validations of dynamic distortion parameters ($\overline{Pt}'_{rms}/\overline{Q}_{ef}$) with two time-step sizes (Δt=0.0005sec. and 0.01sec.) to experimental data[53]

5. Results and discussions

This chapter consists of the following sub-chapters;

5.1. The effects of rime and glaze ice accretion on the performance of an S-duct inlet.

5.2. The combined effects of inlet icing and the free-stream Mach numbers (M_∞=0.13 to 0.85).

5.3. The effects of symmetrical and asymmetrical glaze ice accretion shapes.

5.4. The effects of inlet icing on the dynamic inlet distortion.

5.5. The effects of glaze ice horn thickness.

5.6. The combined effects of the symmetrical glaze ice accretion shapes and angles of attack or sideslip angles.

5.7. The combined effects of the asymmetrical glaze ice accretion shapes and angles of attack or sideslip angles.

5.8. The combined effects of inlet icing and angle of attack or sideslip angle on the dynamic inlet distortion.

5.9. The combined effects of inlet icing and wall heat transfer on the coupled total pressure- temperature distortion.

5.1. Effects of rime and glaze ice

As mentioned in Chapter 3.2 of the present study, the ice accretion types on the aircraft's surfaces are generally classified as rime and glaze, according to the meteorological parameters and flight conditions. In addition, rime ice type has a relatively streamlined-shape, whereas, glaze ice type is characterized by intrusive horns to the inflow. Consequently, the influences of the two ice accretion shapes on the flowfield in an S-duct inlet can be considerably different, due to their geometrical characteristics to the duct inflow. Therefore, the effects of rime and glaze ice accretion shapes on the total pressure distortion and performance of the M2129 S-duct inlet are investigated.

Figures 5.1.1 and 5.1.2 show comparisons of the steady-state flowfield distributions for the clean and iced inlet lips with rime and glaze shapes. The test conditions, such as freestream Mach number and static temperatures are defined according to the icing conditions in Reference 8: V_∞=25m/s: Ts_∞=-29.9°C: LWC=0.2g/m^3: MVD=20.36 μm: icing time=30min. and V_∞=25m/s: Ts_∞=-9.3°C: LWC=0.695g/m^3: MVD=20.36 μm: icing time=30min., for rime and glaze, respectively. Note that difference in the freestream Mach number, although the freestream velocities are the same, is caused by the difference in the static temperature. In addition, the test conditions for the two different clean cases are defined according to the conditions for the rime and glaze cases, respectively. Figure 5.1.1 indicates that there are few changes in total and static pressure, and Mach number distribution due to the rime ice accretion. However, significant changes in the flowfield distributions are observed for the glaze icing type as shown in Figure

5.1.2. For the comparison of total pressure contours, which are presented in Figure 5.1.2(a), the lower total pressure regions occur behind the lower horn of the glaze ice, due to the massive flow separations (or boundary layer separation). These low total pressure regions significantly increase total pressure loss in the duct downstream through the diffusion mechanism. The increase of higher static pressure regions is observed in front of the glaze iced inlet lip, as shown in Figure 5.1.2(b). This is caused by the increase in the stagnation area, which is normal to the upcoming flow due to the un-streamlined shape of the glaze ice accretion. In addition, the flow separation and higher Mach number region around the glaze ice change the characteristics of the entire flowfield downstream, as shown in Figure 5.1.2(c).

Total pressure contours of the clean and glaze ice cases at the different planes normal to the flow are compared in Figure 5.1.3. In each plane, including the engine face station, severe total pressure losses are produced by the effect of the geometrical change of the inlet lip with the glaze ice accretion. Significantly distorted total pressure recovery at the engine face for the glaze ice case suggests that the glaze ice accretion can produce very unfavorable effects on the compressor stage, and on the entire performance of the aircraft engine.

To see the increase of the secondary flow (counter-rotating vortex pair) region with the inlet icing, the secondary flow vectors at the engine face plane for clean and glaze ice cases are compared in Figure 5.1.4. Compared to the clean inlet lip case, a larger secondary flow region is formed at the engine face because of the effect of the glaze ice. The size of the secondary flow region of glaze icing case is approximately 600 percent larger than that of the clean case.

The total pressure recovery ($\overline{Pt}_{ef}/Pt_{\infty}$) at the engine face is shown in Figure 5.1.5 to compare the icing effects just before the compressor stage of an aircraft engine. The levels of the total pressure recovery at the engine face for the rime and glaze ice cases are 0.988 and 0.958, respectively. Therefore, for the rime ice accretion case, the total pressure recovery is decreased by 0.02 percent compared to the clean case, and this decrease can be considered as there is almost no effect with the rime ice. However, an approximately 3.2 percent-decrease occurs when glaze ice is accreted on the inlet lip. Therefore, the level of total pressure distortion, which is generally represented by the magnitude of total pressure recovery, becomes more significant with the glaze ice accretion.

The mass flow rates of different cases at the inlet duct throat are compared in Figure 5.1.6. The difference in the mass flow rate for the rime-clean and glaze-clean cases, although the inlet shapes are the same, is caused by different test conditions and temperatures: Ts_{∞}=-29.9°C and -9.3°C for the rime and glaze ice, respectively. The figure shows that the mass flow rate of the rime ice case is decreased by approximately 0.2 percent, while that of the glaze ice case is reduced by about 26 percent compared to their clean cases. The remarkable reduction in the mass flow rate of the glaze ice case results from the diminished cowl area (highlight area or inlet frontal area), when glaze ice with the thick lower horns develops at the leading edge of the inlet lip. Note that the cowl area is decreased by 21 percent with the simulated glaze ice accretion.

Static pressure distributions (Ps/Pt_{∞}) along the wall surface at θ=0° (top) and 180° (bottom) are also given in Figure 5.1.7. The definition of the circumferential

angle is shown in Figure 4.2.8. In Figure 5.1.7, the rime case represents a similar pressure distribution pattern with clean cases at θ=180°, showing an abrupt decrease of static pressure at the suction part of the first curved section. Furthermore, the static pressure recovers downstream due to the effect of the second curvature at θ=0° wall surface of the S-duct. In contrast to this, the glaze case displays dissimilar pressure distributions and overall static pressure ratios are much lower in comparison with the clean case.

Based on the computational results, it can be concluded that the glaze ice accretion on the inlet lip produces a significant total pressure distortion and a degradation of the inlet performance, due to the effect of its intrusive horns. Stronger flow separation and a wider blocking area to the duct inflow occur under the influence of the glaze ice type. However, the rime ice shape, which is characterized by its relatively stream-lined shape, induces not significant effects on the flowfield in the S-duct inlet.

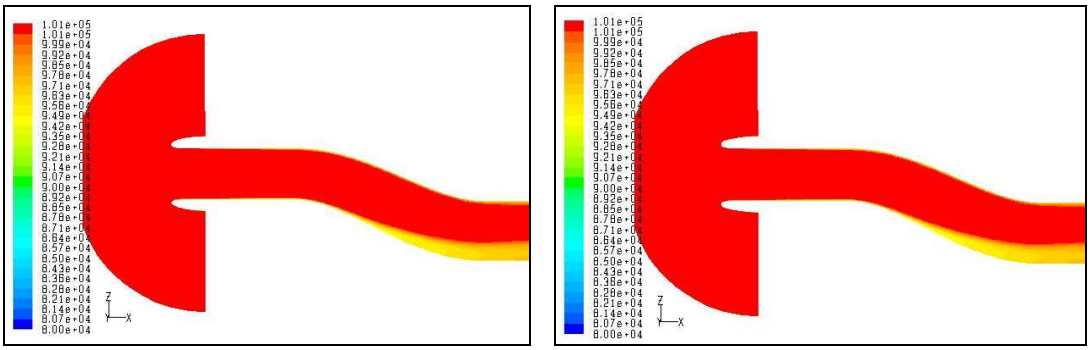

(a) Total pressure (unit: Pa)

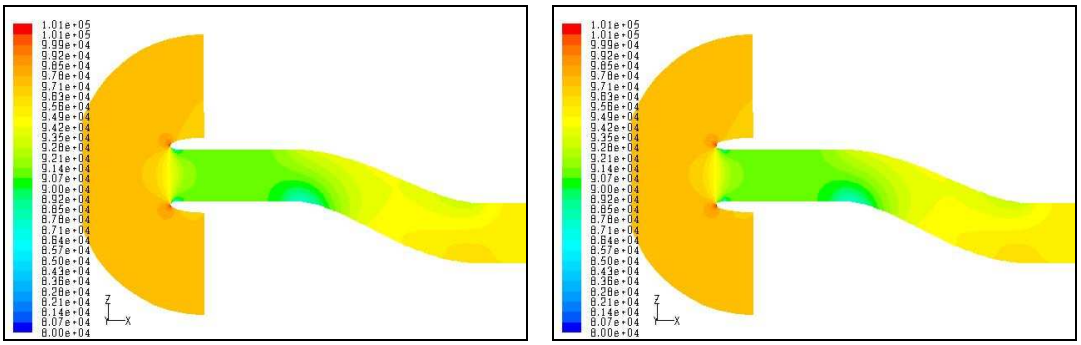

(b) Static pressure (unit: Pa)

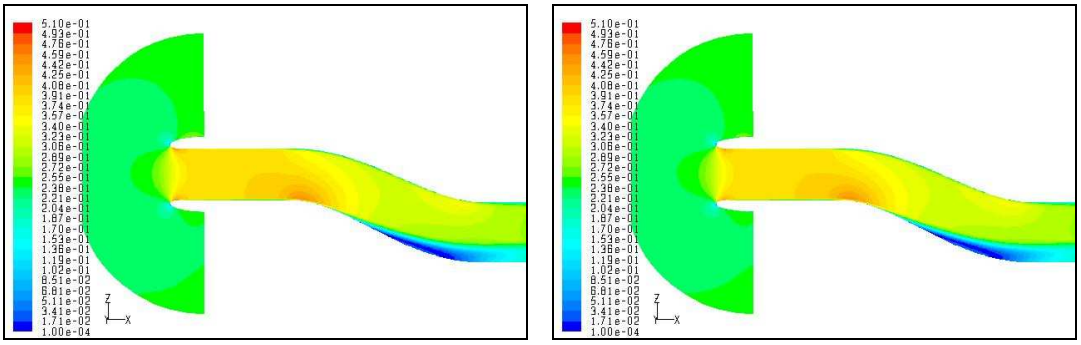

(c) Mach number

i. Clean ii. Rime

Figure 5. 1. 1: Comparison of flowfield distributions in the duct symmetry plane (V_∞=75 m/sec., M_∞=0.24, Ts_∞=-29.9°C, LWC=0.2g/m^3, MVD=20.36 μm, α=β=0º)

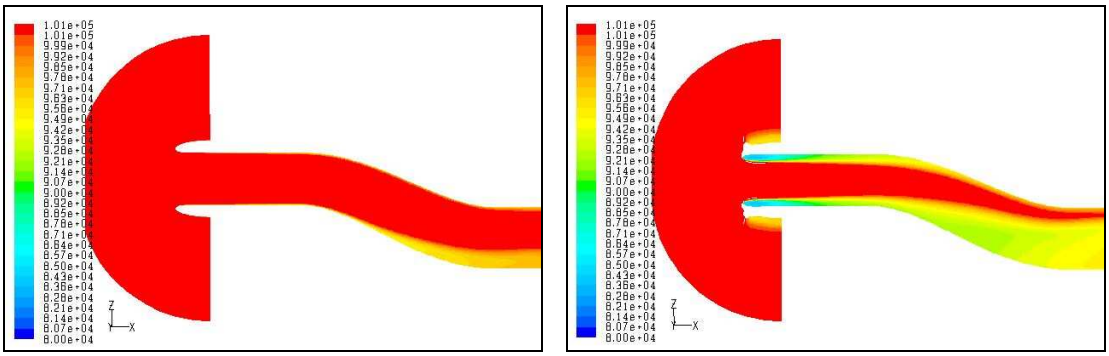

(a) Total pressure (unit: Pa)

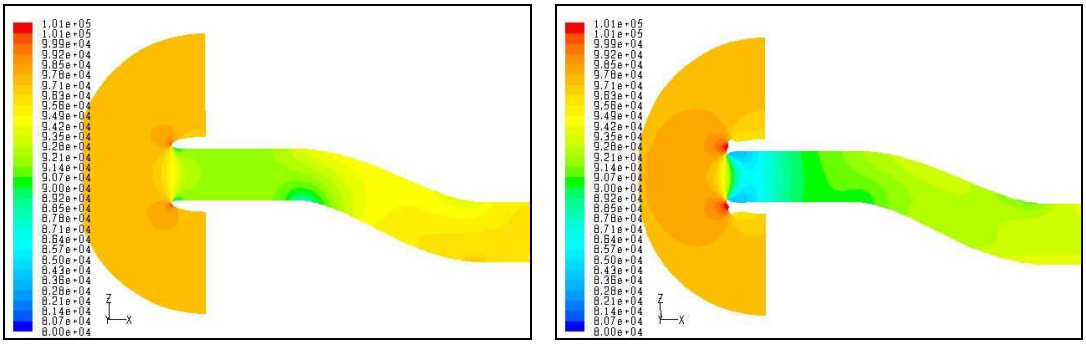

(b) Static pressure (unit: Pa)

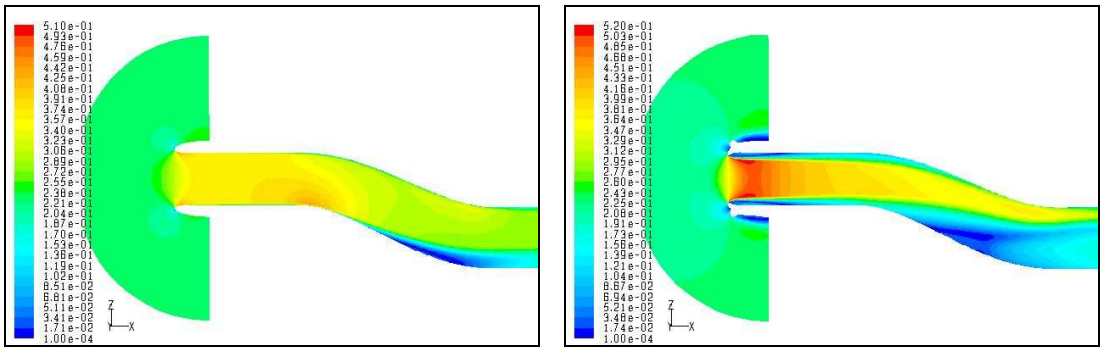

(c) Mach number

i. Clean ii. Glaze

Figure 5. 1. 2: Comparison of flowfield distributions in the duct symmetry plane (V_∞=75 m/sec., M_∞=0.23, Ts_∞=-9.3°C, LWC=0.695g/m^3, MVD=20.36 μm, α=β=0º)

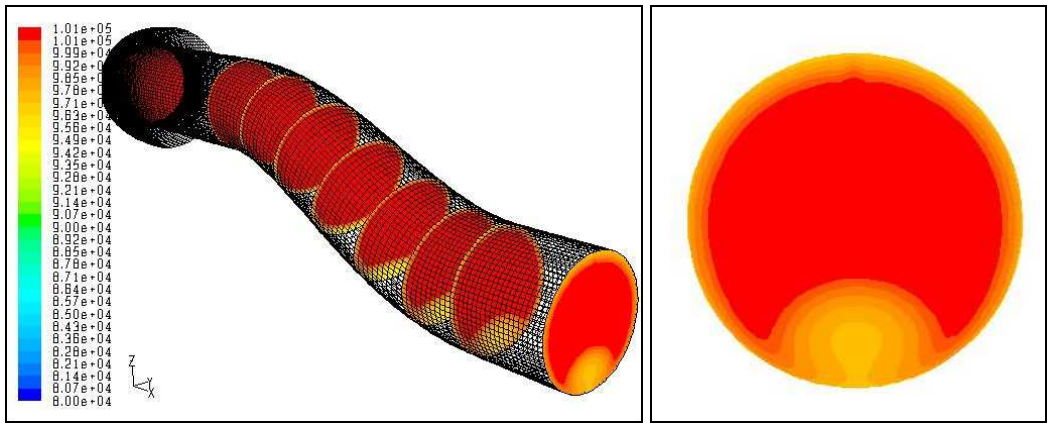

(a) Clean

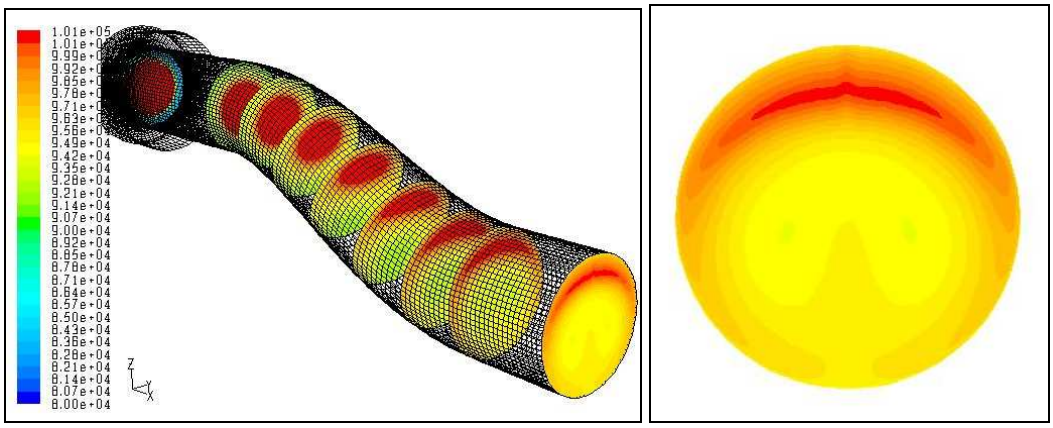

(b) Glaze

i. Different stations ii. Engine face

Figure 5. 1. 3: Total pressure (Pt) contours in the planes normal to the flow (V_∞=75 m/sec., M_∞=0.23, Ts_∞= 9.3°C, LWC=0.695g/m^3, MVD=20.36 μm, unit: Pa)

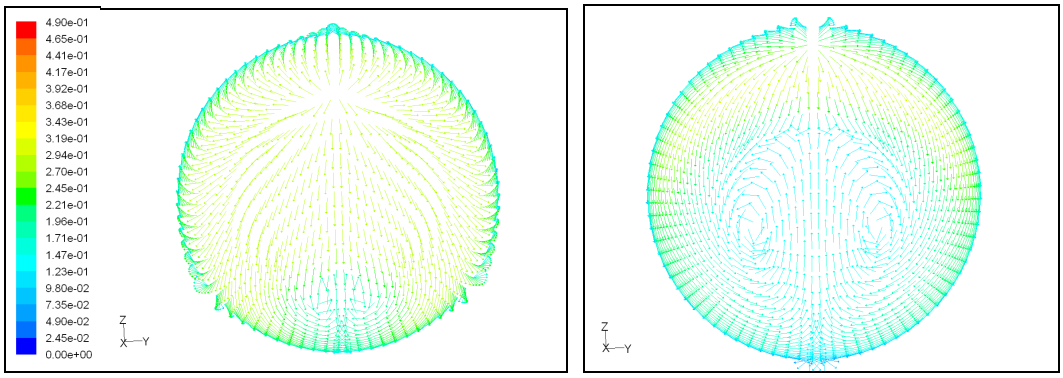

(a) Clean (b) Glaze

Figure 5. 1. 4: Comparison of the secondary flow patterns at the engine face (unit: m/sec.)

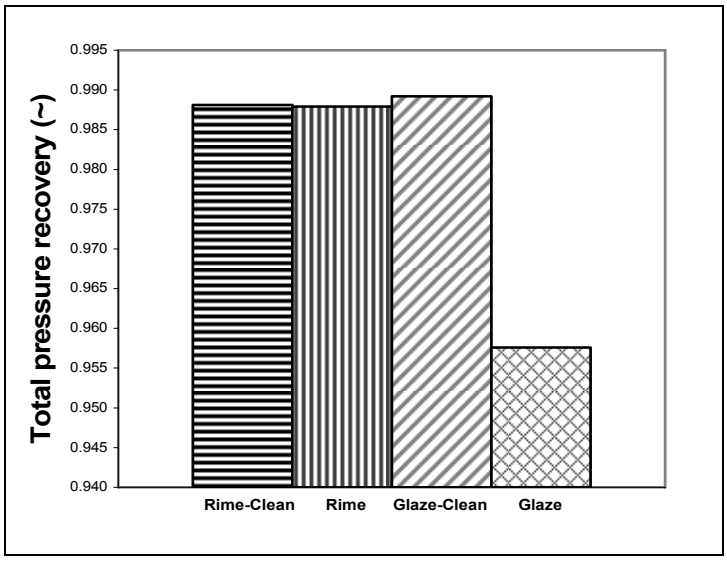

Figure 5. 1. 5: Comparison of total pressure recoveries ($\overline{Pt}_{ef}/Pt_{\infty}$) at the engine face ($Pt_{\infty}$=101.1 kPa)

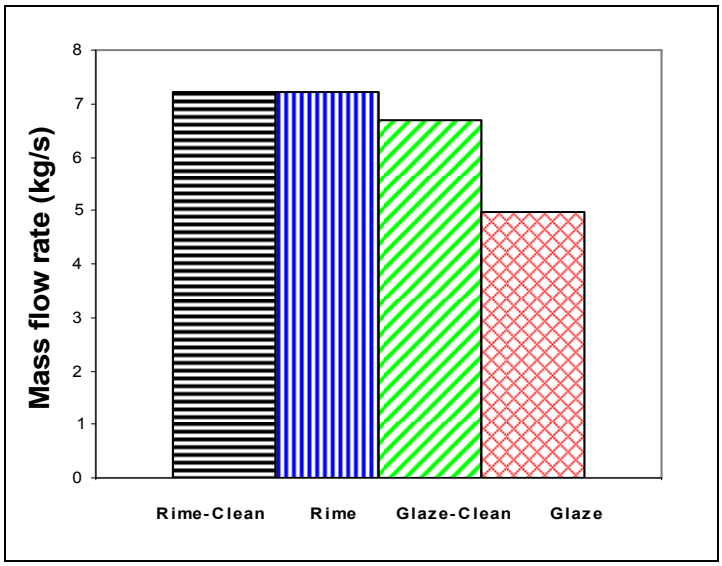

Figure 5. 1. 6: Comparison of inlet mass flow rates

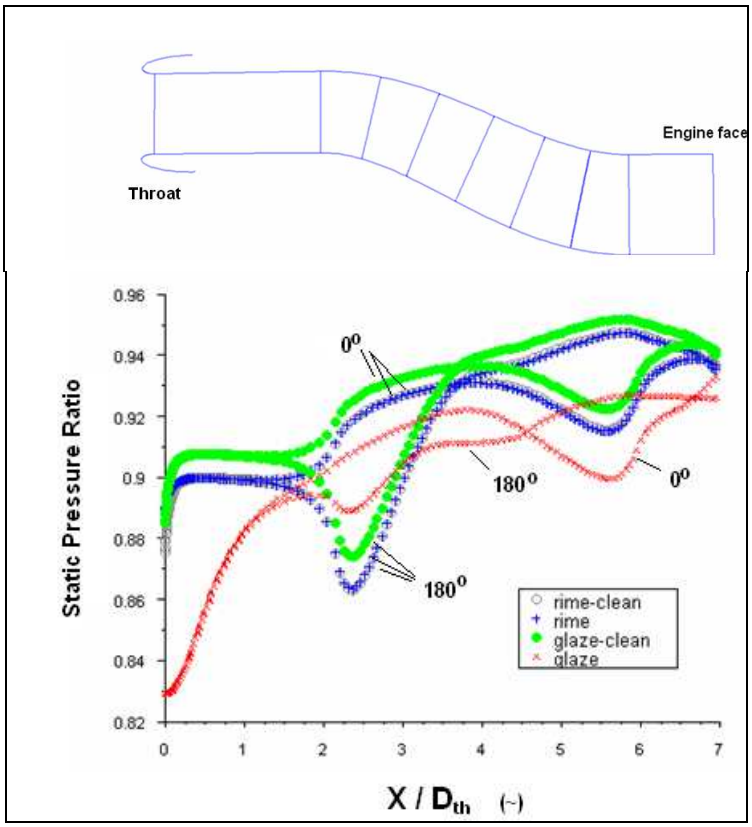

Figure 5. 1. 7: Static pressure ratio (Ps/Pt_∞) distributions along the wall surface at θ = 0° and 180° (Pt_∞=101.1 kPa)

5.2. Combined effects of inlet icing and free-stream Mach number

The effects of the rime ice accretion, which has a more streamlined shape, on the flowfield and performance of the M2129 S-duct inlet were almost negligible as shown in Chapter 5.1. A significant total pressure distortion at the engine face and a substantial degradation in the performance of the duct inlet occurred with the glaze ice shape due to the stronger flow separation from its ice horn. As mentioned before, a diffusing S-duct has an additional disadvantage in potential flow separation due to the streamwise adverse pressure gradient in the diffuser and the secondary flow in the duct curvatures. The combined flow separation and the secondary flow pattern

contribute to a problem of the engine face distortion. Furthermore, it is known that the engine face distortion, in particular the total pressure distortion, is highly dependent on free-stream Mach numbers.[49] The supersonic flow characteristics, which involve shock formations and shock-boundary layer interactions, etc., can occur in a duct inlet at high subsonic free-stream Mach numbers due to the flow acceleration through the diffusing shape and curvatures of an S-duct inlet. The duct flowfield changes in a range of free-stream Mach numbers can also be affected by the ice accretion on the duct-inlet lip. Therefore, combined effects of ice accretion and free-stream Mach numbers on the performance of the M2129 S-duct inlet are investigated. The free-stream Mach number range: M_∞=0.13 to 0.85, is tested, and the corresponding changes in the free-stream temperature: Ts_∞=265.7K to 233K, are considered for the computations.

Only glaze ice shape which produces much more effects on the duct flow is considered in the present study, and the glaze ice shape is symmetrical in the circumferential direction of the inlet lip. In the practical icing conditions, the shape and size of ice accretion are a function of free-stream velocity as proven in the numerical[8] and experimental icing tests.[12] However, a constant shape and size were assumed (a single-phase flow) in this investigation to see the changes in inlet flow pattern only with different free-stream Mach numbers. In addition, the present study should serve as a part of the investigation in determining the worst scenario with inlet icing in design.

Figure 5.2.1 shows the steady-state flowfield variations in the duct symmetry plane for both the clean and glaze ice cases, as the free-stream Mach number

increases from M_∞=0.25 to 0.85. In both cases, a supercritical flow, where the local Mach number is 1, occurs in the free-stream Mach number range between M_∞=0.25 and 0.475. The difference in the local supersonic regions of the clean and glaze ice cases is their location as seen in Figure 5.2.1(b). For the clean inlet case, the flow accelerates to a supersonic velocity at the bottom of the first bend section which is indicated in Figure 3.3.2(b). On the other hand, a decreased effective duct area by the flow separation from the glaze ice causes the supersonic region to form, even a normal shock, at the throat of the glaze iced inlet. With the occurrence of the normal shock, the total pressure is expected to be substantially decreased. As the free-stream Mach number increases up to M_∞=0.65, a diamond shock structure, which contains a series of small normal shocks, develops from the region behind the glaze ice horn, and the inlet lip separation region disappears as shown in Figure 5.2.1(c). At M_∞=0.85, the shock structure extends until the second bend section as presented in Figure 5.2.1(d). Moreover, compared to M_∞=0.65 case, the flow separation at the first bend becomes more intense with a stronger pressure gradient, which is indicated by the relatively lower and higher Mach number region at top (θ=0º) and bottom (θ=180º) sides, respectively, of the first bend. In addition, the decrease of total pressure after the extensive shock structure, caused by the glaze ice accretion, must be another source of total pressure loss at the engine face. Note that in the clean case at M_∞=0.85, there is no flow separation at the first bend. Instead, the supersonic flow accelerates until the second bend due to its diffusing duct shape, and a flow separation occurs at the top side of the second bend.

Also, the total pressure ratio (Pt/Pt_∞) patterns and the secondary flow vectors at the engine face are compared in Figure 5.2.2. The secondary flow vectors are given in the form of the vectors of the secondary flow velocities divided by the free-stream velocities (V/V_∞). With increasing free-stream Mach numbers, the flow separation region at the bottom side of the duct increases in the clean case, but the pattern is totally changed at M_∞=0.85, exhibiting the flow separation from the top side as mentioned before. Note that the direction of the counter-rotating vortices is opposite in these cases because of the location change of the flow separation. For the glaze ice cases, the secondary flow region becomes larger and moves to the bottom side as the free-stream Mach number increases, and another flow separation occurs at the outer-top side at M_∞=0.85. The change in the flow patterns at the engine face is due to the development of a complex flowfield by the glaze icing effect at the higher Mach numbers. In the comparison to the clean cases, the overall sizes of the region of total pressure loss are larger and the loss levels are higher with the glaze ice for all Mach numbers. In particular, the total pressure loss is more obvious at the higher free-stream Mach numbers. This fact indicates that the quality of flow at the engine face is degraded with the glaze ice accretion on the inlet duct lip and the degradation becomes significant with the increase of the free-stream Mach number.

The static pressure distributions (Ps/Pt_∞) along the wall surface at θ=0° (top) and 180° (bottom) are given in Figure 5.2.3. In the clean and glaze cases, the static pressure ratios along the wall surface at θ=0° and 180° decrease with increasing free steam Mach numbers due to the increase of total pressure loss. In the clean cases over M_∞> 0.475, the similar levels and patterns of pressure distribution at the straight

section in front of the duct curvature imply the presence of a choking process in the flow. However, at the curvature parts the pressure distributions on both wall surfaces are all different due to the different locations of the flow separation with different in-flow Mach numbers. At the higher free-stream Mach numbers (M_∞=0.65 and 0.85), the complex pressure distribution patterns with a sudden pressure-increase and -decrease appear in both the clean and glaze ice cases. This is due to the formation of the shocks in a supersonic internal flow at the higher free-stream Mach numbers. The overall static pressure levels of the glaze ice case are slightly lower, compared to the clean cases near the engine face. However, substantially lower pressure distributions start from the throat section of the duct at the higher free-stream Mach numbers, and these patterns indicate the shock structures from the inlet lip with glaze ice. In addition, the static pressure oscillations are observed at M_∞=0.85 in both θ=0° and 180° surfaces because of the strong diamond shock structure formation. Therefore, a more reduction in the total pressure is expected after this complex and strong shock structure with the glaze icing effect.

Figure 5.2.4 shows total pressure recoveries ($\overline{Pt}_{ef}/Pt_\infty$) at the engine face in the Mach numbers range of M_∞=0.13 to 0.85. Reduction in the total pressure recovery in both the clean and glaze ice cases becomes worse as the free-stream Mach numbers increase. However, the total pressure recovery of the glaze ice cases drops faster, compared to the clean cases. Total pressure recoveries of the glaze ice case at M_∞=0.13 and 0.85 are 0.985 and 0.61, while, those of the clean case are 0.998 and 0.79, respectively. Therefore, the total pressure recovery is decreased by 1.3 and 22.8 percent at M_∞=0.13 and 0.85, respectively. The more decreased total pressure

recovery level at higher Mach numbers can be explained by a more intense shock structure in the duct flow with the glaze ice formation. At the relatively low free-stream Mach numbers, flow separation from the ice accretion is the main source of the total pressure loss. However, the occurrence of a strong shock structure with the icing effect at the higher Mach numbers is an additional source of a considerable total pressure reduction at the engine face. Also, note that a military specification[85] defines the requirement for the turbo fan engine performance in the icing condition as:

The engine shall operate satisfactorily under the meteorological conditions with not more than 5 percent total loss in thrust available and 5 percent total increase in specific fuel consumption at all operating conditions above 50 percent maximum continuous power setting.[84]

In addition, it is known that typically 1 percent inlet total pressure degradation leads to an approximately 1.5 percent drop in the net installed thrust in an aircraft gas turbine engine or equivalently about a 1.5 percent increase in its specific fuel consumption.[56] In that sense, the decrease in the total pressure recovery, which is 22.8 percent, with the glaze ice at M_∞=0.85 corresponds to about a 34 percent total loss in the engine thrust (F_n) and 34 percent increase in the specific fuel consumption (SFC). Those degradations are substantial and are far below the minimum requirement for the engine performance under the icing condition. Furthermore, with the glaze icing effect, the steady-state performance of an engine can not meet the requirement at all Mach numbers above M_∞=0.2, as seen in Figure 5.2.5. The total pressure recovery is decreased by 4.4 percent with the glaze icing effect at M_∞=0.25,

and this value corresponds to 6.6 percent-increase in the engine thrust loss and the specific fuel consumption.

Figure 5.2.6 shows a comparison of the total pressure distortion parameters (DP) of the clean and glaze ice cases with the free-stream Mach numbers. The total pressure distortion parameter (DP) is a descriptor that highlights the maximum distortion at the engine face, as defined in Equation (5). The glaze ice cases induce higher levels of DP, compared to those of the clean cases, at all free-stream Mach numbers, as noted earlier in the total pressure distortion patterns as shown in Figure 5.2.2. Moreover, the difference in the DP levels becomes more significant as the Mach number increases: for the clean and glaze cases, DP=0.01 and 0.02, respectively, at M_∞=0.13, while DP=0.74 and 0.9, respectively, at M_∞=0.85.

The variations of the inlet mass flow rate with increasing the free-stream Mach number are shown in Figure 5.2.7. In both cases, the increase of mass flow rate stops around M_∞= 0.5 due to the choking process. However, the levels of inlet mass flow rate for the glaze ice cases are much lower than those for the clean cases, and the gap between the clean and glaze cases has become wider with the increase of the free-stream Mach number until the flow is chocked. At M_∞=0.13, the level of the mass flow rate of the glaze ice case is about 73 percent of that of the clean case, while at M_∞=0.475, which is the Mach number before the choking, the level is approximately 67 percent. This fact suggests that when the glaze ice accretes on the inlet lip, the amount of inward flow to the S-duct inlet is reduced as the free-stream Mach number increases. The results so far indicate that the icing effects on the total pressure distortion and the performance of the M2129 S-duct inlet become more substantial

with increasing the free-stream Mach number, as a result of the development of the stronger and more extensive shock structure in the inlet flow.

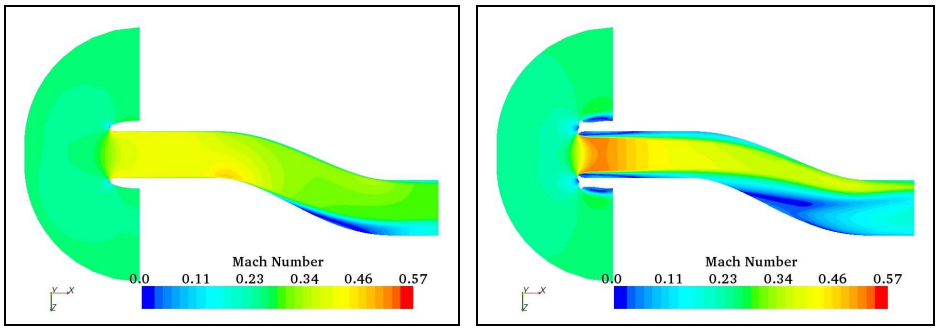

(a) M_∞= 0.25 (range: M = 0.0 - 0.57)

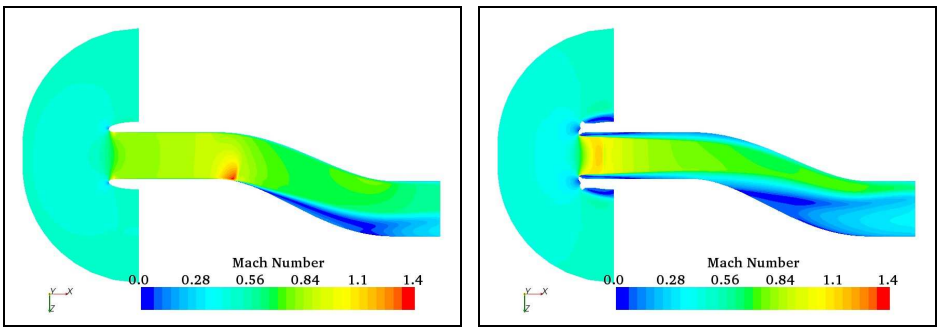

(b) M_∞=0.475 (range: M = 0.0 - 1.4)

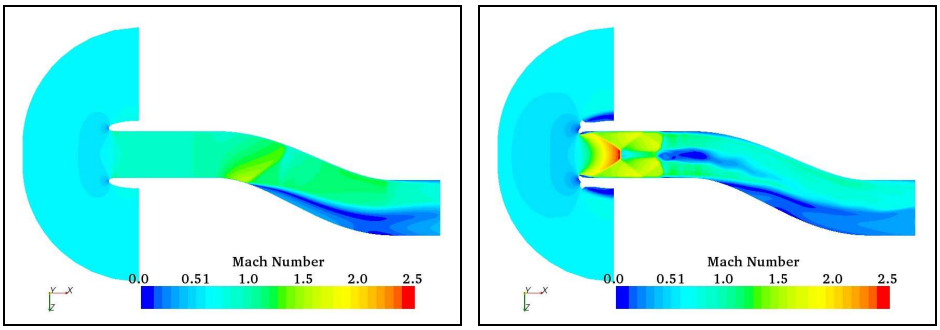

(c) M_∞=0.65 (range: M = 0.0 - 2.54)

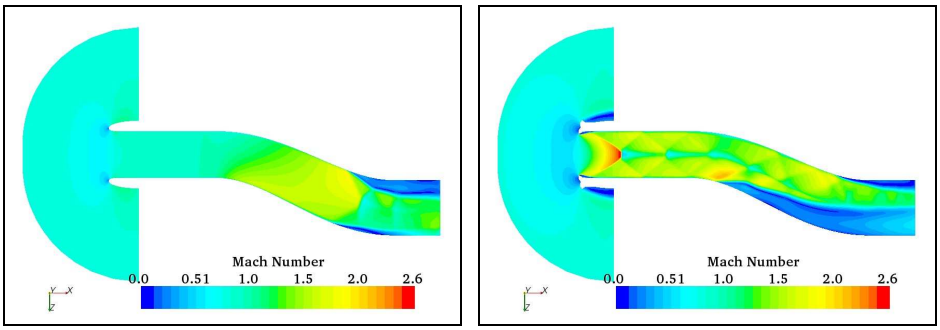

(d) M_∞=0.85 (range: M = 0.0 - 2.56)

i. Clean ii. Glaze

Figure 5. 2. 1: Mach number distributions in the duct symmetry plane with free-stream Mach numbers ($\alpha=\beta=0^o$)

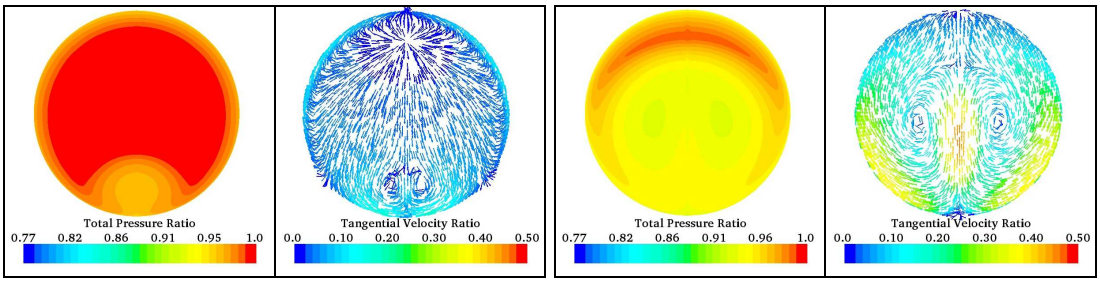

(a) M_∞= 0.25 (Pt/Pt_∞=0.77 - 1.0, Pt_∞=101.1 kPa, and V/V_∞= 0.0 - 0.5)

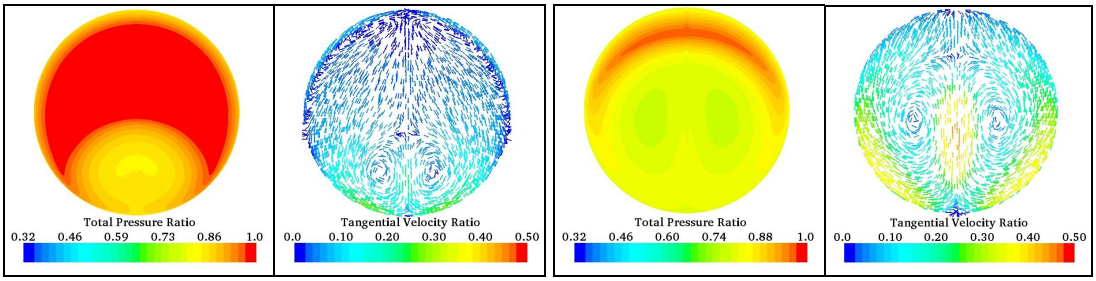

(b) M_∞=0.475 (Pt/Pt_∞=0.32 - 1.0, Pt_∞=101.1 kPa, V/V_∞= 0.0 - 0.5)

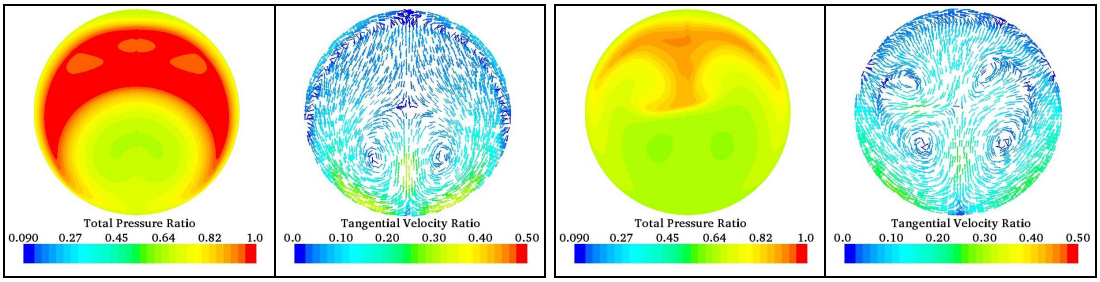

(c) M_∞= 0.65 (Pt/Pt_∞=0.09 - 1.0, Pt_∞=101.1 kPa, and V/V_∞= 0.0 - 0.5)

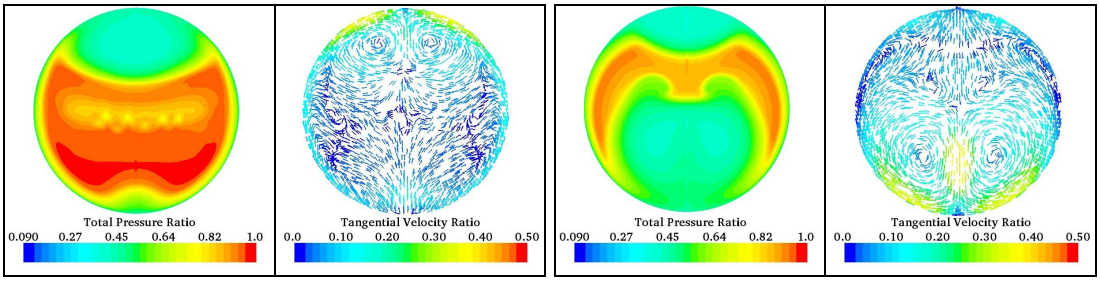

(d) M_∞= 0.85 (Pt/Pt_∞= 0.09 - 1.0, Pt_∞=101.1 kPa, and V/V_∞= 0.0 - 0.5)

i. Clean ii. Glaze

Figure 5. 2. 2: Total pressure contours and the secondary flow vectors at the engine face with free-stream Mach numbers ($\alpha=\beta=0^o$)

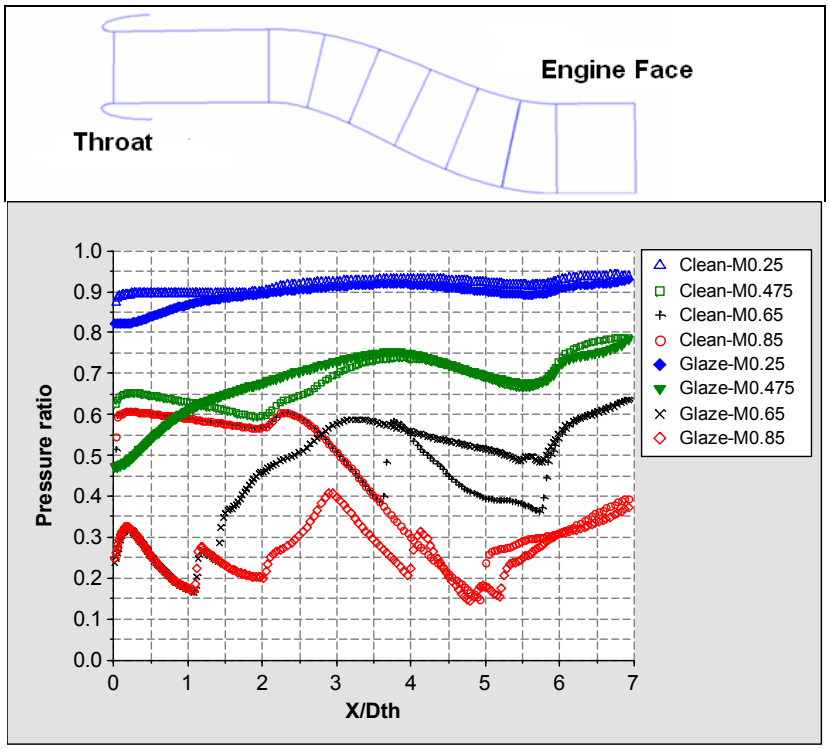

(a) θ=0°

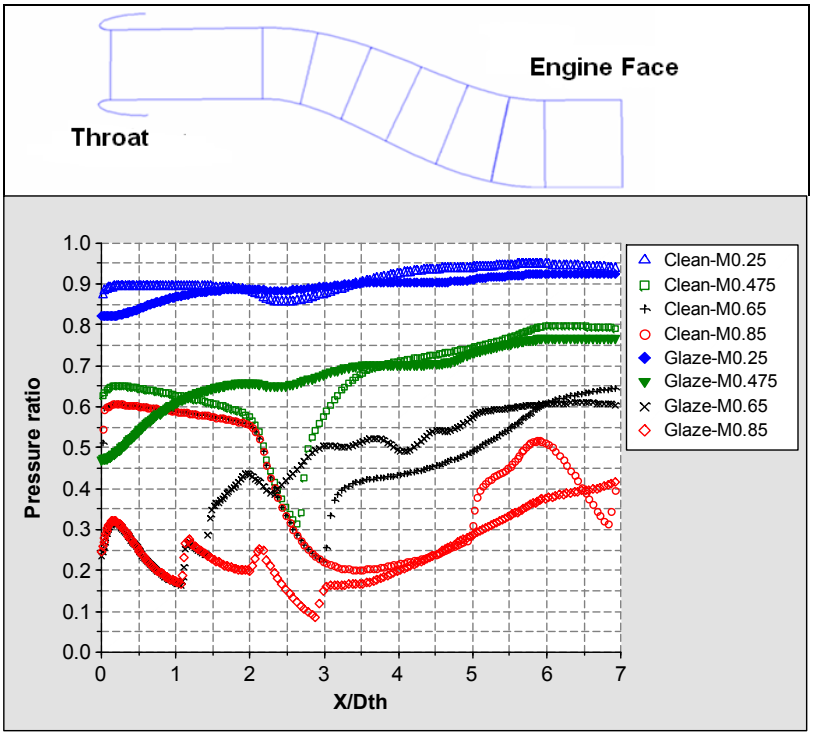

(b) θ=180°

Figure 5. 2. 3: Static pressure (Ps/Pt_{∞}) distributions along the duct wall surfaces with free-stream Mach numbers (Pt_{∞}=101.1 kPa)

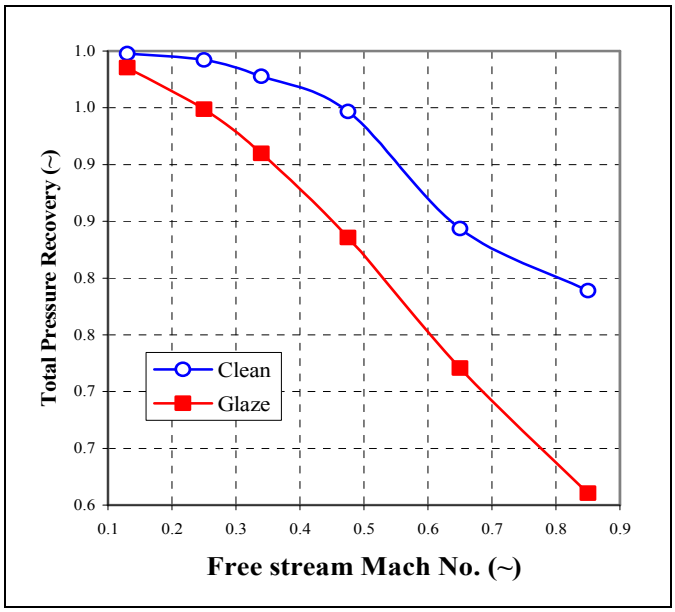

Figure 5. 2. 4: Variation of total pressure-recoveries ($\overline{Pt}_{ef}/Pt_{\infty}$) with free-stream Mach numbers (Pt_{∞}=101.1 kPa)

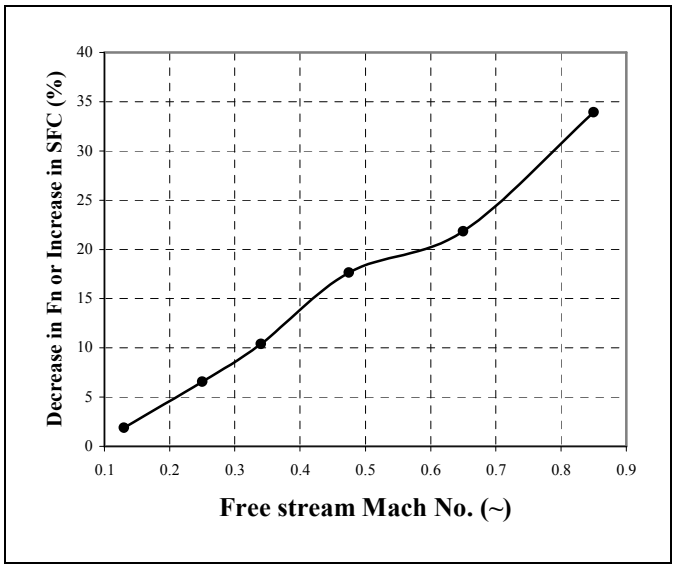

Figure 5. 2. 5: Decrease in engine net thrust (F_n) or increase in specific fuel consumption (SFC) with effect of inlet icing (glaze)

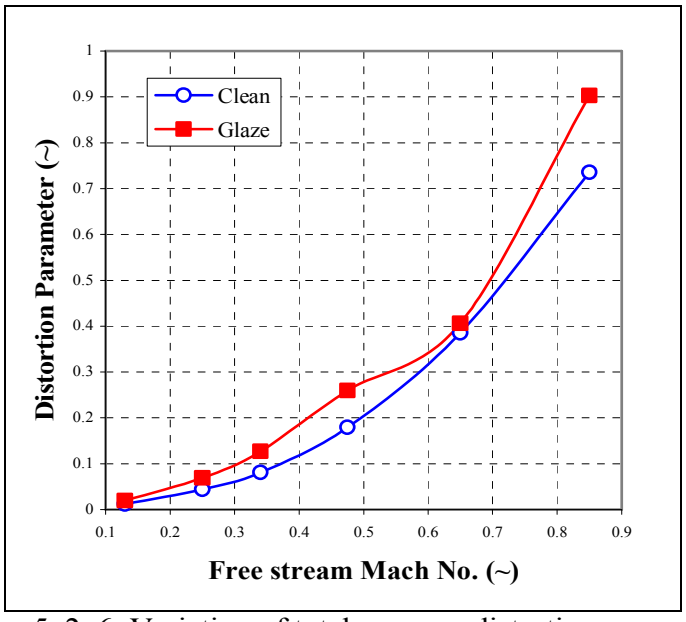

Figure 5. 2. 6: Variation of total pressure distortion parameters (DP) with free-stream Mach numbers

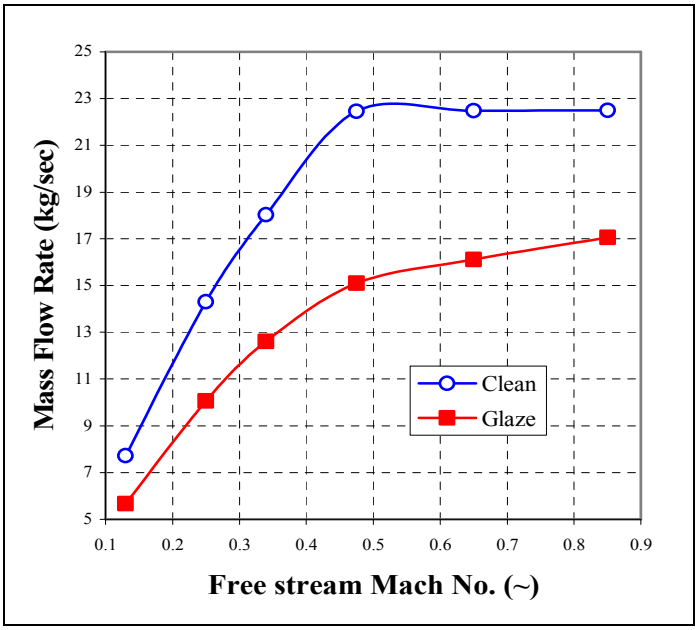

Figure 5. 2. 7: Variation of mass flow rates with free-stream Mach numbers

5.3. Effects of symmetrical and asymmetrical ice accretion

The glaze ice shape in Chapters 5.1 and 5.2 was symmetrical in the circumferential direction of the inlet lip. However, the asymmetrical ice shapes on the top- or bottom-portion of inlet lip, combined with the downward S-duct configuration, can produce a unique flowfield in the M2129 S-duct inlet to affect the performance of the duct inlet differently. Therefore, the effects of the circumferentially asymmetrical glaze ice shapes on the inlet performance are also investigated. The geometries of three different glaze ice shapes: *symmetrical glaze*, *top-asymmetrical glaze*, and *bottom-asymmetrical glaze*, to be examined are shown in Figures 4.2.9(a), (b), and (c), respectively. The top- and bottom-asymmetrical ice shapes have the symmetrical ice accretion only on the inlet portion of θ=315°-45° and θ=135°-225°, respectively. The circumferential angle is defined in Figure 4.2.8. Note that the cowl area (highlight area or inlet frontal area) is decreased by 21 percent with the simulated symmetrical glaze and 5 percent with the simulated asymmetrical ice shapes.

At the two different free-stream Mach numbers, M_∞=0.25 and 0.475, the changes in the Mach number distributions caused by the two different asymmetrical glaze ice cases are compared to the clean and symmetrical glaze ice case as shown in Figure 5.3.1. Figures 5.3.1(c) and (d) show that the internal duct flow is separated from the top- or bottom-side of glaze ice horn at M_∞=0.25. As the free-stream velocity increases to M_∞=0.475, the top-glaze ice case exhibits a strong shock at the throat section, followed by a supersonic region at the first bend. This is caused by fact that the top-glaze ice induces almost no effect on the bottom-side flow at the first

bend, which is the flow of the highest velocity by a centrifugal force, and the effective area of the duct flow at the throat is decreased by the flow separation right behind the top-glaze ice horn. The bottom-glaze also produces a shock at the same region. The intensity is however weaker compared to that in the top-glaze case, since the bottom-side flow at the first bend is affected by the bottom-side ice accretion. However, the overall Mach number level and distribution patterns at the flow duct downstream are not significantly changed with the two asymmetrical glaze shapes, in comparison to the changes in the symmetrical glaze ice case. The reason is that the separated flow from the top- or bottom-glaze ice seems to be reattached before the curved sections of the S-duct inlet. The attachment can be the result of the relatively smaller flow blockage caused by the asymmetrical ice shapes. Also note that in the asymmetrical cases at M_∞=0.475, the shock forms in the partial cross-sectional region of the inlet right behind the asymmetrical ice accretions, while, in the symmetrical case, the shock develops over the entire cross-sectional region. Therefore, the minor changes in the flowfield downstream are produced by the two asymmetrical ice shapes, although the relatively strong shock takes place right behind the asymmetrical ice.

In Figure 5.3.2, the total pressure- and the secondary vector-contours at the engine face are presented. At the higher free-stream Mach number, all cases display the wider region of a total pressure loss, caused by the more extensive secondary flow pattern at the engine faces. The top-glaze ice accretion produces the more distorted total pressure patterns, showing another region of a total pressure loss, which is also represented by the development of another region of counter-rotating vortices at the

outer top-side of the engine face. On the other hand, similar total pressure patterns, but with more enlarged regions of a total pressure loss, when compared to those of the clean inlet case, can be seen in the bottom-glaze ice case. The patterns of the bottom case are induced by the main total pressure loss with flow separation at the first bend, plus an additional loss at the same side with the ice accretion. However, the two asymmetrical cases do not show the prominent pressure losses as well as a notable increase in the velocity of the secondary flows. Therefore, the contours in Figure 5.3.2 suggest that the two asymmetrical ice shapes do not affect the duct flow at the engine face as much as the symmetrical ice shape does.

Figure 5.3.3 shows the static pressure patterns (Ps/Pt_∞) at the θ=0° and 180° duct wall surfaces when the free-stream Mach numbers are M_∞ = 0.25 and 0.475. The static pressure patterns and levels are all different regardless of the ice shapes, due to the different locations of flow separation and of the shock formation with different intensities. However, the overall patterns of the asymmetrical cases have closer similarity to those of the clean inlet cases, than to the symmetrical iced cases. In particular, the pressure distributions induced by the top-glaze ice at the region near the engine face are quite similar. Therefore, the flowfield in the S-duct inlet is relatively less sensitive to the top-glaze ice under the influence of the duct curvature.

A comparison of the total pressure recoveries ($\overline{Pt}_{ef}/Pt_\infty$) over the range of free-stream Mach numbers is given in Figure 5.3.4, which shows the expected trends from the flowfield contours shown in Figure 5.3.2. It is seen that the reductions in the total pressure recovery with the asymmetrical glaze ice cases are much less than the reduction for the symmetrical ice case. The total pressure recoveries of the top-glaze,

bottom-glaze and symmetrical glaze cases at the engine faces are 0.924, 0.922, and 0.836 at M_∞=0.475, and the corresponding reductions, compared to the clean inlet cases, are 2.4, 2.6, and 11.8 percent, respectively. In addition, the two asymmetrical cases show the almost similar total pressure recovery levels. However, a slightly less reduction occurs with the top-glaze ice. The difference can be explained by the fact that a typical duct flow pattern in an S-duct, which exhibits the higher velocity region at the bottom-side of the first bend, is less affected by the top-glaze ice accretion.

Figure 5.3.5 shows the variation of DPs of the symmetrical and asymmetrical glaze ice cases in the range of free-stream Mach numbers. As expected, based on the results of the total pressure recovery in Figure 5.3.4, the symmetrical glaze ice is seen to induce the most serious total pressure distortion. In addition, the distortion levels of the top- and bottom-glaze ice cases are almost similar. However, slightly more distortions are induced in the top-glaze ice case, and this is contrary to the results for the total pressure recovery that shows slightly more reduction in the total pressure recovery with the bottom-glaze ice. Therefore, it is assumed that a level of DP is not sensitively related to the total pressure recovery level.

The inlet mass flow rates at the engine face are also compared in Figure 5.3.6. At M_∞=0.475, the top- and bottom-glaze ice cases produce about 94 and 93 percent of the mass flow rate of the clean inlet cases, respectively, while in the symmetrical glaze ice it is only approximately 67 percent. This is due to the smaller flow blockage induced by the asymmetrical glaze ice accretion. The cowl area is decreased by 5 percent with the top- or bottom-glaze ice, while it is decreased by 21 percent with the symmetrical glaze ice. Also, in this comparison, the top-glaze case

shows a somewhat less decrease in the inlet mass flow rate, although the levels of flow blockage are the same.

In conclusion, the adverse effects of the asymmetrical glaze ice on the performance of the M129 S-duct inlet are not as critical as those of the symmetrical glaze ice. The blocking area of the symmetrical glaze ice is wider than those of the asymmetrical glaze ice by about 4 times. Therefore, the flow blockage level or icing limits on the inlet lip is an important factor for the degradation of the inlet performance. In addition, the bottom-glaze ice causes a slightly more degradation in the inlet performance than the top-glaze ice does, because a typical S-duct flow pattern, characterized by a higher velocity region at the bottom-side of the first bend, is more affected by the bottom-glaze ice accretion.

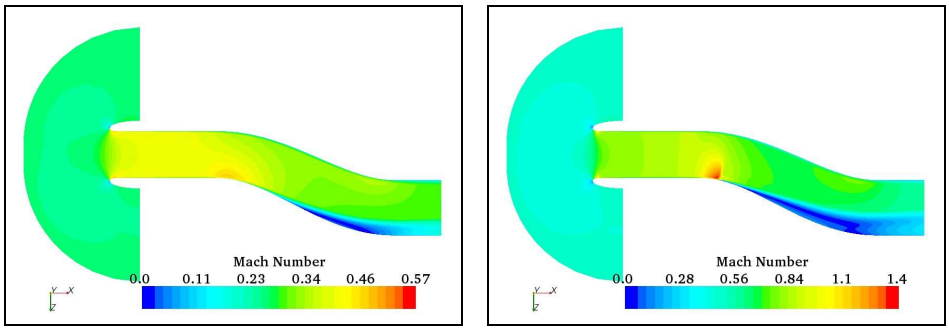

(a) Clean

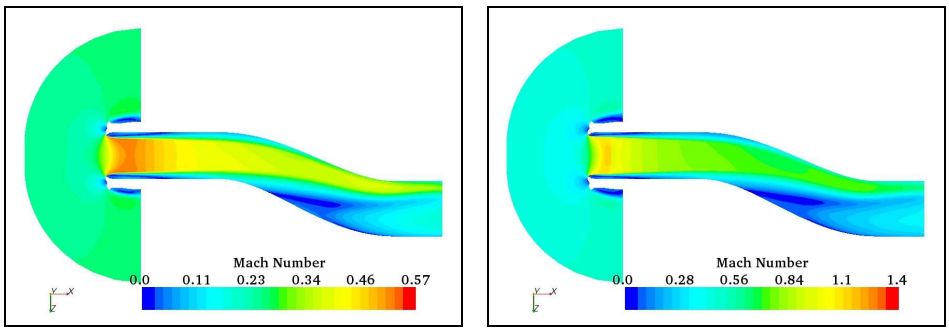

(b) Symmetrical glaze

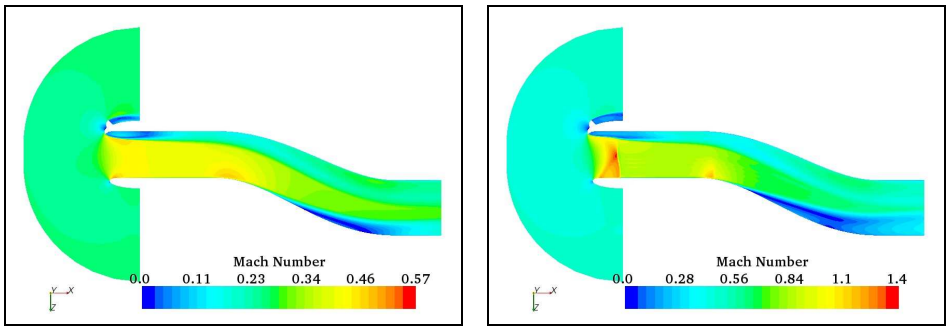

(c) Asymmetrical glaze-top (θ = 315°-45°)

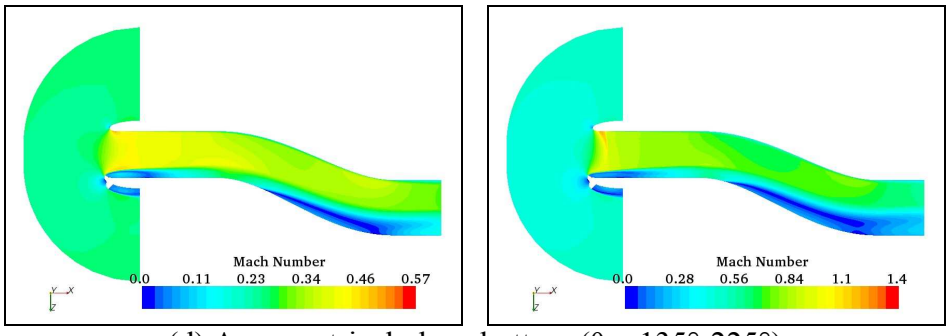

(d) Asymmetrical glaze-bottom (θ = 135°-225°)

i. M_∞ = 0.25 (M = 0.0 - 0.57) ii. M_∞ = 0.475 (M = 0.0 - 1.4)

Figure 5. 3. 1: Mach number distribution in the duct symmetry plane with different glaze ice shapes (α=β=0°)

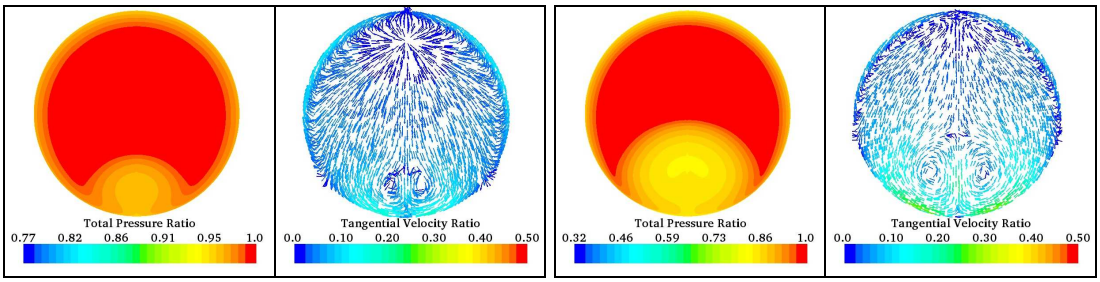

(a) Clean

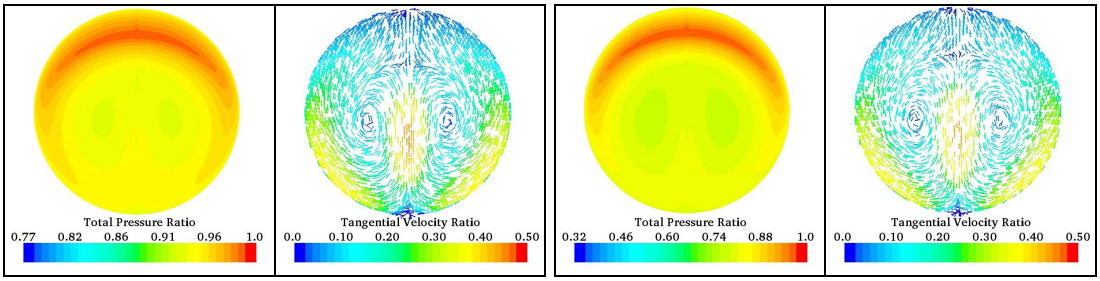

(b) Symmetrical glaze

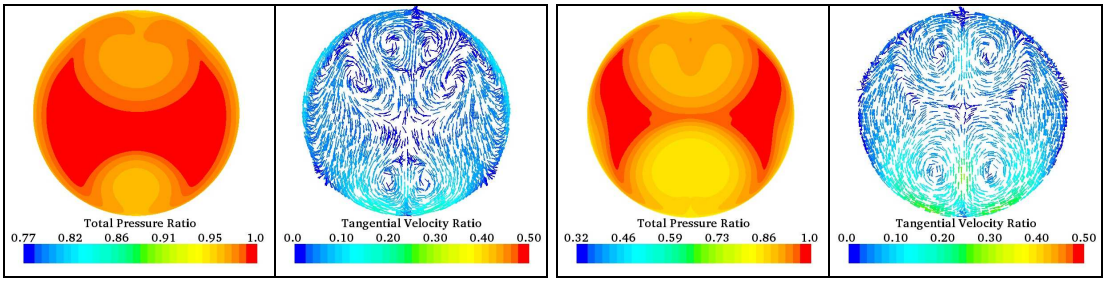

(c) Asymmetrical glaze-top (θ = 315° -45°)

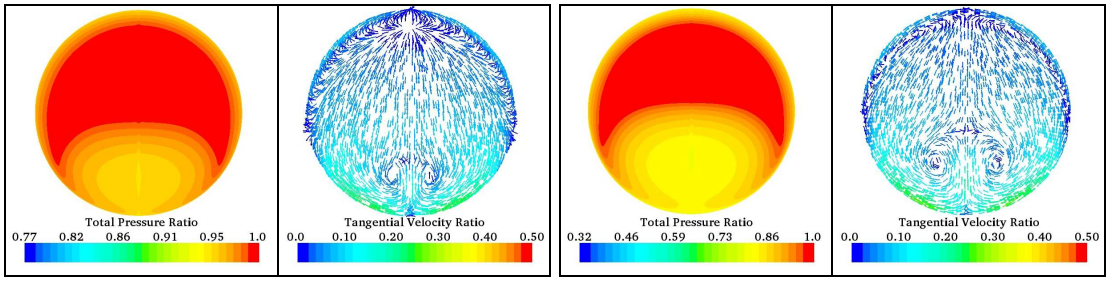

(d) Asymmetrical glaze-bottom (θ = 135°-225°)

i. $M_\infty = 0.25$
($Pt/Pt_\infty = 0.77 - 1.0$, $V/V_\infty = 0.0 - 0.5$)

ii. $M_\infty = 0.475$
($Pt/Pt_\infty = 0.32 - 1.0$, $V/V_\infty = 0.0 - 0.5$)

Figure 5. 3. 2: Total pressure contours and secondary flow vectors at the engine face with different glaze ice shapes (Pt_∞=101.1 kPa, α=β=0º)

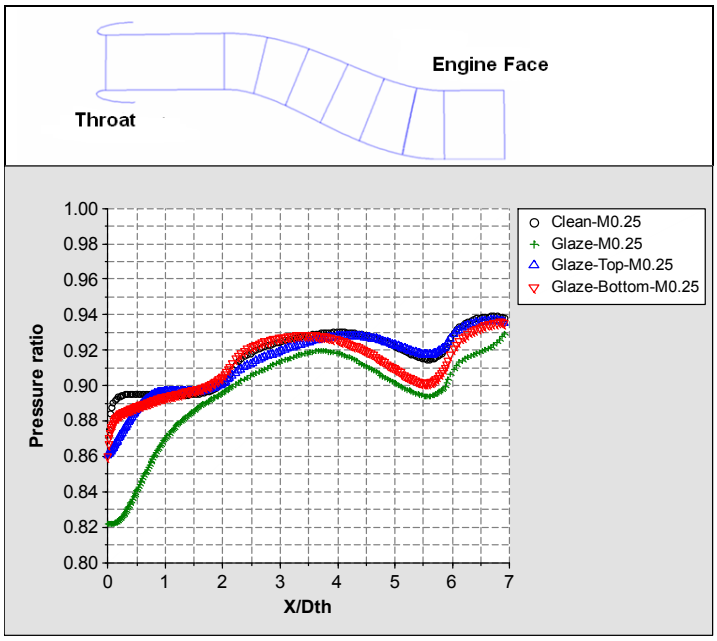

(a) θ=0° and M_∞= 0.25

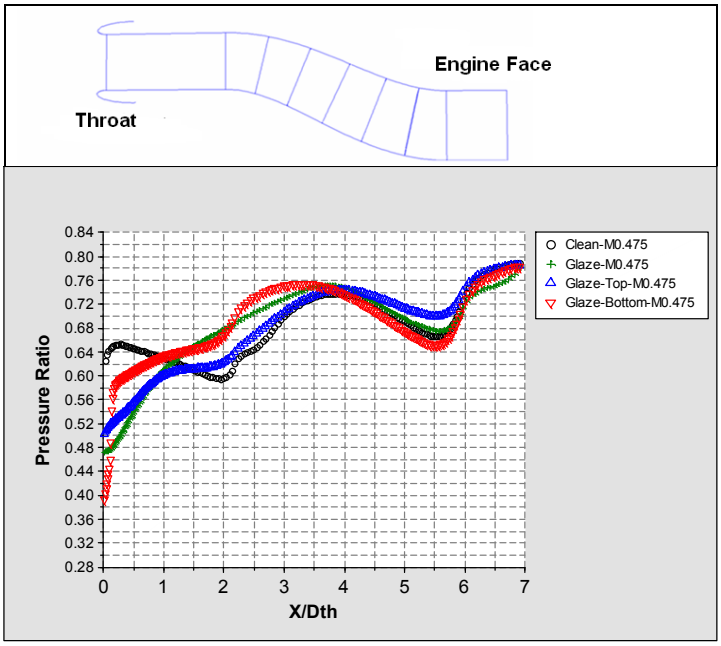

(b) θ=0° and M_∞= 0.475

Figure 5. 3. 3: Static pressure (Ps/Pt_∞) distributions along the duct wall surfaces with different glaze ice shapes (Pt_∞=101.1 kPa)

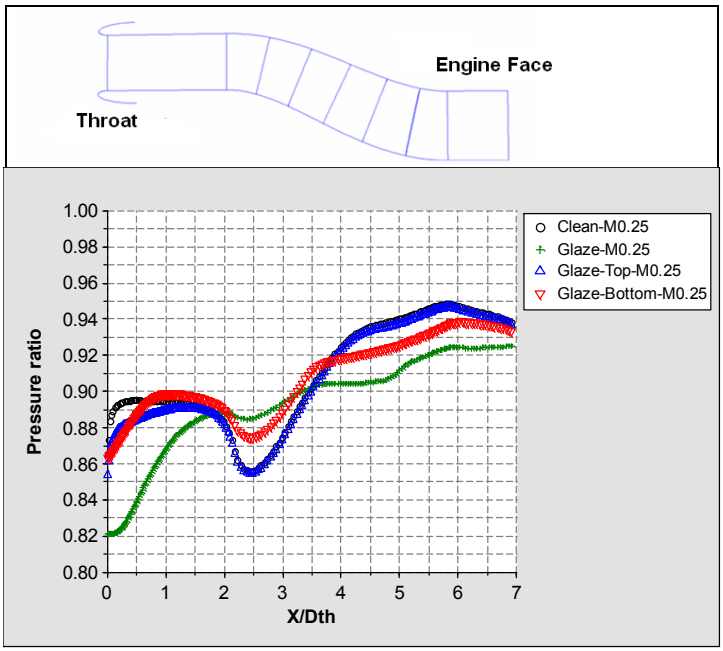

(c) θ = 180° and M_∞ = 0.25

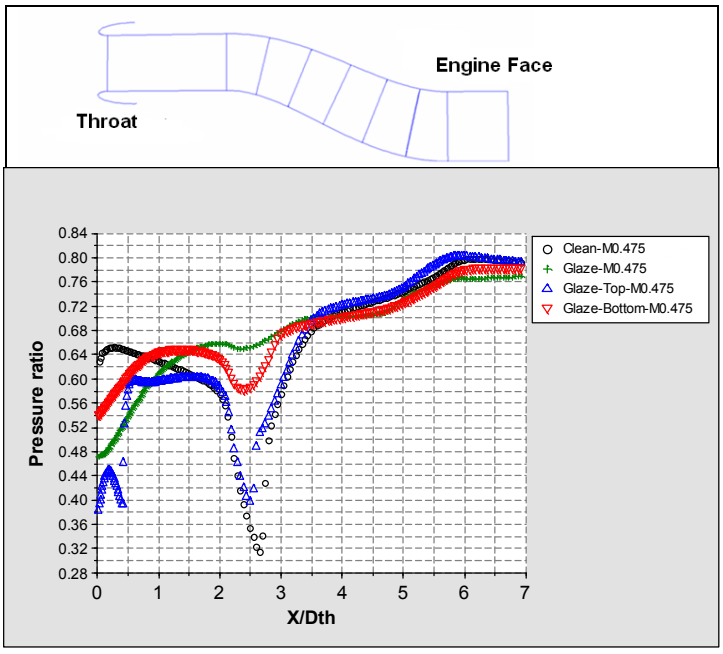

(d) θ = 180° and M_∞ = 0.475

Figure 5. 3. 3: Static pressure (Ps/Pt_∞) distributions along the duct wall surfaces with different glaze ice shapes (Pt_∞=101.1 kPa)

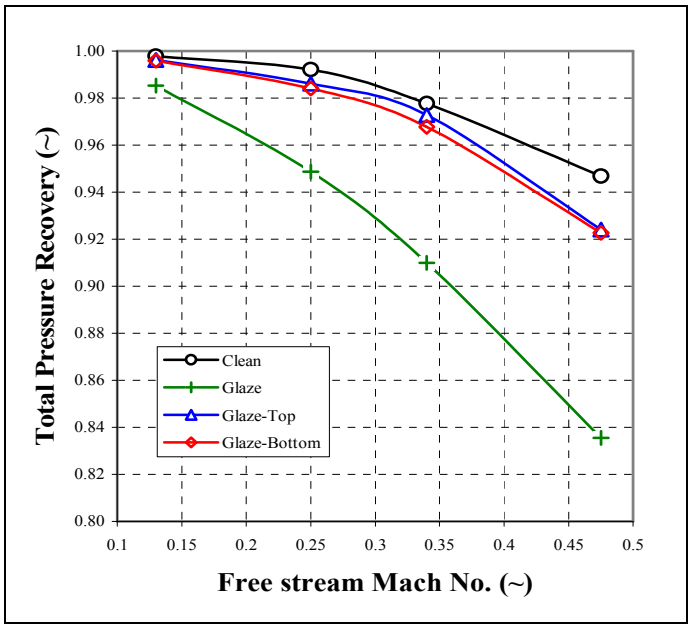

Figure 5. 3. 4: Total pressure recoveries ($\overline{Pt}_{ef}/Pt_{\infty}$) with different glaze ice shapes (Pt_{∞}=101.1 kPa)

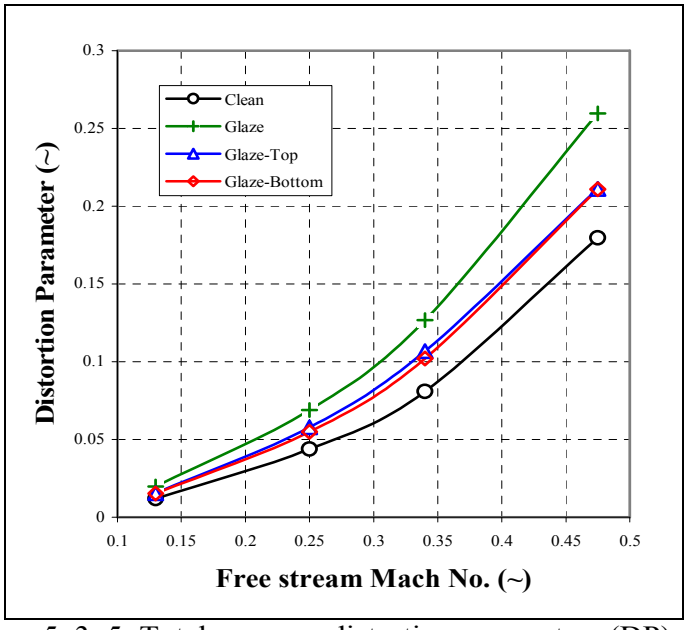

Figure 5. 3. 5: Total pressure distortion parameters (DP) with different glaze ice shapes

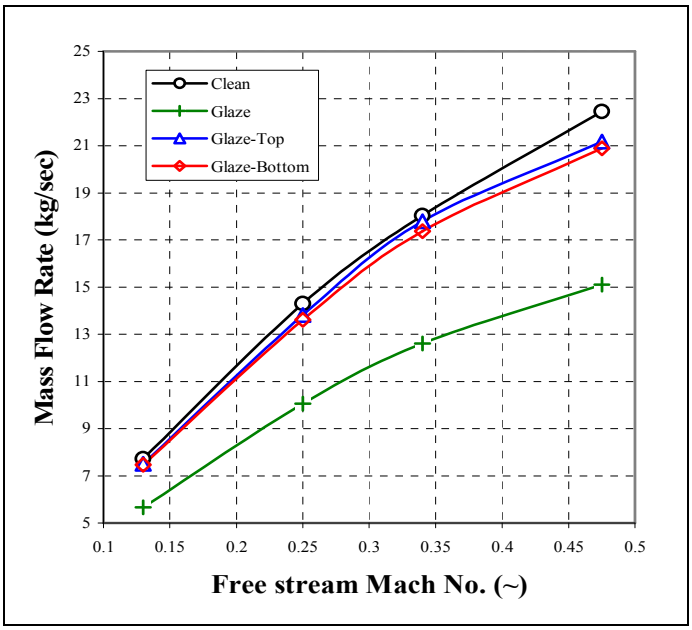

Figure 5. 3. 6: Mass flow rates with different glaze ice shapes

5.4. Effects of inlet icing on dynamic inlet distortion

The *Dynamic inlet distortion*, which is mainly caused by the total pressure fluctuation at the engine face, adversely affects the performance and stability characteristics of the aircraft gas turbine engine system. The sources of total pressure fluctuation include both internally- and externally-generated disturbances. Internally-generated disturbances are caused by flow separation or reattachment, turbulence, buzz, unstart or restart cycles, and interaction with adjacent engines and inlets.[86] On the other hand, externally-generated disturbances include: armament firing, atmospheric gusts, ingestion of wakes emanating from landing gear or aerodynamic surfaces.[86] An *engine stall* can occur when the losses in the *engine surge margin* increases, and when sufficient energy or flow angularities exist at the frequencies of total pressure fluctuation to which an engine compression system may respond. In

particular, ice accretion on the inlet lip may result in a substantial change of the time-dependent stability characteristic of the engine system, since the entire inlet flowfield is dramatically changed by the icing effects, as seen in the steady-state results of the present study. Therefore, the effects of inlet icing on the dynamic distortion are investigated by the unsteady-state computations.

The symmetrical and top-asymmetrical glaze ice shapes are investigated, and the geometries of the ice shapes are shown in Figures 4.2.9(a) and (b), respectively. Figures 5.4.1 to 5.4.3 show the Mach number and static pressure distributions of the clean and glaze ice cases at an instantaneous time. The free-stream Mach number is M_∞=0.34 for all cases. Figure 5.4.1 shows that, in the clean case, the flow separation takes place at the first bend of the S-duct inlet. In particular, the vortices are generated from the first bend, due to the concave shape of the duct at the first bend, as seen in the static pressure distribution plot, Figure 5.4.1(b). Therefore, because of the vortex generation, the flowfield duct downstream is characterized by the complex flow pattern that implies the flow unsteadiness. On the other hand, the flowfield duct upstream remains unperturbed, as seen by the clean inlet case at the instantaneous time. This instantaneous flow pattern indicates that the self-induced flow unsteadiness in the baseline S-duct inlet is mainly caused by the duct curvature.

It is shown in Figure 5.4.2 (a) that, with the symmetrical glaze ice, an apparently higher Mach number region forms at the inlet throat. In addition, the instantaneously-disturbed flow is generated from the ice horn, and it affects the entire flowfield. Moreover, strong vortex shedding occurs behind the ice horn, as shown in Figure 5.4.2(b). However, the vortex shedding structure is dissipative in the range of

approximately 1 D_{th} from the glaze ice horn, as it proceeds into the first bend region. The reason might be that the relatively long length of the straight part of the duct in front of the curvature may contribute to the dissipation of the vortex shedding. It is also possible that the dissipation is caused by the numerical algorithm in having numerical damping.

Figure 5.4.3 shows the instantaneous flowfield distributions of the top-asymmetrical glaze ice case. Similar to the symmetrical case, the instantaneously disturbed flow can be observed in the region behind the ice horn, and it exerts influence on the flowfield downstream. In addition, vortex shedding occurs at the top-glaze ice accretion, although it is weaker compared to that in the symmetrical case.

Figure 5.4.4 shows the time histories of total pressure fluctuation at the engine face of the clean and symmetrical glaze ice cases in a range of free-stream Mach numbers: M_∞=0.13 to 0.34, over the given time period. The calculation is performed using the time step size of Δt=0.01sec. Also note that each value of total pressure at an instantaneous time is an area-averaged value at the engine face. As the free-stream Mach number increases, the overall total pressure levels decrease in both the clean and symmetrical ice cases. This is due to the fact that, for the clean case, flow separation or boundary layer separation at the bend section of the duct becomes stronger at the higher Mach numbers. In addition, the symmetrical glaze cases also induce stronger flow separation from the ice horns at the higher Mach numbers. The intensified unsteady turbulence level at the higher free-stream Mach numbers produces the stronger total pressure fluctuation in both cases.

The time histories of total pressure fluctuation of the clean and symmetrical glaze cases are compared at two different free-stream Mach numbers: M_∞=0.25 and 0.34, as shown in Figure 5.4.5. The levels of total pressure are much lower with the symmetrical glaze ice than with the clean case. This is due to the fact that the inlet icing induces the more serious total pressure distortion at the engine face. In addition, the fluctuation levels of the symmetrical glaze cases are higher than those of the clean cases at all Mach numbers. Therefore, it is evident that the levels of total pressure fluctuation become more intense due to the effects of the symmetrical glaze ice that produces stronger flow separation. Also, the top-glaze cases are presented in Figure 5.4.6. The levels of total pressure with the top-glaze cases are lower that those of the clean cases; however, they are not as low as the symmetrical cases due to the relatively smaller flow blockage from the top-glaze ice accretion. However, the top-glaze also induces slightly stronger fluctuations at the engine face.

To quantify the fluctuation levels, the total pressure fluctuation parameter is defined as $\overline{Pt}'_{rms} / \overline{Pt}_{ef}$. Note that $\overline{Pt}'_{rms}$ represents the rms value of total pressure fluctuation at the engine face, and $\overline{Pt}_{ef}$ denotes the time-averaged total pressure, i.e., steady-state total pressure. The values of this parameter in a range of M_∞=0.13 to 0.34 are presented in Figure 5.4.7. All fluctuation levels increase with the increase of the free-stream Mach number. Also, there is no significant difference in the fluctuation levels of all cases at M_∞=0.13. At the low Mach number, the flow unsteadiness in the S-duct inlet is relatively weak due to less severe flow separation from the duct curvature and the ice horn. However, it becomes more evident that the total pressure fluctuation in the S-duct inlet becomes stronger when ice accretes on

the inlet lip. Moreover, the symmetrical glaze ice causes the more intense fluctuation than the asymmetrical glaze ice does at the higher Mach number. Compared to the clean cases, the levels of the fluctuation with the symmetrical glaze and top-asymmetrical glaze are increased by about 15 and 8 percent at M_∞=0.34, respectively. Therefore, the wider flow blockage caused by the symmetrical glaze ice affects the level of total pressure fluctuation more than the top-glaze ice due to more extensive flow separation. Furthermore, there must be a relation between the steady- and unsteady-inlet performances, because the symmetrical glaze ice also induced the much more serious steady-total pressure distortion as shown in Chapter 5.2. Actually, it is known that the dynamic inlet distortion level, i.e., total pressure fluctuation, is proportional to the steady-state distortion level at an engine face.[87]

Also, it is known that the effect of dynamic inlet distortion can cause an *engine stall* or *engine surge* while the steady-state distortion is substantially below the surge level.[88] In particular, a full-scale ground test of an intake and engine showed that the instantaneous *peak distortion*, which is far higher than the level of steady-state distortion, induced an instant engine surge.[89] Therefore, the changes in the instantaneous peak distortion by the icing effects are investigated. In the present study, the non-dimensional peak distortion parameter, PD, is defined as:

$$PD = \frac{\overline{Pt}_{ef\text{-}clean} - Pt_{PD}}{\overline{Pt}_{ef\text{-}clean}} \qquad \text{Equation (19)}$$

$\overline{Pt}_{ef\text{-}clean}$ denotes the steady-state total pressure recovery of the clean inlet case. Also, Pt_{PD} represents the minimum total pressure value from a time history of total

pressure fluctuation, and it also represents the most severe total pressure distortion during the entire measurement time. Therefore, the difference between $\overline{Pt}_{ef\text{-}clean}$ and Pt_{PD} indicates an instantaneous total pressure drop with the icing effects that can induce a possible engine surge. The values of the peak distortion parameter are compared in Figure 5.4.8. The figure suggests that the peak distortion become more significant with the increase of the free-stream Mach number in all cases. Note that there is also a slight increase in the peak distortion for the clean case. This is due to the increase of flow unsteadiness as Mach number increases. However, the symmetrical glaze case brings about the most substantial peak distortions, compared to other cases at all Mach numbers. At M_∞=0.34, the values of the peak distortion parameter are about 0.003, 0.01, and 0.052 for the clean, top-asymmetrical, and symmetrical glaze cases, respectively.

It can be concluded that the inlet icing affects the dynamic inlet distortion, which is represented by the total pressure fluctuation at the engine face. In addition, the level of peak distortion, which is the indication of a possible engine surge, increases with the icing effects. However, the symmetrical glaze ice induces the most serious dynamic inlet distortion and peak distortion, caused by more extensive flow separation from the wider flow blockage. Furthermore, the level of inlet dynamic distortion is proportionally increases as the steady-state distortion level increases in the S-duct inlet.

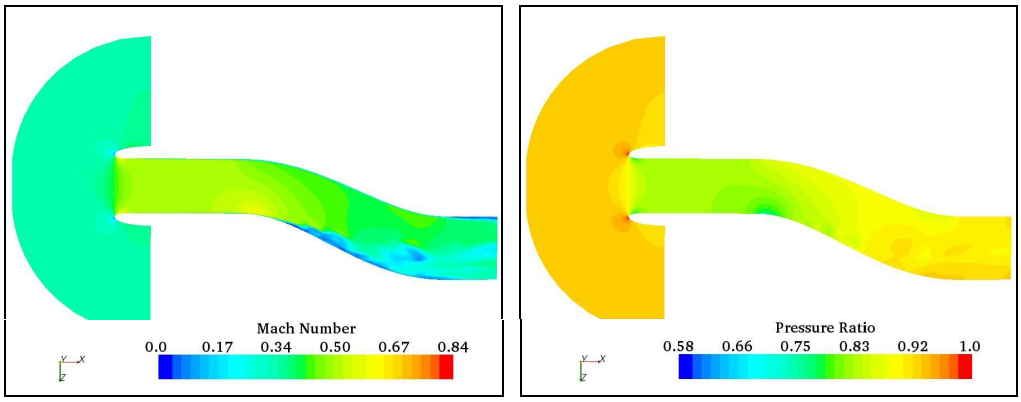

(a) Mach number (b) Pressure ratio (Ps/Pt_∞)

Figure 5. 4. 1: Instantaneous flowfield distributions in the duct symmetry plane (clean, Pt_∞ = 101.1 kPa, M_∞ = 0.34, Δt = 0.01 sec., $\alpha=\beta=0^o$)

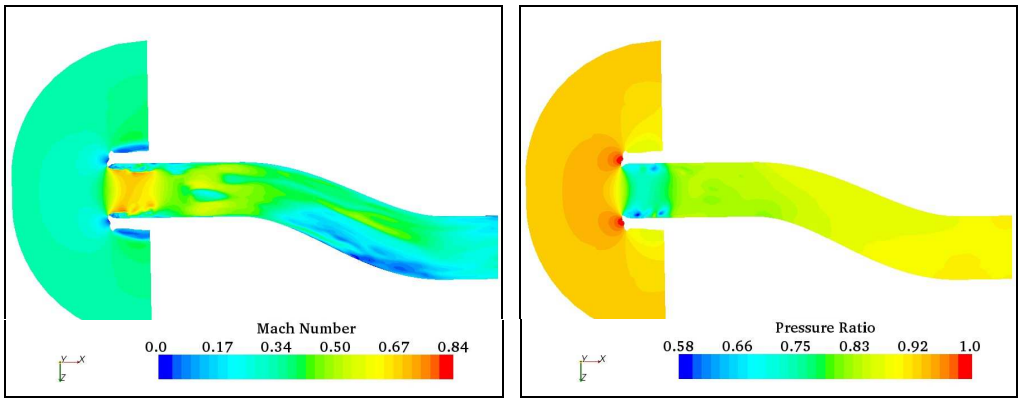

(a) Mach number (b) Pressure ratio (Ps/Pt_∞)

Figure 5. 4. 2: Instantaneous flowfield distributions in the duct symmetry plane (symmetrical glaze, Pt_∞=101.1 kPa, M_∞ = 0.34, Δt = 0.01 sec., $\alpha=\beta=0^o$)

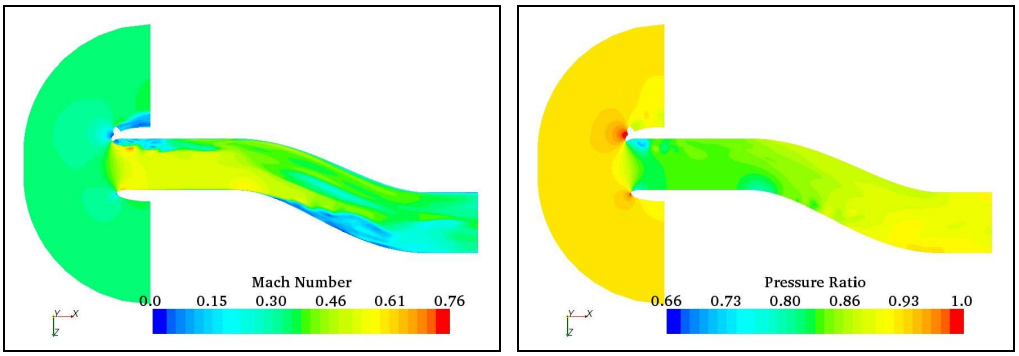

(a) Mach number (b) Pressure ratio (Ps/Pt_∞)

Figure 5. 4. 3: Instantaneous flowfield distributions in the duct symmetry plane (asymmetrical glaze-top, Pt_∞=101.1 kPa, M_∞ = 0.34, Δt = 0.0005 sec., $\alpha=\beta=0^o$)

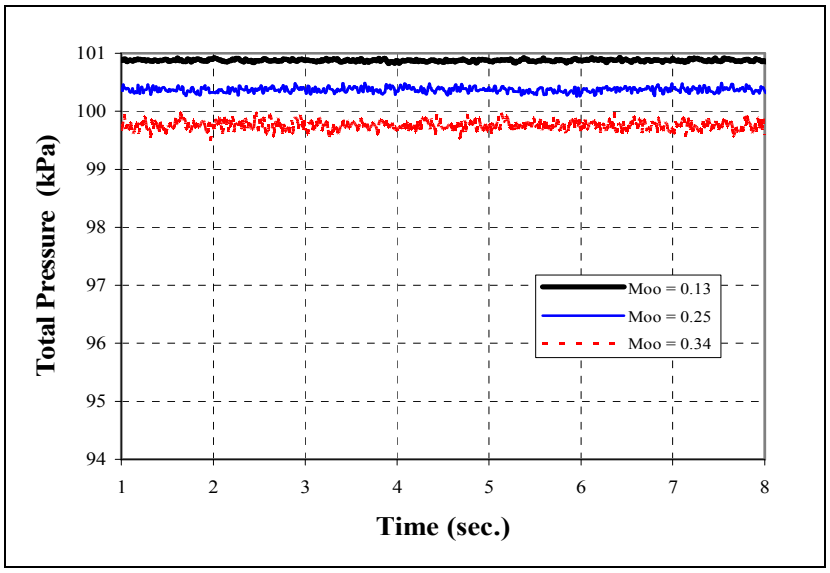

(a) Clean

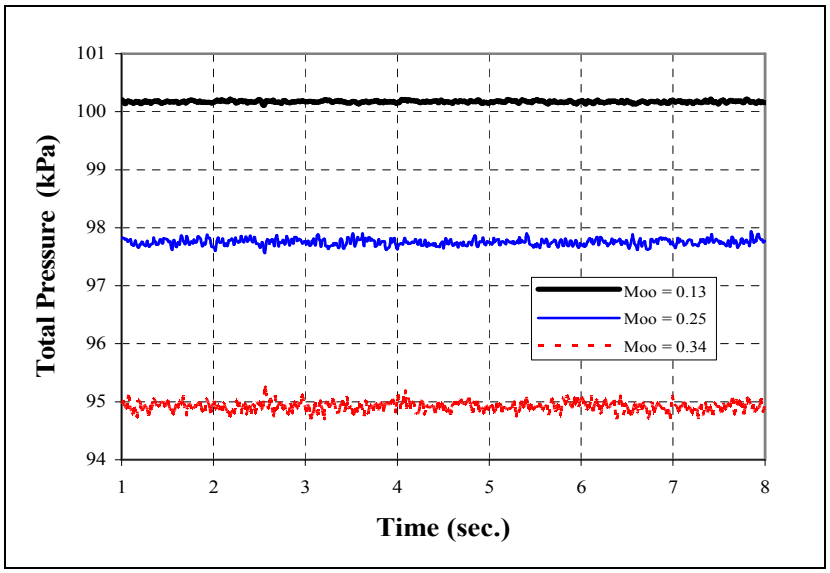

(b) Symmetrical glaze

Figure 5. 4. 4: Variation of total pressure fluctuations at the engine face with free-stream Mach numbers ($\Delta t = 0.01$ sec.)

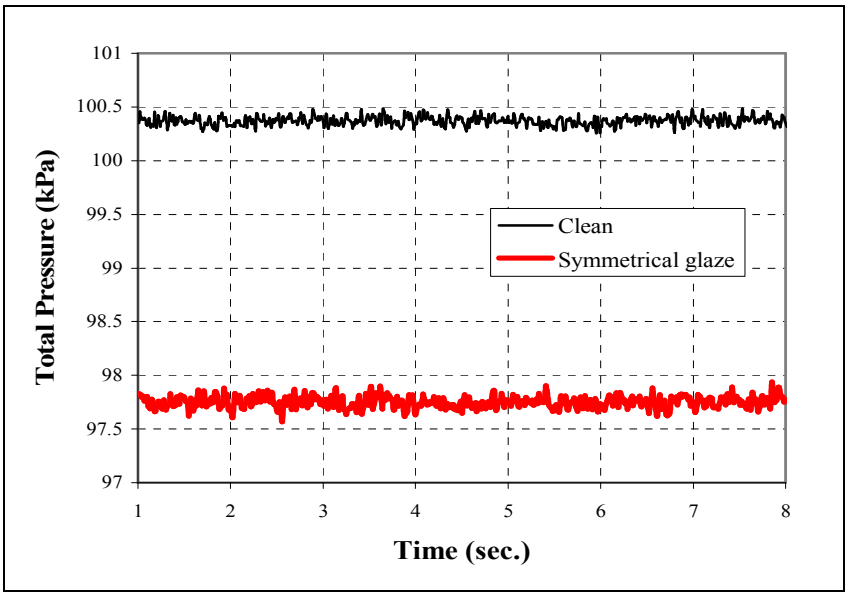

(a) $M_\infty = 0.25$

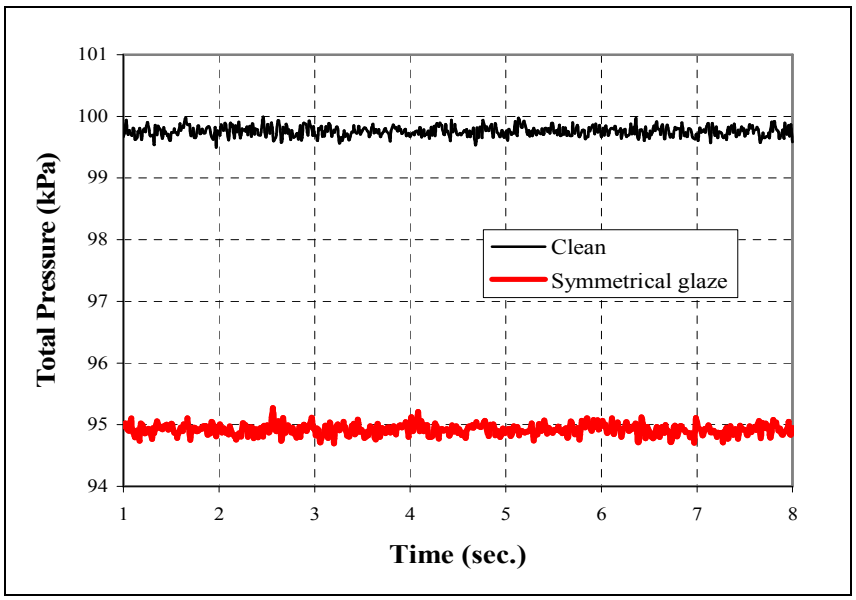

(b) $M_\infty = 0.34$

Figure 5. 4. 5: Comparison of total pressure fluctuations at the engine face (clean VS. symmetrical glaze, $\Delta t = 0.01$ sec.)

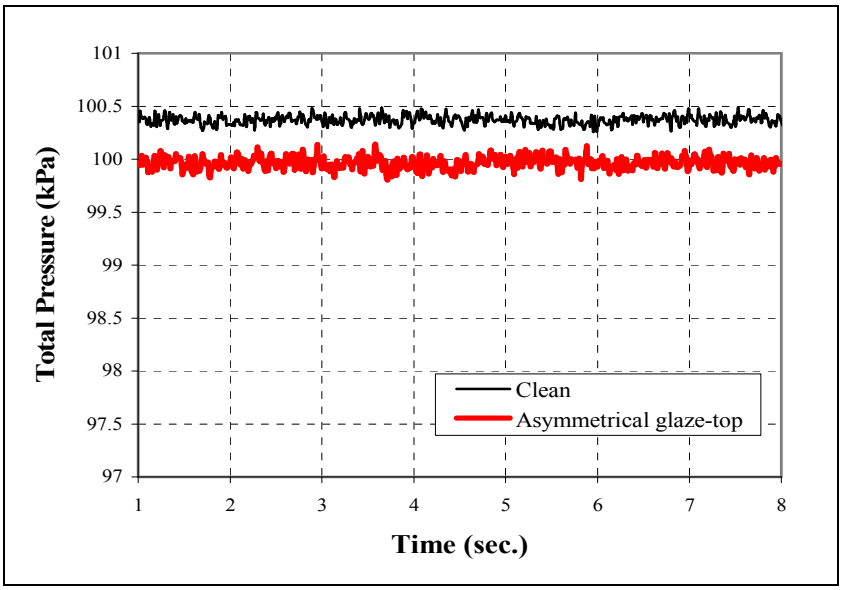

(a) $M_\infty = 0.25$

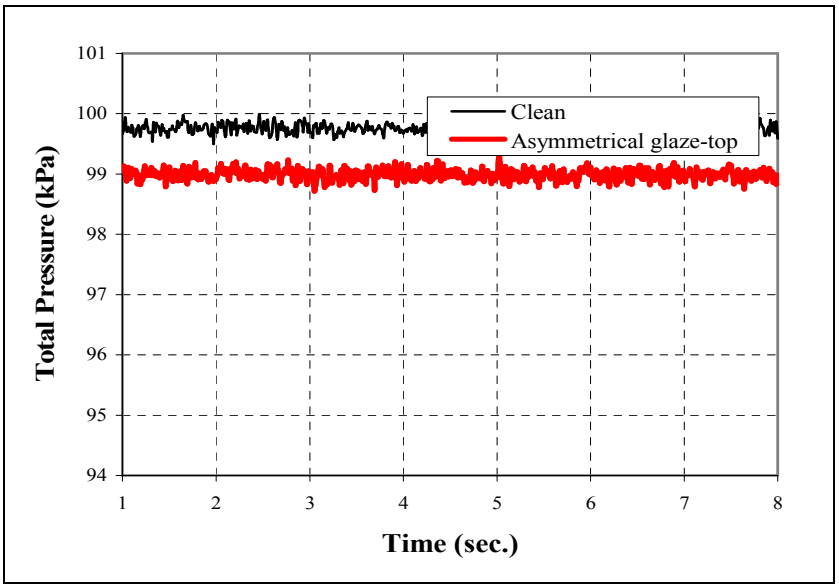

(b) $M_\infty = 0.34$

Figure 5. 4. 6: Comparison of total pressure fluctuations at the engine face (clean VS. asymmetrical glaze-top, $\Delta t = 0.01$ sec.)

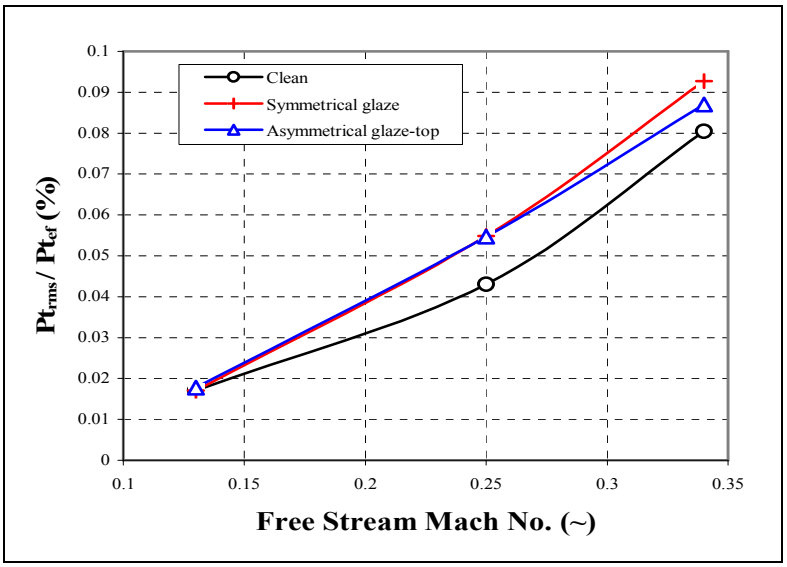

Figure 5. 4. 7: Comparison of total pressure fluctuation ($\overline{Pt}'_{rms} / \overline{Pt}_{ef}$) at the engine face

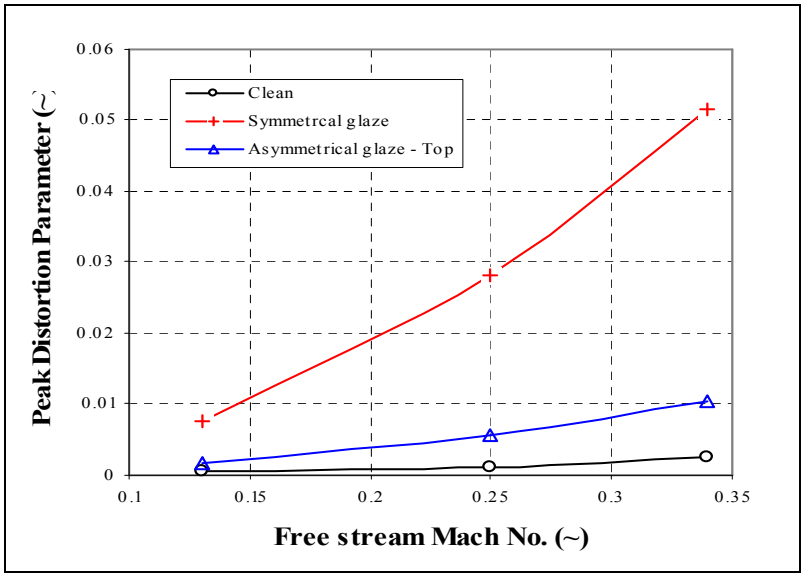

Figure 5. 4. 8: Comparison of peak distortion parameters

5.5. Effects of glaze ice horn thickness

The glaze ice is characterized by an intrusive horn to the inflow. Therefore, it was shown in the present study that the intrusive horn of glaze ice, which induced a

strong flow separation, played an important role in a considerable degradation of the inlet duct-performance. The flow separation from the glaze ice horn is due to the strong pressure gradient over the ice horn. If the glaze ice horn is more sharpened so that it produces stronger pressure gradient, the flowfield in the duct inlet may also be changed. Therefore, the effects of the glaze ice thickness or sharpness on the steady-state flowfield in the M 2129 S-duct inlet are studied. For this study, the thickness of the glaze ice shape is reduced as seen in Figure 4.2.10. The ice shape with the reduced ice horn thickness is defined as *sharp-glaze ice* in the present study. Although the thickness is changed, the height of the sharp-glaze ice horn is the same as that of the *original-glaze ice* horn, producing an identical blocking area to the inflow. As shown in the figure, only the horn part that affects the duct inflow is modified for the sharp-glaze ice shape. The radius of the sharp-glaze ice horn is 0.0104 m, while that of the original-glaze ice horn is 0.0142 m. Therefore, the radius of the ice horn is decreased by approximately 27 percent for the sharp-glaze ice. Note that both the sharp- and original-glaze ice are based on the symmetrical glaze ice shapes.

Figures 5.5.1 to 5.5.3 present the total pressure, static pressure, and Mach number distributions in the duct symmetry plane at M_∞=0.34. The figures suggest that there are no significant changes in the flowfield by the effect of the sharp-glaze ice. The strength of the flow separation at the sharp-glaze and its effect on the duct flow are similar to those of the original-glaze ice. The flow separation from the ice accretion is the main source of the serious distortion at the engine face. The total pressure distortion contours and secondary flow patterns at the engine face are

compared in Figure 5.5.4 to investigate the sharp-glaze effect on the engine face distortion. The patterns of the total pressure distortion are almost identical, except that the vortex-pair structure is tighter in the sharp-glaze case. This result indicates that the overall effect of the sharp-glaze on the level of the engine face distortion is not much different from the effect of the original-glaze. The formation of the counter-rotating vortex pair, as shown in Figures 5.5.4(b) and (d), is originated from the duct curvature, and is enlarged further due to the effect of ice accretion on the inlet lip. However, the change that occurs with the effect of the sharp-glaze ice accretion is not significant.

Figures 5.5.5 and 5.5.6 give the changes in the total pressure recovery and inlet mass flow rate, when the sharp-glaze ice shape is applied. Both the original- and sharp-glaze cause a substantial reduction, compared to the clean cases, in the total pressure recovery and inlet mass flow rates. Similar to the above graphical results, however, both glaze ice shapes show nearly identical trends of decreasing in the total pressure recovery and mass flow rate. Therefore, it is assumed that the ice shapes with different horn thicknesses produce similar effects on the inlet duct as far as they have equivalent blocking areas to the inflow. Moreover, the total pressure recoveries of the sharp-glaze ice are slightly better than those of the original- glaze ice. At M_∞=0.34, the sharp-glaze gives about the 0.18 percent increased total pressure recovery, compared to the original-glaze ice case. However, this increase can be considered negligible. Therefore, it can be inferred from this result that the thickness or sharpness of the glaze ice horn induces little effect on the steady-state flowfield in the duct inlet. A stronger pressure gradient over the sharp-glaze ice horn is not

enough to produce a significant effect on the entire flowfield in the duct inlet. However, the flow blockage level, caused by the extension of ice accretion or icing limits on the inlet lip, is a more critical factor than an ice horn thickness for the performance of the duct inlet, as proven in Chapter 5.3 in the present study.

The effect of the glaze ice horn thickness on the inlet dynamic distortion is also investigated. Figure 5.5.7 shows that the instantaneous flow distributions, induced by the sharp-glaze ice, are compared to those in the clean and original-glaze cases. The free-stream Mach number is M_∞=0.34, and time step size is Δt=0.0005sec. In the clean case, the flow in the duct downstream is significantly disturbed by the vortex generation from the first bend of the duct at the instantaneous time. With both the original- and sharp-glaze ice accretions, the ice horn disturbs the inflow at the instantaneous time, as seen in the Mach number distribution plots, and vortex shedding occurs inside perturbed flow region, as indicated in the static pressure distribution plots. However, the differences in the instantaneous flowfields of the original- and sharp-glaze ice cases are not obvious from these graphical results.

Therefore, the total pressure fluctuation parameters, $\overline{Pt}'_{rms} / \overline{Pt}_{ef}$, are calculated by the unsteady-state simulations based on the time step size of Δt=0.01sec. The levels of the fluctuation parameter for the original- and sharp-glaze ice are found to be 0.093 and 0.103 percent, respectively. The sharp-glaze ice induces a higher fluctuation level by about 11 percent, compared to the original-glaze ice. This result indicates that the sharper ice horn produces a slightly stronger unsteady flow fluctuation. As noted in Figures 5.5.5, the steady-state inlet distortion level is not significantly affected by the effect of the ice horn thickness. However, the thickness

brings about an influence on the level of the unsteady total pressure fluctuation or dynamic inlet distortion.

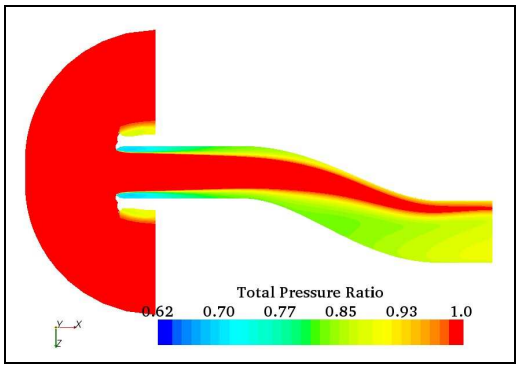

(a) Original-glaze

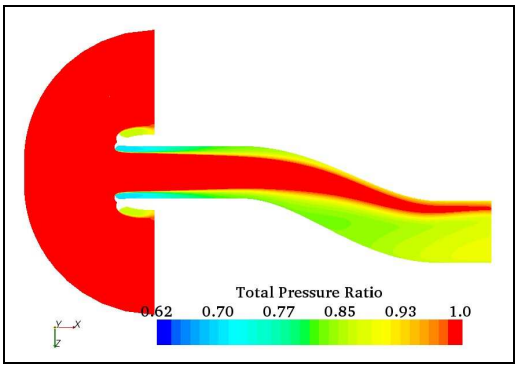

(b) Sharp-glaze

Figure 5. 5. 1: Total pressure distributions (Pt/Pt_{∞}) in the duct symmetry plane (original-glaze VS. sharp-glaze, Pt_{∞}=101.1 kPa, M_{∞} = 0.34, $\alpha=\beta=0^{o}$)

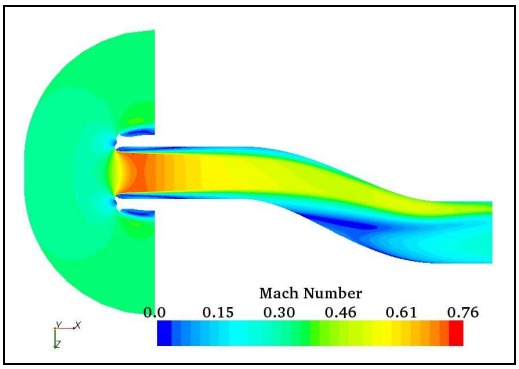

(a) Original-glaze

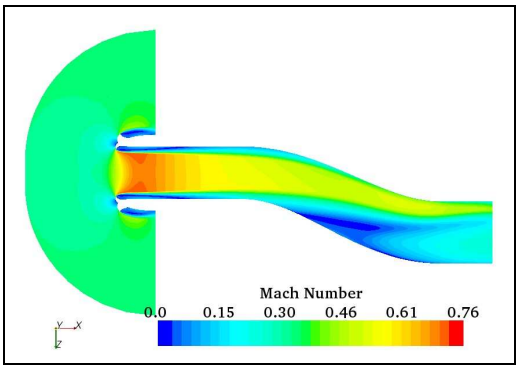

(b) Sharp-glaze

Figure 5. 5. 2: Mach number distributions in the duct symmetry plane (original-glaze VS. sharp-glaze, M_{∞} = 0.34, $\alpha=\beta=0^{o}$)

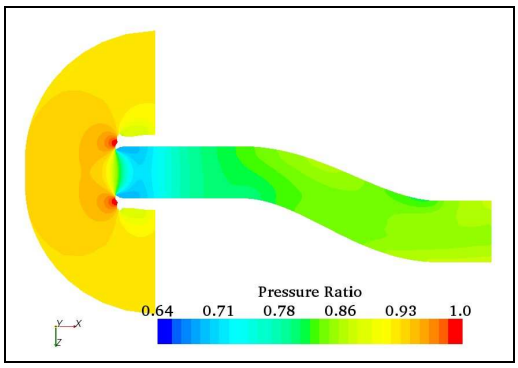

(a) Original-glaze

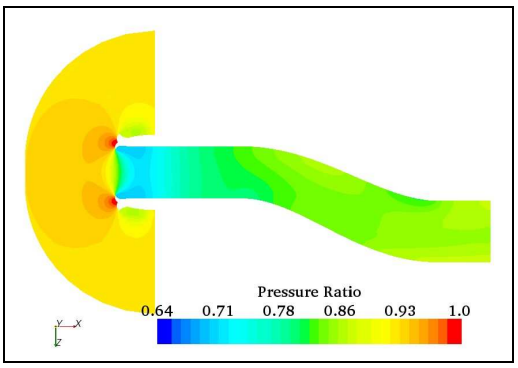

(b) Sharp-glaze

Figure 5. 5. 3: Static pressure distributions (Ps/Pt_{∞}) in the duct symmetry plane (original-glaze VS. sharp-glaze, Pt_{∞}=101.1 kPa, M_{∞} = 0.34, $\alpha=\beta=0^{o}$)

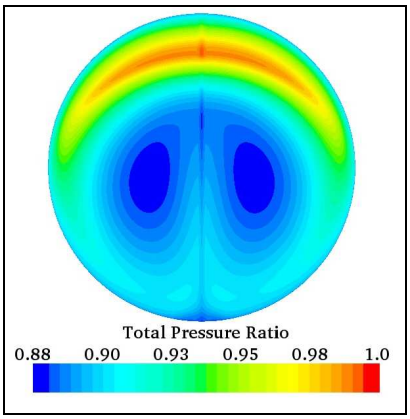

(a) Total pressure

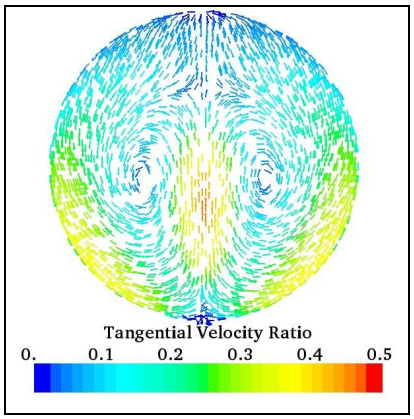

(b) Secondary flow vectors

i. Original-glaze

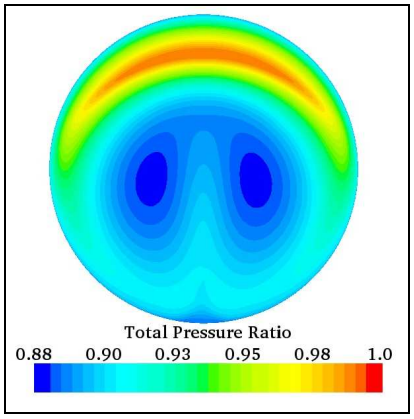

(c) Total pressure

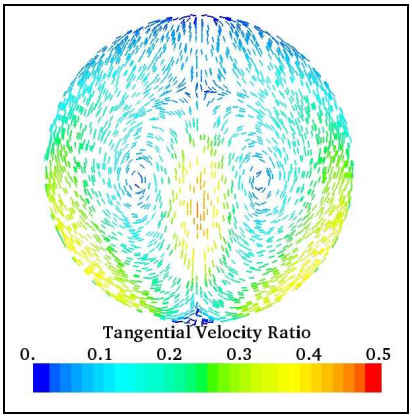

(d) Secondary flow vectors

ii. Sharp-glaze

Figure 5. 5. 4: Total pressure (Pt / Pt_∞) contours and the secondary flow vectors (V / V_∞) at the engine face (original-glaze VS. sharp-glaze, Pt_∞=101.1 kPa, $M_\infty = 0.34$, $\alpha=\beta=0^o$)

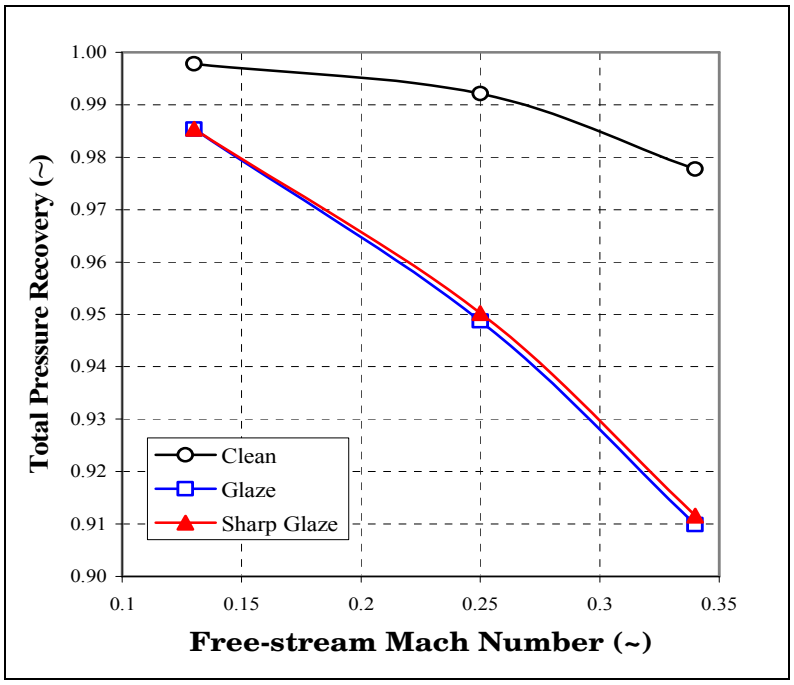

Figure 5. 5. 5: Variation of total pressure recovery ($\overline{Pt}_{ef}/Pt_{\infty}$) with sharp-glaze ($Pt_{\infty}$=101.1 kPa)

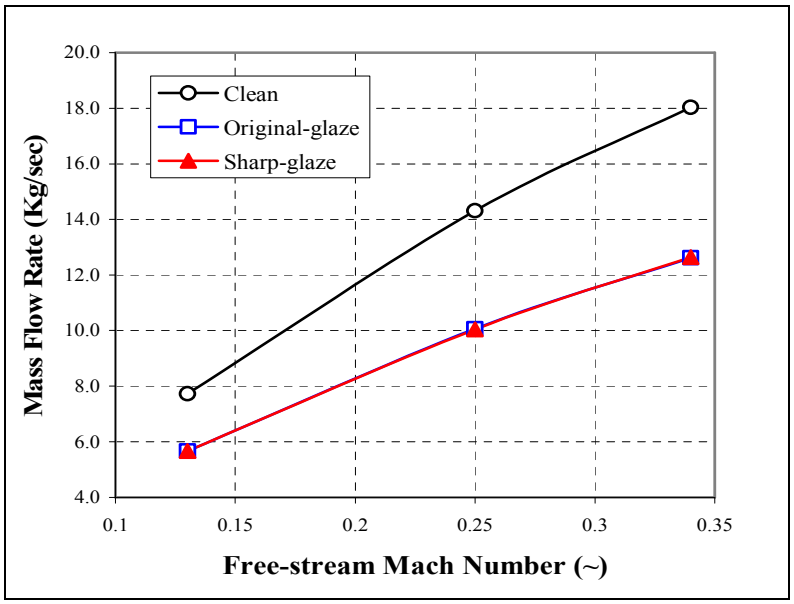

Figure 5. 5. 6: Variation of mass flow rate with sharp-glaze

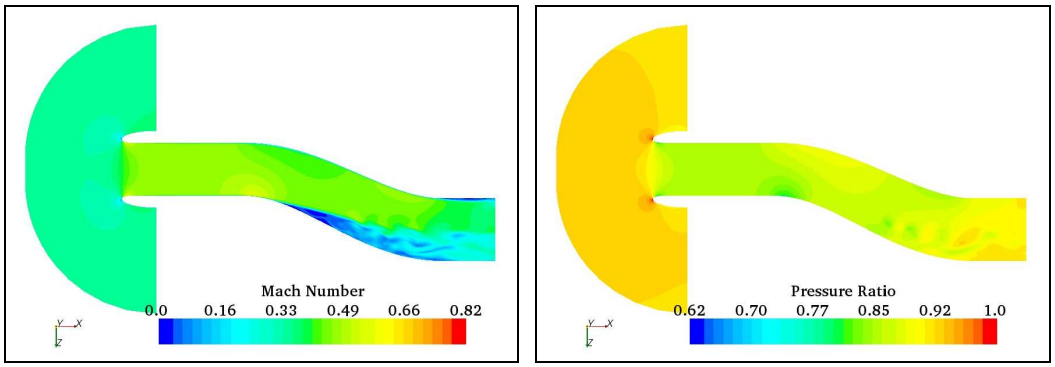

(a) Clean

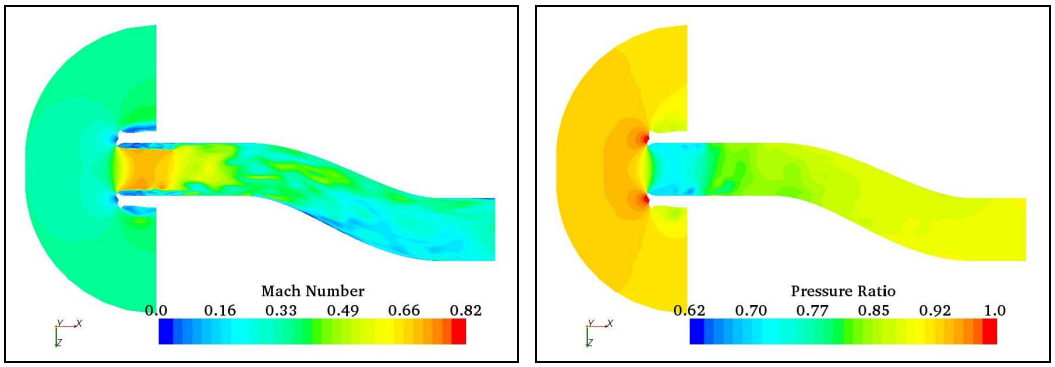

(b) Original-glaze

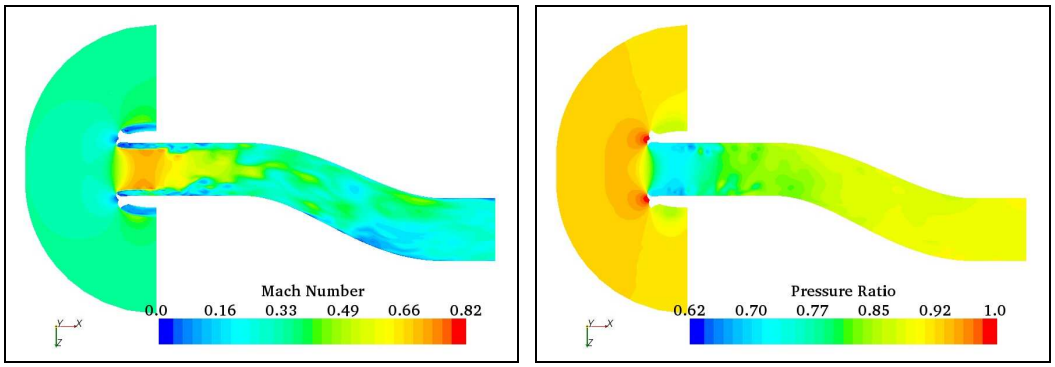

(c) Sharp-glaze

i. Mach number ii. Pressure ratio (Ps/Pt_{∞})

Figure 5. 5. 7: Instantaneous flowfield distributions in the duct symmetry plane (clean VS. original-glaze VS. sharp-glaze, $M_{\infty} = 0.34$, $\Delta t=0.0005$sec., $\alpha=\beta=0^{o}$)

5.6. Combined effects of inlet icing and angle of attack or sideslip angle-symmetrical glaze ice

In practical flight conditions, aircraft maneuver involves the local angle of attack or local sideslip angle to the fuselage, wings, and inlet. Therefore, the performance of an S-duct inlet at high angles of attack or sideslip angles has been also a critical issue. The flowfield characteristics in an S-duct inlet can be changed along with the change of inflow direction in steady flight at an angle of attack, and during the aircraft maneuver.

An experimental study using a rectangular shape S-duct showed that the total pressure recovery and mass flow rate in the duct inlet were adversely affected by the incidence angle.[90] The reduction of total pressure recovery was due to a larger vortex formation around an area of flow separation at the duct curvature at a relatively high angle of attack. In addition, it has been known that a level of flow separation at the incidence angle depends on the inlet lip geometry and flow condition, such as the free-stream Mach number.[90] Therefore, the application of the angle of attack or sideslip angle, along with the change of an inlet lip shape by ice accretion can affect the inlet distortion level and inlet performance. The combined effect of ice accretion, downward duct curvature, and the angle of attack or sideslip angle on the inlet duct performance is worthy of investigation, because an aircraft in a realistic flight condition can experience all factors mentioned above.

Therefore, in this study, the effects of the symmetrical ice shape at local angles of attack or local sideslip angles are investigated. Note that, in the real flight conditions, the application of angle of attack or sideslip angle affects the shape and

size of ice, as proven in the study for the numerical prediction of ice accretion on an axisymmetrical inlet.[8] However, the constant shape and size of ice accretion at an angle of attack or sideslip angle are assumed in the present study. Also note that the symmetrical ice shape is based on the sharp-glaze ice, as introduced in Chapter 5.5.

Figure 5.6.1 gives the definition of the local angle of attack and local sideslip angle. In the present study, local angles of attack: $\alpha=\pm10^{o}$ and $\pm20^{o}$, and local sideslip angles: $\beta=+10^{o}$ and $+20^{o}$ are tested. Note that only positive angles are considered for the sideslip angle, since the identical duct flow patterns are induced by the symmetrical glaze ice at both positive and negative sideslip angles. Figure 5.6.2 shows the steady-state flowfield distributions in the M 2129 S-duct inlet at the angles of attack or sideslip angles, when the symmetrical sharp-glaze ice accretes on the inlet lip. At the angle of attack of $\alpha=+20^{o}$, a much stronger flow separation (or boundary layer separation), compared to the separation level at $\alpha=0^{o}$ in Figure 5.6.2(a), develops from the bottom-portion of the symmetrical ice horn as shown in Figure 5.6.2(b). The stronger flow separation pushes the core flow to the top-side of the wall, causing a serious total pressure loss at the engine face. When the angle of attack is changed to $\alpha=-20^{o}$, the inflow is separated from the top-portion of the symmetrical ice as indicated in Figure 5.6.2(c). Due to the flow separation at the top-portion, the core flow is swept to the bottom-side of the duct, and eventually disappears near the engine face. However, it can be seen by a comparison of Figures 5.6.2(b) and (c) that the total pressure loss at the duct downstream is relatively more obvious at $\alpha=+20^{o}$, although the weakened core flow is maintained until the engine face. Figure 5.6.2(d) shows the flowfield in the duct symmetry plane, when sideslip angle of $\beta=+20^{o}$ is

applied. The sudden flowfield changes near the curvature part of the duct suggest that the flow is separated from the side-portion of the inlet lip at the sideslip angle. Furthermore, the flow in the duct downstream is considerably contaminated by the combined effect of the ice accretion and sideslip angle.

The total pressure patterns, as well as the secondary flow patterns, of the symmetrical-sharp glaze ice cases at the angles of attack or sideslip angles are compared to those of the clean cases as seen in Figure 5.6.3. No significant change is observed in the level of total pressure losses in the clean inlet case under the effect of the angles of attack or sideslip angles. This is contrary to an experiment result which showed a larger vortex pair at the engine face at high incidence angles.[91] The experiment showed that, in an S-duct inlet, the counter-rotating vortex pair became larger, due to the effect of an inlet lip-flow separation at high incidence angle. However, only the curvature part of the S-duct inlet was considered in the experimental study, while the straight duct is added to the upstream of the curvature part of the M 2129 S-duct inlet in the present study. The performance of the S-duct inlet without the straight duct part was sensitive to the inlet lip-flow separation at high incidence angles. On the other hand, in the present study, the strength of the inlet lip-flow separation at the high angle of attack is somewhat attenuated by the existence of the forward duct extension. However, the flow pattern outside the region of the counter-rotating vortex pair is slightly changed with varying the angle of attack or sideslip angle.

Unlike the clean cases, the symmetrical glaze induces significant changes in the total pressure patterns and the secondary flow patterns at the engine face with the

angles of attack or sideslip angles, as shown in Figure 5.6.3. From the symmetrical glaze cases in Figures 5.6.3(b) and (c), it is apparent that the secondary flow pattern at α=0º is significantly distorted by the effects of the positive angles of attack, α=+10º and +20º. Furthermore, the region of the secondary flow disappears at α=+20º. However, a more substantial total pressure loss takes place at the bottom-side of the engine face at α=+20º due to combined effect of the flow separations: the flow separation from the bottom-portion of the symmetrical glaze ice at the positive angle of attack, and the stronger flow separation at the bottom-side of the first duct bend, which is a typical separation in an S-shape duct.

The flow pattern changes at the negative angles of attack are presented in Figures 5.6.3(d) and (e). At α=-10º, the flow separation from the top-portion of the symmetrical ice induces the total pressure loss at the top-side of the engine face. The top-side flow separation pushes the core flow to the bottom, and the core flow region at the engine face is bisected by the effect of the flow separation at the bottom-side of the first duct bend. However, the core flow region totally disappears at the engine face at α=-20º, indicating a serious total pressure loss at the high negative angle of attack.

The sideslip cases are given in Figures 5.6.3(f) and (g). From the figures, a right-left asymmetry is clearly seen in the engine face distortion patterns at the positive sideslip angles. These unique distortion patterns are the result of the flow separation from the right-side (when seen from behind the engine face) of the symmetrical ice at the positive sideslip angles, and the flow separation at the bottom-side of the first duct bend. The core flow region, which is moved to the left-side of

the engine face at β=+10º, eventually disappears at the higher sideslip angle of β=+20º.

The static pressure ratio (Ps/Pt_∞) distributions along the top (θ=0º)- and bottom (θ=180º)-wall of the duct inlet at different angles of attack are presented in Figures 5.6.4 and 5.6.5, respectively. The free-stream Mach number is M_∞=0.34 for all cases. Along both wall surfaces, the overall decrease of static pressures, compared to the clean cases, indicates energy losses by the flow separation in the duct flow, due to the effect of the symmetrical glaze ice at the angles of attack. The most significant change, compared to the case at α=0º, in the top-wall pressure distribution is the sudden pressure jump right behind the inlet lip at α=+20º, as shown in Figure 5.6.4. This is due to the reattachment of the separated flow with the flow being separated from the top-side ice horn and reattached to the top-wall surface at a positive angle of attack. However, in the case of α=+10º, a relatively slight pressure increase occurs behind the inlet lip. Therefore, this fact suggests that an increase of angle of attack in the same direction can induce a different duct flow pattern, although the effect is reduced in the downstream of the duct inlet. In addition, the effect of the second curvature is weakened at the negative angles of attack. Along the top-wall surface of the second bend, pressure decreases with a flow acceleration and then recovers near the engine face. However, the relatively constant pressure distributions occur at top-side of the second bend at the negative angles of attack, due to the massive flow separation at the location. Similar flow patterns occur in the bottom-wall distributions as shown in Figure 5.6.5. The angle of attack of α=-20º generates a sudden pressure increase behind the inlet lip along the bottom-wall, and this can also

be explained by the flow reattachment at the location. Furthermore, the effect of the bottom-wall surface of the first bend, which is presented by a sudden pressure decrease by flow acceleration, is reduced at the positive angles of attack. At the positive angles of attack, the flow separation from the bottom-side ice horn eliminates the flow acceleration at the bottom-side of the first bend.

With the effect of angles of attack or sideslip angles, the decreases of the total pressure recoveries ($\overline{Pt}_{ef}/Pt_{\infty}$) and inlet mass flow rates from those in the corresponding clean cases are compared in Figures 5.6.6 and 5.6.7, respectively. The figures show that all angles of attack or sideslip angles contribute to the degradation of the performance of the M 2129 S-duct inlet, combined with the icing effect in all free-stream Mach numbers. The levels of total pressure recovery, as well as the inlet mass flow rate, decrease with most of the angles of attack or sideslip angles, and the decreases become more significant as the angle or the free-stream Mach number increases. At M_{∞}=0.34, where the decreases by the angles and directions are the most apparent, all the 20º cases induce further decrease in both the total pressure recovery and inlet mass flow rate, when compared to all 10º cases. Also, the greater decrease occurs at the positive angles of attack than at the negative angles of attack, and further decrease takes place at the negative angles of attack then at sideslip angles at M_{∞}=0.34. Therefore, the higher positive angle of attack, α=+20º, causes the most significant reduction in both the total pressure recovery and inlet mass flow rate at M_{∞}=0.34. Compared to the clean cases, the decreases in the total pressure recovery are approximately 6.8 and 8.5 percents at α=0º and +20º, respectively for the symmetrical glaze ice at M_{∞}=0.34. This is due to the fact that the flow separation at

the downward duct curvature, which is the main source of the degradation in inlet performance, becomes more substantial as the positive angle of attack increases.

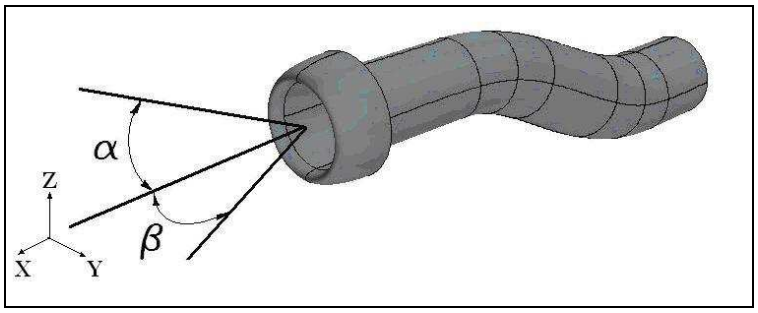

Figure 5. 6. 1: Definition of local angle of attack (α) and local sideslip angle (β)

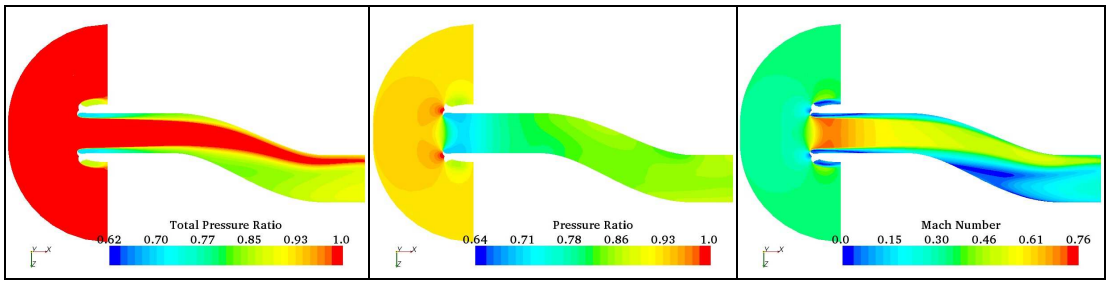

(a) $\alpha = 0^{o}$

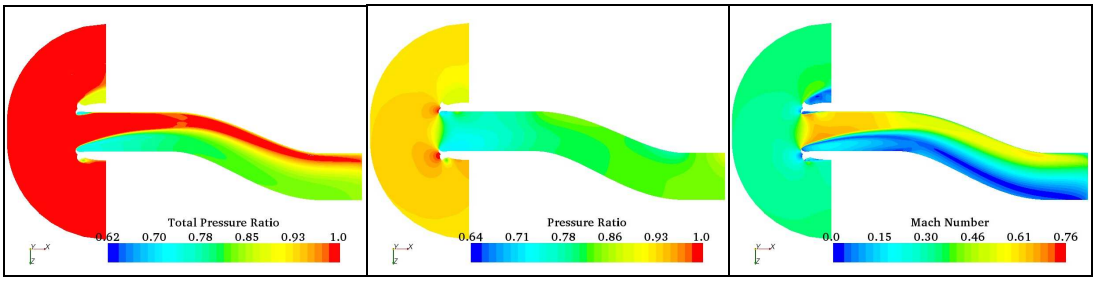

(b) $\alpha = +20^{o}$

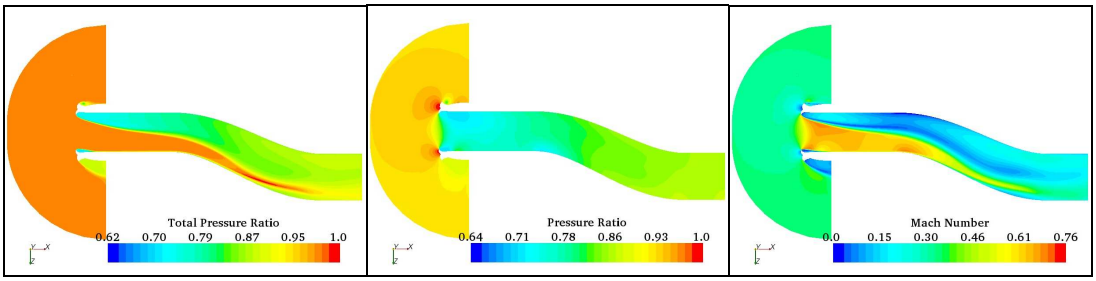

(c) $\alpha = -20^{o}$

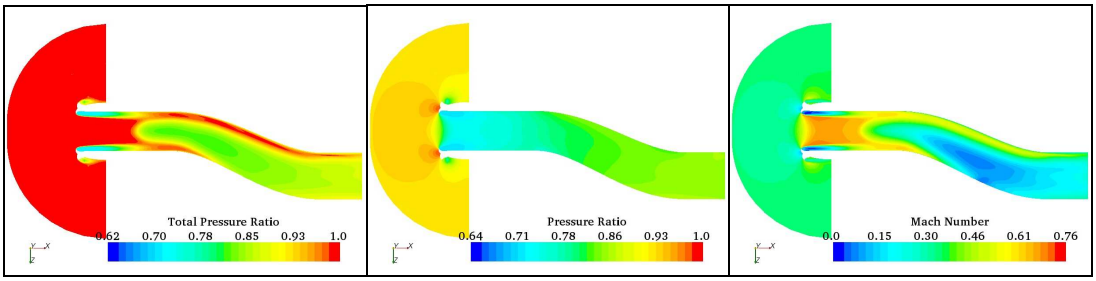

(d) $\beta = +20^{o}$

i. Total pressure (Pt / Pt_{∞}) ii. Static pressure (Ps / Pt_{∞}) iii. Mach number

Figure 5. 6. 2: Flowfield distributions in the duct symmetry plane at angles of attack or sideslip angle (symmetrical sharp-glaze, Pt_{∞}=101.1 kPa, $M_{\infty} = 0.34$)

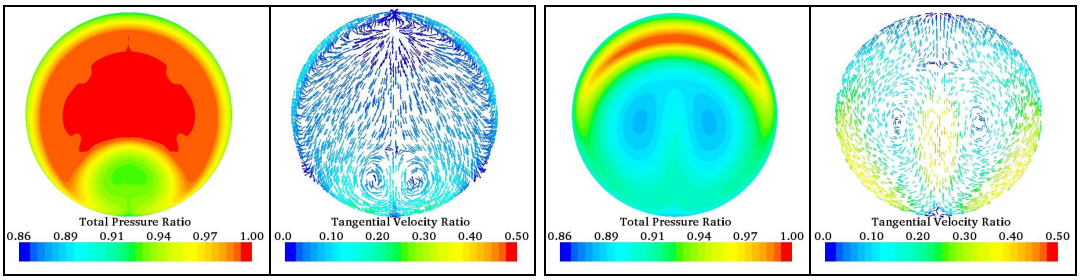

(a) $\alpha = 0^{o}$

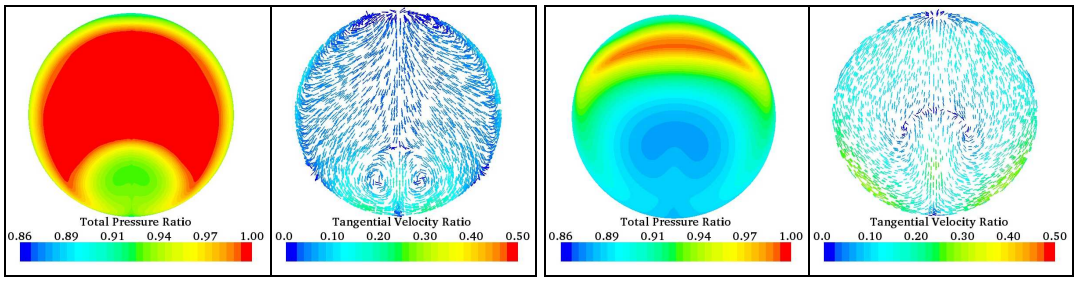

(b) $\alpha = +\ 10^{o}$

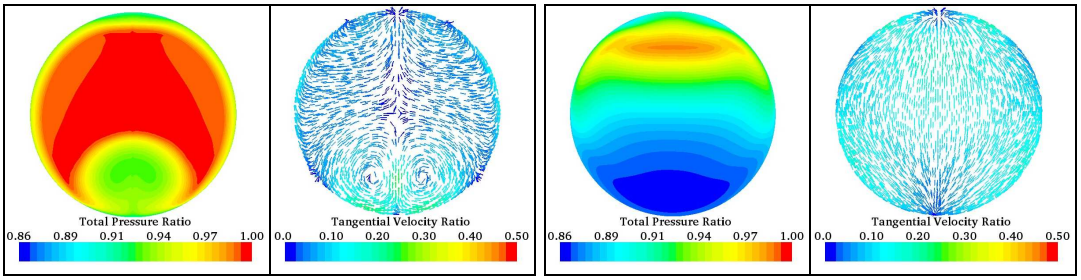

(c) $\alpha = +\ 20^{o}$

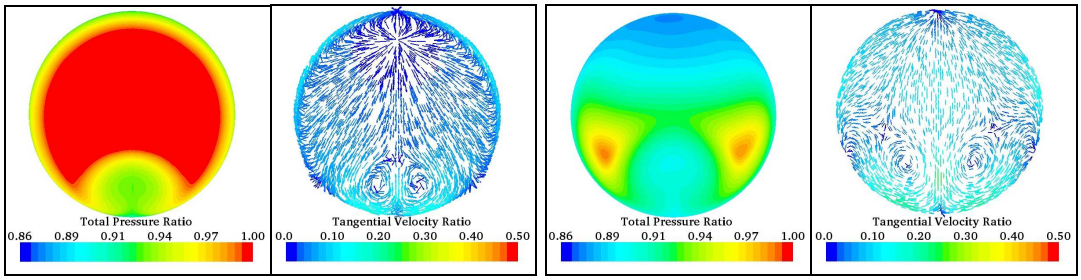

(d) $\alpha = -\ 10^{o}$

i. Clean ii. Symmetrical sharp-glaze

Figure 5. 6. 3: Total pressure (Pt / Pt_{∞}) contours and the secondary flow vectors (V / V_{∞}) at the engine face at angles of attack or sideslip angles (clean VS. symmetrical sharp-glaze, Pt_{∞}=101.1 kPa, $M_{\infty} = 0.34$)

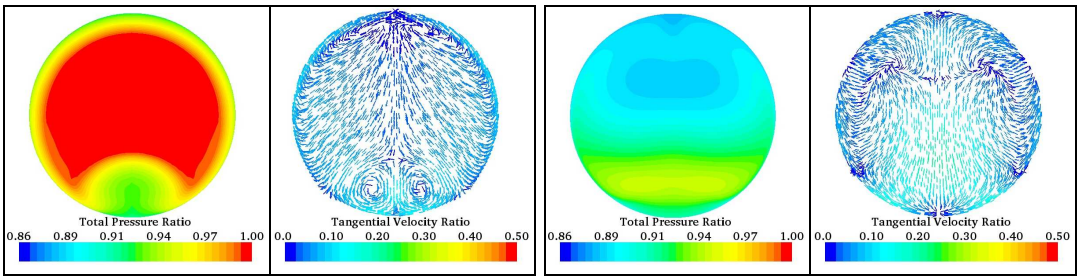

(e) α = - 20º

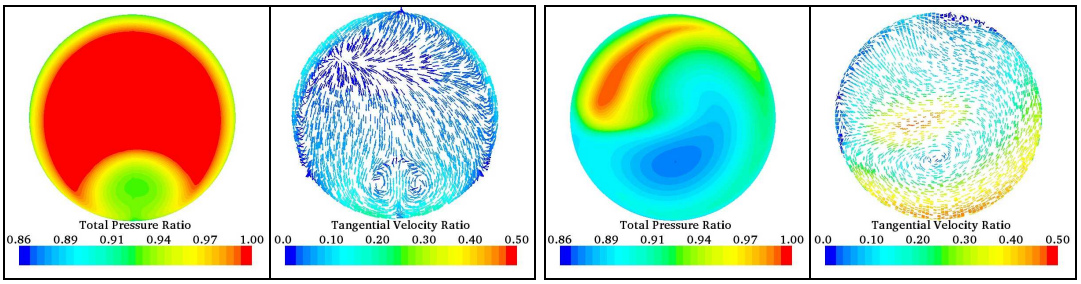

(f) β = + 10º

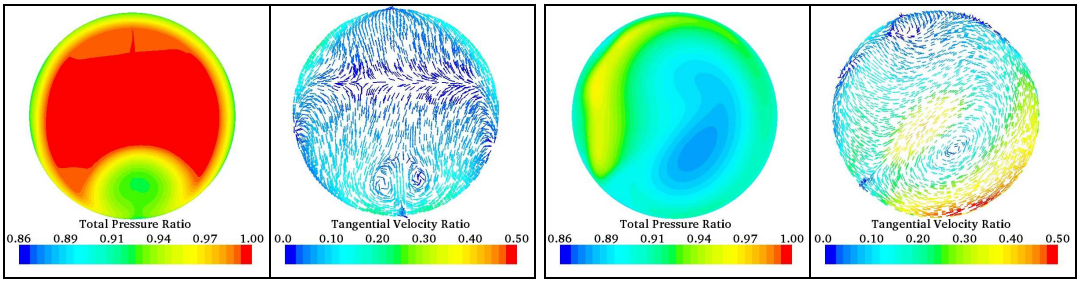

(g) β = + 20º

i. Clean ii. Symmetrical sharp-glaze

Figure 5. 6. 3: Total pressure (Pt / Pt_∞) contours and the secondary flow vectors (V / V_∞) at the engine face at angles of attack or sideslip angles (clean VS. symmetrical sharp-glaze, Pt_∞=101.1 kPa, M_∞ = 0.34)

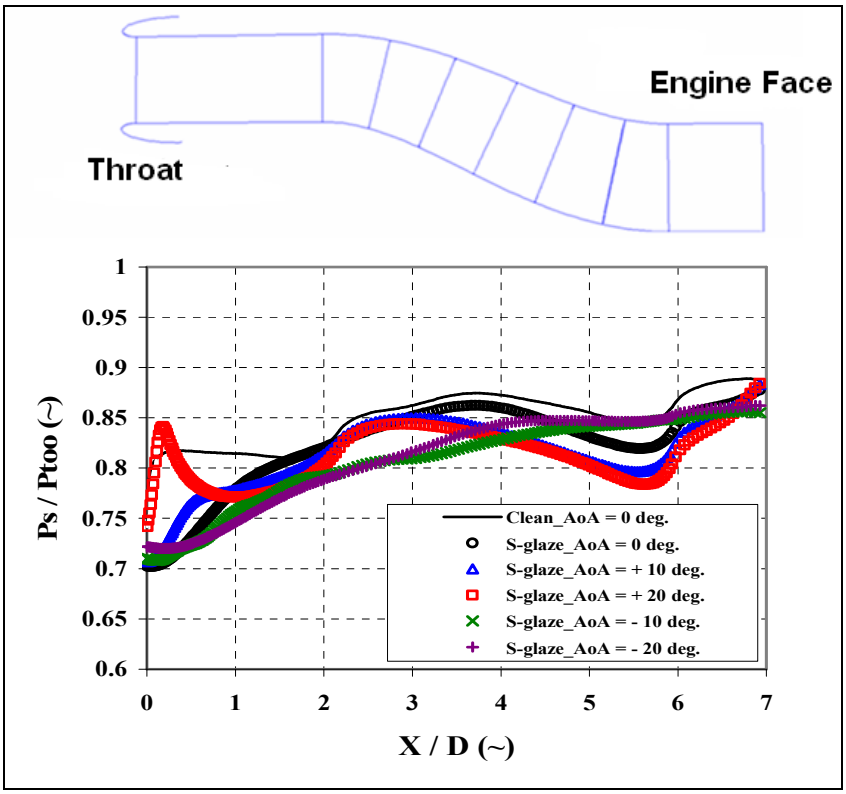

Figure 5. 6. 4: Top-wall pressure ratio (Ps/Pt_{∞}) distributions at angles of attack (symmetrical sharp-glaze, Pt_{∞}=101.1 kPa, M_{∞} = 0.34)

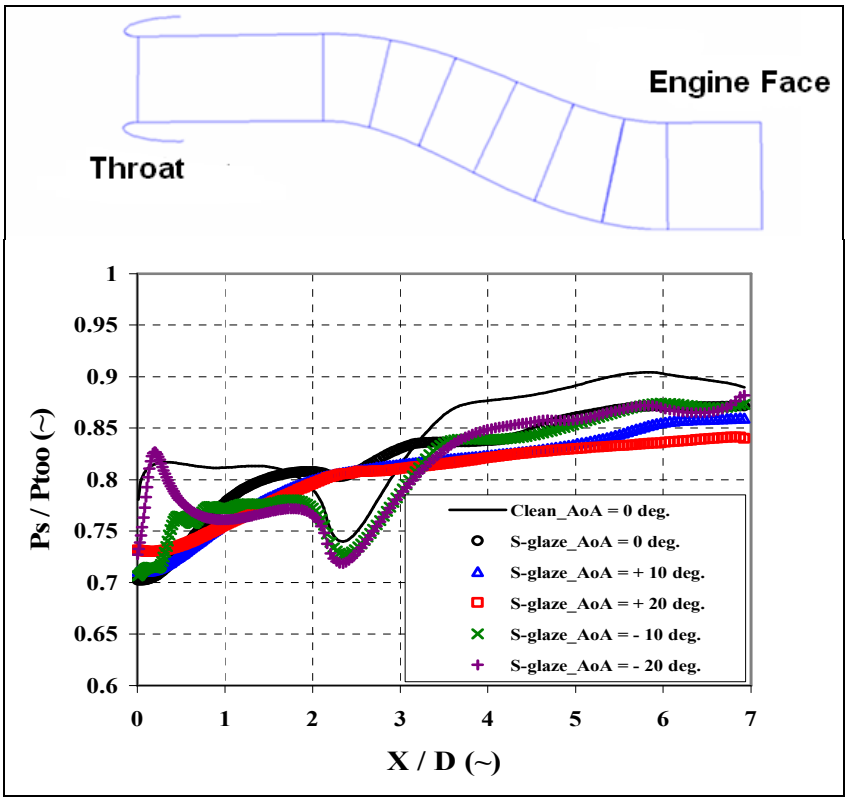

Figure 5. 6. 5: Bottom-wall pressure ratio (Ps/Pt_∞) distributions at angles of attack (symmetrical sharp-glaze, Pt_∞=101.1 kPa, M_∞ = 0.34)

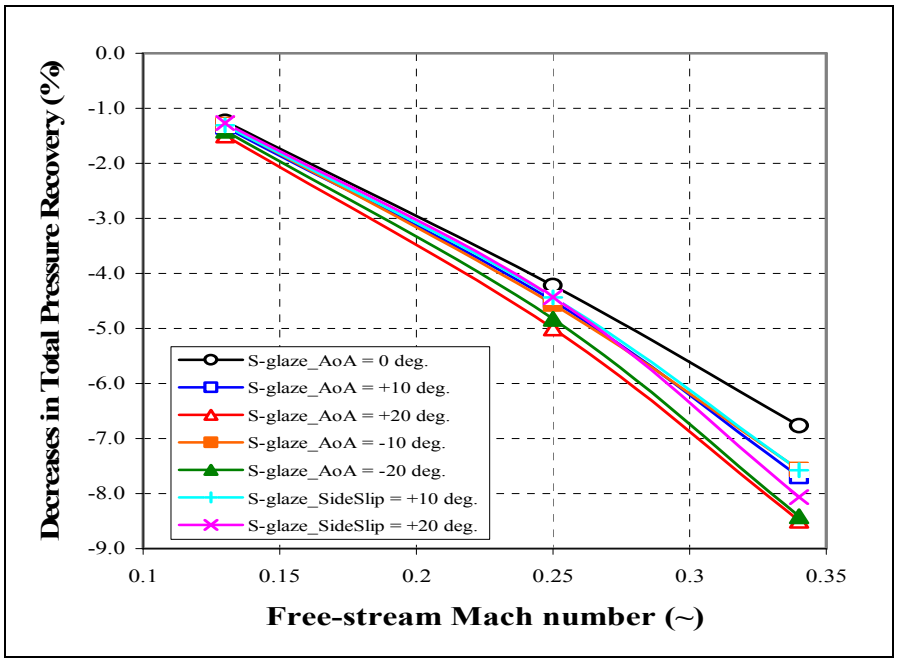

Figure 5. 6. 6: Decreases in total pressure recovery ($\overline{Pt}_{ef}$ / Pt_{∞}) at different angles of attack or sideslip angles (symmetrical sharp-glaze, Pt_{∞}=101.1 kPa)

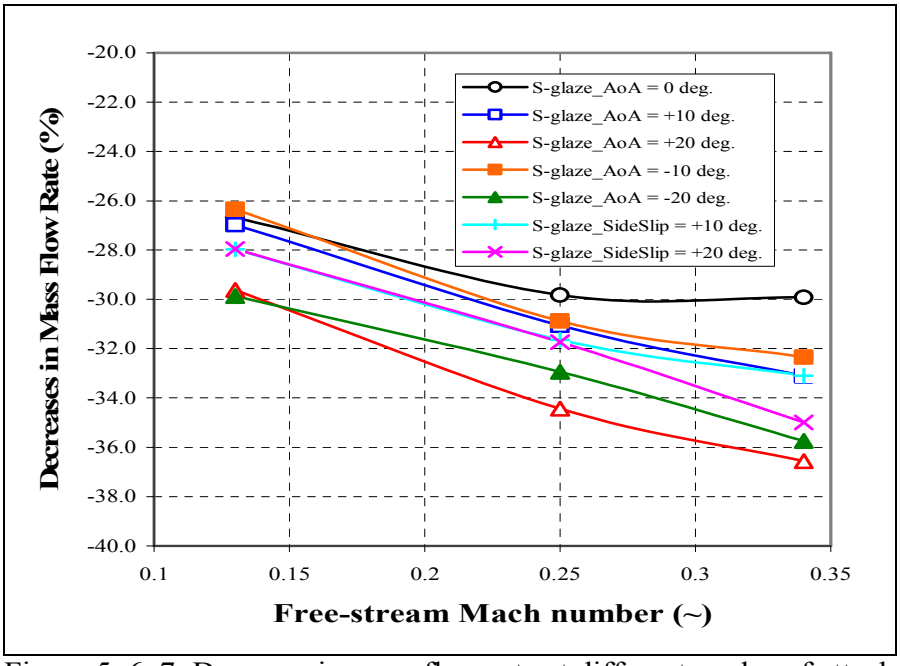

Figure 5. 6. 7: Decrease in mass flow rate at different angles of attack or sideslip angles (symmetrical sharp-glaze)

5.7. Combined effects of inlet icing and angle of attack or sideslip angle-asymmetrical glaze ice

The effects of the asymmetrical glaze ice at different local angles of attack and local sideslip angles are also investigated. The shapes of the asymmetrical ice in this investigation are categorized as *top-*, *bottom-*, and *side-glaze ice* according the location of ice accretion along the inlet lip, as shown in Figures 4.2.9(b), (c), and (d), respectively. Also, the side profile of each asymmetrical glaze ice shapes is based on the sharp-glaze ice. In the present study, local angles of attack: $\alpha=\pm10^{o}$ and $\pm20^{o}$, and local sideslip angles: $\beta=\pm10^{o}$ and $\pm20^{o}$ are examined.

With the top-glaze ice accretion, the steady-state flowfield changes at the different angles of attack are presented in Figure 5.7.1. The free-stream Mach number is $M_{\infty}=0.34$ for all cases. Figures 5.7.1(a) to (c) suggest that the level of flow separation from the top-glaze is reduced, while the level of flow separation from the duct curvature, the bottom-side of the first bend, is enhanced as the positive angle of attack increases. Conversely, the flow separation from the top-glaze is enhanced at the negative angles of attack as shown in Figure 5.7.1(d) to (e). These changes in the flowfield with respect to the angle of attack-change can be more clearly seen in the distortion patterns at the engine face as shown in Figure 5.7.2. Another region of total pressure loss at the outer-top side of the engine face, due to the effect of the top-glaze, becomes smaller at the positive angles of attack; it, however, becomes larger at the negative angles of attack. In particular, the enlarged region of total pressure loss at the top-side at $\alpha=-10^{o}$ is characterized by distinct two pairs of vortices as seen in

the secondary flow pattern in Figure 5.7.2(d). In addition, the vortex patterns disappear at α=-20º as given in Figure 5.7.2(e). Consequently, the magnitude of angle is also an important factor in the total pressure distortion for the asymmetrical ice cases. Furthermore, the total pressure loss at the bottom-side of the engine face, which is caused by a typical flow separation from the duct curvature, is sensitive to the magnitude and direction of the angle. However, it is clear from these distortion contours that more total pressure loss generally occurs at the negative angles of attack, and the loss increases at the bigger negative angle of attack for the top-glaze ice case.

Now, the bottom-glaze ice cases are presented in Figure 5.7.3. Similar to the top-glaze cases, the flow separation from the bottom-glaze is affected by the varying angle of attack. As seen in Figure 5.7.3(a) to (e), the positive angles of attack promote stronger flow separation from the bottom-glaze, and the flow separation at α=+20º is more extensive, compared to that at α=+10º. On the other hand, relatively weaker flow separation occurs at the negative angles of attack. Note that the distinct flow separation can not be observed at the top-portion of inlet, which is not contaminated by ice accretion, at the negative angles of attack, in particular α=-20º. The reason is that an adverse pressure gradient over the streamlined inlet lip-portion without ice accretion is not sufficient to produce flow separation at the relatively high negative angle of attack. The total pressure distortion patterns and the secondary flow vectors at the engine face are also given in Figure 5.7.4. The region of total pressure loss at the bottom-side of the engine face is induced by the effect of the downward duct curvature plus the effect of the bottom-glaze ice accretion. In addition, the size

of the region is enlarged when combined with the effect of the positive angles of attack. However, the formation of the counter-rotating vortex pair, which is originated from the duct curvature, is gradually destroyed at the positive angles of attack as seen in Figures 5.7.4(b) and (c). The negative angles of attack also affect the distortion pattern at the engine face. The case of α=-20º in Figure 5.7.4(e) suggests that the region size of total pressure loss is significantly reduced, even compared to that of α=0º case in Figure 5.7.4(a), showing another counter-rotating vortex pair at the top-side of the engine face. However, the vortex pair does not induce a serious flow separation at the top-side as shown in the total pressure plot in Figure 5.7.4(e). Therefore, it can be concluded that the positive angles of attack cause more total pressure loss when the bottom-glaze ice accreted on the inlet lip.

The effect of the sideslip angles on the side-glaze ice accretion is also investigated. The ice accretion on the portion, θ=45°-135°, is only considered since the other side-glaze portion of θ=225°-315° is exactly symmetric with respect to the duct symmetry plane for the sideslip angle, as shown in Figure 4.2.9(d). Figure 5.7.5 gives the flowfield distributions with the combined effect of the side-glaze and sideslip angles. However, the figure shows that the level of flow separation, due to the side-glaze at the sideslip angles, is not significant, compared to the symmetrical glaze cases at the sideslip angles as shown Figure 5.6.2(d) from Chapter 5.6. This can be explained by the difference in the ice-induced blocking areas. Note that the cowl area (highlight area or inlet frontal area) is decreased by 21 percent with the symmetrical glaze, and decreased by 5 percent with the asymmetrical ice shapes. However, stronger flow separation from the duct curvature is generated by the effect

of the side-glaze at the negative angles of attack, in particular, at β=-20º. The total pressure distortion contours and the secondary flow plots in Figure 5.7.6 support this result. The unique distortion patterns, which are biased to the left-side of the engine face, are the result of the side-glaze ice. Also, the distortion patterns vary as the sideslip angle changes, producing different numbers of the swirling flow as seen in the secondary flow plots. However, the distorted regions are larger with the more severe total pressure losses at the negative sideslip angles, compared to those at the positive sideslip angles. Moreover, the case of β= -20º induces the most serious distortion at the engine face with the side-glaze ice effect.

The quantified results for the inlet performance at the angles of attack or at the sideslip angles are presented in Figures 5.7.7 to 5.7.14. Again, the free-stream Mach number is M_∞=0.34 for all cases. The changes in the total pressure recovery and inlet mass flow rate of the ice cases are given in the figures in terms of *decrease* from those of the corresponding clean inlet cases. Comparing the results of the symmetrical glaze case (Figures 5.7.7 and 5.7.8) to those of the asymmetrical cases (Figures 5.7.9 to 5.7.14), it is very obvious that the reductions in the total pressure recovery and inlet mass flow rate with the symmetrical glaze ice are much more substantial at all angles of attack and sideslip angles. This is due to the wider flow-blockage caused by the symmetrical ice accretion. Also, flow separation from the ice horn, which is a source of the degradation in inlet performance, is more extensive when symmetrical ice accretes on the inlet lip, as seen in Chapter 5.6.

Figures 5.7.9 and 5.7.10 show the decrease in the total pressure recovery and inlet mass flow rate for the top-glaze cases. The figures suggest that the negative

angles of attack produce more reduction in both the total pressure recovery and inlet mass flow rate, and the reduction is more enhanced by the bigger negative angle of attack. At α=-20º, the total pressure recovery and inlet mass flow rate drop about 2.4 and 11.4 percent, respectively, compare to the cases of α=0º. This result is comparable to the graphical results of the distortion patterns at the engine face, as shown in Figure 5.7.2. On the other hand, the positive angles of attack have a minor influence on the inlet performance. In addition, there is no considerable difference between the influence levels of α=+10º and +20º cases. However, the decreases in the total pressure recovery at all angels of attack indicate that the performance of the top-glaze iced inlet duct is adversely affected at all angles of attack.

Bottom-glaze ice cases are also given in Figures 5.7.11 and 5.7.12. Contrary to the top-glaze cases, more decreases are induced at the positive angles of attack. Surprisingly, however, both the total pressure recovery and inlet mass flow rate increase at the negative angles of attack. This result can be confirmed in Figure 5.7.4(e), which shows that the distorted region is reduced at α=-20º. The reason for this is that the effect of the bottom-glaze ice is diminished at the negative angles of attack, combined with the effect of the downward duct curvature. The negative angles of attack mitigate the strong flow separation from the downward duct bend, allowing more core flow to the engine face. Also, the separated flow from the bottom-glaze is reattached at the negative angles of attack; therefore, the negative angles of attack induce less effect on the engine face. In addition, the top-portion of the inlet lip, which is an ice-free portion, does not induce additional flow separation at the negative angles of attack, and does not affect the flowfield at the engine face. The

total pressure recovery and inlet mass flow rate are increased by 1.1 and 5.2 percent, respectively, at α=-20º, while at α=+20º decreased by 2.3 and 9.7 percent, respectively, compare to the cases of α=0º.

Figures 5.7.13 and 5.7.14 indicate that the degraded inlet performance occurs at the negative sideslip angles along with the side-glaze, as predicted in Figure 5.7.6. Compared to the case of β=0º, the total pressure recovery is reduced by about 2.7 percent, and inlet mass flow rate is decreased by 11.3 percent at β=-20º. However, the effects of the positive sideslip angles are not significant, as shown in the figure. Furthermore, the total pressure recovery and inlet mass flow are less decreased at β=+20º than at β=+10º.

The quantified total pressure recoveries and mass flow rates of all ice cases at M_∞=0.34 are listed in Table 5.7.1. The overall levels of total pressure recovery for the symmetrical glaze cases are lower than those of asymmetrical glaze cases, when the angles of attack or sideslip angle are applied. At angles of attack, the levels of total pressure recovery drop about 5 to 8 percent with the symmetrical glaze case, compared to the top-glaze cases. This is indication of that the steady-state inlet distortion is more affected by the flow blockage, which induced by ice accretion, than by an angle of attack or sideslip angle. In addition, the most serious distortion occurs at α=-20º for the top-glaze, at α=+20º for the bottom-glaze, and at β=-20º for the side-glaze ice case. Moreover, the total pressure recovery of the bottom-glaze case at its most distortion angle (α=+20º) is slightly lower than those of the other asymmetrical cases at their most distortion angles. However, the total pressure recoveries of the ice cases at their most distortion angles are similar to each other;

total pressure recoveries of the most distortion angle in top-, bottom-, and side-glaze cases are 0.9496, 0.9445, and 0.9466, respectively. This fact suggests that the total pressure recovery of approximately 0.95 is the minimum level, when the inlet duct is deviated from the direction of the free-stream flow by 20º in any direction.

In conclusion, the performance of the S-duct inlet is also sensitive to the angles of attack or sideslip angles with the asymmetrical ice shapes; top-, bottom-, and side-glaze ice. However, the influence of each ice shape on the inlet performance becomes more significant at a specific angle, due to the coupled effect of the angles, icing locations, and downward duct curvature. The most serious reduction in inlet performance occurs at α=-20º, α=+20º, and β=-20º for the top-, bottom-, and side-glaze ice cases, respectively. However, the flow blockage is still a critical issue for the inlet performance since the symmetrical glaze induces substantially less total pressure recoveries, compared to the asymmetrical glaze cases, at all angles of attack or sideslip angles.

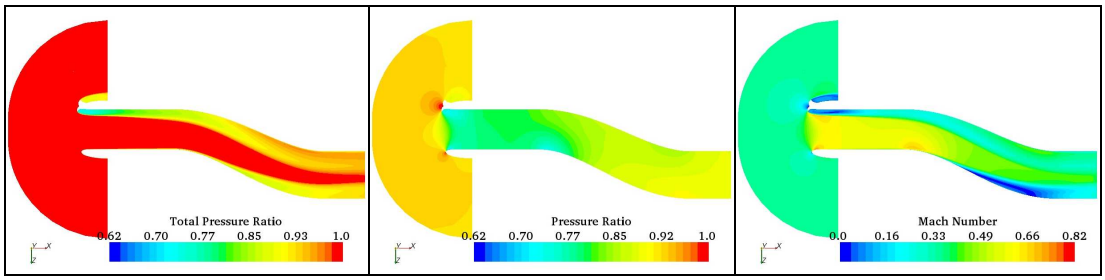

(a) $\alpha = 0^{o}$

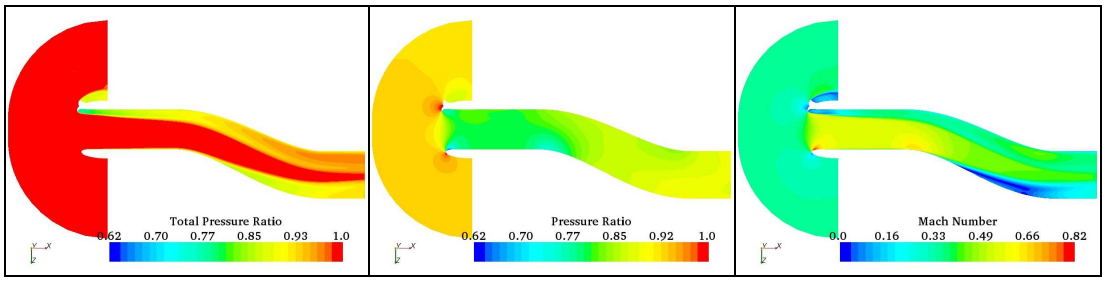

(b) $\alpha = +10^{o}$

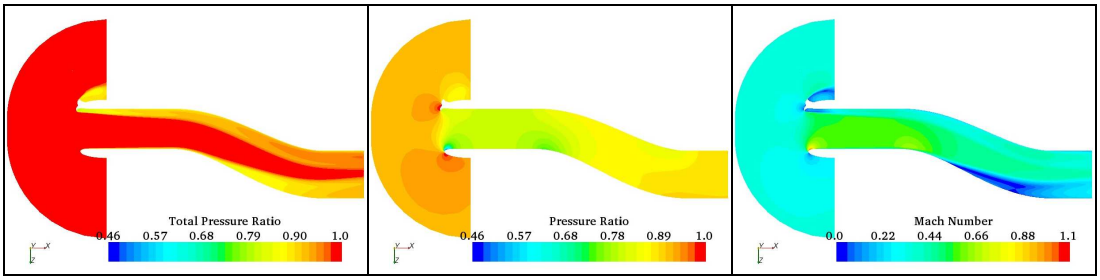

(c) $\alpha = +20^{o}$

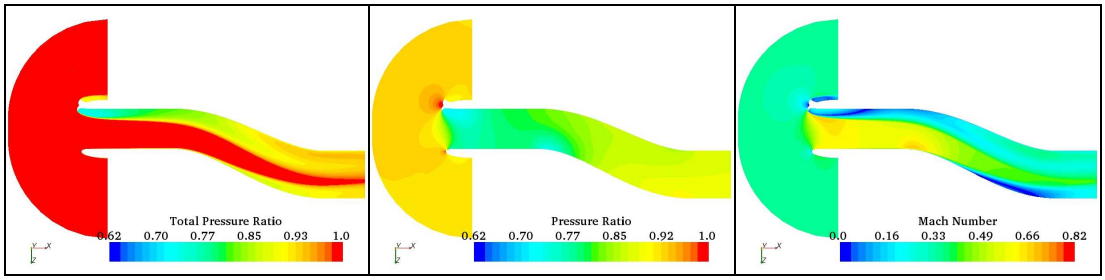

(d) $\alpha = -10^{o}$

i. Total pressure (Pt / Pt_{∞}) ii. Static pressure (Ps / Pt_{∞}) iii. Mach number

Figure 5. 7. 1: Flowfield distributions in the duct symmetry plane at angles of attack (asymmetrical sharp-glaze-top, Pt_{∞}=101.1 kPa, $M_{\infty} = 0.34$)

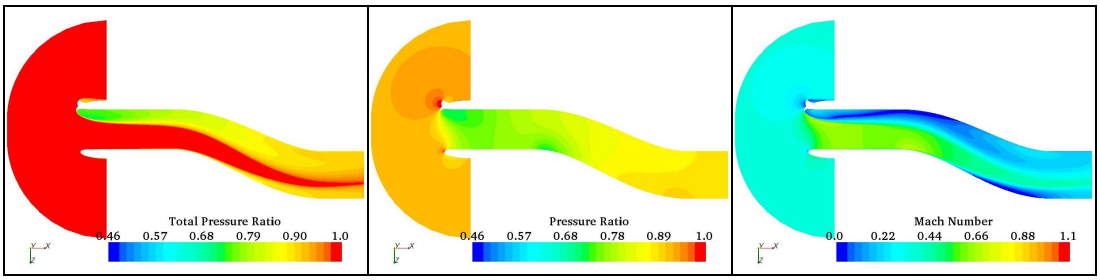

(e) α = - 20º

i. Total pressure (Pt / Pt_{∞}) ii. Static pressure (Ps / Pt_{∞}) iii. Mach number

Figure 5. 7. 1: Flowfield distributions in the duct symmetry plane at angles of attack (asymmetrical sharp-glaze-top, Pt_{∞}=101.1 kPa, M_{∞} = 0.34)

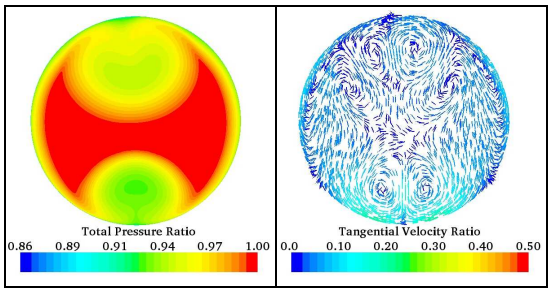

(a) $\alpha = 0^{o}$

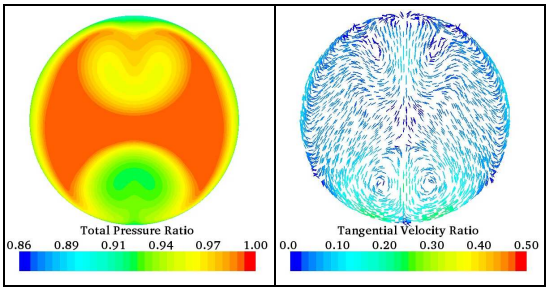

(b) $\alpha = +10^{o}$

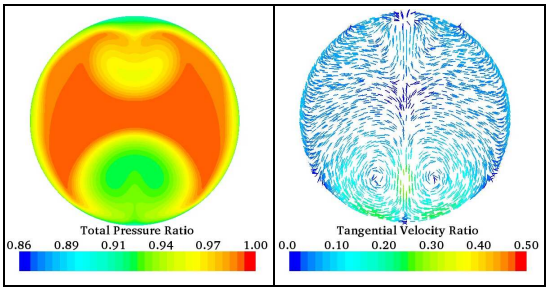

(c) $\alpha = +20^{o}$

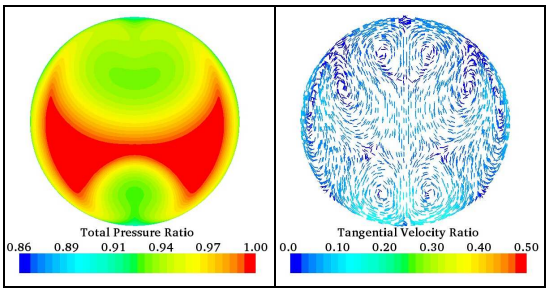

(d) $\alpha = -10^{o}$

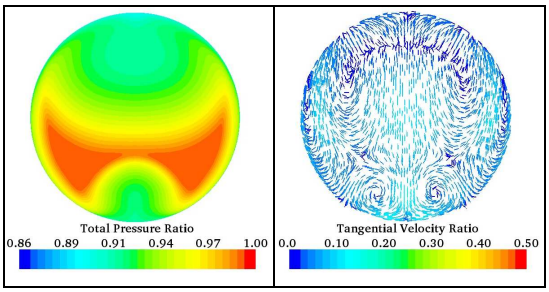

(e) $\alpha = -20^{o}$

Figure 5. 7. 2: Total pressure (Pt / Pt_{∞}) contours and the secondary flow vectors (V / V_{∞}) at the engine face at angles of attack (asymmetrical sharp-glaze-top, Pt_{∞}=101.1 kPa, $M_{\infty} = 0.34$)

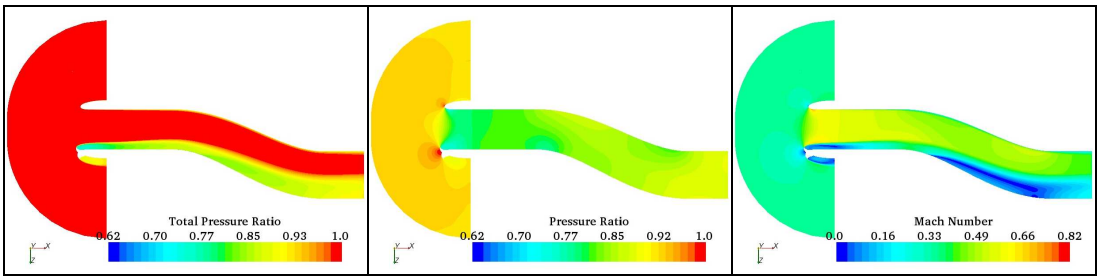

(a) $\alpha = 0^{o}$

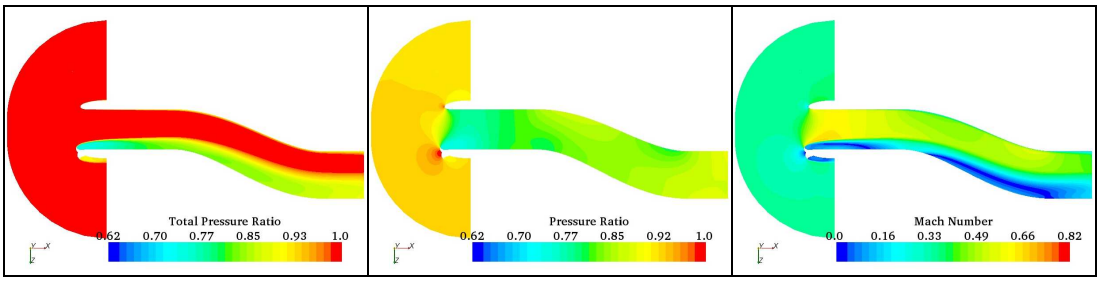

(b) $\alpha = +10^{o}$

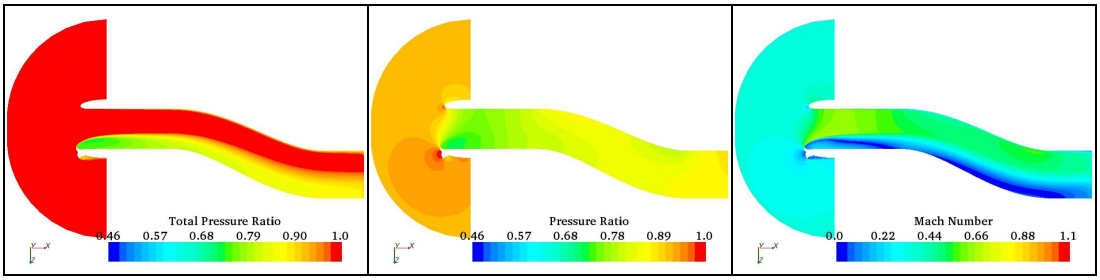

(c) $\alpha = +20^{o}$

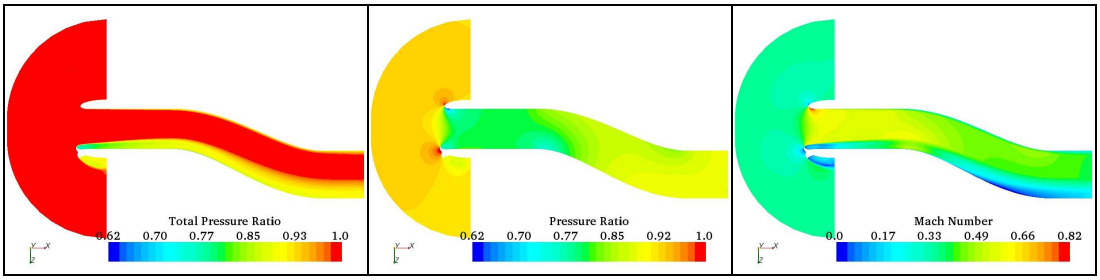

(d) $\alpha = -10^{o}$

i. Total pressure (Pt / Pt_{∞}) ii. Static pressure (Ps / Pt_{∞}) iii. Mach number

Figure 5. 7. 3: Flowfield distributions in the duct symmetry plane at angles of attack (asymmetrical sharp-glaze-bottom, Pt_{∞}=101.1 kPa, $M_{\infty} = 0.34$)

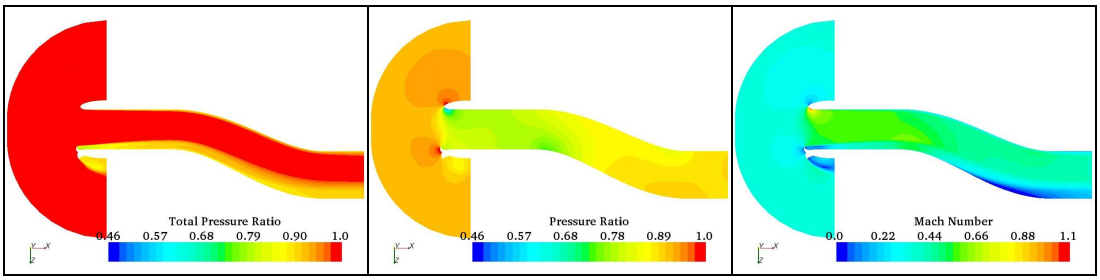

(e) α =- 20º

i. Total pressure (Pt / Pt_{∞}) ii. Static pressure (Ps / Pt_{∞}) iii. Mach number

Figure 5. 7. 3: Flowfield distributions in the duct symmetry plane at angles of attack (asymmetrical sharp-glaze-bottom, Pt_{∞}=101.1 kPa, M_{∞} = 0.34)

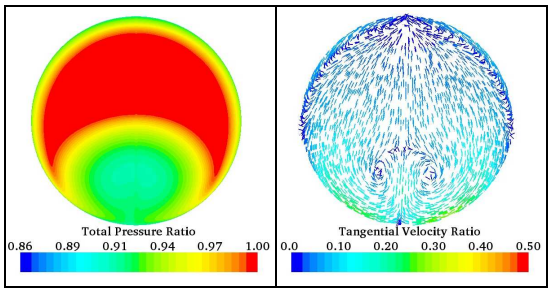

(a) $\alpha = 0^{o}$

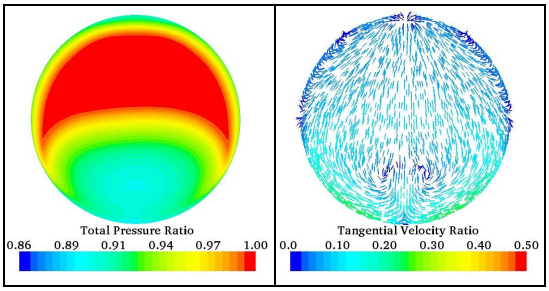

(b) $\alpha = +10^{o}$

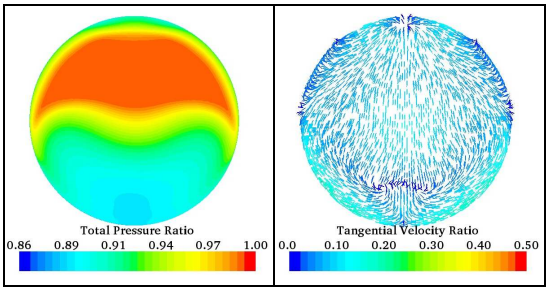

(c) $\alpha = +20^{o}$

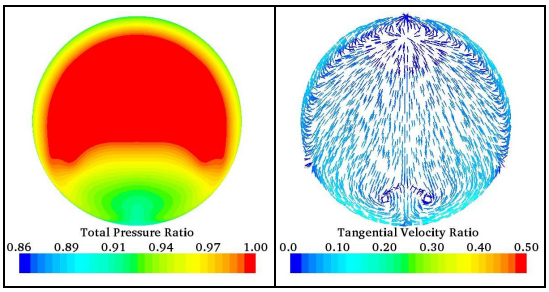

(d) $\alpha = -10^{o}$

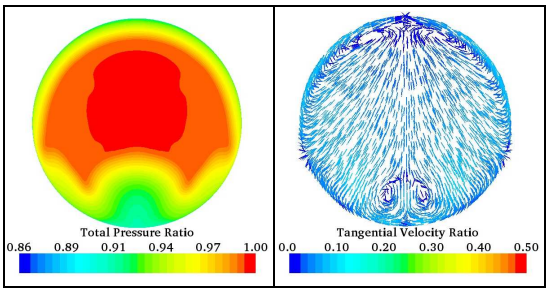

(e) $\alpha = -20^{o}$

Figure 5. 7. 4: Total pressure (Pt / Pt_{∞}) contours and the secondary flow vectors (V / V_{∞}) at the engine face at angles of attack
(asymmetrical sharp-glaze-bottom, Pt_{∞}=101.1 kPa, $M_{\infty} = 0.34$)

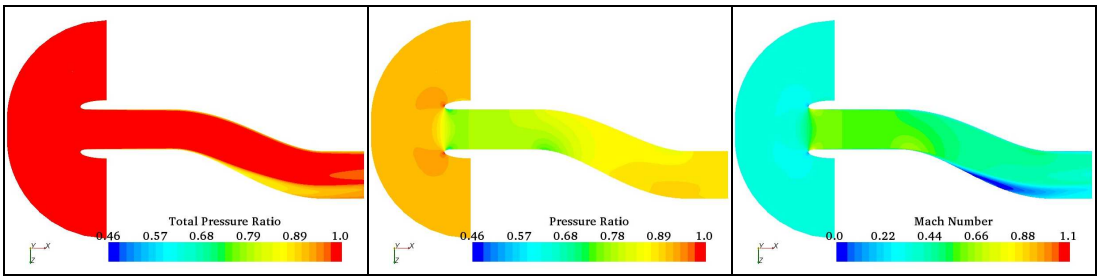

(a) β = 0º

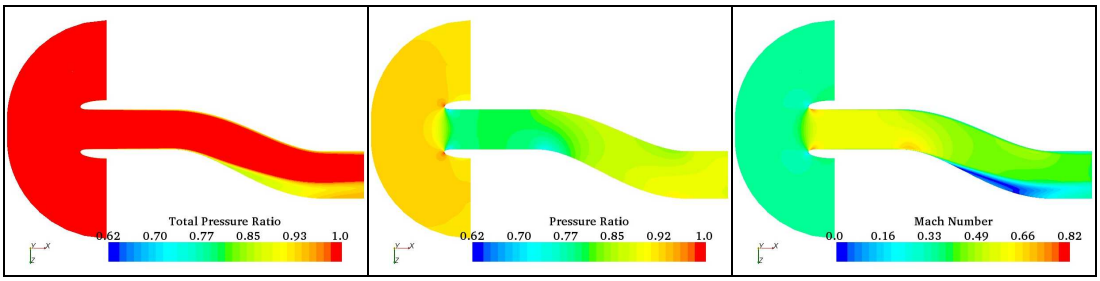

(b) β = + 10º

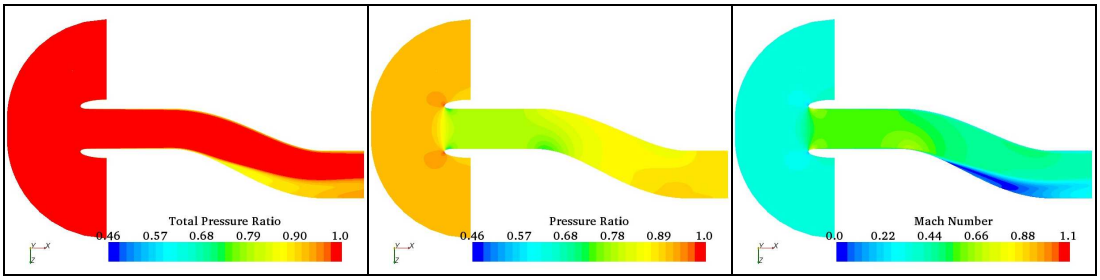

(c) β = + 20º

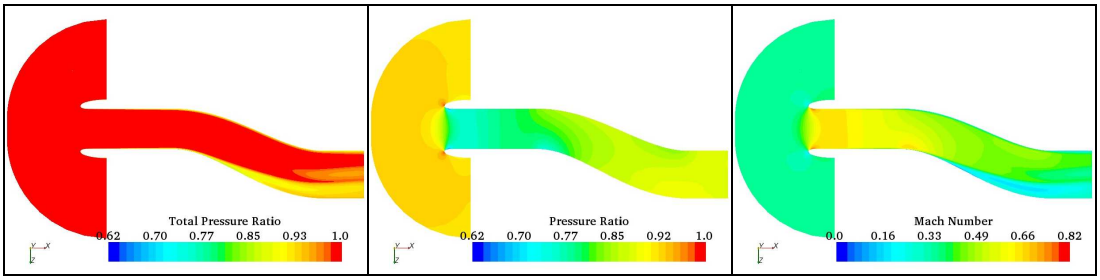

(d) β = - 10º

i. Total pressure (Pt / Pt) ii. Static pressure (Ps / Pt_∞) iii. Mach number

Figure 5. 7. 5: Flowfield distributions in the duct symmetry plane at sideslip angles (asymmetrical sharp-glaze-side, Pt_∞=101.1 kPa, M_∞ = 0.34)

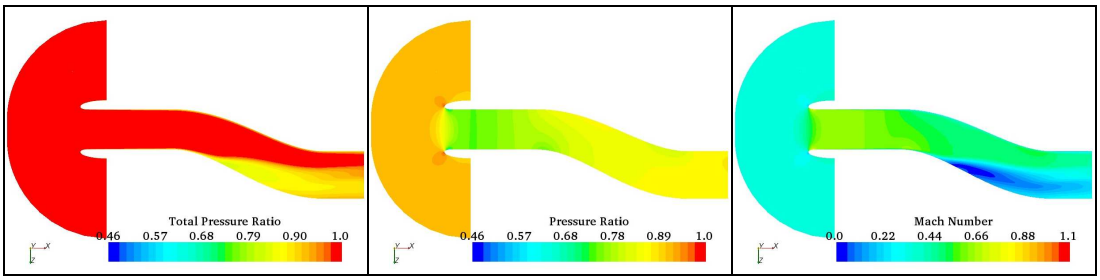

(e) β = - 20º

i. Total pressure (Pt / Pt) ii. Static pressure (Ps / Pt_∞) iii. Mach number

Figure 5. 7. 5: Flowfield distributions in the duct symmetry plane at sideslip angles (asymmetrical sharp-glaze-side, Pt_∞=101.1 kPa, M_∞ = 0.34)

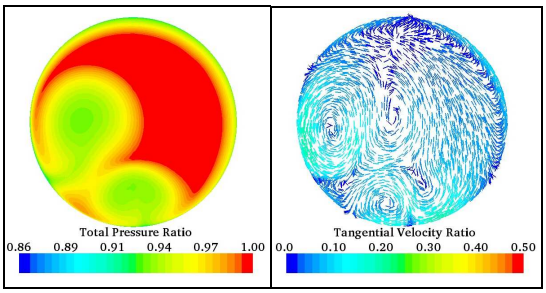

(a) β = 0º

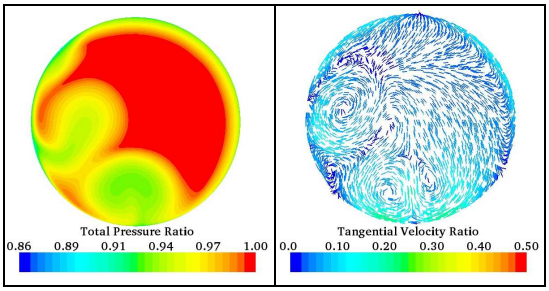

(b) β = +10º

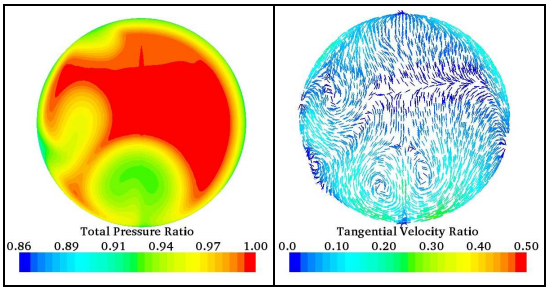

(c) β = + 20º

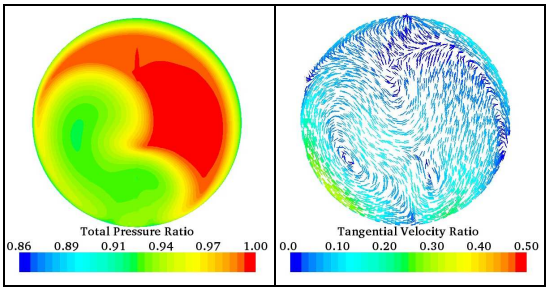

(d) β = -10º

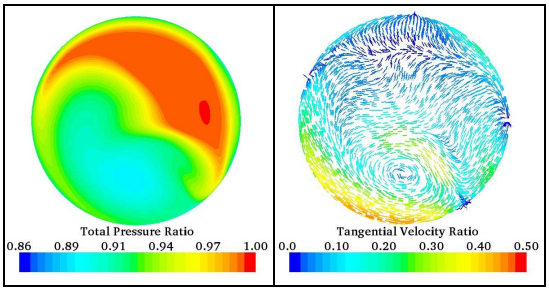

(e) β = - 20º

Figure 5. 7. 6: Total pressure (Pt / Pt_∞) contours and the secondary flow vectors (V / V_∞) at the engine face at sideslip angles
(asymmetrical sharp-glaze-side, Pt_∞=101.1 kPa, M_∞ = 0.34)

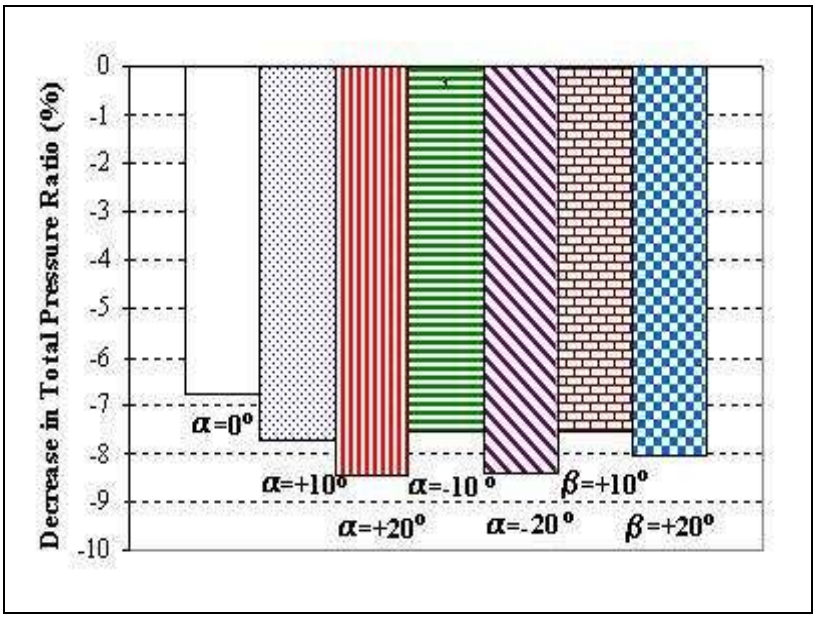

Figure 5. 7. 7: Decrease in total pressure recovery ($\overline{Pt}_{ef}$ / Pt_∞) compared to clean cases (symmetrical sharp-glaze, Pt_∞=101.1 kPa, M_∞ = 0.34)

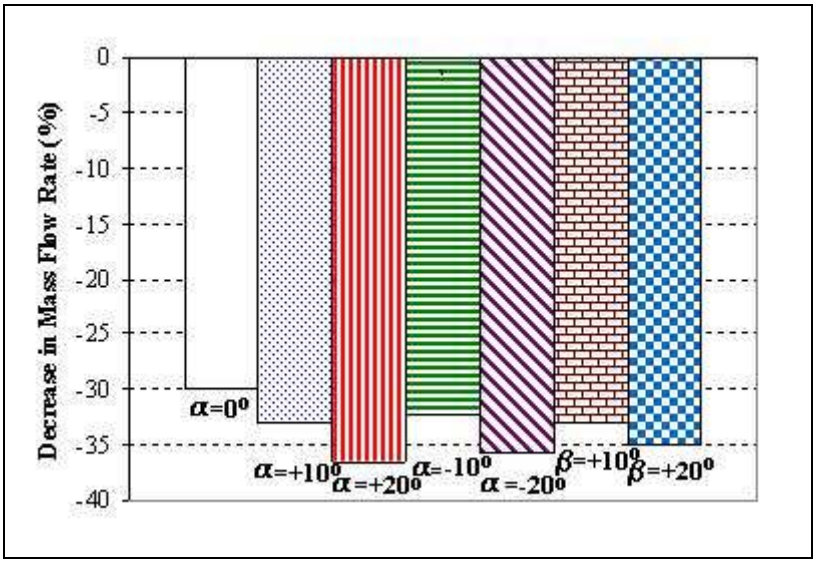

Figure 5. 7. 8: Decrease mass flow rate compared to clean cases (symmetrical sharp-glaze, M_∞ = 0.34)

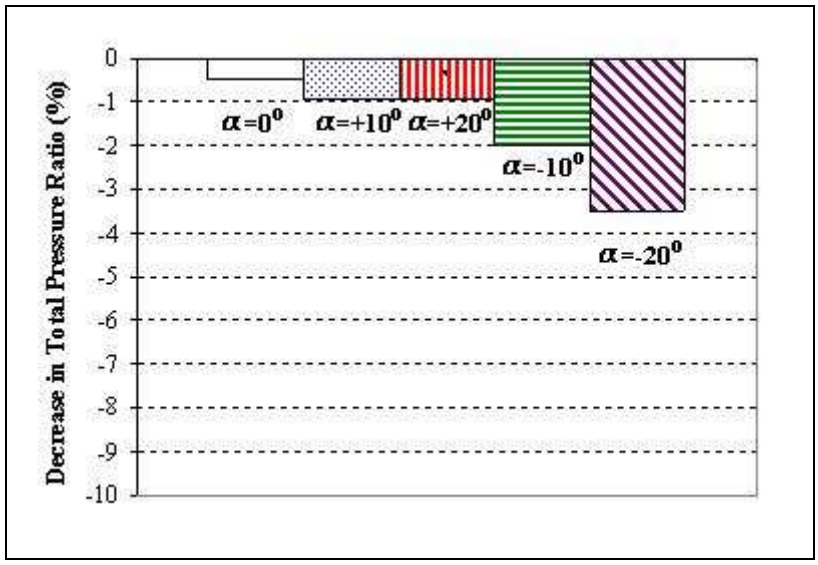

Figure 5. 7. 9: Decrease in total pressure recovery ($\overline{Pt}_{ef}$ / Pt_{∞}) compared to clean cases (asymmetrical sharp-glaze-top, Pt_{∞}=101.1 kPa, M_{∞} = 0.34)

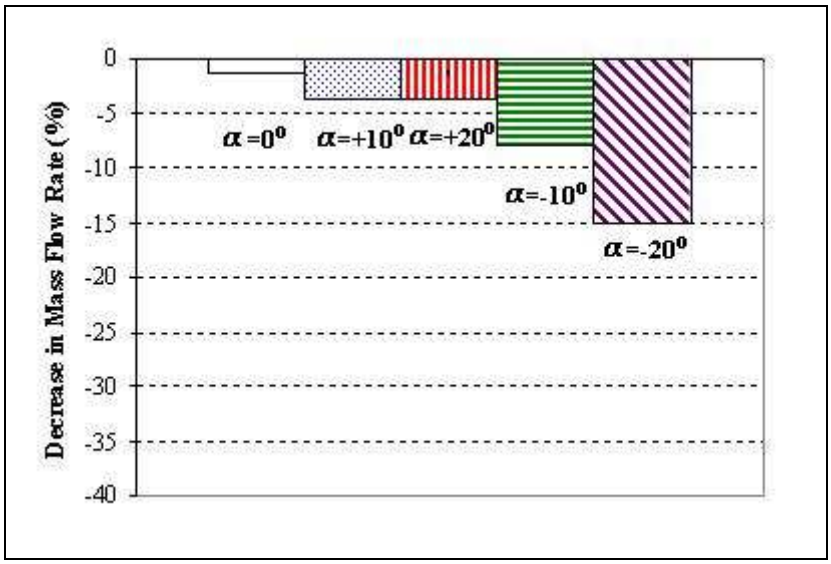

Figure 5. 7. 10: Decrease in mass flow rate compared to clean cases (asymmetrical sharp-glaze-top, M_{∞} = 0.34)

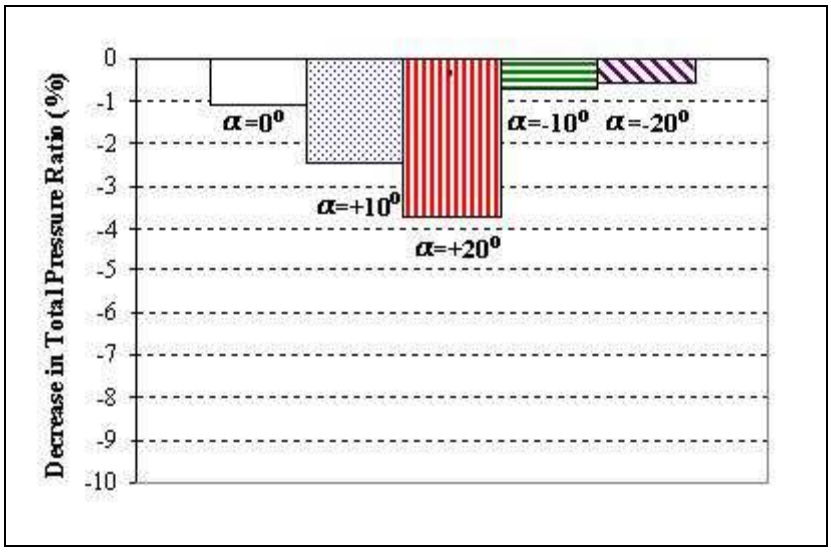

Figure 5. 7. 11: Decrease in total pressure recovery ($\overline{Pt}_{ef}$ / $P_{t\infty}$) compared to clean cases (asymmetrical sharp-glaze ice-bottom, Pt_∞=101.1 kPa, M_∞ = 0.34)

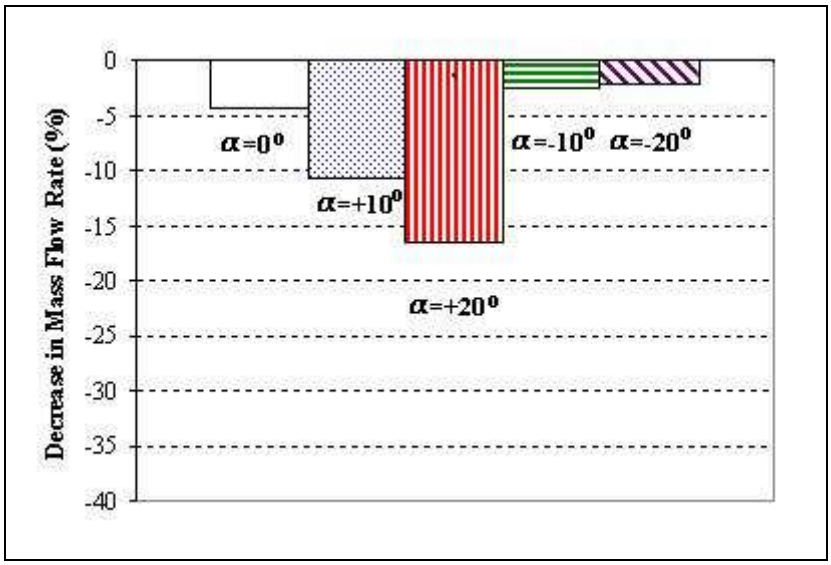

Figure 5. 7. 12: Decrease in mass flow rate compared to clean cases (asymmetrical sharp-glaze ice-bottom, M_∞ = 0.34)

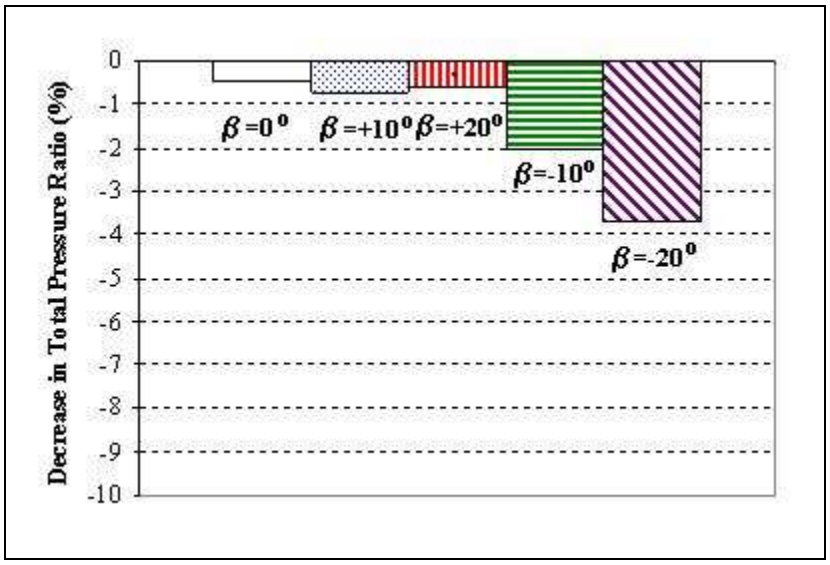

Figure 5. 7. 13: Decrease in total pressure recovery ($\overline{Pt}_{ef}$ / $P_{t\infty}$) compared to clean cases (asymmetrical sharp-glaze ice-side, Pt_∞=101.1 kPa, M_∞ = 0.34)

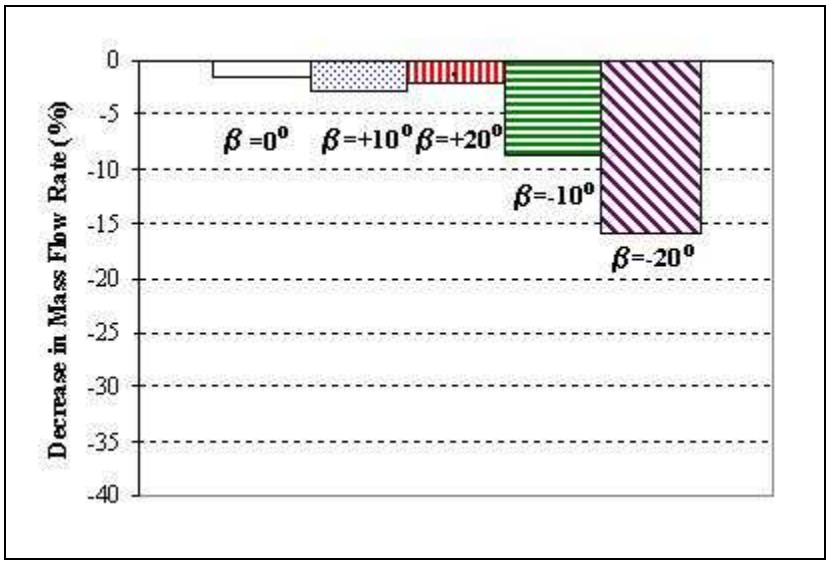

Figure 5. 7. 14: Decrease in mass flow rate compared to clean cases (asymmetrical sharp-glaze ice-side, M_∞ = 0.34)

Table 5. 7. 1: Comparison of total pressure recoveries ($\overline{Pt}_{ef}$ / Pt_∞) and inlet mass flow rates (Pt_∞=101.1 kPa, M_∞ =0.34)

Ice type	Angle of attack or sideslip angle	Total pressure recovery	Mass flow rate (kg/sec.)
Symmetrical Glaze	α = 0 º	0.9116	12.634
	α = + 10 º	0.9057	12.4059
	α = + 20 º	**0.8979**	**11.8419**
	α = - 10 º	0.9098	12.5545
	α = - 20 º	0.9011	11.928
	β = + 10 º	0.9091	12.5064
	β = + 20 º	0.9038	12.1910
Asymmetrical Glaze-Top (θ =315° - 45°)	α = 0 º	0.9731	17.7968
	α = + 10 º	0.9719	17.8518
	α = + 20 º	0.9722	17.9541
	α = - 10 º	0.9646	17.0646
	α = - 20 º	**0.9496**	**15.7753**
Asymmetrical Glaze-Bottom (θ =135° - 225°)	α = 0 º	0.9668	17.2674
	α = + 10 º	0.9569	16.5858
	α = + 20 º	**0.9445**	**15.5858**
	α = - 10 º	0.9772	18.0819
	α = - 20 º	0.9778	18.1715
Asymmetrical Glaze-Side (θ =45° - 135°)	β = 0 º	0.9729	17.7594
	β = + 10 º	0.9763	18.1675
	β = + 20 º	0.9773	18.3526
	β = - 10 º	0.9635	17.0713
	β = - 20 º	**0.9466**	**15.7569**

5.8. Combined effects of inlet icing and angle of attack or sideslip angle on dynamic distortion

The present study investigates the effects of angles of attack or sideslip angles, combined with the effects of different ice shapes: symmetrical and asymmetrical, on the unsteady-state flowfield in the M2129 S-duct inlet. The factors: the ice shape, icing location, angle of attack or sideslip angle, and flow unsteadiness, are considered in the present study to see more realistic icing effects in practical flight

conditions. The factors can be combined with each other and they can produce particular unsteady flow patterns in the S-duct inlet.

The instantaneous flow distributions, at non-zero angles of attack and sideslip angles, are given in Figures 5.8.1 to 5.8.5. The free-stream Mach number is M_∞=0.34, and time step size is Δt=0.0005sec**.** Figure 5.8.1 shows the clean inlet cases, and it suggests that the instantaneous flowfield distributions in the clean inlet are sensitive to all angles of attack and sideslip angles.

Figure 5.8.2 shows the symmetrical glaze ice cases. The strong instantaneous perturbation takes place from the bottom-side of the symmetrical glaze ice at the positive angle of attack (α=+20º), and from the top-side at the negative angle of attack (α=-20º). The strong-instantaneous perturbation in the unsteady flow is the indication of the strong flow unsteadiness. Also, vortex shedding structures are observed at all angles of attack and sideslip angles. However, the strongest vortex shedding occurs at α=+20º. Note that the results in Chapter 5.6 showed that the most severe flow separation, as well as the greatest steady-state total pressure distortion, occurred with the symmetrical glaze ice at α=+20º.

Figures 5.8.3 to 5.8.5 show the cases of the asymmetrical glaze ice shapes: top-glaze, bottom-glaze, and side-glaze ice. Similar to the steady-state results, the levels of the instantaneous perturbation by the asymmetrical glaze ice shapes are all sensitive to the angles of attack or sideslip angles. The flow direction of vortex shedding also changes with the variation of the angle of attack. However, the detailed changes in the unsteady flowfield can not be observed in these instantaneous distribution contours. Therefore, to obtain more detailed information of the effects of

angle of attack or sideslip angle on the flow unsteadiness in the S-duct inlet, the magnitudes of total pressure fluctuation at the engine face are calculated.

Figures 5.8.6 to 5.8.9 show the calculated total pressure fluctuation parameters, $\overline{Pt}'_{rms}/\overline{Pt}_{ef}$, for the symmetrical, and asymmetrical glaze cases at M_∞=0.34. Note that $\overline{Pt}'_{rms}$ denotes the rms value of total pressure fluctuation at the engine face, and $\overline{Pt}_{ef}$ indicates the time-averaged total pressure, i.e., steady-state total pressure at the engine face. In addition, the fluctuations are calculated using the time step size of Δt=0.01sec. In the symmetrical glaze ice cases, presented in Figure 5.8.6, all angles of attack and sideslip angle cause significant increases in the magnitude of total pressure fluctuation, when compared to the cases of at α=0º (or β=0º). However, the most severe total pressure fluctuation is produced at the sideslip angle, β=+20º (or β= -20º). Also, a strong fluctuation is induced at α=+20º. Note that, in the steady-state computation results, the positive angle of attack, α=+20º, caused the greatest total pressure distortion. In addition, as shown in Figure 5.8.2(b), the most apparent vortex shedding from the glaze ice horn is shown in the case of α=+20º. Therefore, it is evident that the magnitude of total pressure fluctuation is related to the level of the steady-state total pressure distortion or to the strength of vortex shedding. The inlet dynamic distortion level, i.e., total pressure fluctuation, is known to be proportional to the steady-state distortion level at an engine face.[87] At α=+20º, the level of fluctuation, $\overline{Pt}'_{rms}/\overline{Pt}_{ef}$, raises about 165 percent, compared to the fluctuation at α=0º.

Figures 5.8.7 and 5.8.8 present the calculated magnitude of fluctuation for the top- and bottom-asymmetrical glaze ice cases at the angles of attack. In the top- and bottom-glaze ice cases, the highest magnitudes of the total pressure fluctuations are generated at α=-20º and +20º, respectively. Also note that the most severe steady-state total pressure distortions in the top- and bottom-glaze ice cases occurred at α=-20º and +20º, respectively. However, the levels of fluctuation decrease at α=+20º and -20º for the top- and bottom-glaze cases, respectively. In addition, the side-asymmetrical glaze ice cases are shown in Figure 5.8.9. The figure indicates that the sideslip angle of β=-20º affects the increase of the total pressure fluctuation most. Again, at β=-20º, the inlet total pressure distortion of the side-glaze case in the steady-state condition was most seriously distorted, as given in Chapter 5.7. Therefore, it can be seen that, with the angles of attack or sideslip angles, the steady-state inlet distortion still exerts a direct influence on the total pressure fluctuation level or dynamic inlet distortion, regardless of the ice accretion shapes.

The values of the total pressure fluctuation parameters, $\overline{Pt}'_{rms} / \overline{Pt}_{ef}$, with the different ice shapes are compared at each angle of attack or sideslip angle, as given in Figures 5.8.10 to 5.8.14. Again, the free-stream Mach number is M_∞=0.34, and time step size is Δt=0.01sec. for all cases. Figure 5.8.10 shows a comparison of the fluctuation parameters at α=0º (or β=0º). Compared to the clean case, all ice shape cases induce the increases in total pressure fluctuation at the engine face when angle of attack or sideslip angle is zero. However, the level of total pressure fluctuation for the symmetrical glaze ice case is slightly higher than those of other ice shape cases. The increment of total pressure fluctuation with the symmetrical glaze ice is about 28

percent when angle of attack is zero, compared to the clean case. The effects of angles of attack or sideslip angles are presented in Figures 5.8.11 to 5.8.14. It is shown from the figures that the magnitudes of total pressure fluctuation of the ice cases are higher than those of the clean cases at angles of attack and sideslip angles, except some cases: top-glaze at α=+20º and bottom glaze at α=-20º. As shown in the steady-state results in Chapter 5.7, the least effects were induced at α=+20º and -20º for the top- and bottom-glaze cases, respectively. In particular, substantial increases in the fluctuation occur due to the symmetrical glaze ice accretion at all angles of attack and sideslip angles. With the symmetrical glaze ice, the levels of total pressure fluctuation are increased by about 270 and 290 percent at α=+20º and β=±20º, respectively, compared to the clean cases.

Therefore, it can be concluded that the adverse effects of the inlet icing on the dynamic distortion, in particular total pressure fluctuation, of the S-duct inlet become more substantial at non-zero angles of attack or sideslip angles. Also, the level of the dynamic inlet distortion proportionally increases as the level of steady-state inlet distortion increases at an angle of attack or sideslip angle. In addition, the effects of the asymmetrical glaze ice shapes on the flow unsteadiness are less than those of the symmetrical glaze ice at all angles of attack or sideslip angles. The symmetrical glaze ice is characterized by a wider area of ice accretion on the inlet lip that induces a larger blocking area to the inflow, compared to the asymmetrical ice shapes. Therefore, the flow blockage level is still an important factor for the dynamic inlet distortion with angles of attack or sideslip angles.

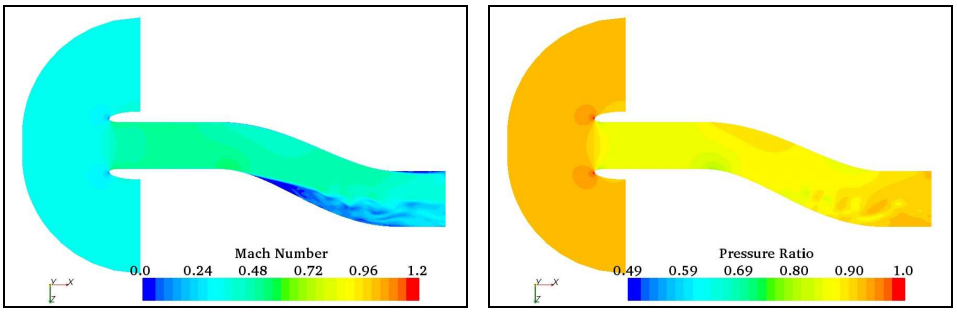

(a) $\alpha = 0^{o}$

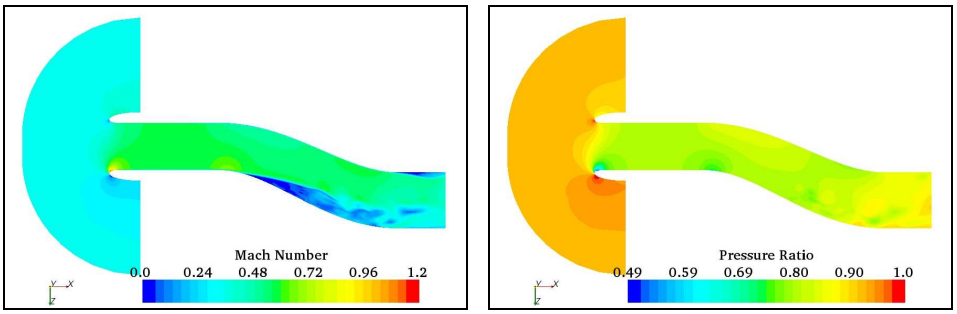

(b) $\alpha = +20^{o}$

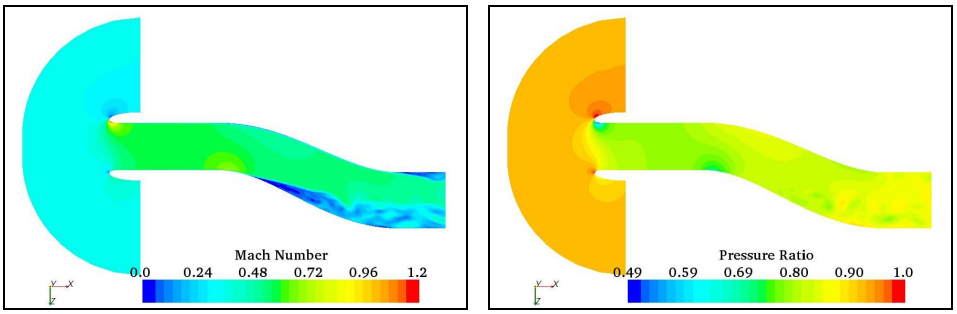

(c) $\alpha = -20^{o}$

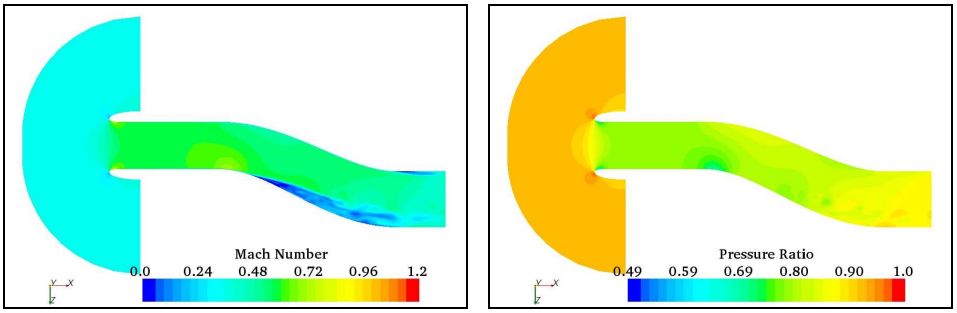

(d) $\beta = +20^{o}$

i. Mach number ii. Pressure ratio (Ps/Pt_{∞})

Figure 5. 8. 1: Instantaneous flowfield distributions in the duct symmetry plane at angles of attack or sideslip angle (clean, Pt_{∞}=101.1 kPa, $M_{\infty} = 0.34$, $\Delta t = 0.0005$ sec.)

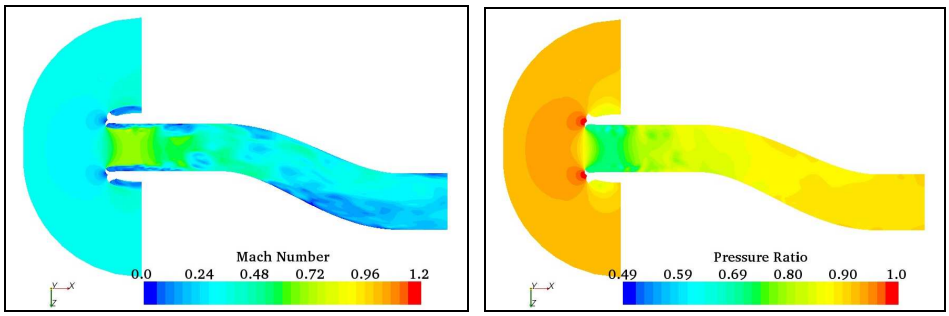

(a) $\alpha = 0^{o}$

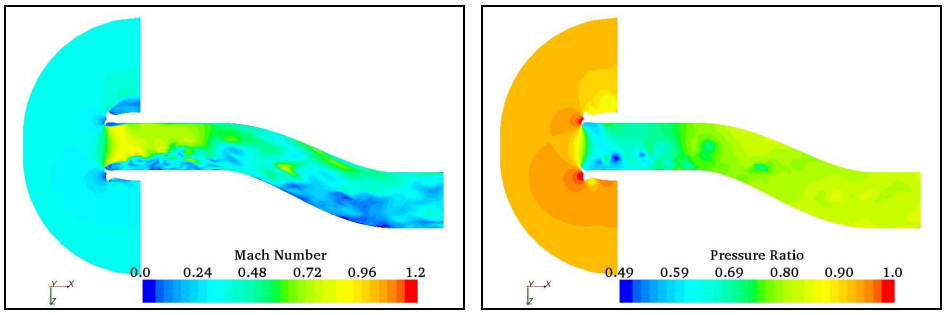

(b) $\alpha = +20^{o}$

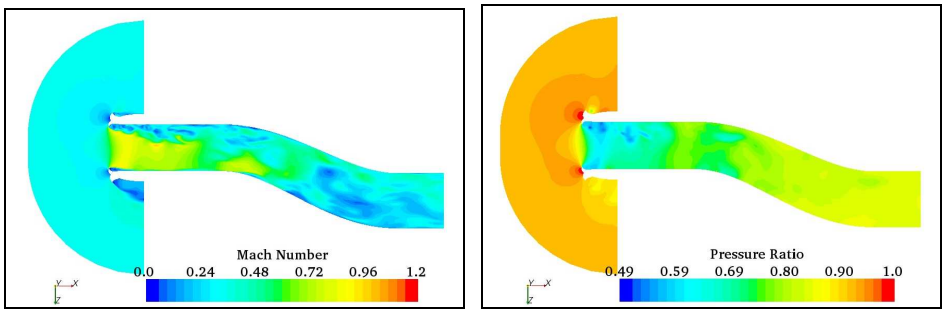

(c) $\alpha = -20^{o}$

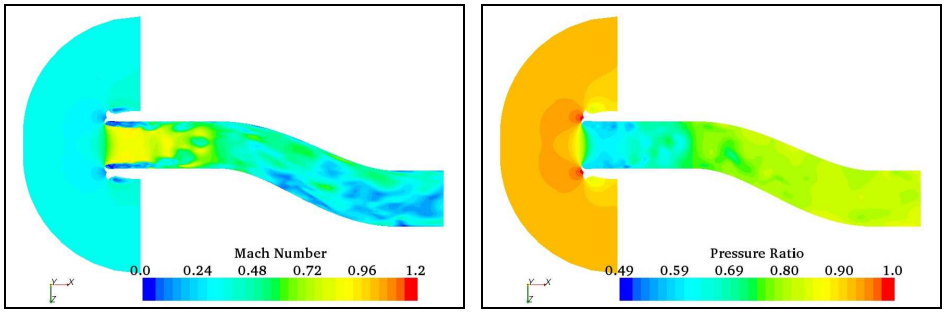

(d) $\beta = +20^{o}$

i. Mach number ii. Pressure ratio (Ps/Pt_{∞})

Figure 5. 8. 2: Instantaneous flowfield distributions in the duct symmetry plane at angles of attack or sideslip angle (symmetrical sharp-glaze, Pt_{∞}=101.1 kPa, $M_{\infty} = 0.34$, $\Delta t = 0.0005$ sec.)

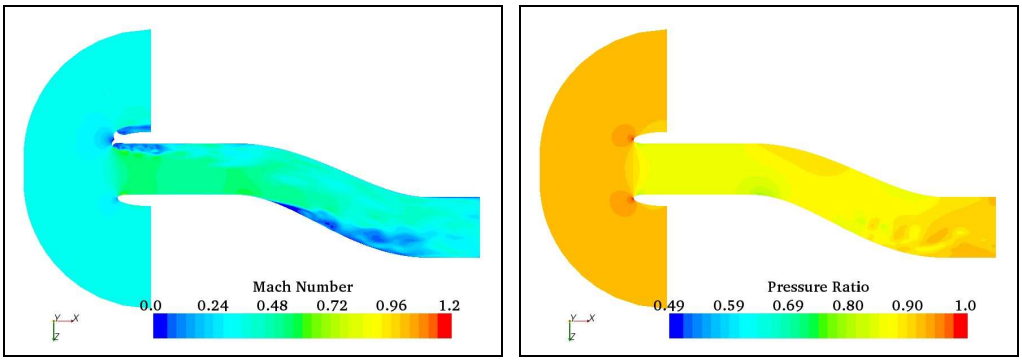

(a) $\alpha = 0^{o}$

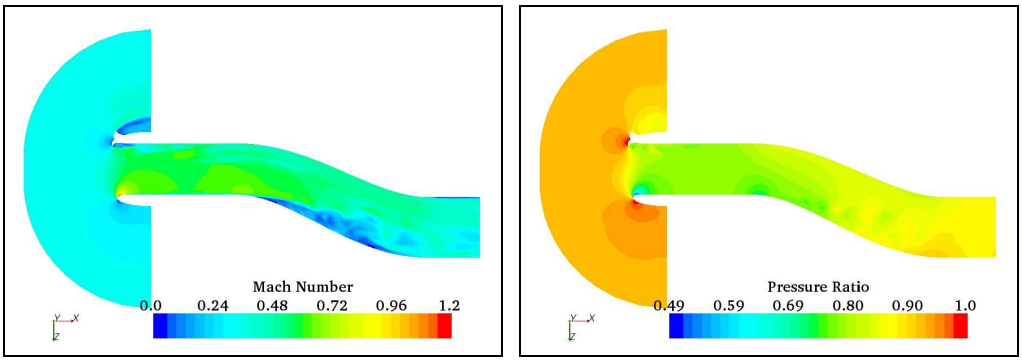

(b) $\alpha = +20^{o}$

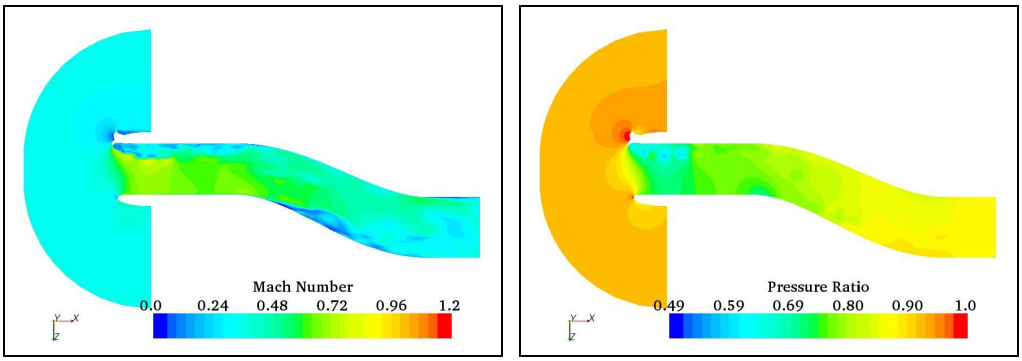

(c) $\alpha = -20^{o}$

i. Mach number ii. Pressure ratio (Ps/Pt_{∞})

Figure 5. 8. 3: Instantaneous flowfield distributions in the duct symmetry plane at angles of attack (asymmetrical sharp-glaze-top, Pt_{∞}=101.1 kPa, M_{∞} = 0.34, Δt = 0.0005 sec.)

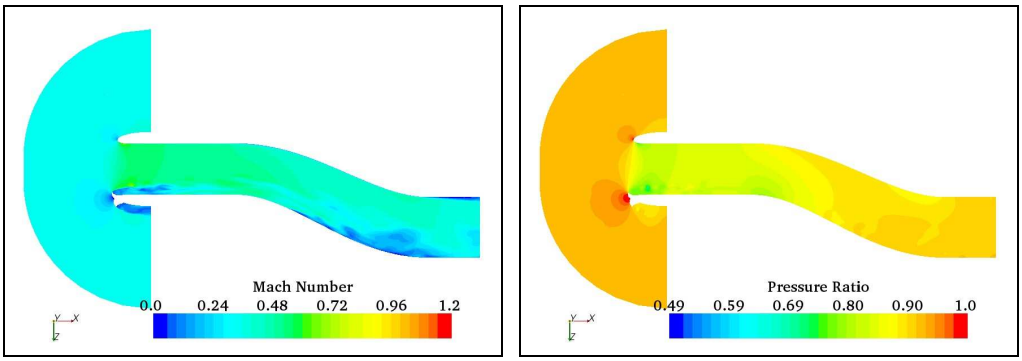

(a) $\alpha = 0^{o}$

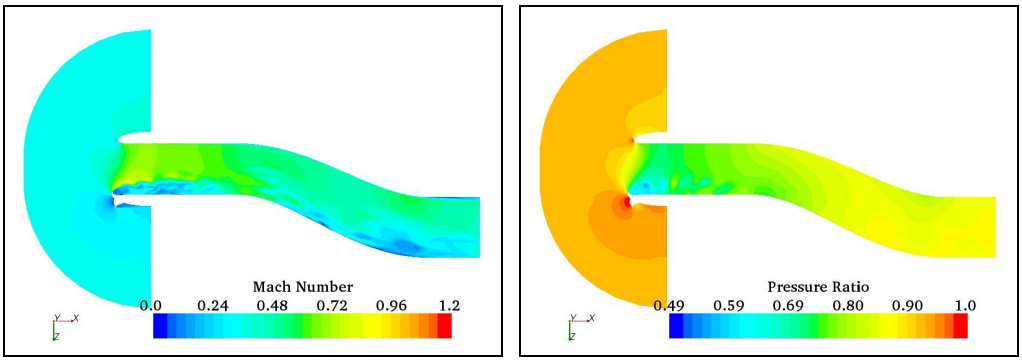

(b) $\alpha = +20^{o}$

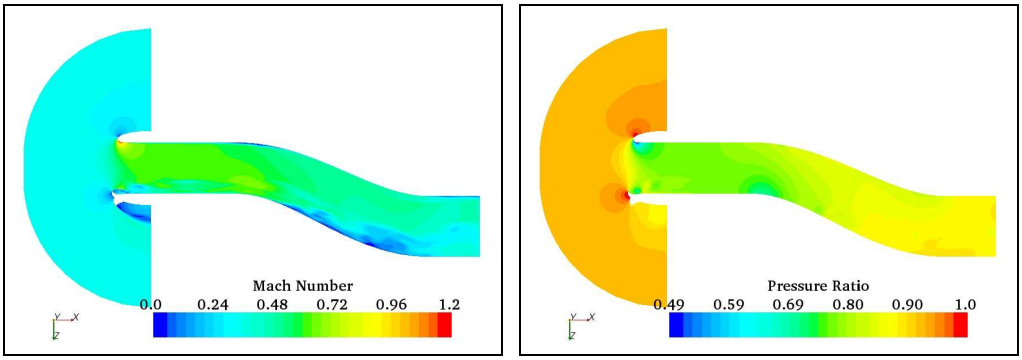

(c) $\alpha = -20^{o}$

i. Mach number ii. Pressure ratio (Ps/Pt_{∞})

Figure 5. 8. 4: Instantaneous flowfield distributions in the duct symmetry plane at angles of attack (asymmetrical sharp-glaze-bottom, Pt_{∞}=101.1 kPa, $M_{\infty} = 0.34$, $\Delta t = 0.0005$ sec.)

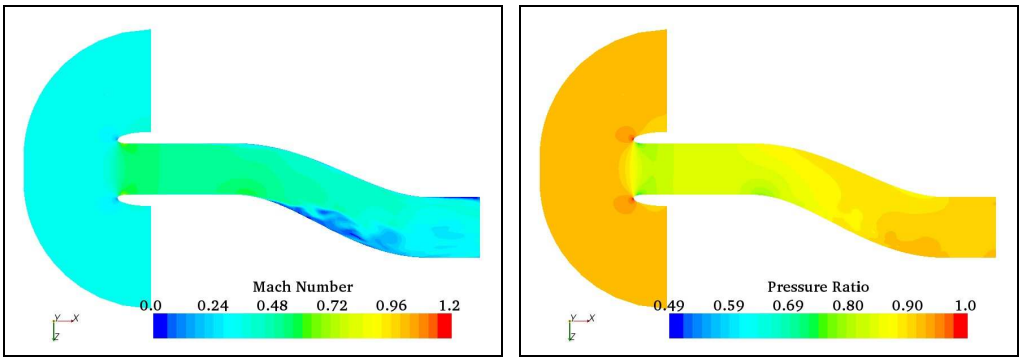

(a) β = 0º

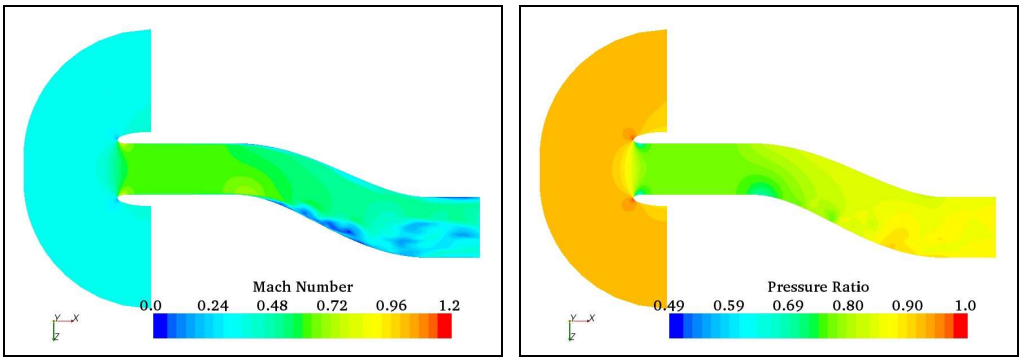

(b) β = + 20º

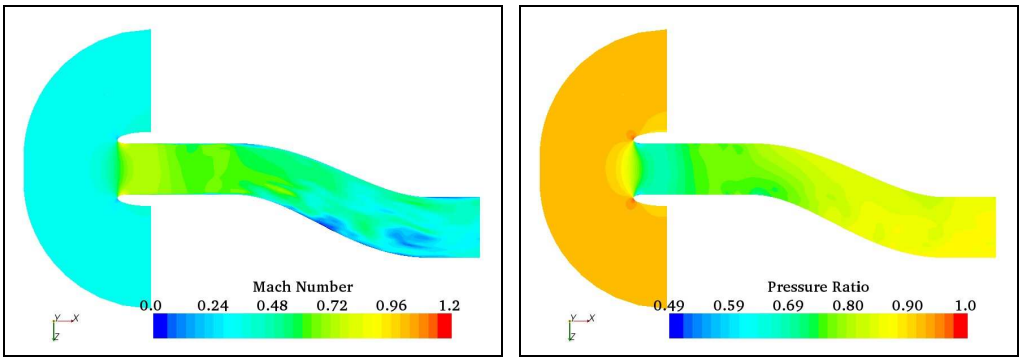

(c) β = - 20º

i. Mach number ii. Pressure ratio (Ps/Pt_∞)

Figure 5. 8. 5: Instantaneous flowfield distributions in the duct symmetry plane at sideslip angles (asymmetrical sharp-glaze-side, Pt_∞=101.1 kPa, M_∞ = 0.34, Δt = 0.0005sec.)

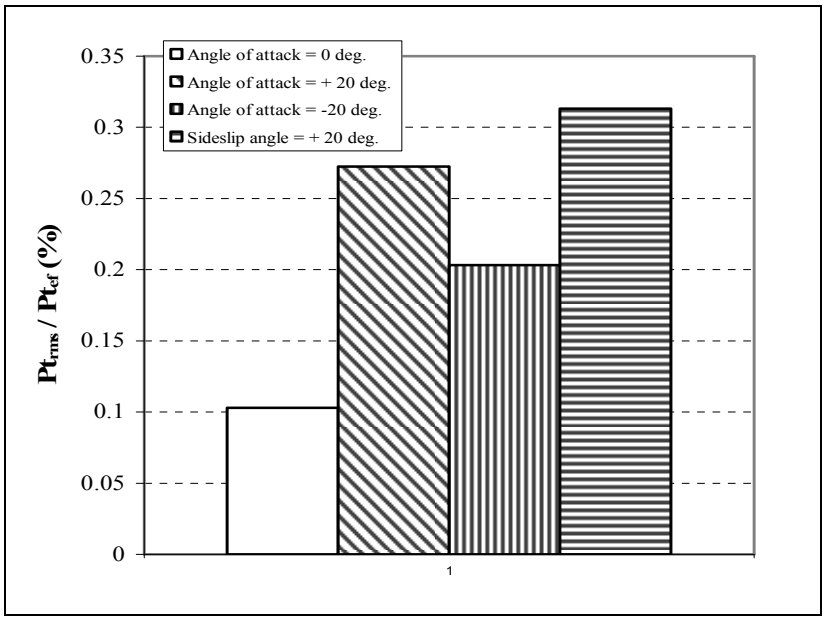

Figure 5. 8. 6: Comparison of $\overline{Pt}'_{rms} / \overline{Pt}_{ef}$ at the angles of attack or sideslip angle (symmetrical sharp-glaze, $M_\infty = 0.34$, $\Delta t = 0.01$ sec.)

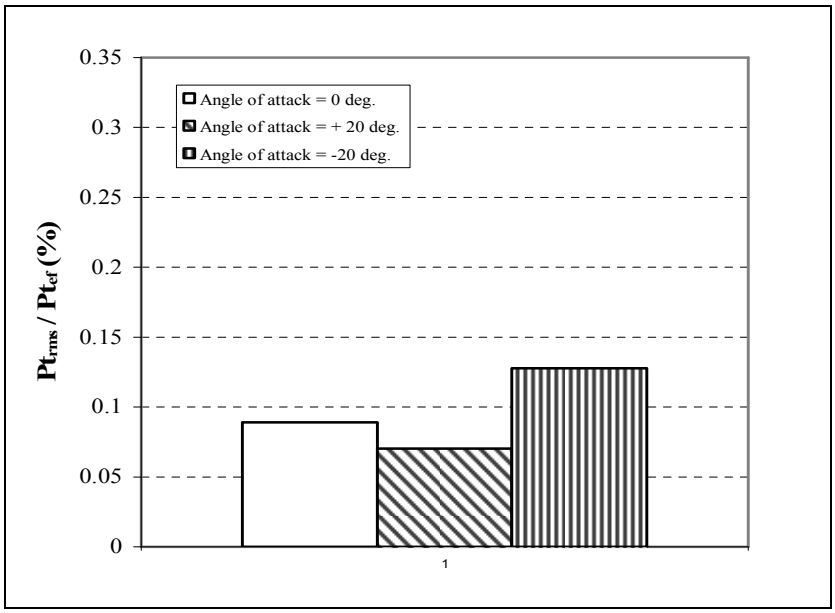

Figure 5. 8. 7: Comparison of $\overline{Pt}'_{rms} / \overline{Pt}_{ef}$ at the angles of attack (asymmetrical sharp-glaze-top, $M_\infty = 0.34$, $\Delta t = 0.01$ sec.)

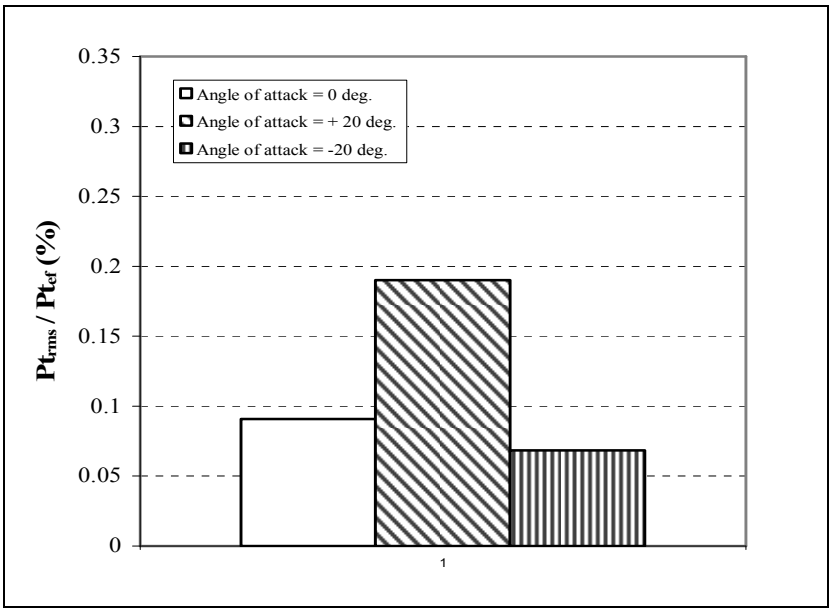

Figure 5. 8. 8: Comparison of $\overline{Pt}'_{rms} / \overline{Pt}_{ef}$ at the angles of attack (asymmetrical sharp-glaze-bottom, $M_\infty = 0.34$, $\Delta t = 0.01$ sec.)

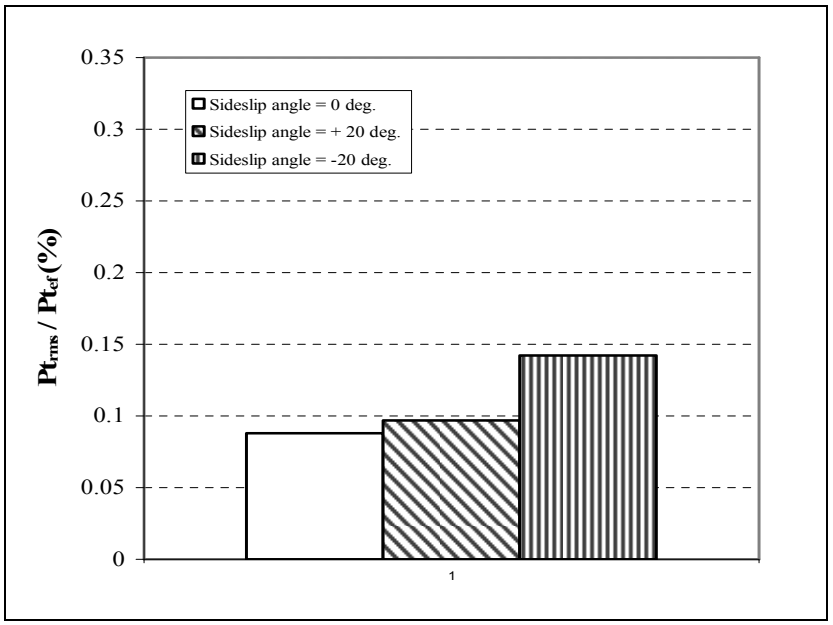

Figure 5. 8. 9: Comparison of $\overline{Pt}'_{rms} / \overline{Pt}_{ef}$ at sideslip angles (asymmetrical sharp-glaze-side, $M_\infty = 0.34$, $\Delta t = 0.01$ sec.)

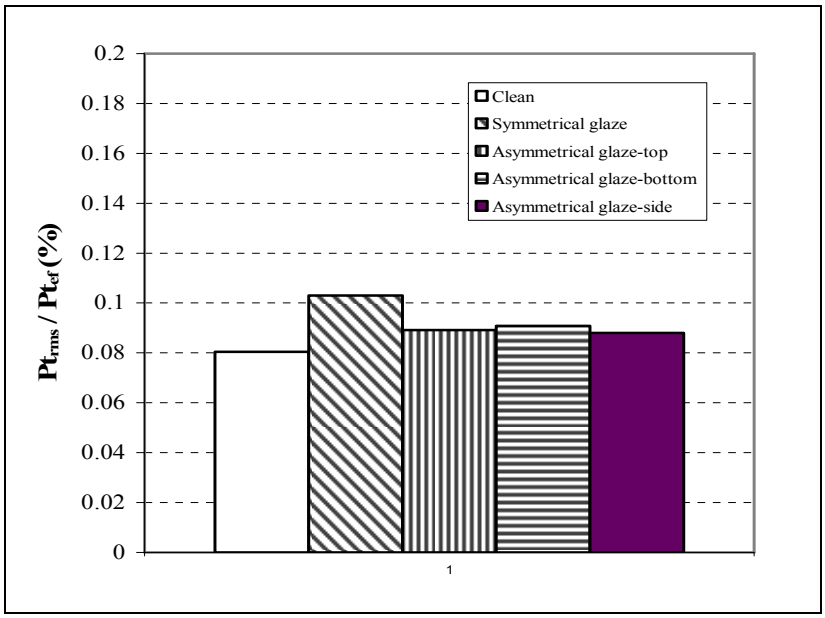

Figure 5. 8. 10: Comparison of $\overline{Pt}'_{rms} / \overline{Pt}_{ef}$ with the symmetrical and asymmetrical ice cases ($\alpha = 0^o$, $M_\infty = 0.34$, $\Delta t = 0.01$ sec.)

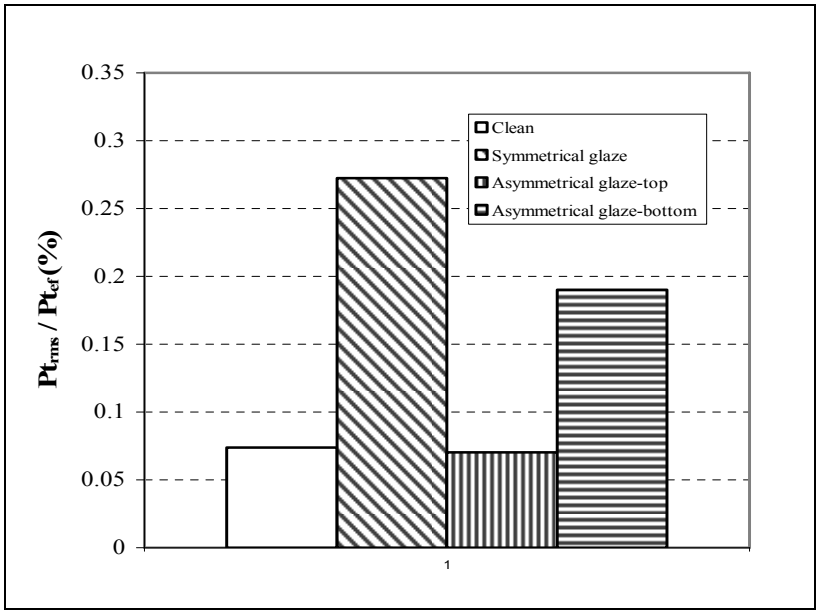

Figure 5. 8. 11: Comparison of $\overline{Pt}'_{rms} / \overline{Pt}_{ef}$ with the symmetrical and asymmetrical ice cases ($\alpha = +20^o$, $M_\infty = 0.34$, $\Delta t = 0.01$ sec.)

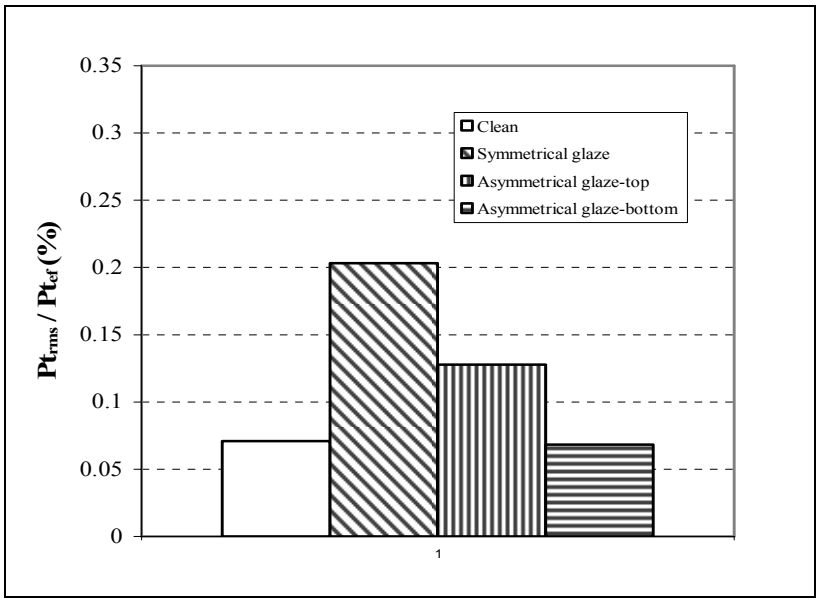

Figure 5. 8. 12: Comparison of $\overline{Pt}'_{rms} / \overline{Pt}_{ef}$ with the symmetrical and asymmetrical ice cases (α = - 20º, M_∞ = 0.34, Δt = 0.01 sec.)

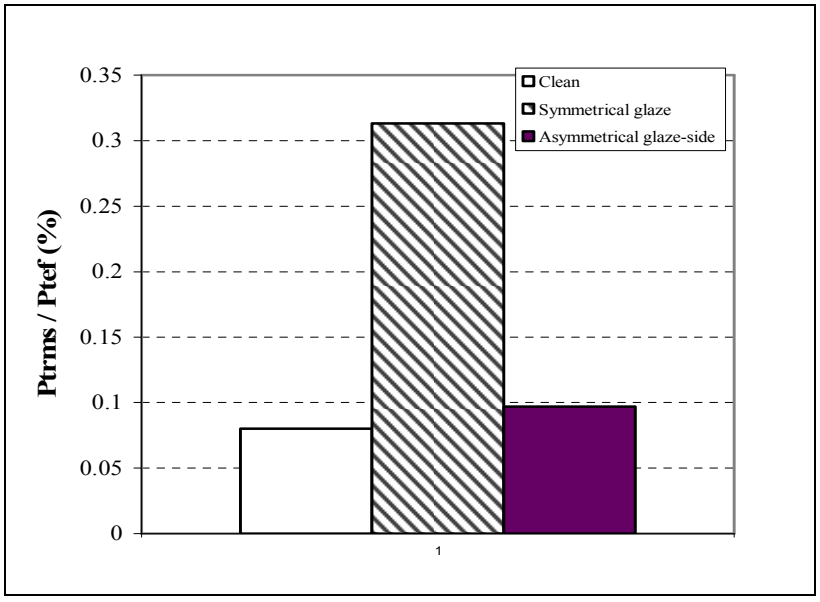

Figure 5. 8. 13: Comparison of $\overline{Pt}'_{rms} / \overline{Pt}_{ef}$ with the symmetrical and asymmetrical ice cases (β = + 20º, M_∞ = 0.34, Δt = 0.01 sec.)

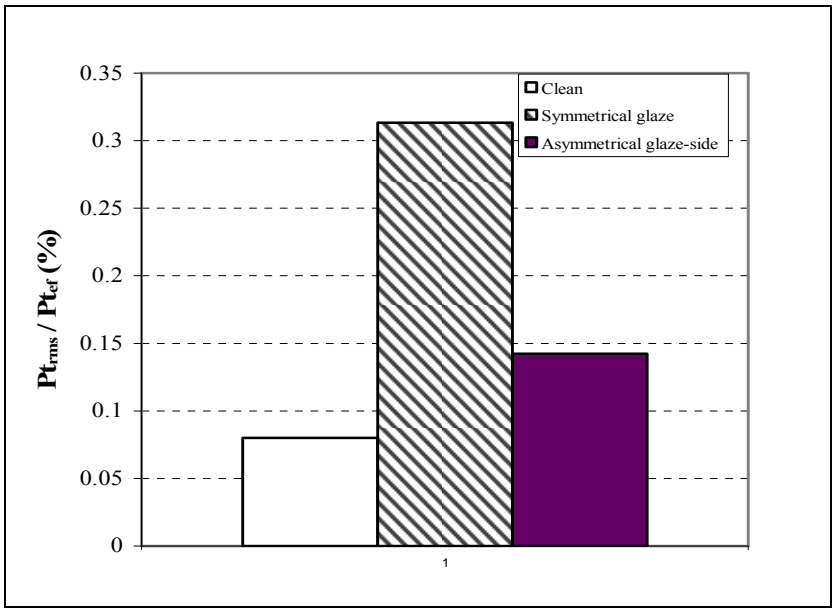

Figure 5. 8. 14: Comparison of $\overline{Pt}'_{rms} / \overline{Pt}_{ef}$ with the symmetrical and asymmetrical ice cases (β = - 20º, M_∞ = 0.34, Δt = 0.01 sec.)

5.9. Combined effects of inlet icing and wall heat transfer on coupled total pressure- temperature distortion

As mentioned in Chapter 3.5 of the present study, one of the factors causing temperature distortion is the inlet wall heating. Therefore, wall temperature conditions are considered, and their effects, combined with the icing effect, on the pressure and temperature distortion at the engine face are investigated. The wall thermal boundary condition for zero heat transfer (adiabatic flow) and the heated wall boundary condition can allow for the simulation of realistic temperature distortion at the engine face under inlet icing conditions. Moreover, the coupling effect between total pressure distortion and temperature distortion on the inlet duct-performance is examined.

The total pressure distribution in the duct symmetry plane for the cases of clean and glaze at M_∞=0.475 is shown in Figure 5.9.1. Note that only the symmetrical glaze ice shape is examined in this chapter. Boundary layer separation or flow separation is visible in both the clean and glaze cases. However, the extent of the separation is considerably increased in the inlet with glaze ice. Figures 5.9.2 and 5.9.3 show the Mach number and static temperature distributions, respectively, in the duct symmetry plane for the clean and the glaze iced inlet at M_∞=0.475. The Mach number contours show a massive separation from the glaze ice that starts at the convex corner of the first bend, which does not occur in the clean case. The temperature contour in the glaze case shows a similarly massive region in the duct separated flow that exhibits a higher temperature than the clean case. The engine face static temperature contours are shown in Figure 5.9.4. Temperature distortion is severer in the glaze case, as compared to the clean inlet, due to massive flow separation that was noted earlier in Figures 5.9.1 to 5.9.3.

The effect of higher free-stream Mach number, namely M_∞=0.85, on distortion levels are shown in Figures 5.9.5 to 5.9.7. The total pressure contours in Figure 5.9.5 show massive flow separation and subsequent lower total pressure recovery in the glaze ice case as compared to the clean inlet. The effect of higher free-stream Mach number is seen in the appearance of shocks in the duct with subsequent flow separation. Therefore, the engine face distortion level is exacerbated by a higher free-stream Mach number. The Mach distribution in the duct symmetry plane is shown in Figure 5.9.6. The intersecting oblique shocks and their multiple reflections from the wall are visible in the glaze ice case. The shock cell structure

starts at the throat and multiple cells persist into the first and second bends of the S-duct inlet. The static temperature profile in the duct symmetry plane is shown in Figure 5.9.7. The static temperature distortion is dominated by the shocks and massive flow separation in the duct. The clean inlet case shows a large separation zone at the top of the duct ($\theta=0^o$), whereas the glaze ice case shows a massive flow separation on the bottom, i.e., $\theta=180^o$. Therefore, the engine face temperature distortion corresponds to the separated zones in the two cases, as shown in Figure 5.9.8.

The effect of the free-stream Mach number on engine face temperature distortion, for a clean inlet, is shown in Figure 5.9.9. Two separated zones on top and bottom of the (clean) S-duct inlet at $M_\infty=0.85$ versus a single separation at the bottom ($\theta=180^o$) for $M_\infty=0.475$ are the dominant sources of temperature non-uniformity at the engine face. Therefore, the higher free-stream Mach number exacerbates temperature distortion at the engine face, primarily due to the appearance of the shocks in the duct and flow separation topology. The effect of the free-stream Mach number on temperature distribution at the engine face in the glaze iced inlet is shown in Figure 5.9.10. It is noted that the lower free-stream Mach number ($M_\infty=0.475$) creates a smoother temperature profile at the engine face than the case of $M_\infty=0.85$, where repeated shock cells appeared in the duct and flow separation at the engine face become massive. As a result, temperature distortion is much more pronounced in the glazed ice case with the higher free-stream Mach number.

To simulate a heated wall and the study of engine face distortion, a constant wall temperature of $T_w=350$ K is considered. The area-averaged engine face

parameters, for the clean inlet, at two free-stream Mach numbers are summarized in Table 5.9.1. The case of glaze ice is also summarized in Table 5.9.2. The results suggest that the total pressure recovery is reduced with the heated wall at both low and high free-stream Mach numbers. Also, the mass flow rate drops 2.54 percent for the glazed ice inlet at M_∞=0.85 with the heated wall boundary condition. The reduced mass flow rate corresponds to lower densities in the flow when the wall is heated, as expected.

The total pressure distortion at the engine face with the adiabatic and heated wall boundary conditions for the clean inlet case at M_∞=0.85 is shown in Figure 5.9.11. The impact of heated wall is seen to be small for the clean inlet. Temperature distortion is more pronounced with heated wall, as shown in Figure 5.9.12. It is shown in the figure that a vivid separation of cold versus hot zones in the clean inlet case with heated wall. The glaze ice results at the engine face are shown in Figures 5.9.13. The total pressure distortion is larger and more pronounced with wall heating, as closer examination of Figure 5.9.13 reveals. Similar behavior is observed for the temperature distortion at the engine face as shown in Figure 5.9.14, where higher gradients and larger low and high temperature zones are produced in the heated wall case.

The amplitude of static temperature distortion at the engine face, $\Delta T_{ef,max}$ is also a critical parameter, as evidenced in engine tests[57] shown in Figure 3.5.1. Therefore, the temperature distortion amplitudes in the glaze case with adiabatic and heated wall are also examined in the present study. The non-dimensional distortion parameters for the cases of clean and glazed ice are summarized in Tables 5.9.3 and

5.9.4. The parameters, DP, DC, $\Delta T_{ef,\ max}$, and TD, are defined by Equations (5), (6), (8), and (9), respectively, in Chapters 3.4 and 3.5. The clean inlet at M_∞=0.85 shows the total pressure recovery of 0.789 (adiabatic wall). At the same free-stream Mach number, the glazed ice inlet gives 0.61 of total pressure recovery. This significant drop in the inlet performance is due to the glaze ice horns that induce a flow blockage and boundary layer separation, and reflected shock cells in the S-duct inlet.

Also, the effect of heated wall in both the clean and glaze iced inlet is examined. The total pressure recovery remains to within 0.5 percent of the heated case versus the adiabatic wall for the clean inlet and about 0.5 percent reduction in the glaze ice case. It is also noted that the total pressure distortion parameter, DP, is 6.97 percent higher in the heated wall case, as compared to adiabatic wall in the glazed ice inlet. This coupled performance degradation between the temperature and total pressure distortion may also be seen in the DC(60) parameter, which shows 4.24 percent higher distortion with heating. The temperature distortion parameter, TD, shows a considerable rise in heated wall case, as expected, i.e., an increase of approximately 67 percent when the wall is heated to T_w=350 K.

The amplitude of temperature distortion, $\Delta T_{ef,\ max}$, is however more substantial. In the glaze ice case and at M_∞=0.85, the maximum temperature distortion amplitude reaches about 87 K (or ^oC) level, which is equivalent to about 156 ^oR (or ^oF). This result shows much higher amplitude for temperature distortion than the engine tests reported in Figure 3.5.1. In the engine tests, a ΔT=100 ^oF (i.e., 55.6 ^oC) distortion of about 90^o-100^o circumferential extent is seen to stall the high-pressure compressor operating at its 90 percent corrected flow. The temperature

distortion of the glaze ice case at M_∞=0.85 occurs at about 100° circumferential extension as shown in Figure 5.9.14. Consequently, the similar level of stall pressure degradation with temperature distortions in the S-duct inlet is expected, as compared to engine tests results shown in Figure 3.5.1. Therefore, these amplitudes are significant enough to warrant additional studies in inlet icing with heated walls.

The conclusion is that the temperature distortion in inlets with icing effects is real and significant. The free-stream Mach number and heated wall exacerbate the distortion levels at the engine face. Also, temperature distortion couples with total pressure distortion to create a higher engine face distortion level that may lead to a compressor stall or engine surge. The amplitude of temperature distortion in the glaze ice accretion case at the high subsonic free-stream Mach number is large, and it may adversely affect the performance of the M2129 S-duct and the compressor stall margin.

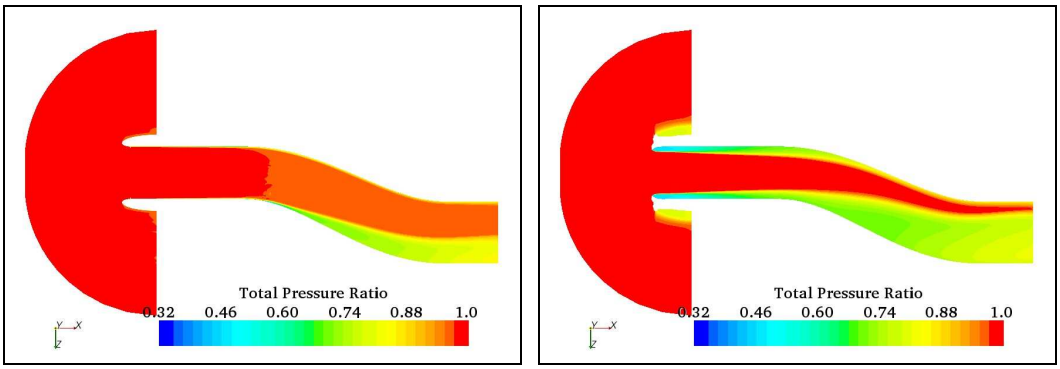

(a) Clean (b) Glaze

Figure 5. 9. 1: Total pressure (Pt/Pt_∞) distribution in the duct symmetry plane (Pt_∞=101.1 kPa, M_∞=0.475, $\alpha=\beta=0^o$)

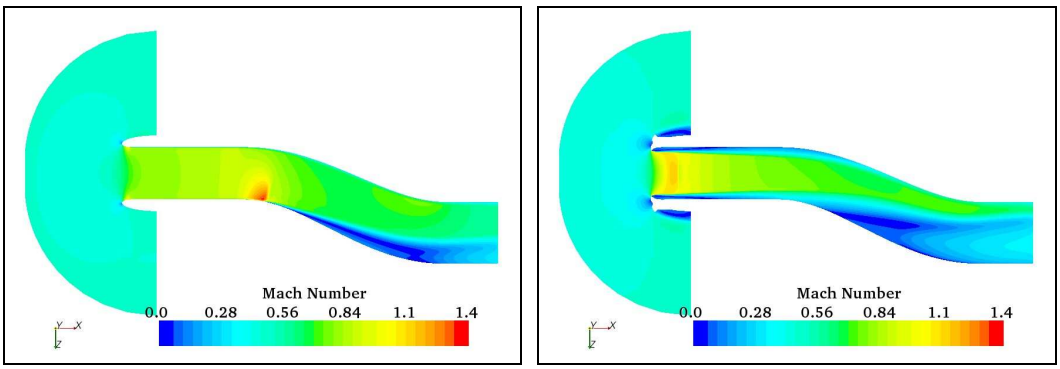

(a) Clean (b) Glaze

Figure 5. 9. 2: Mach number distribution in the duct symmetry plane (M_∞=0.475, $\alpha=\beta=0^o$)

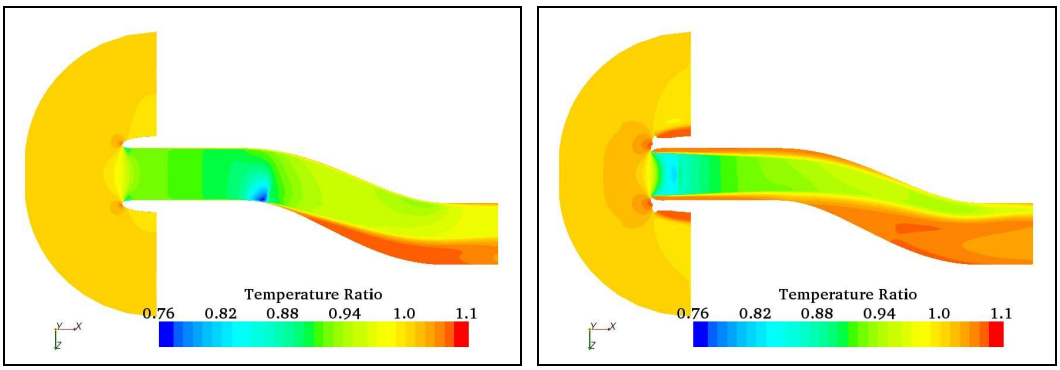

(a) Clean (b) Glaze

Figure 5. 9. 3: Static temperature (Ts/Ts_∞) distribution in the duct symmetry plane (Ts_∞= 255 K, M_∞= 0.475, $\alpha=\beta=0^o$)

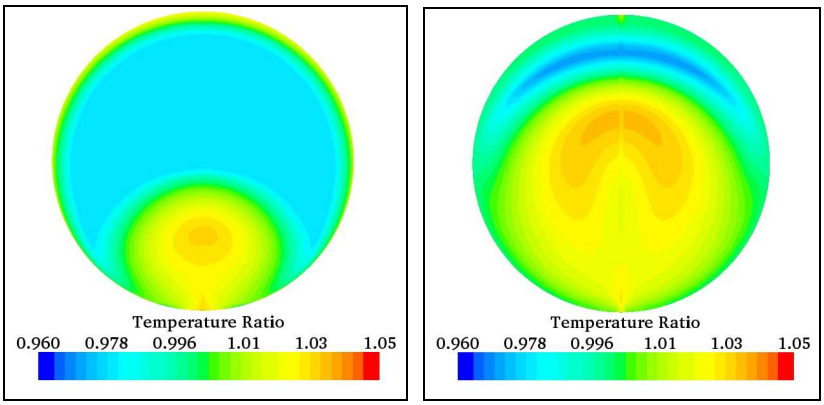

(a) Clean (b) Glaze

Figure 5. 9. 4: Static temperature (Ts/Ts_∞) distribution at the engine face (Ts_∞= 255 K, M_∞ = 0.475, $\alpha=\beta=0^o$)

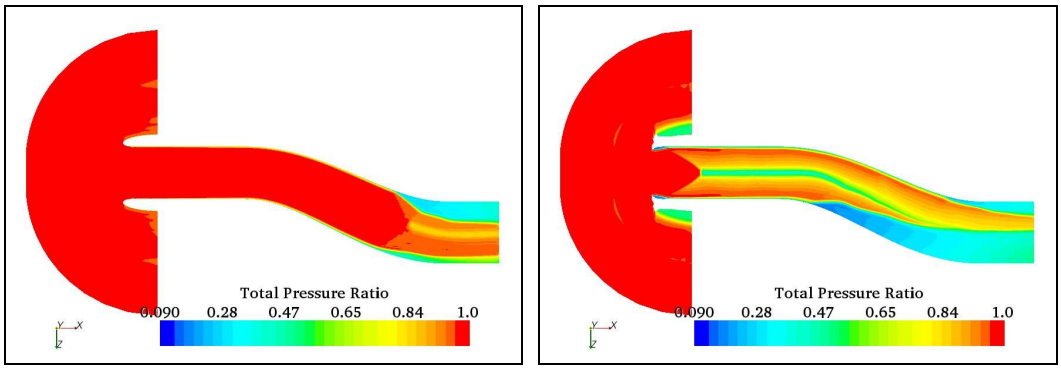

(a) Clean (b) Glaze

Figure 5. 9. 5: Total pressure (Pt/Pt_∞) distribution in the duct symmetry plane (Pt_∞=101.1 kPa, M_∞=0.85, $\alpha=\beta=0^o$)

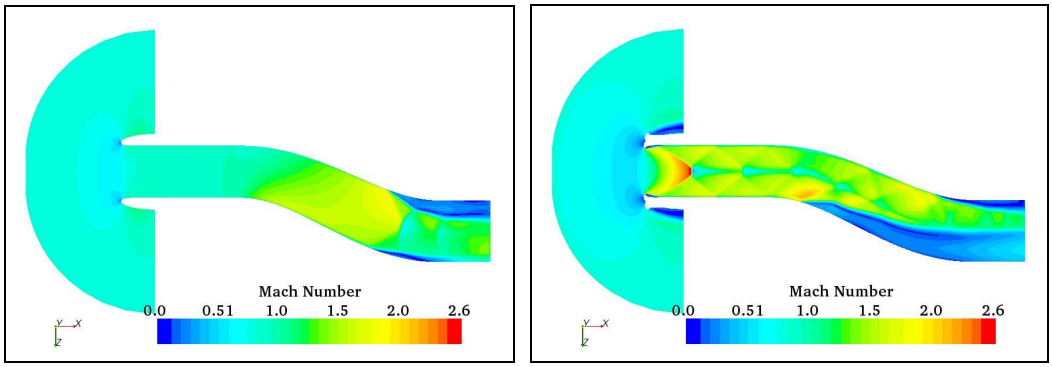

(a) Clean (b) Glaze

Figure 5. 9. 6: Mach number distribution in the duct symmetry plane (M_∞=0.85, $\alpha=\beta=0^o$)

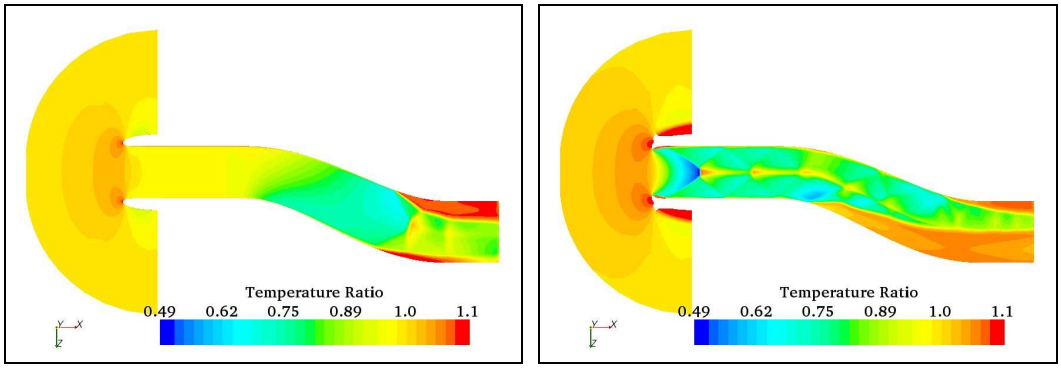

(a) Clean (b) Glaze

Figure 5. 9. 7: Static temperature (Ts/Ts_∞) distribution in the duct symmetry plane (Ts_∞= 233 K, M_∞= 0.85, $\alpha=\beta=0^o$)

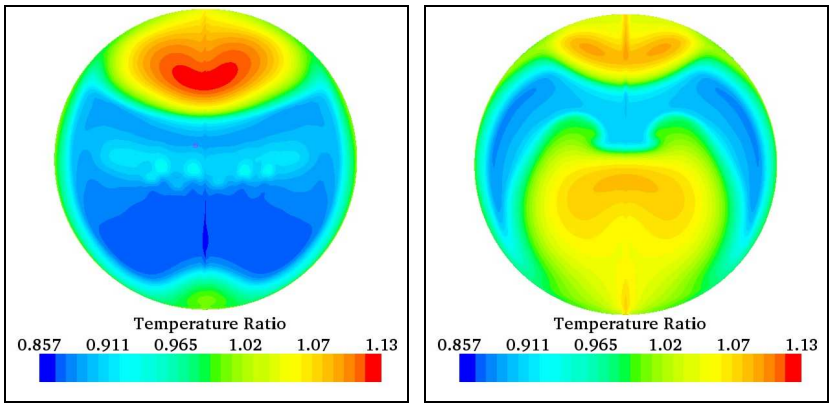

(a) Clean (b) Glaze

Figure 5. 9. 8: Static temperature (Ts/Ts_∞) distribution at the engine face (Ts_∞= 233 K, M_∞ = 0.85, $\alpha=\beta=0^o$)

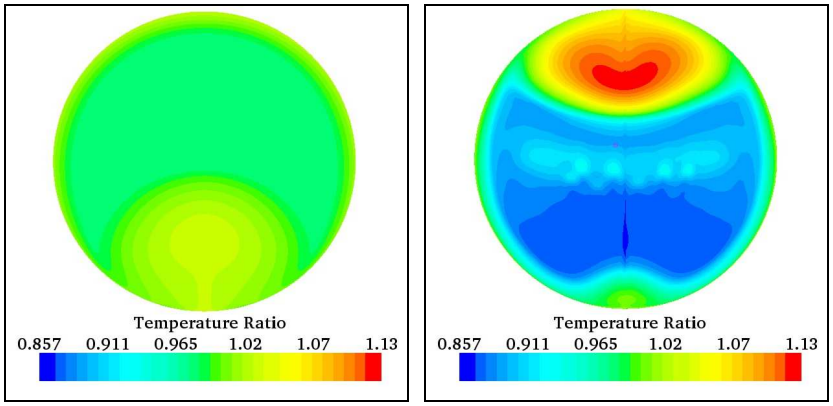

(a) Ts_∞= 255 K, M_∞= 0.475 (b) Ts_∞= 233 K, M_∞= 0.85

Figure 5. 9. 9: Static temperature (Ts/Ts_∞) distribution at the engine face (clean)

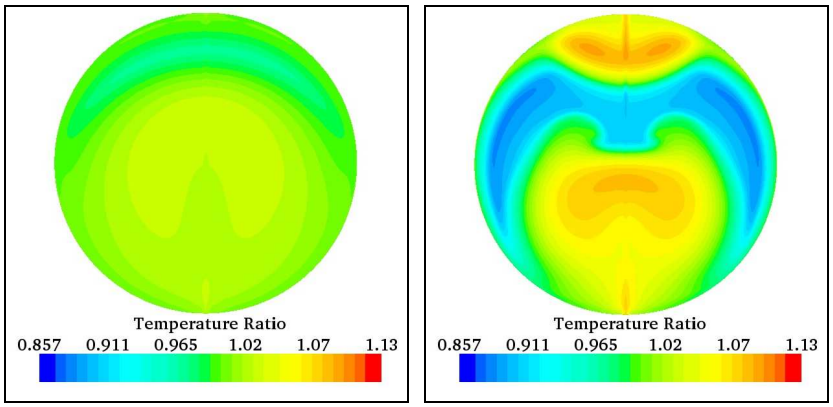

(a) Ts_∞= 255 K, M_∞= 0.475 (b) Ts_∞= 233 K, M_∞= 0.85

Figure 5. 9. 10: Static temperature (Ts/Ts_∞) distribution at the engine face (glaze)

Table 5. 9. 1: Changes in area-averaged properties at the engine face with adiabatic and heated wall (clean)

Flowfield Properties	Clean M_∞= 0.475 Adiabatic wall	Clean M_∞= 0.475 T_W =350 K	Increment (%)	Clean M_∞= 0.85 Adiabatic wall	Clean M_∞= 0.85 T_W =350 K	Increment (%)
Total pressure (kPa)	95.751	95.654	-0.11	79.770	80.034	0.33
Static pressure (kPa)	80.217	79.941	-0.34	37.325	37.517	0.52
Static temperature (K)	253.58	257.41	1.51	215.54	220.83	2.45
Mach No.	0.50	0.50	0.68	1.05	1.04	-0.70
Mass flow Rate (kg/sec.)	22.45	22.39	-0.27	22.49	22.40	-0.44

Table 5. 9. 2: Changes in area-averaged properties at the engine face with adiabatic and heated wall (glaze)

Flowfield Properties	Glaze M_∞= 0.475 Adiabatic wall	Glaze M_∞= 0.475 T_W =350 K	Increment (%)	Glaze M_∞= 0.85 Adiabatic wall	Glaze M_∞= 0.85 T_W =350 K	Increment (%)
Total pressure (kPa)	84.497	84.379	-0.14	61.726	61.415	-0.51
Static pressure (kPa)	76.319	76.021	-0.39	38.562	38.081	-1.25
Static temperature (K)	258.87	265.46	2.55	232.15	239.35	3.10
Mach No.	0.37	0.37	1.08	0.76	0.76	-0.04
Mass flow Rate (kg/sec.)	15.10	15.03	-0.42	17.05	16.61	-2.54

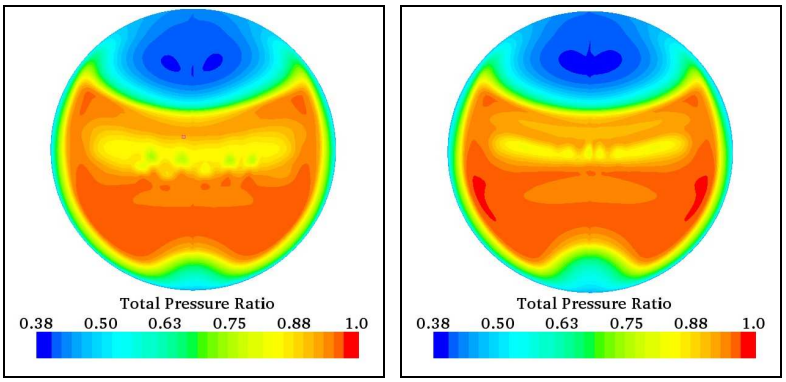

(a) Adiabatic wall (b) Heated wall (T_W= 350 K)

Figure 5. 9. 11: Total pressure distortion at the engine face with adiabatic and heated wall boundary conditions (clean, M_∞= 0.85, α=β=0º)

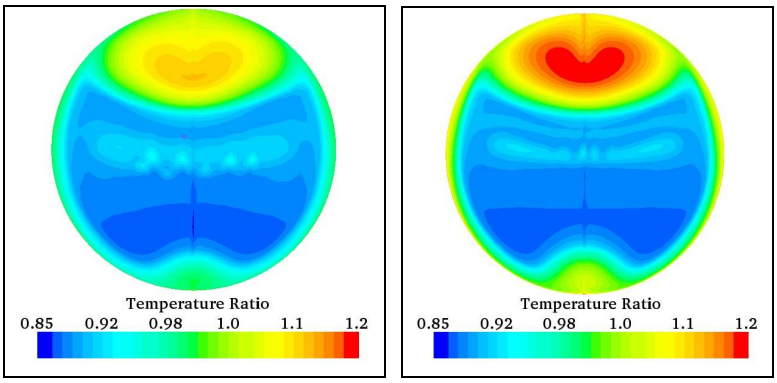

(a) Adiabatic wall (b) Heated wall (T_W= 350 K)

Figure 5. 9. 12: Static temperature distortion at the engine face with adiabatic and heated wall boundary conditions (clean, M_∞= 0.85, α=β=0º)

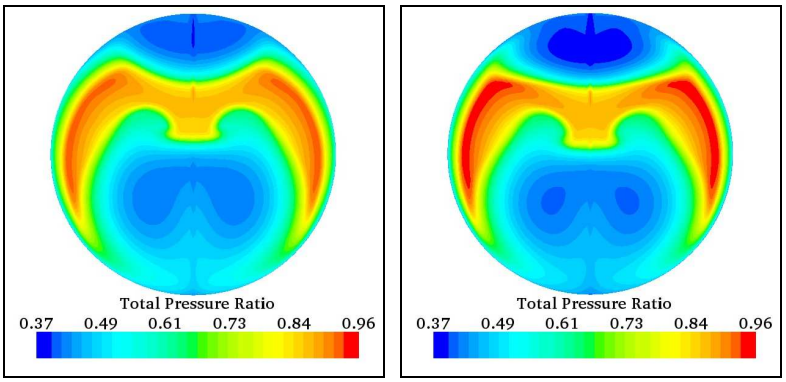

(a) Adiabatic wall (b) Heated wall (T_W= 350 K)

Figure 5. 9. 13: Total pressure distortion at the engine face with adiabatic and heated wall boundary conditions (glaze, M_∞= 0.85, α=β=0º)

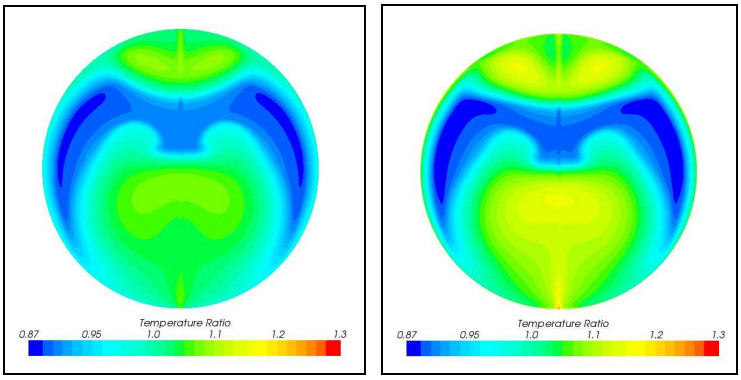

(a) Adiabatic wall (b) Heated wall (T_W= 350 K)

Figure 5. 9. 14: Static temperature distortion at the engine face with adiabatic and heated wall boundary conditions (glaze, M_∞= 0.85, α=β=0º)

Table 5. 9. 3: Distortion parameters at the engine face (clean)

Flowfield Properties	Clean M_∞= 0.475 Adiabatic wall	Clean M_∞= 0.475 T_W =350 K	Increment (%)	Clean M_∞= 0.85 Adiabatic wall	Clean M_∞= 0.85 T_W =350 K	Increment (%)
Total pressure recovery	0.9469	0.9459	-0.11	0.7888	0.7914	0.33
DC(60)	0.6643	0.6314	-4.95	1.0677	1.0650	-0.25
DP	0.1796	0.1846	2.78	0.7354	0.7418	0.87
$\Delta T_{ef,max}$ (K)	14.77	62.4	322.48	62.8	73.34	16.78
TD	0.0582	0.2424	316.49	0.2914	0.3321	13.97

Table 5. 9. 4: Distortion parameters at the engine face (glaze)

Flowfield Properties	Glaze M_∞= 0.475 Adiabatic wall	Glaze M_∞= 0.475 T_W = 350 K	Increment (%)	Glaze M_∞= 0.85 Adiabatic wall	Glaze M_∞= 0.85 T_W =350 K	Increment (%)
Total pressure recovery	0.8356	0.8344	-0.14	0.6104	0.6073	-0.51
DC(60)	0.3696	0.3772	2.06	0.8018	0.8358	4.24
DP	0.2597	0.2601	0.15	0.9028	0.9657	6.97
$\Delta T_{ef,max}$ (K)	17.07	46.33	171.41	50.25	86.59	72.32
TD	0.0659	0.1745	164.80	0.2165	0.3618	67.11

6. Conclusions

The steady- and unsteady-state computational studies have investigated the performance of the M2129 S-duct inlet when different ice shapes were simulated on the inlet lip. Based on the results presented and discussed in Chapter 5, the following conclusions can be made:

- The effects of the rime ice accretion, which induced a relatively streamlined inlet lip shape, on the performance of the S-duct inlet were insignificant. However, the glaze ice accretion produced a substantial degradation of the inlet performance due to the massive flow separation from its intrusive ice horn. Total pressure recovery ($\overline{Pt}_{ef}/Pt_{\infty}$), which indicated the steady-state inlet distortion level of the S-duct inlet, was decreased by just 0.02 percent with the rime ice at M_{∞}=0.24, while the glaze ice induced a 3.2 percent decrease at M_{∞}=0.23. In addition, the glaze ice caused a nearly 26 percent reduction in the inlet mass flow rate.

- The degradation of the inlet performance, caused by the glaze ice accretion, became more significant as the free-stream Mach number increased to M_{∞}=0.85, due to the development of stronger and more extensive shock formation in the inlet flow. At M_{∞}=0.85, the level of total pressure recovery with the glaze ice was further decreased by about 22.8 percent, compared to the clean case.

- Therefore, the performance of the glaze iced inlet could not meet the requirement of MIL-E-5007D in steady-state inlet distortion within the free-stream Mach number range investigated, since the glaze ice accretion caused more than 5 percent of the estimated total thrust loss and a 5 percent increase in the specific fuel consumption above M_∞=0.2.

- The asymmetrical glaze ice accretion on the top (θ=315°-45°)- or bottom (θ=135°-225°)-portion of the inlet lip affected the inlet performance less, compared to the symmetrical glaze ice, due to the smaller flow blocking area. The reductions in the total pressure recovery were only 2.4 and 2.6 percent for the top- and bottom-asymmetrical glaze ice shapes at M_∞=0.475, respectively, whereas an 11.8 percent decrease occurred with the symmetrical glaze ice shape at the same free-stream Mach number. The effects of the bottom-asymmetrical glaze ice were slightly more significant than that of the top-asymmetrical glaze ice, because the typical S-duct flow pattern was more affected by the bottom-asymmetrical glaze ice.

- The inlet icing also aggravated the dynamic inlet distortion, which was represented by the total pressure fluctuation at the engine face ($\overline{Pt}'_{rms} / \overline{Pt}_{ef}$). However, the ice-induced flow blockage was also a critical issue for the dynamic inlet distortion, because the total pressure fluctuation level increased by 15 percent with the symmetrical glaze ice at M_∞=0.34, while it increased by just 8 percent with the top-asymmetrical glaze ice.

- The level of the steady-state inlet distortion was not significantly affected by the glaze ice horn thickness. However, the sharper glaze ice horn with the radius decreased by 27 percent induced an 11 percent higher total pressure fluctuation, compared to the original-glaze ice.

- All local angles of attack and local sideslip angles contributed to the degradation of the inlet performance, combined with the effects of the symmetrical glaze ice. In particular, higher positive angles of attack resulted in more serious steady-state inlet distortion. At α=0º, the reduction in the total pressure recovery by the symmetrical glaze ice was about 6.8 percent. However, it further decreased to 8.5 percent at α=+20º from the total pressure recovery of the clean case.

- With the asymmetrical glaze ice shapes, the inlet performance was also adversely affected by the local angles of attack or local sideslip angles. However, the influence of each ice shape became more significant at a specific angle, due to the combined effect of the angle of attack or sideslip angle, icing location, and downward duct curvature. Both the steady-state and dynamic inlet distortion became most severe at the highest angles tested, α=-20º, α=+20º, and β=-20º, for the top (θ=315^o-45°)-, bottom (θ=135^o-225°)-, and side (θ=45^o-135°)-glaze ice, respectively. Therefore, the level of dynamic inlet distortion was proportional to the steady-state inlet distortion level, regardless of the ice accretion shapes.

- Under the icing condition, the inlet wall heating exacerbated both the total pressure and temperature distortion at the engine face. The levels of total pressure distortion parameter (DP) and temperature distortion parameter (TD) increased 6.97 and 67.11 percent, respectively, with the glaze ice accretion and heated wall condition (T_w=350 K) at M_∞=0.85. Therefore, the temperature distortion combined with the total pressure distortion to create a higher engine face distortion that may lead to a compressor stall or engine surge.

7. Recommendations

The following recommendations can be made from the present study for future investigations:

- The investigation of more various ice accretion shapes, such as run back ice shape and different glaze ice shapes on the performance of an S-duct inlet are needed. Run back ice is a ridge shape ice formed behind the heating type-anti icing system at the leading edge of an inlet lip.[92] Also, in a real meteorological and flight icing conditions, including non-zero angle of attack condition, various glaze ice shapes exist with different horn lengths, horn angles, stagnation region thicknesses, etc.[18]

- The simulation of a time-dependent multiphase flow is required to investigate the effect of more realistic icing phenomena on an S-duct inlet. It is known that a shape of ice accretion on a surface of aircraft changes with time according to the icing time, free-stream velocity (V_∞) and temperature (Ts_∞), liquid water contents (LWC), etc.[8]

- As mentioned in the present study, the flow blockage induced by ice accretion on an inlet lip was an important factor for the degradation of an inlet performance. Therefore, the effect of various flow blockage levels must be investigated to find the most critical icing limit on the inlet performance.

- The effects of ice accretion that take place on different sections of an S-duct inlet, other than an inlet lip, should be investigated. An experimental study showed that ice accretion occurred not only at an external inlet lip, but also along the interior side wall of an inlet duct.[13]

- The effects of S-duct inlet geometry, combined with icing effects, need to be investigated. Curvature effects in an S-duct inlet can change the formation of a counter-rotating vortex pair from the duct curvature, and subsequently alter the secondary flow development at the engine face. Also, an S-duct inlet with out-of-plane, where a duct symmetry plane does not exist, can induce an asymmetrical secondary flow pattern at the engine face.

- The validation of the unsteady-state computations in the present study was unsatisfactory at some free-stream Mach numbers, since the computational setup was not optimized for all Mach number ranges. Therefore, the validation must be improved by controlling the parameters for an unsteady-state computation, such as a mesh size, time-step size, and the maximum inner iteration number.

- Using a much smaller time-step size, the frequency contents of total pressure fluctuation at the engine face must be investigated to obtain more detailed information of the dynamic inlet distortion under the icing condition.

- Under the icing conditions, the effects of the atmospheric gusts or atmospheric turbulence on the dynamic inlet distortion should be studied. The total pressure fluctuations investigated in the present study were caused by the internally-generated unsteadiness from the duct curvature. However, the externally-generated disturbances, including atmospheric gusts, can be another source of the dynamic inlet distortion.[86] Actually, an experimental study showed that the velocities of the atmospheric gust were related to the degradation of dynamic performance of a supersonic inlet.[93]

- The present study showed that the amplitude of temperature distortion in the glaze iced S-duct inlet was significant with the heated wall condition, as compared to data from the actual engine performance tests.[57] Therefore, further investigation is required to clarify the mechanism of the increased temperature distortion in an iced S-duct inlet with heated walls.

References

[1] Cole, J. and Sand, W., "Statistical Study of Aircraft Icing Accidents," AIAA Paper 91-0558, Jan. 1991.

[2] Koenig, G. G., Ryerson, C. C., and Kmiec, R., "UAV Icing Flight Simulation," AIAA Paper 2002-0812, Jan. 2002.

[3] Poots, G., "Ice and Snow Accretion on Structures," *Research Studies Press LTD*, UK, 1996.

[4] Macklin, W. C., "The Density and Structure of Ice Formed by Accretion," *Quarterly Journal of the Royal Meteorological Society*, Vol. 88, No. 1, pp. 30~50, 1962.

[5] Steven, D. G., "A Study of U.S. Inflight Icing Accidents and Incidents, 1978 to 2002," AIAA Paper 2006-82, Jan. 2006.

[6] Broughton, H., Owens, J., Sims, J. J., and Bond, T. H., "Determination of Shed Ice Particle Size Using High Speed Digital Imaging," NASA TM-107406, 1997.

[7] Mason, J. G., Strapp, J. W., and Chow, P., "The Ice particle Threat to Engines in Flight," AIAA Paper 2006-206, Jan. 2006.

[8] Bidwell, C. S. and Mohler, S. R. Jr., "Collection Efficiency and Ice Accretion Calculations for a Sphere, a Swept MS(1)-317 Wing, a Swept NACA-0012 Wing Tip, an Axisymmetric Inlet, and a Boeing 737-300 Inlet," AIAA Paper 95-0755, 1995.

[9] GAMBIT Software Package, Ver. 2.2.30, Fluent Inc., Lebanon, NH, 2004.

[10] FLUENT Software Package, Ver. 6.2.16, Fluent Inc., Lebanon, NH, 2005.

[11] STAR-CCM+ Software Package, Ver. 2.10.013, CD-adapco Inc., Melville, NY, 2007.

[12] Addy. Jr., H. E., "Ice Accretions and Icing Effects for Modern Airfoils," NASA TP-2000-210031, 2000.

[13] Papadakis, M., Hung, K. E., Vu, G. T., Yeong, H. W., Bidwell, C. S., Breer, M. D., and Bencic, T. J., "Experimental Investigation of Water Droplet Impingement on Airfoils, Finite Wings, and an S-Duct Engine Inlet," NASA TM 2002-211700, Oct. 2002.

[14] Hansman, R. J., "Analysis of Surface Roughness Generation in Aircraft in Ice Accretion," AIAA Paper 92-0298, Jan. 1992.

[15] Hansman, R. J., Breuer, K. S., Hazan, D., Reehorst, A., and Vargas, M., "Close-Up Analysis of Aircraft Ice Accretion," NASA TM 105952, 1993.

[16] Venkataramani, K. S., Caney, R. D., Balan, C., and Plybon, R. C., "Wind Tunnel Tests and Modeling Studies of Ice Accretion Relevant to Aircraft Engines," AIAA Paper 2003-906, Jan. 2003.

[17] Wright, W. B., "Users Manual for the Improved NASA Lewis Ice Accretion Code LEWICE 1.6," NASA CR-198355, 1995.

[18] Wright, W. B., "Validation Results for LEWICE 2.0," NASA CR-1998-208690, 1998.

[19] Chung, J., Reehorst, A. L., Choo, Y. K., and Potapczuk, M. G., "Effect of Airfoil Ice Shape Smoothing on the Aerodynamic Performance," AIAA Paper 98-3242, Jul. 1998.

[20] Bidwell, C. S. and Potapczuk, M. G., "Users Manual for the NASA Lewis Three-Dimensional Ice Accretion Code (LEWICE3D), NASA TM-105974, 1993.

[21] Papadakis, M., Zumwalt, G. W., Elangonan, R., Freund, G. A. Jr., Breer, M., and Whitmer, L., "An Experimental Method for Measuring Water Droplet Impingement Efficiency on Two- and Three-Dimensional Bodies," NASA CR-4257, 1989.

[22] Acker, L. W. and Kleinknecht, K. S., "Effects of Inlet Icing on Performance of Axial-Flow Turbojet Engine in Natural Icing Conditions," NACA Research Memorandum E50C15, 1950.

[23] Gelder, T. F., "Total-Pressure Distortion and Recovery of Supersonic Nose Inlet with Conical Centerbody in Subsonic Icing Conditions," NACA Research Memorandum E57G09, 1957.

[24] Bragg, M. B., Khodadoust, A., and Spring, S. A., "Measurement in a Leading-Edge Separation Bubble due to a Simulated Airfoil Ice Accretion," *AIAA Journal*, Vol. 30, No. 6, pp 1462-1467, 1992.

[25] Kim, H. S. and Bragg, M. B., "Effects of Leading –Edge Ice Accretion Geometry on Airfoil Performance," AIAA Paper 99-3150, Jun. 1999.

[26] Broeren, A. P., Addy. Jr., H. E., and Bragg, M. B., "Flowfield Measurements about an Airfoil with Leading-Edge Ice Shapes," AIAA Paper 2004-559, Jan. 2004.

[27] Potapczuk, M. G., "Numerical Analysis of an NACA 0012 Airfoil with Leading-Edge Ice Accretion," *Journal of Aircraft*, Vol. 25, No. 3, pp 193-194, Mar. 1988.

[28] Shim, J., Chung, J., and Lee, K. D., "A Comparison of Turbulence Modeling in Flow Analysis of Iced Airfoils," AIAA Paper 2000-3920, Aug. 2000.

[29] Bush, R. H., Power, G. D., and Towne, C. E., "WIND: The Production Flow Solver of the NPARC Alliance," AIAA 98-0935, Jan. 1998.

[30] Shim, J., Chung, J., and Lee, K. D., "A Computational Investigation of Ice Geometry Effects on Airfoil Performances," AIAA Paper 2001-0540, Jan. 2001.

[31] Thompson, D., Mogili, P., and Chalasani, S., "A Computational Icing Effects Study for a Three-Dimensional Wing," AIAA Paper 2004-561, Jan. 2004.

[32] Grismer, M. J., Strang, W. Z., Tomaro, R. F., and Witzeman, F. C., "Cobalt: A parallel, implicit, unstructured Euler/Navier-Stokes solver," Advances in Engineering Software, Vol. 29, No. 3, pp. 365-373(9), Apr. 1998.

[33] Chi, X., Li, Y., Chen, H., Addy, H. E., Choo, Y. K., and Shih, T. I-P., "Comparative Study Using CFD to Predict Iced Airfoil Aerodynamics," AIAA Paper 2005-1371, Jan. 2005.

[34] Lee, S., Loth, E., Broeren, A. P., and Bragg, M. B., "Simulation of Icing on a Cascade of Stator Blades," AIAA Paper 2006-208, Jan. 2006.

[35] Poots, G., "Ice and Snow Accretion on Structures," Research Studies Press LTD, UK, 1996.

[36] Mason, B. J., "The Physics of Clouds," Clarendon Press, Oxford, 1957.

[37] Brown, R. D. and Krishnasamy, S. G., "Climatological Ice Accretion Modeling," Report No. 84-10, Atmospheric Environment Service, Ontario, Canada, 1984.

[38] Politovich, M. K., "Predicting Glaze or Rime Ice Growth on Airfoils," *Journal of Aircraft*, Vol. 37, No.1, Jan.-Feb., 2000.

[39] Henry, R., Guffond, D., Aschettino, S., and Duprat, G., "Characterization of Ice Roughness and Influence on Aerodynamic Performance of Simulated Ice Shapes," AIAA Paper 2001-0092, Jan. 2001.

[40] Ting, C. T., Kaldschmidt, G., and Syltebo, B. E., "Design and Testing of New Center Inlet and S-Duct for B-727 Airplane with Refanned JT8D Engines," AIAA Paper 75-0059, Jan. 1975.

[41] Liebeck, R. H., Page, M. A., and Rawdon, B. K., "Blended-Wing-Body Subsonic Commercial Transport," AIAA Paper 98-0438, Jan.1998.

[42] Roman, D., Aleen, J. B., and Liebeck, R. H., "Aerodynamic Design Challenges of the Blended-Wing-Body Subsonic Transport," AIAA Paper 2000-4335, Aug. 2000.

[43] West, T. G., and Luttrell, J. P., "F-22 Inlet and Duct Ice Detection and Accretion Test," AIAA Paper 1998-572, Jan 1998.

[44] Brear, M. J., Warfield, Z., Mangus, J. F., Braddom, S., Paduano, J. D., and Philhower, J. S., "Flow Separation Within the Engine Inlet of an Uninhabited Combat Air Vehicle (UCAV)," *Journal of Fluids Engineering*, Vol. 126, Issue 2, pp. 266-272, Mar. 2004.

[45] Jirasek, A., "Development and Application of Design Strategy for Design of Vortex Generator Flow Control in Inlets," AIAA Paper 2006-1050, Jan. 2006.

[46] Willmer, A. C., Brown, T. W., and Goldsmith, E. L., "Effects of Intake Geometry on Circular Pitot Intake Performance at Zero and Low Forward Speeds," Aerodynamics of Power Plant Installation, AGARD CP301, Paper 5, pp 51-56, Toulouse, France, May 1981.

[47] Anderson, B. H. and Farokhi, S., "A study of Three Dimensional Turbulent Boundary Layer Separation and Vortex Flow Control Using the Reduced Navier Stokes Equations," *Turbulent Shear Flow Symposium*, Munich, Germany, Sept. 1991.

[48] Harloff, G. J., Reichert, B. A., and Wellborn, B. A., "Navier-Stokes Analysis and Experimental Data Comparison of Compressible Flow in a Diffusing S-Duct," AIAA Paper 92-2699, Jun. 1992.

[49] Anderson, B. H., Reddy D. R., and Kapoor, K., "Study on Computing Separating Flows within a Diffusing Inlet S-Duct," *Journal of Propulsion and Power,* Vol. 10, No. 5, Sept-Oct. 1994.

[50] Marquis, A. J. and Ong, L. Y., "The Use of Linear and Non-Linear Low Reynolds Number Models in the Calculations of Flow in a RAE M2129 S-Duct," *Symposium on Turbulent Shear Flows, 11th, Proceeding*, Vol. 1, pp. 3-7 to 3-12, 8-10 Sept. France, 1997.

[51] Menzies, R. D. D., Badcock, K. J., Barakos, G. N., and Richards, B. E., "Validation of the Simulation of Flow in an S-Duct," AIAA Paper 2002-2808, Jun. 2002.

[52] Lee, B. J., Kim, C., and Rho, O., "Optimal Shape Design of the S-Shaped Subsonic Intake Using NURBS," AIAA Paper 2005-455, Jan. 2005.

[53] Anderson, B. H. and Gibb, J., "Vortex Generator Installation Studies on Steady State and Dynamic Inlet Distortion," NASA TM-107220, 1996

[54] Anderson, B. H., Miller, D. N., Addington, G. A, and Agrell, J., "Optimal Micro-Vane Flow Control for Compact Air Vehicle Inlets," NASA TM 2004-212936, 2004.

[55] Mohler, S. R. Jr., "WIND-US Flow Calculations for the M2129 S-Duct Using Structured and Unstructured Grids," AIAA Paper 2004-525, Jan. 2004.

[56] Johnson, R. W., "The Handbook of Fluid Dynamics," the 1st edition, Springer publishing Co., 1998.

[57] Burcham, F. W. Jr., Calogeras, J. E., Meyer, C. L., Povolny, J. H., and Rudey, R. A., "Effects of Engine Inlet Disturbances on Engine Stall Performance," Paper in NASA-SP 259, Aircraft Propulsion, pp. 313-341, 1971.

[58] Farokhi, S., "Aircraft Propulsion," John Wiley & Sons, Inc., New York, 2008.

[59] Seddon, J. and Goldsmith, E. L., "Intake Aerodynamics," the 2nd edition, AIAA Inc. and Blackwell Science Ltd., Osney, UK, 1999.

[60] Greitzer, E. M., Tan, C. S., and Graf, M. B., "Internal Flow: Concepts and Applications," Cambridge University Press, Cambridge, UK, 2004.

[61] Sundaresan, S., Glasser, B. J., and Kevrekidis, I. G., "From Bubbles to Clusters in Fluidized Beds, *Physical Review Letters*, Vol. 81, No. 9, pp. 1849-1852, 1998.

[62] "FLUENT 6.2.12 User's Guide," Fluent Inc., Lebanon, NH, USA, Jan. 2005.

[63] Dhanabalan, S. S. and Won, K. S., “S-shaped Intake Duct Parametrization,” AIAA Paper 2006-3317, Jun. 2006.

[64] Hunt, D. L. and May, N. E., “Practical Use of Transport Turbulence Models in Aerospace-CFD Implementation and Applications,” AIAA Paper 99-3137, Jun. 1999.

[65] Slater, J. W., “CFD Methods for Computing the Performance of Supersonic Inlets,” AIAA Paper 2004-3404, July 2004.

[66] Spalart, P. R. and Allmaras, S. R., "A One-Equation Turbulence Model for Aerodynamic Flows", AIAA Paper 92-0439, Jan. 1992.

[67] Shih, T. H., Liou, W. W., Shabbir, A., Yang, Z., and Zhu, J., “A New κ-ε Eddy-viscosity Model for High Reynolds Number Turbulent Flows-Model Development and Validation,” *Computers Fluids,* 24 (3): 227-238, 1995.

[68] Menter, F. R., “Influence of Freestream Values on κ-ω Turbulence Model Predictions,” AIAA Journal, Vol. 30, No. 6, pp 1657~1659, Jun. 1992.

[69] Menter, F. R., “Two-Equation Eddy-Viscosity Turbulence Models for Engineering Applications,” *AIAA Journal*, Vol. 32, No. 8, pp 1598-1605, Aug, 1994.

[70] Shaw, J. A., Peace, A. J., May, N. E., and Pocock, M. F., “Verification of the CFD simulation system SAUNA for complex aircraft configurations,” AIAA Paper 94-393, Jan. 1994.

[71] May, N. E., “A New Vortex Generator Model for Use in Complex Configuration CFD Solvers,” AIAA Paper 2001-2434, Jun. 2001.

[72] Allan, B. G., Yao, C. S., and Lin, J. C., "Numerical Simulations of Vortex Generator Vanes and Jets on a Flat Plate," AIAA Paper 02-3160, Jun. 2002.

[73] Berrier, B. L. and Allan, B. G., "Experimental and Computational Evaluation of Flush-Mounted, S-Duct Inlets," AIAA Paper 2004-764, Jan. 2004.

[74] Allan, B. G. and Owens, L. R., "Numerical Modeling of Flow Control in a Boundary-Layer Ingesting Offset inlet Diffuser at Transonic Mach Number," AIAA Paper 2006-845, Jan. 2006.

[75] AGARD FTP Working Group 13, "Air Intakes for High Speed Vehicles," AR.270, Sept. 1991.

[76] Shur, M., Spalart, P. R., Strelets, M., and Travin, A., "Detached-Eddy Simulation of an Airfoil at High Angle of Attack," In *4th Intl. Symposium on Eng. Tub. Modeling and Experiments*, Corsia, France, May 1999.

[77] "STAR-CCM+ 2.10.013 User's Guide," CD-adapco Inc., Melville, NY, 2007.

[78] Smagorinsky, J., "General Circulation Experiments with the Primitive Equations: I. The Basic Equations," *Mo. Weather Rev.* 91, pp. 99-164, 1963.

[79] Deardorff, J. W., "Three-Dimensional Numerical Study of the Height and Mean Structure of a Heated Planetary Boundary Layer," *Boundary-Layer Meteorol. 7*, pp. 81-106, 1974.

[80] Pope, S. B., "Turbulent Flow," Cambridge University Press., New York, 2000.

[81] Incropera, F. P., Dewitt, D. P., Bergman, T. L., and Lavine, S., "Fundamentals of Heat and Mass Transfer, the 6th edition," John Wiley & Sons, Inc., Hoboken, NJ, USA, 2007.

[82] Pianko, M. and Wazelt, F., "Propulsion and Energetics Panel Working Group 14 on Suitable Averaging Techniques in Non-uniform Internal flows," AGARD Advisory Report, No. 182, Advisory Group for Aerospace Research and Development, Neuilly Sur Seine, France, 2004.

[83] Cumpsty, N. A. and Horlock, J. H., "Averaging Nonuniform Flow for a Purpose," *Journal of Turbomachinery*, Vol. 128, Issue 1, pp. 120-129, Jan. 2006.

[84] Myburgh. R., "A Computational and Experimental Investigation of the Longitudinal Stability Characteristics of the Kline-Fogleman Wing Design," Master's thesis, the University of Kansas, 2005.

[85] MIL-E-5007D General Specification for Engines, Aircraft, Turbojet and Turbofan.

[86] Macmiller, C. J. and Haagenson, W. R., "Unsteady Inlet Distortion Characteristics with the B-1B," *the Propulsion and Energetic 68th (A) Specialists' Meeting*, Munich, Germany, 1986.

[87] Freeman, C., "The Relationship between Steady and Unsteady Spacial Distortion," the 46th meeting of the AGARD Propulsion and Energetics Panel, 1976.

[88] Zaman, K. B. M. Q. and Potapczuk, M. G., "The Low Frequency Oscillation in the Flow over a NACA 0012 Airfoil with an 'Iced' Leading Edge," NASA TM-102018, 1989.

[89] Hercock, R. G. and Williams, D. D., "Distortion-Induced Engine Instability and Aerodynamic Response," AGARD, LS72-Paper No. 3, 1974.

[90] Guo, R. W. and Seddon, J., "An Investigation of the Swirl in an S-Duct," *Aeronautical Quarterly*, Vol. 33., Issue 1, pp. 25-58, 1982.

[91] Jakubowski, A. K. and Luidens, R. W., "Internal Cowl-Separation at High Incidence Angles," AIAA Paper 75-64, Jan. 1975.

[92] Whalen, E. A., Broeren, A. P., Bragg, M. B., and Lee S., "Characteristics of Runback Ice Accretions on Airfoils and their Aerodynamic Effects," AIAA Paper 2005-1065, Jan. 2005.

[93] Barry, F. W., "Effects of Atmospheric Gust Criteria on Supersonic Inlet Performance," AIAA Paper 1966-367, Mar. 1966.